Search for supersymmetry using Higgs boson to diphoton decays and search for long-lived particles using out-of-time trackless jets at $\sqrt{s}$ = 13 TeV

Thesis by
Jiajing Mao

In Partial Fulfillment of the Requirements for the
Degree of
Doctor of Philosophy

CALIFORNIA INSTITUTE OF TECHNOLOGY
Pasadena, California

2023
Defended May 16, 2023

Jiajing Mao
ORCID: 0009-0002-8988-9987

ACKNOWLEDGEMENTS

I would like to express my deepest gratitude to my thesis advisor, Dr. Maria Spiropulu, whose guidance and support have been instrumental in the completion of this thesis. Her expertise, dedication, and patience throughout the research and writing process have been invaluable. I am grateful for the opportunities she has provided me to learn and grow as a researcher, and for her unwavering belief in my abilities. Her feedback and guidance have shaped my research and writing, and I am proud to have had the privilege of working with her. I would like to extend my heartfelt thanks to Dr. Maria Spiropulu for her mentorship, inspiration, and encouragement throughout my academic journey.

I would also like to express my greatest gratitude to my thesis committee members, Dr. Alan J. Weinstein, Dr. Mark B. Wise, and Dr. Sunil Golwala, who provided guidance and feedback throughout the research and writing process. Their expertise and knowledge in the field were invaluable in shaping the direction of my research and refining the content of my thesis. I am grateful for their dedication, time, and effort in reviewing my work and providing constructive criticism, which greatly improved the quality of my research. Their commitment to my project and willingness to share their knowledge and insights has been a tremendous help to me.

I would like to extend my gratitude to the senior researchers who have supported me throughout my thesis research: Dr. Si Xie, Dr. Cristian H. Pena, Dr. Lisa Benato, Dr. Nan Lu, Dr. Adolf Bornheim, Dr. Maurizio Pierini, Dr. Javier M. Duarte, Dr. Anthony LaTorre, Dr. Jean-Roch Vlimant, and Dr. Artur Apresyan. Their expertise, guidance, and mentorship have been invaluable in shaping my understanding of the field and in advancing my research project. I am particularly grateful for the time and effort they dedicated to answering my questions and providing feedback on my work, and I look forward to continuing to learn from them in the future.

In addition, I would like to extend my appreciation to the computing experts, Justas Balcas, and Andres M. Ignatov, and the lab engineer, Lautaro Narvaez, who provided technical support and assistance throughout my research project. Their expertise and knowledge were essential in resolving complex technical issues and challenges that arose during the course of my research. I am grateful for their invaluable support and assistance, and for generously sharing their time and expertise.

I would like to express my heartfelt appreciation to the members of the CALTECH CMS research group, who have provided an encouraging and stimulating environment throughout my thesis journey: Dr. Dustin Anderson, Dr. Zhicai Zhang, Dr. Thong Nguyen, Dr. Irene Dutta, Dr. Olmo Cerri, Jay Lawhorn, and Christina W. Wang. Their collaboration and camaraderie have made my academic experience more enjoyable and fulfilling. I am honored to have worked with such a talented and inspiring group of researchers, and I will always cherish the memories of our time together.

I would like to express my sincere gratitude to the following people and many others, who have been a constant source of support and encouragement throughout my academic journey:
- My Skype group friends: Dr. Yongbin Feng, Dr. Xunwu Zuo, and Dr. Miao Hu.
- My friends I have met at CERN: Dr. Xinmei Niu, Dr. Jue Chen, Dr. Zhi Zheng, Dr. Weidi Yuan, Dr. Yuanyuan Zhang, Le Li.
- My friends I encountered in life: JD. Teona Chan, Xiaozheng Wei.
- My friends I have met at Caltech: Zhiyuan Gao, Dr. Liting Xiao, Yameng Zhang, Yibing Wei, Mengyu Liu, Ge Chen, Dr. Linghui Wang, Chen Li, Dr. Han Hsin Lin, Jinrui Hou, Ziran Zhou, Duxing Hao, Yijun Wang, Jiawei Zhao, Dr. Haolu Zhang, Dr. Xichen Shi, Jiajun Shi.
- My friends from undergraduate school: Sishao Zeng, Lianghuan Liao, Dr. Bo Du.
Thank you all for your constant belief in my abilities and your words of encouragement, which have helped me to persevere during challenging times. I would like to extend my heartfelt thanks to all my friends who have helped me along the way, and I look forward to continuing to cherish our friendships in the years to come.

Finally, I would like to express my deepest gratitude to my family, whose unconditional love, support, and encouragement have been a constant source of strength throughout my academic journey. Their belief in me, even during times of self-doubt, has been invaluable in helping me to persevere and complete this thesis. Their sacrifices, whether big or small, have made it possible for me to focus on my studies and pursue my academic goals. I am grateful for the many ways in which they have supported me, and for always being there to offer words of encouragement and love. I would like to extend my heartfelt thanks to my parents, Jian Mao and Furong He, my brother, Jianing Mao, and my extended family members for their love and support throughout my academic journey.

ABSTRACT

The thesis describes two searches conducted at the Large Hadron Collider with a center-of-mass energy of 13 TeV, using proton-proton collison data collected by the CMS experiment. The supersymmetry (SUSY) search focus on the production of at least one Higgs boson that decays into two photons in the decay chains of pair-produced SUSY particles. The data used has an integrated luminosity of 77.5 fb^{-1}. The events are classified into different search regions based on charged leptons, Higgs boson candidates, and kinematic variables to make them sensitive to different SUSY scenarios. The results reveal no statistically significant excess of events compared to the standard model predictions. The searches exclude bottom squark pair production for bottom squark masses below 510 GeV and a lightest SUSY particle mass of 1 GeV. The wino-like chargino-neutralino production in gauge-mediated SUSY breaking (GMSB) is excluded for chargino and neutralino masses below 235 GeV, with a gravitino mass of 1 GeV. Furthermore, the higgsino-like chargino-neutralino production in GMSB, where the neutralino decays exclusively to a Higgs boson and a gravitino, is excluded for neutralino masses below 290 GeV. The thesis also reports a search for long-lived particles that decay in the outer regions of the CMS silicon tracker or in the calorimeters. The search uses data with an integrated luminosity of 138 fb^{-1}. The identification of long-lived particle decays utilizes a novel technique that combines nearly trackless and out-of-time jet information into a deep neural network discriminator. The results are interpreted using a simplified GMSB model of chargino-neutralino production, where the neutralino is the next-to-lightest supersymmetric particle that decays to a gravitino and either a Higgs or Z boson. The search achieves the highest sensitivity for neutralino proper decay lengths of approximately 0.5 meters and excludes masses up to 1.18 TeV at a 95% confidence level. This search represents the most stringent constraint to date in the mass range from the kinematic limit imposed by the Higgs boson mass up to 1.8 TeV.

PUBLISHED CONTENT AND CONTRIBUTIONS

[1] CMS Collaboration. "Search for long-lived particles using out-of-time trackless jets in proton-proton collisions at $\sqrt{s} = 13$ TeV." In: (Dec. 2022). arXiv: 2212.06695 [hep-ex].
J.M. was one of the leading contributors to this anlysis and the paper is accepted by JHEP.

[2] CMS MTD Collaboration. "Test beam characterization of sensor prototypes for the CMS Barrel MIP Timing Detector." In: *Journal of Instrumentation* 16.07 (2021), P07023. DOI: 10.1088/1748-0221/16/07/P07023. arXiv: 2104.07786 [physics.ins-det].
J.M. participated in the test beam experiments to characterize the performance of the BTL module.

[3] CMS Collaboration. "The Phase-2 Upgrade of the CMS Level-1 Trigger." In: (2020). Final version. URL: https://cds.cern.ch/record/2714892.
J.M. studied the timing level-1 trigger for HL-LHC and the study was included by this TDR.

[4] CMS Collaboration. "Search for supersymmetry using Higgs boson to diphoton decays at $\sqrt{s} = 13$ TeV." In: *Journal of High Energy Physics* 11 (2019), p. 109. DOI: 10.1007/JHEP11(2019)109. arXiv: 1908.08500 [hep-ex].
J.M. was one of the leading contributors to the EWP analysis which was optimized for the electroweak supersymmetry productions.

[5] Federico De Guio. "First results from the CMS SiPM-based hadronic endcap calorimeter." In: *Journal of Physics: Conference Series* 1162.1 (2019), p. 012009. DOI: 10.1088/1742-6596/1162/1/012009.
J.M. participated in the installation of the upgraded hadronic endcap and performed the first result using 2017 and 2018 data.

TABLE OF CONTENTS

LIST OF ILLUSTRATIONS

LIST OF TABLES

Part I

Introduction

Chapter 1

THE STANDARD MODEL OF PARTICLE PHYSICS

In 2012, the Large Hadron Collider (LHC) at CERN announced the discovery of the Higgs boson, a crucial element of the Standard Model (SM) that describes the behavior of fundamental particles and their interactions. The Higgs boson gives particles mass, and its measured properties are consistent with those predicted by the SM. However, there is still a possibility of deviations in its couplings and the existence of additional scalar particles. Given the significance of the Higgs boson discovery, Higgs physics has become an essential component of high-energy physics.

The Standard Model (SM) of particle physics is currently the most widely accepted theory for describing the fundamental building blocks of the universe. In this model, all known matter is made up of particles called quarks (which combine to form protons and neutrons) and leptons (which include electrons). The SM also describes the role of bosons, a group of force-carrying particles, in influencing the behavior of quarks and leptons.

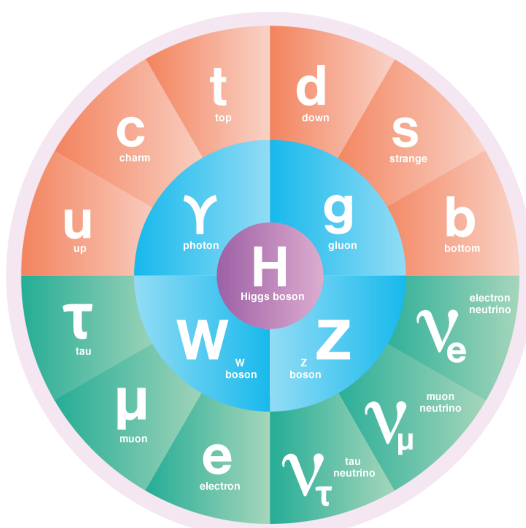

Figure 1.1: The Standard Model includes the matter particles (quarks and leptons), the force carrying particles (bosons), and the Higgs boson [1].

The Standard Model of particle physics describes fundamental interactions in nature, excluding gravity. It includes three interactions: the electromagnetic interaction (quantum electrodynamics or QED), which influences particles with an electric charge; the weak interaction (quantum flavor dynamics or QFD), which influences particles with a weak charge; and the strong interaction (quantum chromodynamics or QCD), which influences particles with a color charge. The Brout-Englert-Higgs (BEH) field is a scalar field that induces spontaneous symmetry-breaking and gives mass to all particles it interacts with, known as the Higgs mechanism. Additionally, the Higgs particle (H) couples with any other particle that has mass, including itself.

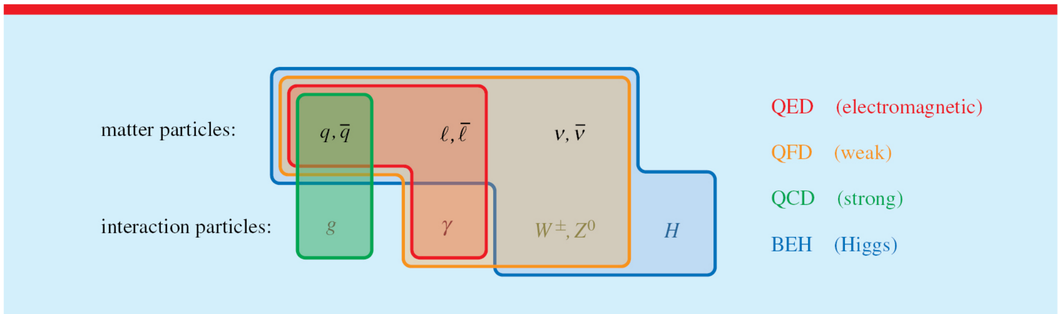

Figure 1.2: Matter particles can be divided into three groups: quarks (q) and antiquarks ($\bar{q}$); electrically charged leptons (l) and antileptons ($\bar{l}$); neutrinos (ν) and antineutrinos ($\bar{\nu}$). Gluons (g) couple to colour charge, which only quarks, antiquarks, and gluons themselves, have. Photons (γ) couple to electric charge, which is found in (anti)quarks and electrically charged (anti)leptons. The weak bosons (W, W^+ , Z^0) couple to the weak charge, which all matter particles have. Weak bosons can also interact with the photon (but this is a pure weak interaction, not an electromagnetic one). And finally, the Brout–Englert–Higgs field interacts with particles that have mass (all particles except the gluon and the photon) [2].

An ultra-short, four-line, coffee mug version of the SM Lagrangian is commonly known (as shown in Fig. 1.3):

$$
\begin{aligned}
\mathcal{L} = -\frac{1}{4}F_{\mu\nu}F^{\mu\nu} \\
+ i\bar{\psi}\not{D}\psi + h.c. \\
+ \psi_i y_{ij}\psi_j\phi + h.c. \\
+ |D^{\mu}\phi|^2 - V(\phi)
\end{aligned}
\tag{1.1}
$$

where

1. $-\frac{1}{4}F_{\mu\nu}F^{\mu\nu}$: This term is the scalar product of the field strength tensor $F_{\mu\nu}$, representing all interaction particles, excluding the Higgs boson.
2. $i\bar{\psi}\not{D}\psi$: This term describes how interaction particles interact with matter particles, where the fields ψ and $\bar{\psi}$ represent quarks and leptons, respectively. The covariant derivative, denoted as $\not{D}$, features all the interaction particles, except for the Higgs boson. Notably, the covariant derivative does not include self-interaction.
3. $h.c.$: Hermitian conjugate of term 2.
4. $\psi_i y_{ij} \psi_j \phi$: This term describes how matter particles couple to the BEH field ϕ and thereby obtain mass, where the y_{ij} is the Yukawa coupling.
5. $h.c.$: Hermitian conjugate of term 4;
6. $|D^{\mu}\phi|^2$: This term describes how the weak interaction particles couple to the BEH field, which results in the particles obtaining mass through the Higgs mechanism.
7. $-V(\phi)$: This term describes the potential of the BEH field, and how Higgs bosons couple to each other.

Figure 1.3: Lagrangian on a coffee mug [2].

1.1 The SM Higgs mechanism

The Higgs mechanism is a fundamental concept in the Standard Model of particle physics that explains how fundamental particles acquire mass. It involves the Higgs field ϕ, which is a scalar field that exists throughout space. The Higgs field interacts with particles in a way that gives them mass through spontaneous symmetry breaking.

The potential of the Higgs field ϕ is

$$V(\phi) = -\mu^2\phi^\dagger\phi + \lambda(\phi^\dagger\phi)^2. \tag{1.2}$$

The Higgs field has a non-zero vacuum expectation value $v = \sqrt{\mu^2/\lambda}$, which means that it has a value even in empty space. When particles interact with the Higgs field, they experience a resistance similar to moving through a viscous fluid. This resistance is what gives particles their mass.

The Higgs mechanism also predicts the existence of a new particle, the Higgs boson, which was discovered in 2012 at the Large Hadron Collider (LHC) at CERN. The discovery of the Higgs boson confirmed the mechanism by which particles acquire mass in the Standard Model.

Chapter 2

SEARCHES FOR PHYSICS BEYOND THE STANDARD MODEL AT THE LHC

Cosmological observations indicate that the standard model can only account for approximately 5% of the total mass-energy present in the universe, with the remaining 95% being made up of dark matter (26%) and dark energy (69%). In particle physics, BSM stands for Beyond the Standard Model, which refers to theories that attempt to explain phenomena that are not accounted for by the Standard Model (SM) of particle physics.

The SM of particle physics does not account for several phenomena, such as the existence of dark matter, the matter-antimatter asymmetry in the universe, and the hierarchy problem. The hierarchy problem refers to the large discrepancy between the mass of the Higgs boson and the Planck scale, which is the scale at which gravity becomes as strong as the other fundamental forces.

2.1 Hierarchy problem and supersymmetry (SUSY)

The hierarchy problem in particle physics is a long-standing issue that arises from the observed mass of the Higgs boson, which is much lighter than the natural scale of particle physics known as the Planck scale. The mass of Higgs boson has been measured to be approximately 125 GeV. The Planck scale, on the other hand, is the energy scale at which gravity becomes as strong as the other fundamental forces and is given by the Planck energy, which is approximately 10^{19} GeV.

The hierarchy problem arises because the quantum fluctuations in the Higgs boson mass are proportional to the energy scale of the virtual particles. As the energy scale of the virtual particles increases, the quantum fluctuations become larger, and the Higgs boson mass becomes heavier. If the energy scale of the virtual particles is much larger than the Higgs boson mass, the quantum fluctuations can become so large that the Higgs boson mass becomes inconsistent with the observed value.

The mass of the Higgs boson, m_H, can be written as a sum of its bare mass, m_{H^0}, and the radiative corrections, Δm_H:

$$m_H^2 = m_{H^0}^2 + \Delta m_H^2. \tag{2.1}$$

The radiative corrections are proportional to the energy scale of the virtual particles, which can be written as Λ. In the absence of new physics, the radiative corrections are expected to be of order:

$$\Delta m_H^2 \sim \frac{\Lambda^2}{16\pi^2}. \tag{2.2}$$

The natural scale of particle physics is the Planck scale, $M_{\text{Pl}} \approx 10^{19}$ GeV, which is the energy scale at which the gravitational force becomes as strong as the other fundamental forces. If we take Λ to be the Planck scale, the radiative corrections would be of order:

$$\Delta m_H^2 \sim \frac{M_{\text{Pl}}^2}{16\pi^2} \approx (10^{18}\ \text{GeV})^2. \tag{2.3}$$

This is many orders of magnitude larger than the observed value of the Higgs boson mass, which is approximately 125 GeV.

Supersymmetry (SUSY) provides a solution to the hierarchy problem by introducing a new symmetry between fermions and bosons. SUSY proposes the existence of a new set of particles, known as supersymmetric particles (as shown on the right of Fig. 2.1). Each particle in the Standard Model would have a corresponding supersymmetric partner, with the same mass and spin but different quantum numbers. For example, the supersymmetric partner of the electron (a fermion) would be a particle called a selectron (a scalar boson).

The contribution of the superpartners to the Higgs boson mass is proportional to the masses of the superpartners. Because the superpartners are not observed, they can have large masses without affecting the observed Higgs boson mass. The cancellation of the quantum corrections to the Higgs boson mass is maintained up to energies of order M_{SUSY}, which is the energy scale at which SUSY is broken.

If we take M_{SUSY} to be of order 1 TeV, the radiative corrections to the Higgs boson mass are reduced to:

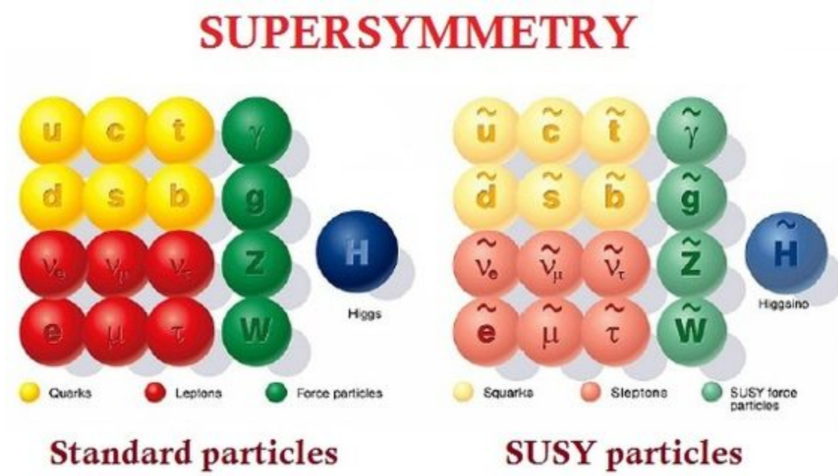

Figure 2.1: Supersymmetry proposes that every particle in the Standard Model, shown at left, has a superpartner particle still awaiting discovery.

$$\Delta m_H^2 \sim \frac{M_{\mathrm{SUSY}}^2}{16\pi^2} \approx (100\ \mathrm{GeV})^2. \tag{2.4}$$

This is much closer to the observed value of the Higgs boson mass, and the parameters of the Standard Model do not need to be finely tuned to achieve this value. Therefore, SUSY provides a natural solution to the hierarchy problem.

In essence, SUSY provides a possible solution to the hierarchy problem by introducing new particles that can cancel out the large quantum corrections to the Higgs boson mass. These new particles are known as supersymmetric partners of the Standard Model particles, and the cancellation occurs due to a delicate interplay between their masses. However, despite extensive searches at the LHC and other experiments, no evidence supporting the existence of SUSY has been found yet.

2.2 The minimal supersymmetric extension of the Standard Model (MSSM)

The MSSM, or minimal supersymmetric extension of the Standard Model, extends the Standard Model by including the fields of a two-Higgs-doublet model, along with their corresponding superpartners. Each particle in the MSSM has a corresponding superpartner forming a supermultiplet [3]. Table 2.1 shows the field content and gauge quantum numbers of the supermultiplets in the MSSM. The electric charge of a particle can be determined by its third component of weak isospin (T_3) and the $U(1)$ weak hypercharge (Y) as $Q = T_3 + \frac{1}{2}Y$.

Table 2.1: The fields of the MSSM and their $SU(3) \times SU(2) \times U(1)$ quantum numbers are listed. For simplicity, only one generation of quarks and leptons is exhibited. For each lepton, quark, and Higgs super-multiplet, there is a corresponding anti-particle multiplet of charge-conjugated fermions and their associated scalar partners [3].

Field content of the MSSM						
Supermultiplets	Superfields	Bosonic fields	Fermionic partners	$SU(3)$	$SU(2)$	$U(1)$
gluon/gluino	$\hat{V}_8$	g	$\tilde{g}$	8	1	0
gauge/	$\hat{V}$	$W^{\pm}, W^0$	$\tilde{W}^{\pm}, \tilde{W}^0$	1	3	0
gaugino	$\hat{V}'$	B	$\tilde{B}$	1	1	0
slepton/	$\hat{L}$	$(\tilde{\nu}_L, \tilde{e}_L^-)$	$(\nu, e^-)_L$	1	2	-1
lepton	$\hat{E}^c$	$\tilde{e}_R^+)$	e_L^c	1	1	2
squark/	$\hat{Q}$	$(\tilde{u}_L, \tilde{d}_L)$	$(u, d)_L$	3	2	1/3
quark	$\hat{U}^c$	$\tilde{u}_R^*)$	u_L^c	$\bar{3}$	1	-4/3
	$\hat{D}^c$	$\tilde{d}_R^*)$	d_L^c	$\bar{3}$	1	2/3
Higgs/	$\hat{H}_d$	(H_d^0, H_d^-)	$(\tilde{H}_d^0, \tilde{H}_d^-)$	1	2	-1
Higgsino	$\hat{H}_u$	(H_u^+, H_u^0)	$(\tilde{H}_u^+, \tilde{H}_u^0)$	1	2	1

In the MSSM, the Higgsino is a neutral, spin-1/2 particle that is a supersymmetric partner of the Higgs boson. It mixes with the electroweak gauge bosons (the Z and W bosons) to form the neutralino and chargino particles, which are also predicted by the MSSM. The Higgsino's interactions with the neutralinos and charginos affect their masses and properties, and the neutralino is a leading candidate for dark matter. Thus, the Higgsino plays a crucial role in both the phenomenology and cosmology of the MSSM.

2.2.1 Higgsino and neutralinos

The Higgsinos are of great interest in particle physics because they are considered as potential dark matter candidates and are predicted to be the lightest supersymmetric particles (LSPs) in certain regions of the MSSM parameter space. Their experimental discovery would provide important evidence for supersymmetry and could potentially help us understand the nature of dark matter.

The MSSM predicts the existence of four neutralinos, which are fermionic superpartners of the neutral gauge bosons (the photon, Z boson, and the neutral components of the Higgs doublets) and are denoted as $\tilde{\chi}_i^0$ (where $i = 1, 2, 3, 4$). The neutralinos are mixtures of the superpartners of the neutral gauge bosons, the Bino ($\tilde{B}$), the Wino ($\tilde{W}^0$), and the Higgsinos ($\tilde{H}_u^0$ and $\tilde{H}_d^0$), and their exact composition depends on the MSSM parameters.

The Higgsino is a linear combination of the superpartners of the neutral Higgs fields and is defined as:

$$\tilde{H}^0 = \tilde{H}_u^0 \cos\theta + \tilde{H}_d^0 \sin\theta, \tag{2.5}$$

where θ is the mixing angle between the two Higgs doublets.

The other neutralinos are similarly defined as mixtures of the Bino, Wino, and Higgsino:

$$\tilde{\chi}_1^0 = N_{11}\tilde{B} + N_{12}\tilde{W}^0 + N_{13}\tilde{H}_u^0 + N_{14}\tilde{H}_d^0, \tag{2.6}$$
$$\tilde{\chi}_1^0 = N_{21}\tilde{B} + N_{22}\tilde{W}^0 + N_{23}\tilde{H}_u^0 + N_{24}\tilde{H}_d^0, \tag{2.7}$$
$$\tilde{\chi}_3^0 = N_{31}\tilde{B} + N_{32}\tilde{W}^0 + N_{33}\tilde{H}_u^0 + N_{34}\tilde{H}_d^0, \tag{2.8}$$
$$\tilde{\chi}_4^0 = N_{41}\tilde{B} + N_{42}\tilde{W}^0 + N_{43}\tilde{H}_u^0 + N_{44}\tilde{H}_d^0, \tag{2.9}$$

where N_{ij} are the elements of the neutralino mixing matrix.

The masses and couplings of the neutralinos are determined by the mixing angles and the parameters of the MSSM, such as the Higgsino mass parameter (μ), the gaugino masses (M_1, M_2), and the ratio of the vacuum expectation values of the two Higgs doublets ($\tan\beta$). The properties of the neutralinos are of great importance in the context of supersymmetric particle searches at colliders, as well as in astrophysical and cosmological studies.

2.2.2 Charginos

In the context of the MSSM, the chargino is a mass eigenstate of the electroweak gauge bosons, formed by the mixing of the charged Wino and Higgsino states. The charged Wino and Higgsino fields can be expressed as two-component spinors:

$$\tilde{W}^{\pm} = \begin{pmatrix} W_L^{\pm} \\ W_R^{\pm} \end{pmatrix}, \tilde{H}^{\pm} = \begin{pmatrix} H_L^{\pm} \\ H_R^{\pm} \end{pmatrix}, \tag{2.10}$$

where the superscripts $\pm$ denote the electric charge, and the subscripts L and R indicate the left- and right-handed components, respectively.

The chargino mass matrix can be written as:

$$\mathcal{M}_{\tilde{W}^{\pm}\tilde{H}^{\pm}} = \begin{pmatrix} M_2 & \sqrt{2}m_W \sin\beta \\ \sqrt{2}m_W \cos\beta & \mu \end{pmatrix} \tag{2.11}$$

where M_2 is the mass of the Wino, m_W is the mass of the W boson, β is the mixing angle in the Higgs sector, and μ is the Higgsino mass parameter.

The chargino mass eigenstates $\tilde{\chi}^{\pm}_{1,2}$ can be obtained by diagonalizing the mass matrix:

$$\begin{pmatrix} \tilde{\chi}^{\pm}_1 \\ \tilde{\chi}^{\pm}_2 \end{pmatrix} = \begin{pmatrix} \cos\theta_W & \sin\theta_W \\ -\sin\theta_W & \cos\theta_W \end{pmatrix} \begin{pmatrix} \tilde{W}^{\pm} \\ \tilde{H}^{\pm} \end{pmatrix}, \tag{2.12}$$

where θ_W is the chargino mixing angle. The chargino masses are given by:

$$m_{\tilde{\chi}^{\pm}_{1,2}} = \frac{1}{2}\left[M_2 + \mu \mp \sqrt{(M_2 - \mu)^2 + 4m_W^2 \sin^2\beta}\right], \tag{2.13}$$

thus the charginos are formed by the mixing of the charged Wino and Higgsino states, and their masses depend on the masses of the Wino, Higgsino, and W boson, as well as the mixing angle in the Higgs sector.

2.2.3 Gravitinos

The gravitino is a hypothetical particle that arises in certain models of supersymmetry, including the Minimal Supersymmetric Standard Model (MSSM). In the MSSM, the gravitino is the superpartner of the graviton, which mediates the force of gravity.

The gravitino is a spin-3/2 fermion that is electrically neutral and interacts very weakly with matter. It is often considered a candidate for dark matter since it does not interact with electromagnetic radiation and other forms of matter in the same way as normal matter.

In the MSSM, the gravitino is typically associated with the Higgsino, neutralino, and chargino particles. This is because these particles are the superpartners of the Higgs boson and the electroweak gauge bosons, which are responsible for the weak nuclear force. The Higgsino, neutralino, and chargino particles can all decay into a gravitino and a corresponding standard model particle.

The coupling of the gravitino to the Higgsino, neutralino, and chargino particles is described by a coupling constant known as the gravitino-gauge coupling. This coupling constant determines the strength of the interaction between the gravitino and the electroweak gauge bosons.

2.3 The gauge mediated supersymmetry breaking (GMSB) models

In Gauge Mediated Supersymmetry Breaking (GMSB) models, the SUSY breaking is communicated to the MSSM particles through gauge interactions. In this framework, the lightest supersymmetric particle (LSP) is stable and provides a good candidate for dark matter.

In GMSB models, the gravitino ($\tilde{G}$) is the lightest SUSY particle (LSP), and the next-to-lightest SUSY particle (NLSP) is a neutralino ($\tilde{\chi}^0$) or a chargino $\tilde{\chi}^{\pm}$. The neutralino and chargino masses and mixing angles depend on the SUSY-breaking scale and the messenger sector. The messenger sector consists of particles that mediate the communication between the SUSY-breaking sector and the MSSM particles.

The neutralinos and charginos in GMSB models are mixtures of the superpartners of the neutral gauge bosons (the Bino and the Wino) and the neutral Higgs bosons (the Higgsinos) and charged gauge bosons (W bosons). The neutralino mass matrix is determined by the mixing between these superpartners and can be written as:

$$\begin{pmatrix} \tilde{B} & \tilde{W}_3 & \tilde{H}_d^0 & \tilde{H}_u^0 \end{pmatrix} \begin{pmatrix} M_1 & 0 & -m_Z \sin\theta_W \cos\beta & m_Z \sin\theta_W \sin\beta \\ 0 & M_2 & m_Z \cos\theta_W \cos\beta & -m_Z \cos\theta_W \sin\beta \\ -m_Z \sin\theta_W \cos\beta & m_Z \cos\theta_W \cos\beta & 0 & -\mu \\ m_Z \sin\theta_W \sin\beta & -m_Z \cos\theta_W \sin\beta & -\mu & 0 \end{pmatrix} \begin{pmatrix} \tilde{B} \\ \tilde{W}_3 \\ \tilde{H}_d^0 \\ \tilde{H}_u^0 \end{pmatrix}, \quad (2.14)$$

where $\tilde{B}$ and $\tilde{W}_3$ are the Bino and Wino fields, respectively, $\tilde{H}_d^0$ and $\tilde{H}_u^0$ are the Higgsino fields, M_1 and M_2 are the Bino and Wino masses, μ is the Higgsino mass parameter, m_Z is the Z boson mass, θ_W is the weak mixing angle, and β is the ratio of the vacuum expectation values of the two Higgs fields.

The chargino mass matrix is similarly given by:

$$\begin{pmatrix} \tilde{W}_1^+ & \tilde{W}_2^+ \\ \tilde{H}_u^+ & \tilde{H}_d^+ \end{pmatrix} \begin{pmatrix} M_2 & \sqrt{2} m_W \sin\theta_W \\ \sqrt{2} m_W \cos\theta_W & \mu \end{pmatrix} \begin{pmatrix} \tilde{W}_1^- \\ \tilde{W}_2^- \end{pmatrix}, \quad (2.15)$$

where $\tilde{W}_1^+$ and $\tilde{W}_2^+$ are the two Wino fields, $\tilde{H}_u^+$ and $\tilde{H}_d^+$ are the Higgsino fields, M_2 is the Wino mass, μ is the Higgsino mass parameter, m_W is the W boson mass, and β is the ratio of the vacuum expectation values of the two Higgs fields.

The neutralino and chargino masses and mixing angles can be obtained by diagonalizing the mass matrices, which depend on the parameters described earlier. The lightest neutralino, which is typically the LSP in GMSB models, has a mass in the range of a few GeV to a few hundred GeV, depending on the SUSY-breaking scale and the messenger sector. The NLSP, which can be either a neutralino or a chargino, has a mass slightly larger than the LSP and typically decays into the LSP and a photon or a Z boson, leading to a final state with missing energy and a photon or a Z boson in collider experiments.

In summary, GMSB models provide a natural framework for generating the correct amount of dark matter through the stable LSP, while also satisfying experimental constraints from collider searches and precision measurements.

Fig. 2.2 shows signal models considered in Chap. 5. The upper left Feynman diagram shows the bottom squark pair production, the upper right shows the Wino-like chargino-neutralino production. The lower diagrams are the two relevant decay modes for higgsino-like neutralino pair production in the GMSB scenario.

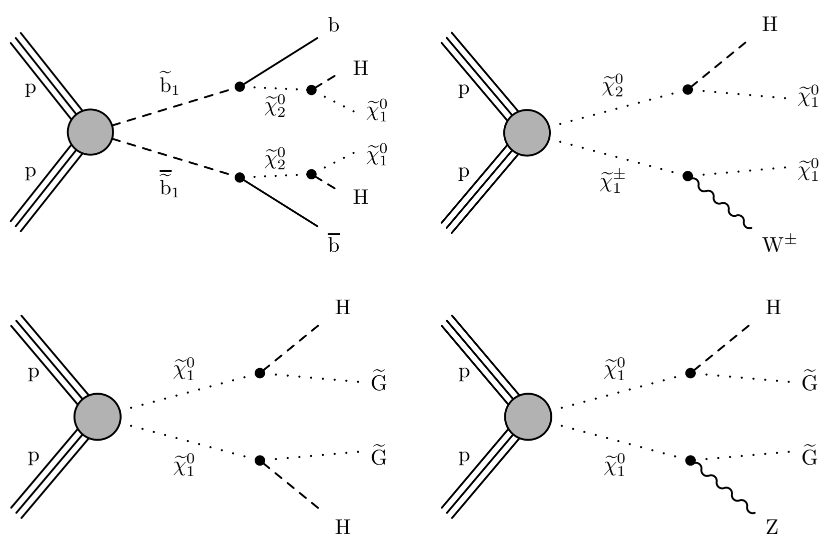

Figure 2.2: Diagrams displaying the simplified models that are being considered in Chap. 5. Upper left: bottom squark pair production; upper right: wino-like chargino-neutralino production; lower: the two relevant decay modes for higgsino-like neutralino pair production in the GMSB scenaro.

2.3.1 Difference between MSSM and GMSB

GMSB and MSSM differ in the way they generate masses for the charginos and neutralinos.

In GMSB, the charginos and neutralinos obtain their masses from the gauge-mediated supersymmetry breaking (GMSB) sector, which communicates the breaking of supersymmetry to the observable sector through gauge interactions. Therefore, the masses of the charginos and neutralinos in GMSB depend on the details of the GMSB sector, such as the number and masses of the messenger fields.

In contrast, in the MSSM, the masses of the charginos and neutralinos are generated by the Higgs mechanism, in which the Higgs bosons acquire vacuum expectation values that break the electroweak symmetry. Therefore, the masses of the charginos and neutralinos in the MSSM depend on the parameters of the Higgs sector, such as the masses of the Higgs bosons and the mixing angles.

As a result, the charginos and neutralinos in GMSB and MSSM can have different masses and compositions depending on the specific model and the values of the parameters. Furthermore, GMSB predicts the existence of light gravitinos, which can have important implications for cosmology and astrophysics.

2.4 The mass-degenerated GMSB models

In the case of mass-degenerate GMSB models, the neutralino and chargino mass matrices simplify considerably. The neutralino mass matrix (Eq. 2.14) becomes:

$$\begin{pmatrix} M_1 & 0 & -m_Z \sin\theta_W \cos\beta & m_Z \sin\theta_W \sin\beta \\ 0 & M_2 & m_Z \cos\theta_W \cos\beta & -m_Z \cos\theta_W \sin\beta \\ -m_Z \sin\theta_W \cos\beta & m_Z \cos\theta_W \cos\beta & 0 & -\mu \\ m_Z \sin\theta_W \sin\beta & -m_Z \cos\theta_W \sin\beta & -\mu & 0 \end{pmatrix}, \tag{2.16}$$

where M_1 and M_2 are the soft supersymmetry-breaking masses for the Bino and Wino, respectively, and $M_1 = M_2 = M$, m_Z is the Z boson mass, θ_W is the weak mixing angle, $\tan\beta$ is the ratio of the vacuum expectation values of the two Higgs doublets, and μ is the Higgsino mass parameter.

The neutralino masses are given by the eigenvalues of the above matrix, and can be written in terms of the Bino, Wino, and Higgsino content of the mass eigenstates. For example, the lightest neutralino mass (which is typically the lightest supersymmetric particle, or LSP) can be written as:

$$m_{\tilde{\chi}_1^0} = \frac{1}{2}\sqrt{-M^2 - 2\mu^2 + 4m_Z^2 \sin^2\theta_W \cos^2\beta}, \tag{2.17}$$

where θ_W is the weak mixing angle.

Similarly, the chargino mass matrix (Eq. 2.15) becomes:

$$\begin{pmatrix} M_2 & \sqrt{2} m_W \sin\theta_W \\ \sqrt{2} m_W \cos\theta_W & \mu \end{pmatrix}. \tag{2.18}$$

It is worth noting that in the limit of large $\tan\beta$, the mass of the lightest neutralino is predominantly Higgsino-like, while the masses of the charginos and heavier neutralinos are dominated by the gaugino-like states. In the opposite limit of small $\tan\beta$, the lightest neutralino is predominantly Bino-like.

2.4.1 Free parameter: lifetime

In the mass-degenerate case of GMSB, the lightest neutralino (NLSP) is typically a mixture of the Bino ($\tilde{B}$) and the Wino ($\tilde{W}$), with only a small amount of Higgsino ($\tilde{H}$) admixture. The lifetime of the NLSP depends on various factors, including the GMSB mediation scale (represented by the parameter Λ), the mass of the NLSP itself (m_{NLSP}), and the mass of the charged slepton ($m_{\tilde{l}}$). The relation can be expressed mathematically as:

$$c\tau_{\text{NLSP}} \sim \frac{\Lambda^2}{m_{\text{NLSP}}^5}. \tag{2.19}$$

This relation can be derived from the decay rate of the NLSP, which is proportional to the interaction strength between the NLSP and the messenger particles, which is characterized by the coupling constant g and the mediation scale Λ. The decay rate can be written as:

$$\Gamma_{\text{NLSP}} \propto g^2 \frac{m_{\text{NLSP}}^5}{\Lambda^4}, \tag{2.20}$$

where m_{NLSP} is the mass of the NLSP. This expression shows that the decay rate is proportional to the inverse square of the mediation scale Λ.

The lifetime of the NLSP is related to its decay rate through the formula

$$c\tau_{\text{NLSP}} = \frac{\hbar c}{\Gamma_{\text{NLSP}}}, \tag{2.21}$$

where $\hbar$ is the reduced Planck constant. Thus, we have:

$$c\tau_{\mathrm{NLSP}} \propto \frac{\hbar c}{g^2 m_{\mathrm{NLSP}}^5/\Lambda^4} = \frac{\hbar c}{g^2}\frac{\Lambda^4}{m_{\mathrm{NLSP}}^5}. \tag{2.22}$$

This equation shows that the lifetime is a free parameter that depends on the NLSP mass m_{NLSP}, the coupling constant g, and the mediation scale Λ. In the mass-degenerate case, where the mass of the messenger particles $M_{\mathrm{mess}} = M$ and the number of messenger particles $N_{\mathrm{mess}} = 1$, the NLSP mass is determined by the scale of supersymmetry breaking, which is directly related to the mediation scale Λ. Therefore, the NLSP mass and the mediation scale are not independent parameters, and the dependence of the NLSP lifetime on Λ becomes weak.

In long-lived particle searches in the context of mass-degenerate GMSB, the lifetime of the NLSP is typically treated as a free parameter. The NLSP can have a wide range of lifetimes depending on the choice of the mediation scale Λ and the NLSP mass. Treating the NLSP lifetime as a free parameter allows experimental searches to explore a wider range of possible GMSB scenarios. The NLSP lifetime can also affect the experimental signature of GMSB since it determines the distance that the NLSP travels before it decays, which can lead to distinctive signals in the detector such as displaced vertices or delayed energy deposits. This enables researchers to gain a better understanding of the underlying physics.

Fig. 2.3 shows signal models considered in Chap. 7, where the $\widetilde{\chi}_1^0$ is the long-lived particle with $c\tau$ as a free parameter.

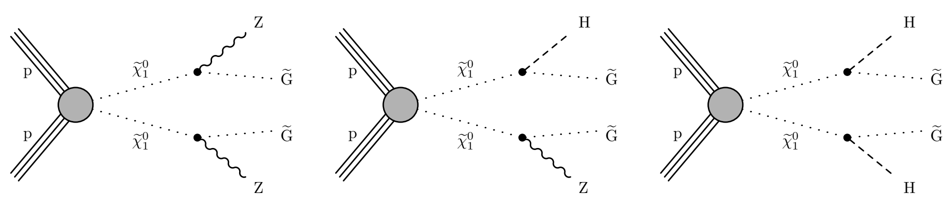

Figure 2.3: Feynman diagrams of the effective neutralino pair production in the GMSB simplified model in which the two neutralinos decay into two gravitinos and two Z bosons (left), a Z and a Higgs boson (H) (center), or two Higgs bosons (right).

Part II

The LHC and the CMS

Chapter 3

THE LARGE HADRON COLLIDER

The Large Hadron Collider (LHC) [4] is the world's largest and highest-energy particle collider. It is situated at the border of Switzerland and France and consists two rings with counter-rotating beams. These beams are located underground in a 27 km tunnel. There are four major experiments on the LHC ring, namely ALICE, ATLAS, CMS and LHCb as shown in Fig. 3.1. In 2012, CERN announced evidence of the Higgs boson, which was observed independently by ATLAS and CMS.

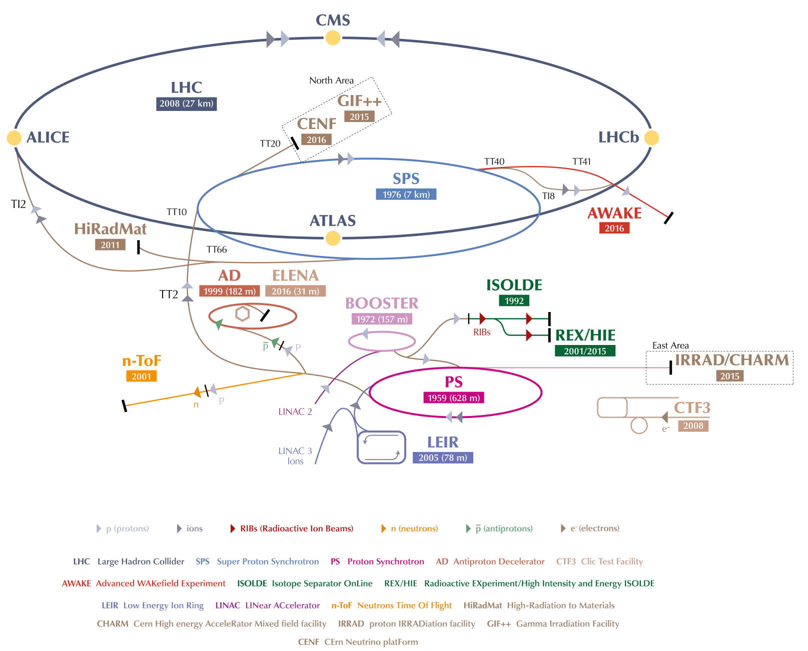

Figure 3.1: The CERN accelerator complex. Complexe des accélérateurs du CERN [5].

The LHC relies on a superconducting magnet system that cools the magnets to a temperature below 2 K and operates at fields above 8 T. The cryodipoles are essential to the design of the LHC, both in terms of machine performance and cost. The cross section of the cryodipole is shown in Fig. 3.2.

LHC reused CERN Large Electron-Positron Collider (LEP) tunnel with internal diameter of 3.7 m for cost-saving purpose and this spacial limit led to the twin-bore magnet design that was proposed by John Blewett [6] at the Brookhaven laboratory (BNL) in 1971.

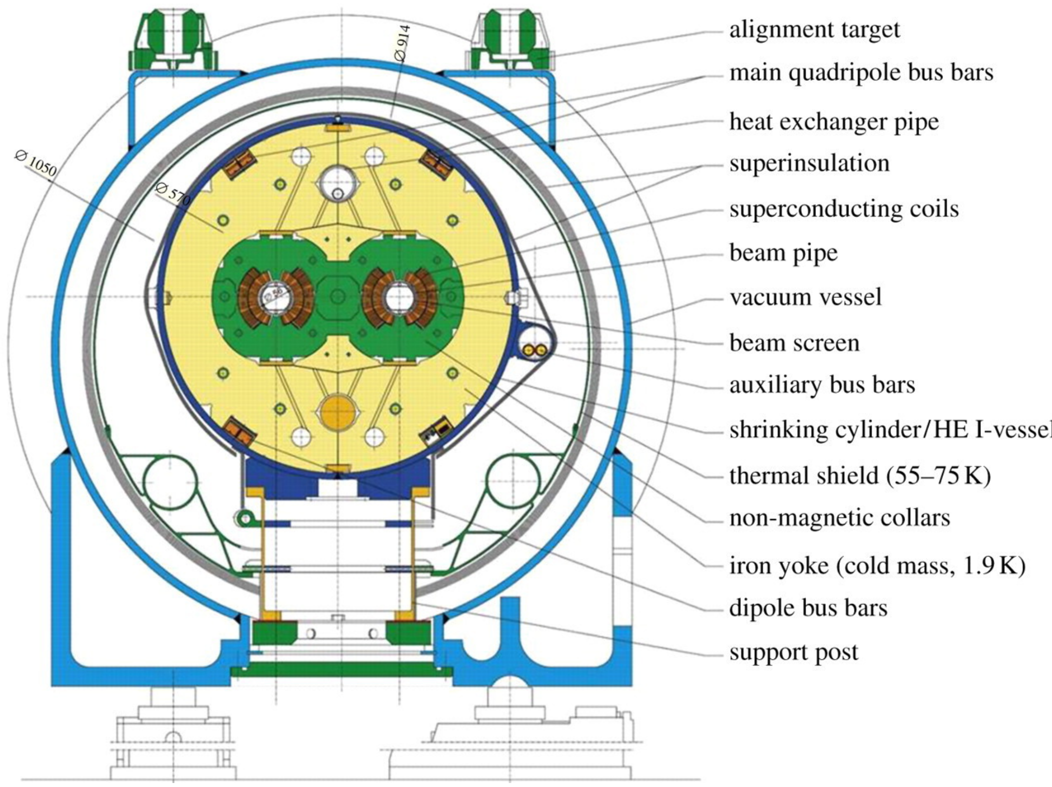

Figure 3.2: Cross-section of cryodipole (lengths in mm) [4].

The LHC is designed to reveal the nature of new physics up to center-of-mass of 14 TeV [7]. The expected number of events N_{exp} for a certain process is:

$$N_{\text{exp}} = \sigma_{\text{exp}} \int \mathcal{L}(t)dt, \tag{3.1}$$

where σ_{exp} is the expected cross-section of the process, and $\mathcal{L}(t)$ is the instantaneous luminosity, defined as:

$$\mathcal{L} = \frac{N_b^2 n_b f_{rev} \gamma_r}{4\pi\epsilon_n\beta^*} F, \tag{3.2}$$

where N_b is the number of protons per bunch $N_b = 1.15 \times 10^{11}$, n_b is the number of bunches per beam $n_b = 2808$, f_{rev} is the revolution frequency $f_{rev} = 11.252kHz$, γ_r is the relativistic factor, ϵ_n is the normalized transverse beam emittance (measuring the average spread of the beam) $\epsilon_n = 3.75\mu m$, β^* is the beta function at the collision point (measuring the transverse size of the beam) $\beta^* = 0.55m$, and F is the geometric luminosity reduction factor due to non-zero crossing angle at the interaction point (IP) $F \approx 1$. F is defined as:

$$F = \left[1 + \frac{\theta_c \sigma_z}{2\sigma^*}^2\right]^{-\frac{1}{2}} \tag{3.3}$$

where θ_c is the full crossing angle at the IP $\theta_c = 295\mu rad$, σ_z is the RMS bunch length $\sigma_z = 7.55cm$ and σ^* is the transverse RMS beam size at the IP $\sigma^* = 16.7\mu m$.

The LHC is designed to have an instantaneous luminosity of $\mathcal{L} = 10^{34}\ cm^{-2}s^{-1}$, which means that in the LHC detectors might produce 10^{34} collisions per second and per cm^2.

In Run II of the LHC, the integrated luminosity delivered for proton-proton (pp) collisions at$\sqrt{s}$ = 13 TeV (Fig. 3.3) was about 41.0 fb^{-1}, 49.8 fb^{-1}, and 67.9 fb^{-1} during 2016, 2017 and 2018, respectively. The integrated luminosity recorded by the CMS detector which is good for physics was 35.9 fb^{-1}, 41.5 fb^{-1}, and 59.7 fb^{-1} during 2016, 2017, and 2018, respectively. In 2015, LHC delivered around 4 fb^{-1} data which is such a small amount of data and not considered in most physics analysis comparing the benefit to the effort of data processing, simulation and calibration.

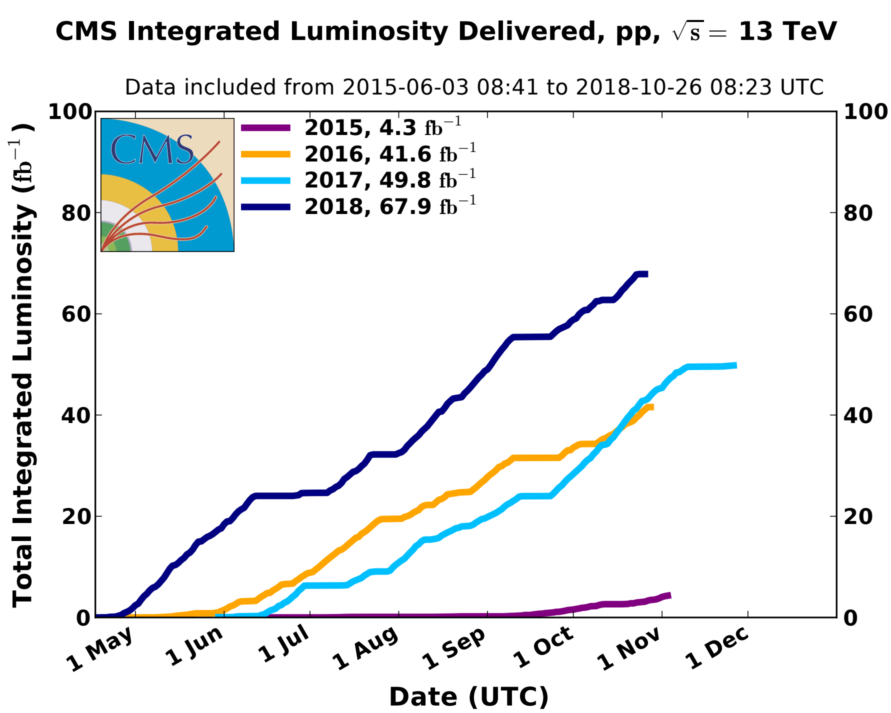

Figure 3.3: Delivered luminosity versus time with $\sqrt{s}$ = 13 TeV data for Run II (2015-2018, pp data only) [8].

At LHC, one bunch crossing occurs when two bunches of protons pass through each other. Pileup (PU, denoted by μ) is the number of simultaneous pp interactions occurring in the same bunch crossing:

$$\mu = \frac{\sigma_{in}\mathcal{L}(t)}{f_{rev}n_b} \tag{3.4}$$

where the inelastic pp collision cross section measured by CMS is

$$\sigma_{in} = 68.6 \pm 0.5(\text{syst}) \pm 1.6(\text{lumi})\text{mb [9]}, \tag{3.5}$$

that gives pileup $\mu \approx 21$ at instantaneous luminosity $\mathcal{L}(t) = 10^{34}\ cm^{-2}s^{-1}$.

Fig. 3.4 shows pileup distribution at CMS for Run II (2015-2018), which uses $\sigma_{in} = 80.0$mb [10]. In 2018, at peak luminosity of $\mathcal{L}(t) = 2.1 \times 10^{34}\ cm^{-2}s^{-1}$ with number of bunches per beam $n_b = 2556$, the largest pileup is $\mu = 58$.

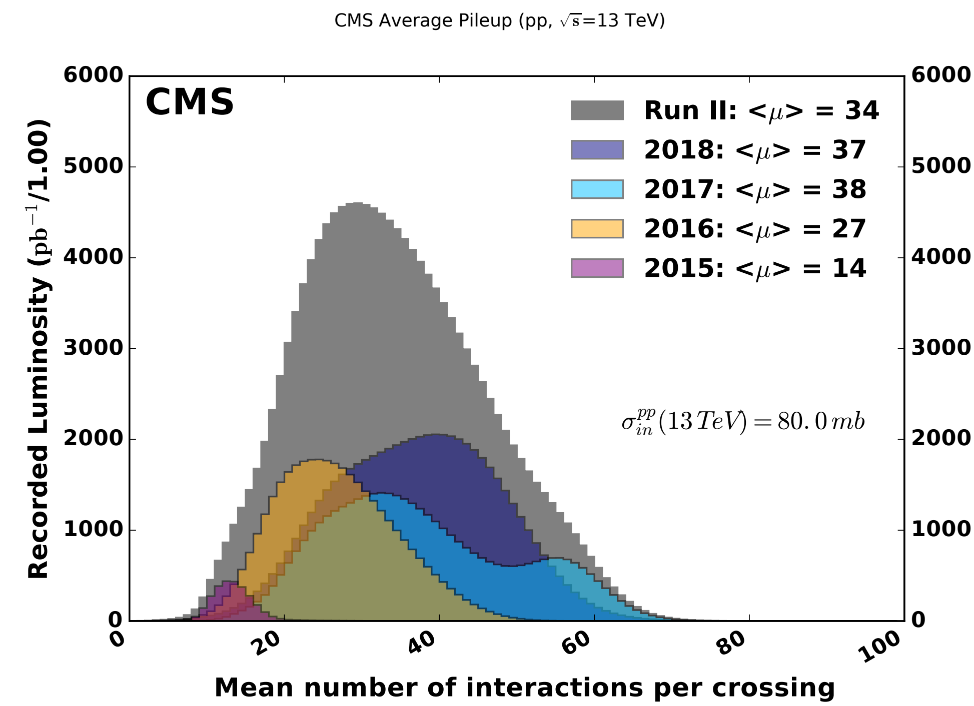

Figure 3.4: Interactions per crossing (pileup) for Run II (2015-2018). The overall mean values and the minimum bias cross sections are also shown [8].

Chapter 4

THE COMPACT MUON SOLENOID

The Compact Muon Solenoid (CMS) is a multi-purpose detector at the LHC. The overall layout of CMS is shown in Fig. 4.1. The central feature of the CMS detector is a superconducting solenoid of 6 m internal diameter, providing a magnetic field of 3.8 T. Within the solenoid volume are a silicon pixel and strip tracker, a lead tungstate crystal electromagnetic calorimeter (ECAL), and a brass and scintillator hadron calorimeter, each composed of a barrel and two endcap sections. Forward calorimeters extend the angular coverage provided by the barrel and endcap detectors. Muons are measured in gas-ionization detectors embedded in the steel flux-return yoke outside the solenoid.

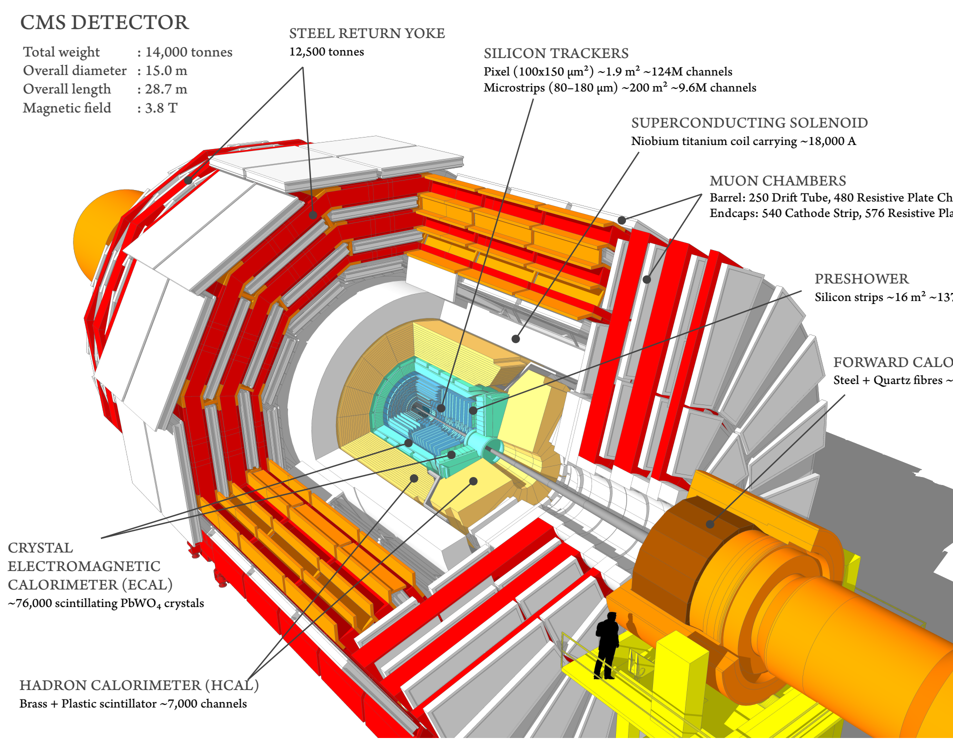

Figure 4.1: A cutaway view of CMS detector after Phase I upgrade of pixel detector [11].

The CMS detector has the ability to do particle identification (PID), as shown in Fig. 4.2. The silicon tracker measures tracks of charged particles. The ECAL measures the energy of electrons and photons. The HCAL measures the energy of charged and neutral hadrons. The muon system measures the momentum of muons.

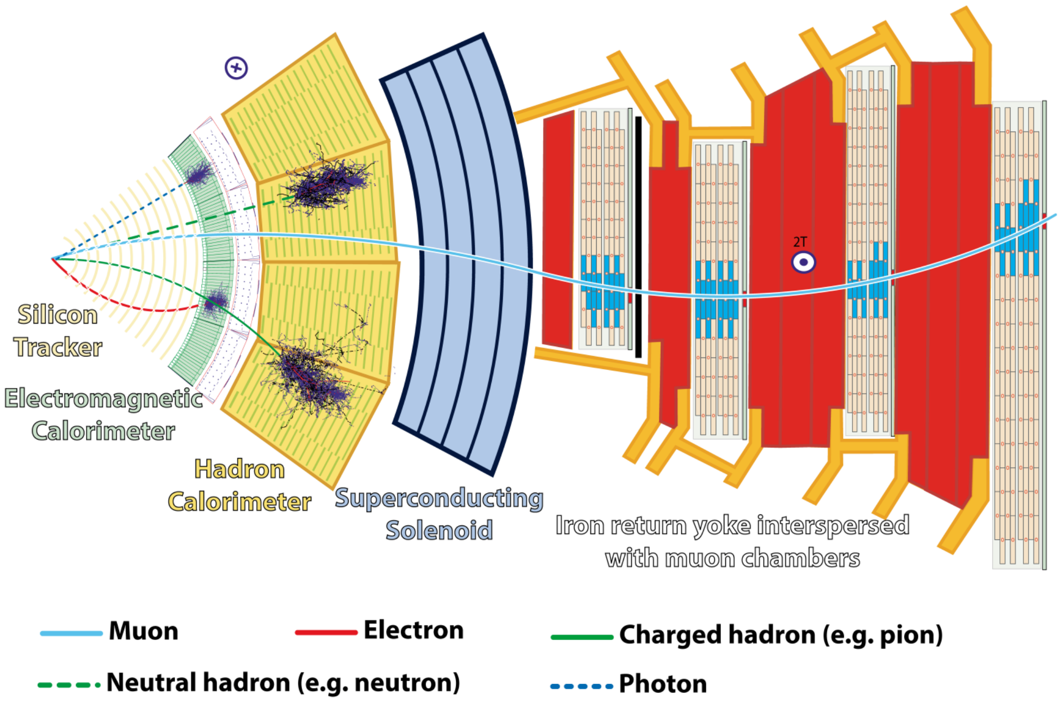

Figure 4.2: A cross-sectional-slice view of the CMS detector illustrating the inter-actions of various particle types with different detector components [12].

4.1 The superconducting solenoid

The superconducting solenoid at CMS is the largest and most powerful superconducting solenoid ever built [13–16]. It operates at a central magnetic flux density of 3.8 T. Values of the magnetic field and magnetic field lines are shown in Fig. 4.3. Its distinctive features include a 6 m free bore diameter, and a 12.5 m long superconducting solenoid enclosed inside a 10,000 tonne return yoke (yoke is shown in Fig. 4.4).

The yoke is made of common structural steel. It is composed of five three-layered dodecagonal barrel wheels and three endcap disks at each end. The main role of the yoke is to increase the field homogeneity in the tracker volume and to return the magnetic flux of the solenoid to reduce the stray field. The steel plates act as an absorber for the four muon stations (interleaved layers) of muon chambers, which measure the muon momentum independent of the inner tracking system.

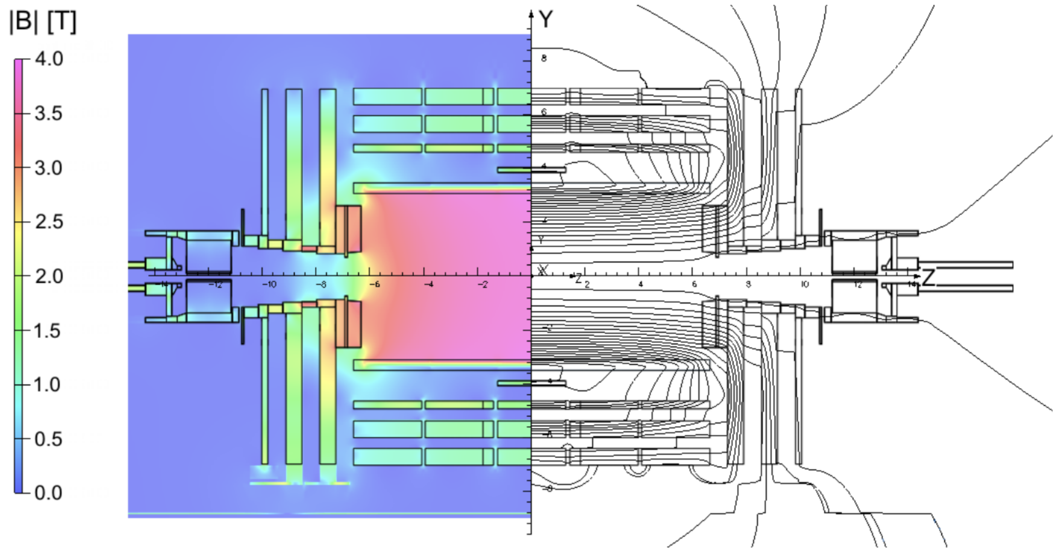

Figure 4.3: The values of magnetic field $|B|$ (left) and magnetic field lines (right) produced by the CMS superconducting magnet system [17].

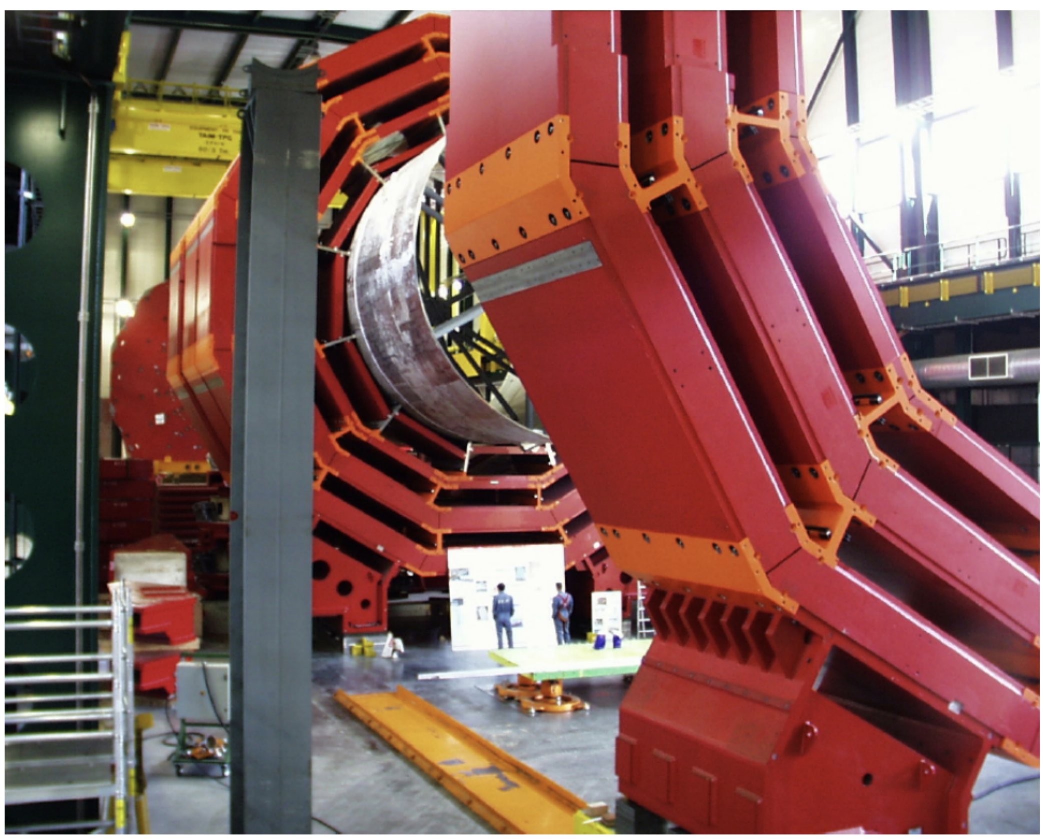

Figure 4.4: A view of the CMS solenoid yoke at an early stage of magnet assembly. The central barrel supports the vacuum chamber of the superconducting coil. At the rear, one of the closing endcap disks is visible [15].

4.2 The inner tracker

The inner tracking system of CMS is designed to provide high granularity and fast response for measurements of the trajectories of charged particles and reconstruction of secondary vertices. The tracker must withstand severe radiation damage caused by the intense particle flux, which was also an important factor considered in the 12 to 15 years to design, develop and build this unique device [18].

The CMS inner tracking system is composed of a pixel detector with four barrel layers at radii of 3.0, 6.8, 10.9 and 16.0 cm and a silicon strip tracker with 10 barrel detection layers extending outwards to a radius of 1.1m as shown in Fig. 4.5 after Phase I upgrade of pixel detector [19]. Each system is completed by endcaps which consist of 6 disks in the pixel detector at z coordinates of ±29.1, ±39.6 and ±51.6 cm and 3 plus 9 disks in the strip tracker on each side of the barrel, extending the acceptance of the tracker up to a pseudorapidity of $|\eta| < 2.5$. Fig. 4.6 shows the material budget of the CMS tracker after Phase I pixel detector upgrade, both in units of radiation lengths and nuclear interaction lengths, as estimated from simulation.

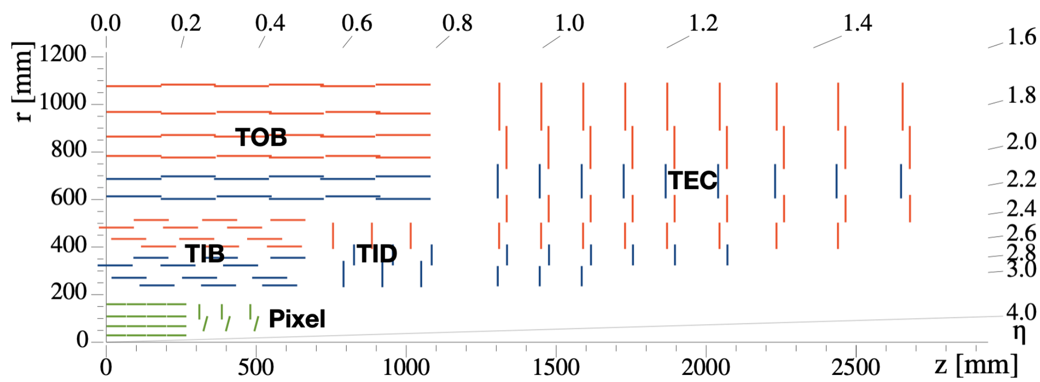

Figure 4.5: Sketch of one quarter of the Phase I CMS tracking system in r-z view. The pixel detector is shown in green, while single-sided and double-sided strip modules are depicted as red and blue segments, respectively [20].

Phase I pixel detector upgrade [22] is characterized by higher efficiencies, lower fake rates, lower dead-time/data-loss, and an extended lifetime of the detector. This leads to better muon ID, b-tagging, photon/electron ID, and tau reconstruction, both offline and in the HLT (High-Level Trigger). This upgrade also allowed the improvement of the offline missing energy reconstruction by a particle flow algorithm at CMS [23]. Furthermore, the addition of the fourth outer layer of the new pixel detector as shown in Fig. 4.7 largely offsets data-loss, especially at high pile-up, when the inner layers of the TIB (Tracker Inner Barrel, 4-layer strip detector) are compromised.

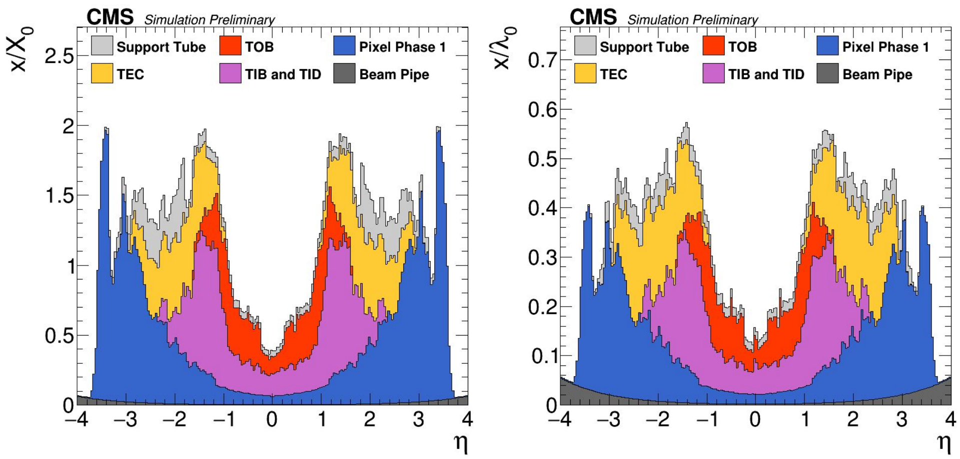

Figure 4.6: Total thickness x of the tracker material traversed by a particle produced at the nominal interaction point, as a function of pseudorapidity η, expressed in units of radiation length X_0 (left) and nuclear interaction length λ_I (right). The contribution of the support tube (light gray), the beam pipe (dark gray), and sub-detectors: TOB (red, Tracker Outer Barrel, 6-layer strip detector), Pixel Phase I (blue), TEC (yellow, Tracker Endcap) and TID+TIB (magenta, Tracker Inner Disks + Tracker Inner Barrel) are stacked [21].

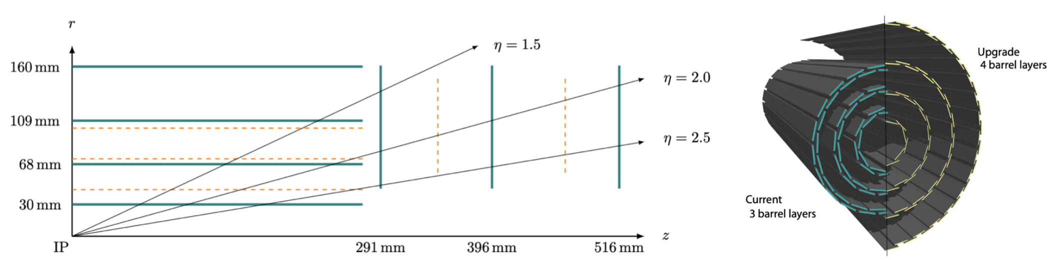

Figure 4.7: Comparison of Phase-I and Phase-0 pixel detector. Left: Geometry of the Phase-1 barrel and forward pixel detectors. Shown is one quadrant of the detector, the layer radii and disk positions are given relative to the interaction point (IP). The dashed lines indicate the layer positions of the Phase-0 pixel detector [19]. Right: Transverse-oblique view comparing the pixel barrel layers in the current (Phase 0) and Phase I detectors [22].

The tracking performance quantities, the charged particle track reconstruction efficiency and fake rate, are defined as follows:

$$\text{Tracking efficiency} = \frac{\text{Number of truth tracks matched to reconstructed tracks}}{\text{Number of truth tracks}}, \tag{4.1}$$

$$\text{Tracking fake rate} = \frac{\text{Number of reconstructed tracks not matched to truth tracks}}{\text{Number of reconstructed tracks}}. \tag{4.2}$$

Fig. 4.8 shows the expected tracking performance of the Phase 0 and Phase I upgraded pixel detector in various pile-up scenarios (PU = 0, 50 and 100) in simulated $t\bar{t}$ events. Performance of the Phase 0 pixel detector is only slightly degraded at $1 \times 10^{34}\ cm^{-2}s^{-1}$ (25 ns crossing time), but rapidly deteriorates with higher pileup losing efficiency as well as suffering from more fake tracks. While for the upgraded pixel detector, the situation is significantly improved such that only very little efficiency is lost even at $2 \times 10^{34}\ cm^{-2}s^{-1}$ (25 ns crossing time), though degradation starts to become significant if running at a crossing time of 50 ns.

4.3 The electromagnetic calorimeter (ECAL)

The electromagnetic calorimeter of CMS (ECAL) [24] is a homogeneous and hermetic calorimeter made of $61,200$ lead tungstate ($PbWO_4$) scintillating crystals mounted in the central barrel part (EB), closed at each endcap (EE) by $7,324$ crystals. A preshower detector (PS) is placed in front of the endcap crystals. Avalanche photodiodes (APDs) [25, 26] are used as photodetectors for the EB and vacuum phototriodes (VPTs) [27] for the EE.

The lead tungstate ($PbWO_4$) crystals are chosen due to they have high density (8.28 g/cm^3), short radiation length (X_0 = 0.89 cm), and small Molière radius (R_M = 2.19 cm), which has allowed the design of a fast, compact and radiation resistant calorimeter with fine granularity [24]. In Table 4.1, the properties of $PbWO_4$ are compared with those of other crystals used in electromagnetic calorimeters.

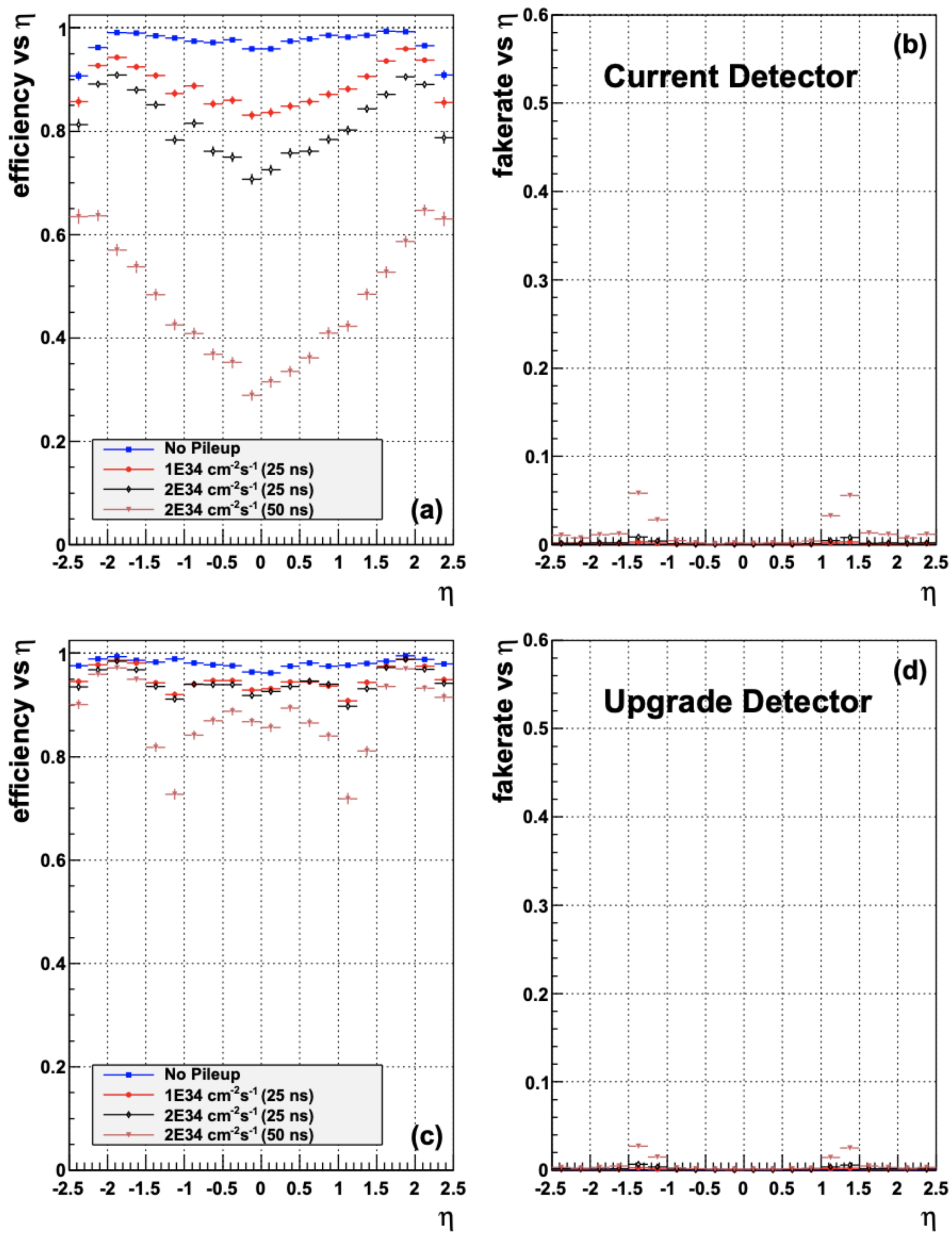

Figure 4.8: Tracking efficiency (a,c) and fake rate (b,d) for the $t\bar{t}$ sample as a function of track η, for the current detector (a,b) and the upgrade pixel detector (c,d). Results are shown for zero pileup (blue squares), an average pileup of 25 (red dots), an average pileup of 50 (black diamonds), and an average pileup of 100 (brown triangles) with ROC data loss simulation expected at the given luminosities as detailed in the text [22].

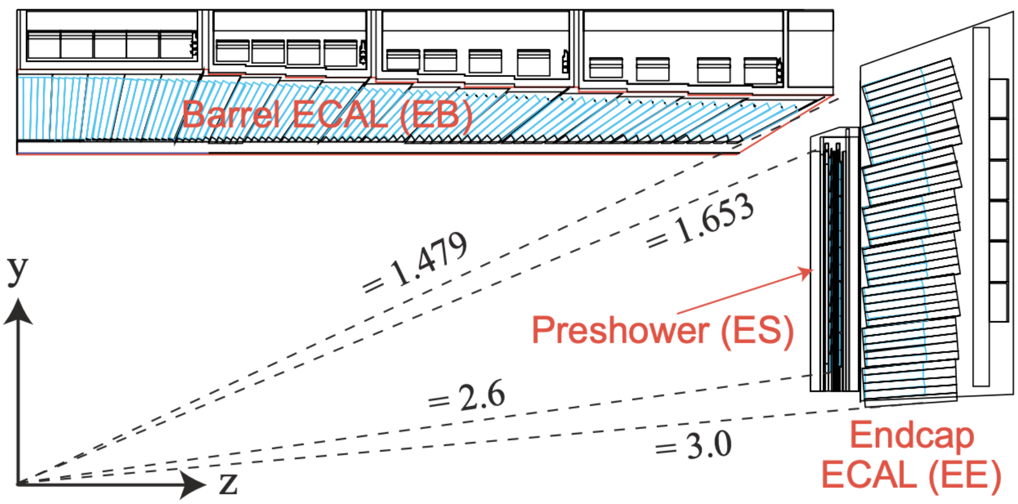

Figure 4.9: Transverse section through the ECAL, showing geometrical configuration [28].

Table 4.1: Comparison of properties of various crystals [24].

	NaI(Tl)	**BGO**	**CSI**	**BaF_2**	**CeF_3**	**$PbWO_4$**
Density [g/cm^3]	3.67	7.13	4.51	4.88	6.16	8.28
Radiation length [cm]	2.59	1.12	1.85	2.06	1.68	0.89
Interaction length [cm]	41.4	21.8	37.0	29.9	26.2	22.4
Molière radius [cm]	4.80	2.33	3.50	3.39	2.63	2.19
Light decay time [ns]	230	60 300	16	0.9 630	8 25	5 (39%) 15 (60%) 100 (1%)
Refractive index	1.85	2.15	1.80	1.49	1.62	2.30
Maximum of emission [nm]	410	480	315	210 310	300 340	440
Temperature coefficient [%/°C]	0	-1.6	-0.6	-2/0	0.14	-2
Relative light output	100	18	20	20/4	8	1.3

$PbWO_4$ does experience a very slight, dose rate dependent decrease of its transparency under irradiation, and recovers to a large extent in irradiation-free periods. Its variation of transparency is monitored by a high precision laser system [29]. The monitoring system is based on the injection of laser light at 447 nm (from 2012 onwards, 440 nm in 2011) into each crystal, which is close to the emission peak of scintillation light from $PbWO_4$ [30]. Fig. 4.10 shows history of ECAL response in six different η bins with laser data during 2011-2018. The response change observed in the ECAL channels is up to 13% in the barrel ($|\eta| < 1.4$) and it reaches up to 62% at $\eta \sim 2.5$, the limit of the tracker acceptance. The response change is up to 96% in the region closest to the beam pipe ($|\eta| > 2.7$).

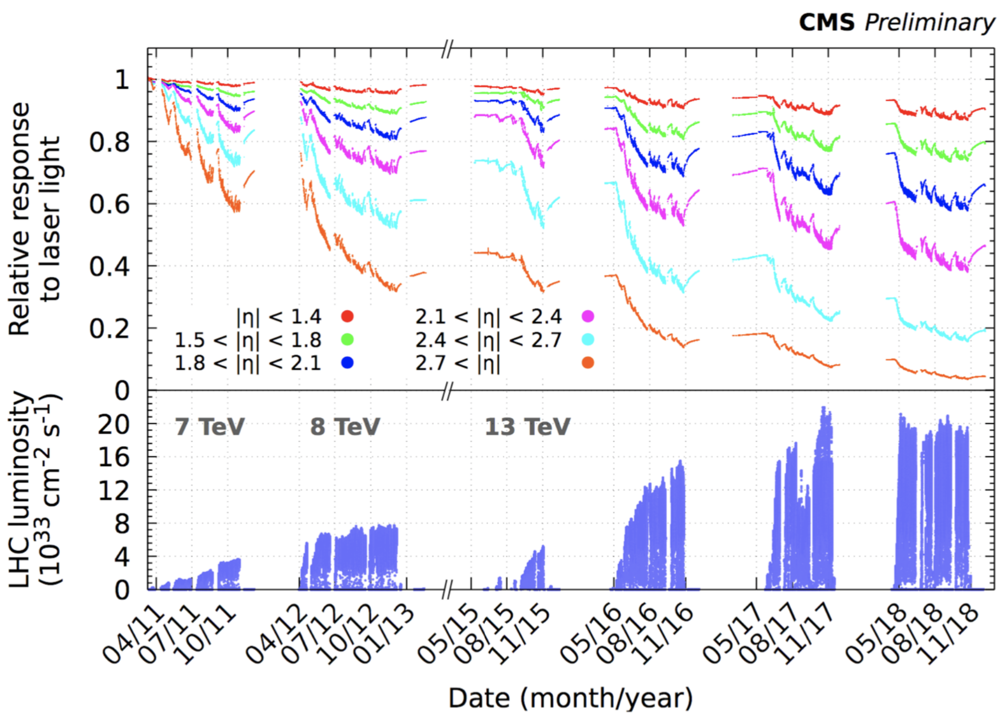

Figure 4.10: Relative response to laser light (440 nm in 2011 and 447 nm from 2012 onwards) injected in the ECAL crystals, measured by the ECAL laser monitoring system, averaged over all crystals in bins of pseudorapidity (η), for the 2011, 2012, 2015, 2016, 2017 and 2018 data taking periods, with magnetic field at 3.8 T. The response change observed in the ECAL channels is up to 13% in the barrel and it reaches up to 62% at η 2.5, the limit of the tracker acceptance. The response change is up to 96% in the region closest to the beam pipe. The recovery of the crystal response during the periods without collisions is visible. The bottom plot shows the instantaneous LHC luminosity delivered during this time period [31].

The energy resolution of ECAL is measured by fitting a Voigtian (Breit-Wigner convolved with Gaussian) function to the reconstructed energy distributions [24, 28, 30, 32]. It has been parameterized as a function of energy, with the function:

$$\left(\frac{\sigma_E}{E}\right)^2 = \left(\frac{S}{\sqrt{E}}\right)^2 + \left(\frac{N}{E}\right)^2 + C^2, \tag{4.3}$$

where S is the stochastic term, N the noise and C the constant term [28]. There are three main sources that contribute to the stochastic term (S):

i) fluctuations on the lateral containment that contributes $\sim 1.5\%$,
ii) fluctuations on the energy deposited in the preshower absorber that contributes $\sim 5\%$,
iii) a photostatistics contribution of 2.3%.

There are also three contributions to the noise term (N):

i) preamplifier noise (~153 MeV, a quadrature sum of 30 MeV per channel in EB and 150 MeV per channel in EE),
ii) digitization noise (150 MeV at EB and 750 MeV at EE),
iii) pileup noise (significant at the highest pseudorapidity η regions at high luminosity).

The most relevant contributions for the constant term (C) are:

i) non-uniformity of the longitudinal light collection (0.3%),
ii) crystal-to-crystal intercalibration errors (0.4%),
iii) leakage of energy from the back of the crystal ($< 0.2\%$),
iv) uncorrected and imperfectly corrected geometrical effects ($< 0.2\%$).

Table 12.1 in Ref. [24] has a more detailed breakdown of those terms for both the EB ($\eta = 0$) and the EE ($\eta = 2$). Fig. 4.11 shows Run 2 ECAL energy resolution as a function of pseudorapidity η measured by Z→ee decays. The relative ECAL energy resolution (σ_E/E) is around 2% at the EB ($\eta = 0$) and 4% at the EE ($\eta = 2$). The CMS ECAL detector has maintained a stable energy resolution throughout Run 2 at LHC.

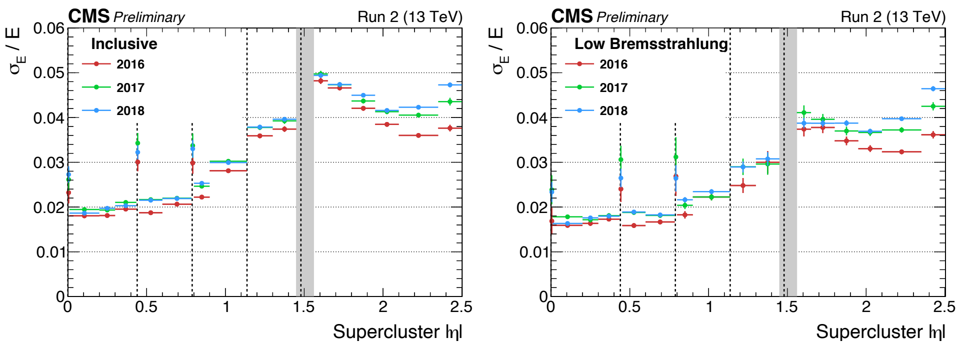

Figure 4.11: Relative electron (ECAL) energy resolution unfolded in bins of pseudorapidity η for the ECAL Barrel and Endcap. Electrons from Z→ee decays are used. The resolution is shown separately for all electrons (inclusive, left), and for low bremsstrahlung electrons (right). The plot compares the resolution achieved after a refined calibration of the data collected at 13 TeV during Run 2 in 2016, 2017, and 2018. The relative resolution σ_E/E is extracted from an unbinned likelihood fit to Z→ee events, using a Voigtian (Breit-Wigner convolved with Gaussian) as the signal model. A stable ECAL energy resolution is observed over the course of Run 2 despite the increased LHC luminosity and the ageing of the detector [32].

The fast signal from the $PbWO_4$ scintillation also enables time measurements in proton-proton collisions with high-energy electrons and photons [33]. The time resolution for seed crystals of the clusters of the two electrons from Z→ee decays is calculated as following:

$$\sigma(t_1 - t2)^2 = (\frac{N}{E_{\text{eff}}})^2 + 2C^2, \tag{4.4}$$

where E_{eff} is the effective energy. The ombined result of the global timing resolution, which is on the order of 200 ps for energies above 40 GeV in EB, for the 2016, Legacy 2017 and 2018 data is shown in Fig. 4.12.

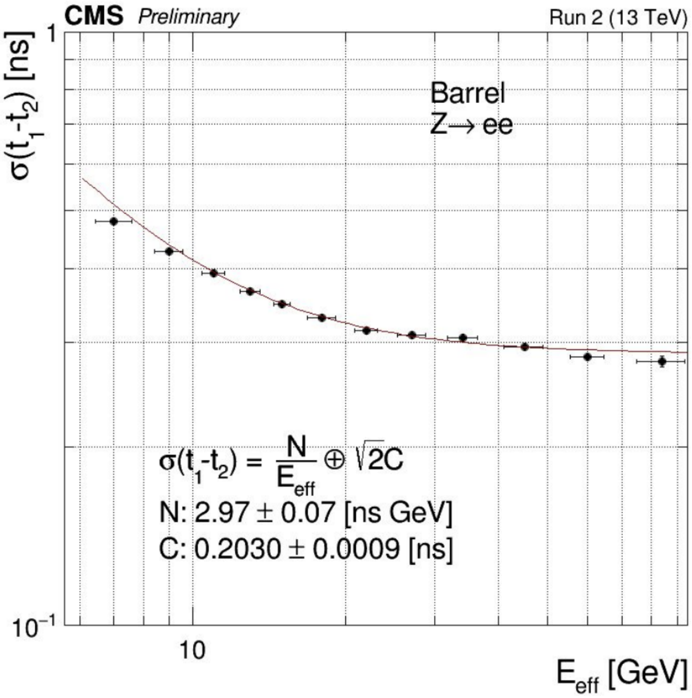

Figure 4.12: The resolution of time difference between the times of the seed crystals of the clusters of the two electrons from Z→ee decays, as a function of the effective energy in the ECAL Barrel for 2016, Legacy 2017 and 2018 data combined together. A global timing resolution of the order of 200 ps for energies above 40 GeV is measured [34].

4.4 The hadron calorimeter (HCAL)

The hadron calorimeter (HCAL) of CMS is essential for the measurements of hadron jets and neutrinos or exotic particles [35]. The conjuction of the ECAL and HCAL in CMS forms a complete calorimetry system for the measurements of jets and missing transverse energy [36]. Fig. 4.13 shows layout of barrel (HB, $|\eta| < 1.4$), endcap (HE, $1.3 < |\eta| < 3$) and forward (HF, $2.9 < |\eta| < 5$) sub-detector of HCAL at Phase-0 (left) and Phase-1 (right) including the depth segmentation. The HF is placed at 11.2 m from the interaction point (IP) to measure energetic forward jets optimized to discriminate the narrow lateral shower profile and to increase the hermeticity of the missing transverse energy measurement. There is also an outer barrel hadronic calorimeter (HO) located outside the magnet to improve central shower contaunment in the region of $|\eta| < 1.26$ [15, 28].

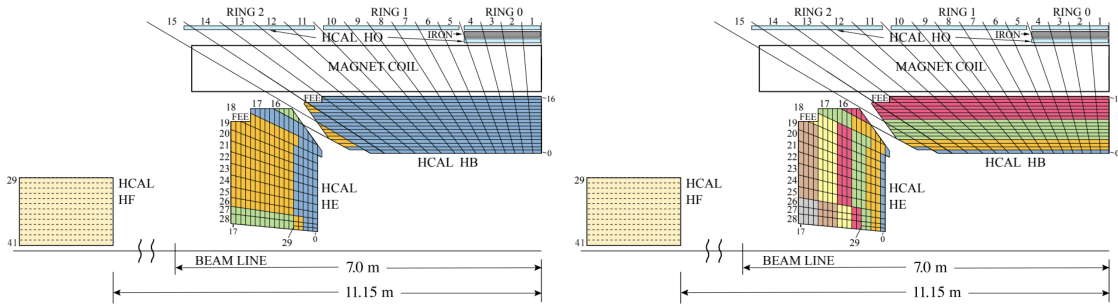

Figure 4.13: An r-Z schematic view of the CMS hadron calorimeters showing the locations of the HB, HE, HO, and HF calorimeters for Phase-0 (left) and Phase-1 (right). The locations of the front-end electronics for the HB and HE calorimeters are indicated by "FEE." The depth segmentation of the HB and HE detectors is also shown. Light from layers that are depicted with the same color are optically added together before reaching the photosensors [37–39].

The HB consists of 36 identical azimuthal wedges (Fig. 4.14, left) which form the two half-barrels (HB+ and HB–, based on z direction). Each wedge is segmented into four azimuthal angle (ϕ) sectors. The HE consists of 36 identical wedges (72 megatiles; every two megatiles make one wedge at HE) which form two endcaps (HE+ and HE-, based on z direction). The wedges are constructed out of flat brass absorber plates (70% Cu, 20% Zn, density at 8.53 g/cm^3, radiation length X_0 = 1.49 cm, interaction length λ_I = 16.42 cm).

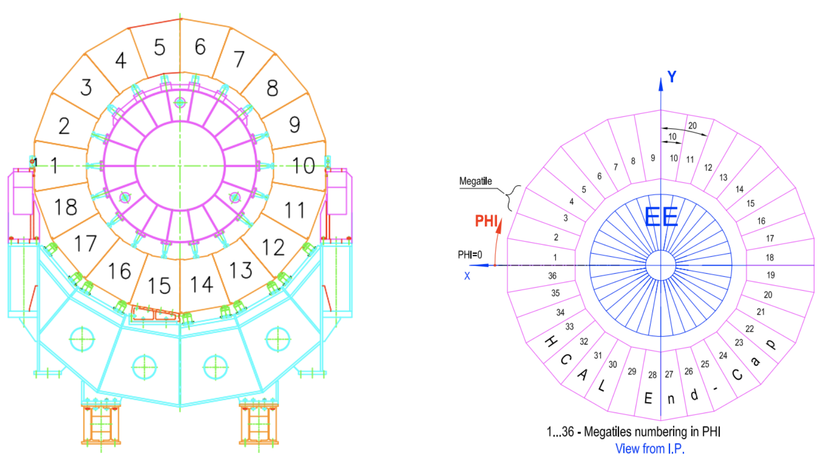

Figure 4.14: Numbering scheme for the HB (left) and HE megatiles (right). Wedge or megatile 1 is on the inside (+x direction) of the LHC ring [15].

Given the increased longitudinal granularity of the upgraded detector in Phase-1, it is essential to ensure that the response of each longitudinal segment is equalized. To achieve this, inter-depth calibration of the HE energy deposits is performed using muons that transverse the scintillator tiles. The tracks of muons are reconstructed and extrapolated to the front and back layers of the HCAL using information from the tracking system, the muon momentum, and the magnetic field. Only tracks that remain in the same tower while passing through the HE are selected for calibration.

A Gaussian convoluted with a Landau, with the mean of the Gaussian set to zero, is used to fit the energy spectra. The location parameter of the Landau function is used as the most probable value for the muon energy deposit in the HCAL depths. The dependence on the muon momentum is found to be negligible in the range of the selected muon sample.

The left plot in Fig. 4.15 shows a comparison between the reconstructed muon signal from collision events in a HE tower readout via Silicon Photomultipliers (SiPMs) (Phase-1 crystal) and the signal from a tower readout via Hybrid Photodiode (HPD) (Phase-0 crystal). At Phase-1, the same portion of scintillator material that was previously read out by a single HPD channel is now read out via 4 SiPMs. Thus, the plot compares 4 depth readouts from SiPMs to one single depth readout from HPD. It can be seen that the resolution of the reconstructed muon peak is significantly improved due to the upgraded readout.

The right plot in Fig. 4.15 shows the measured amount of energy per layer as a function of the depth number. The response is relatively flat through depth 2 to depth 6, which has a constant sampling fraction. The amount of passive material in front of depth 1 is larger, resulting in a lower energy response in this depth. The calibration using muons ensures that the response of each longitudinal segment is well equalized in the upgraded HCAL detector.

4.5 The muon system

The CMS muon system has three primary functions: muon identification, momentum measurement, and triggering [15, 41–43]. The 3.8 T solenoidal magnet and its flux-return yoke enable precise muon momentum resolution and trigger capability. Additionally, the yoke serves as a hadron absorber for the identification of muons. The thickness of the material crossed by muons as a function of pseudorapidity is shown in Fig. 4.16.

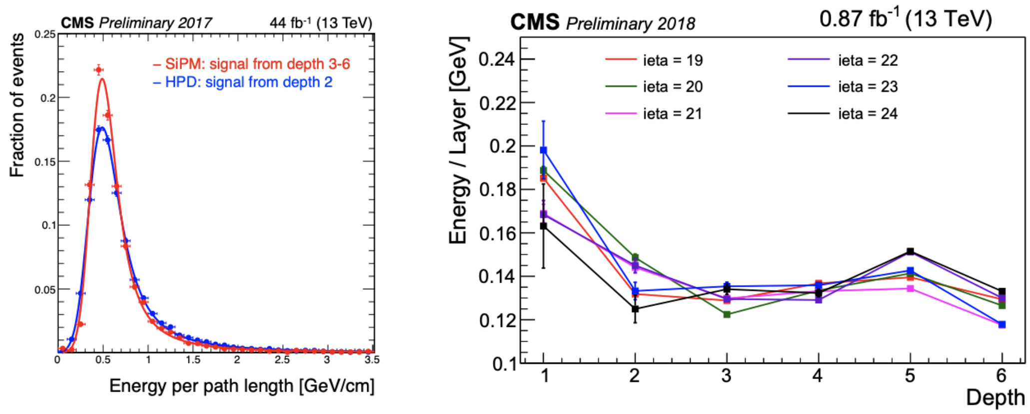

Figure 4.15: Results of Phase-I HE SiPM performance. Left: the reconstructed muon signal from collision events in a HE tower readout via SiPM (ieta=24, iphi=63) is compared with the signal from a tower readout via HPD (ieta=-24, iphi=63). The signal is divided by the muon track length in the active material. Right: Muon deposits in HE towers for different eta regions and depths. Muons from collision events are considered when their track traverses the HCAL while remaining within the same tower. The muon signal peak is fitted with the convolution of a Gaussian and a Landau. The Landau location parameter is divided by the number of scintillator layers in the considered depth [40].

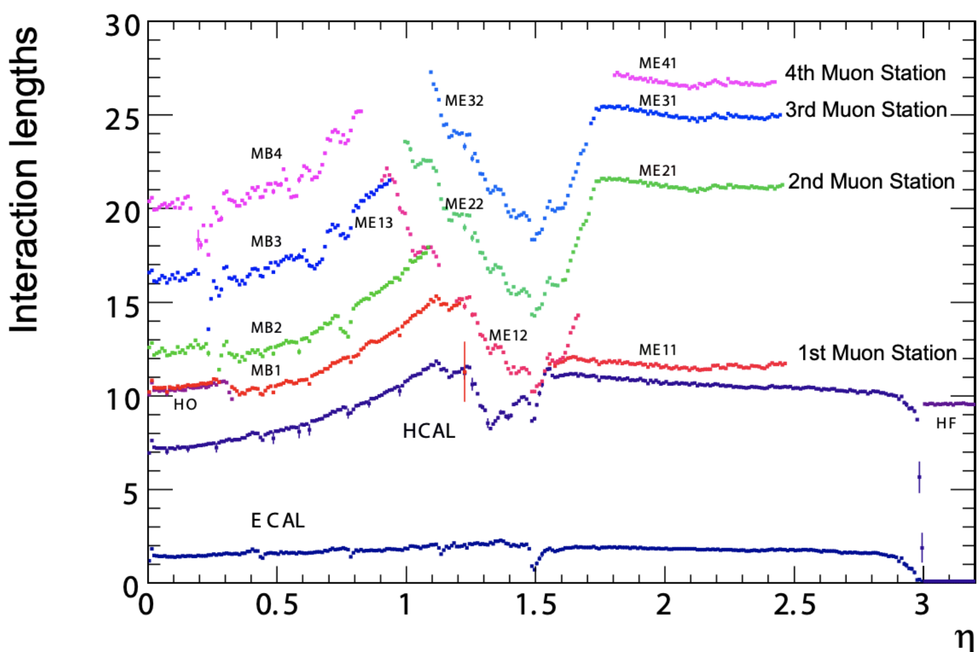

Figure 4.16: Material thickness in interaction lengths at various depths, as a function of pseudorapidity [15].

The CMS muon system is composed of three types of gas ionization chambers: drift tube chambers (DTs), cathode strip chambers (CSCs), and resistive plate chambers (RPCs). These chambers are interspersed within the layers of the steel flux-return yoke, enabling detection of a muon at multiple points along its path. The DT and CSC chambers are situated in the barrel region with $|\eta| < 1.2$ and in the endcaps with $0.9 < |\eta| < 2.4$, respectively. The RPC detectors complement the DT and CSC chambers in both barrel and endcaps regions, with the maximum pseudorapidity coverage extending up to $|\eta| = 1.9$, as shown in Fig. 4.17.

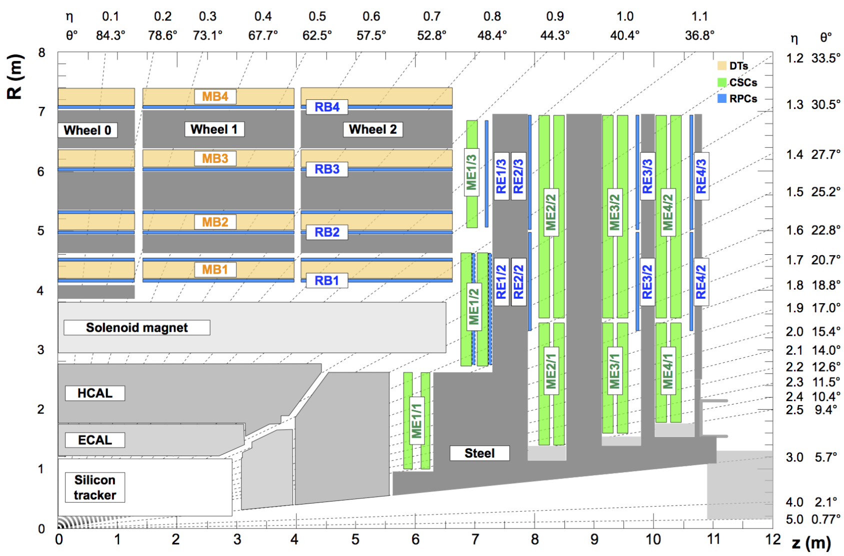

Figure 4.17: An R-z cross section of a quadrant of the CMS detector with the axis parallel to the beam (z) running horizontally and the radius (R) increasing upward. The interaction point is at the lower left corner. The locations of the various muon stations and the steel flux-return disks (dark areas) are shown. The drift tube stations (DTs) are labeled MB ("Muon Barrel") and the cathode strip chambers (CSCs) are labeled ME ("Muon Endcap"). Resistive plate chambers (RPCs) are mounted in both the barrel and endcaps of CMS, where they are labeled RB and RE, respectively. [41].

The CMS barrel muon detector is composed of 4 stations arranged in concentric cylinders around the beam line: the 3 inner cylinders each have 60 drift chambers, while the outer cylinder has 70 chambers (totaling 250 DTs). The detector contains approximately 172,000 sensitive wires that are around 2.4 m in length. The DTs are divided into long aluminum drift cells. To determine the position of a transversing muon, the drift time to the anode wire in the middle of the cell is measured with an optimally shaped electric field. The high spatial resolution of about 100 μm per 8-layer chamber is achieved thanks to the resolution per cell of 250 μm or better, making it possible to use drift chambers as the tracking detectors for the barrel muon system. Figure 4.18 displays the layout of one wheel of muon DT chambers, a single drift cell, and a photograph of several DT muon chambers inside the CMS magnet yoke.

The CMS endcap muon detector is composed of 540 cathode strip chambers (CSCs), which are multiwire proportional chambers comprised of 6 anode wire planes (gas gaps) interleaved among 7 cathode panels. The overall gas volume is larger than 50 m^3, and the number of wires is about 2 million. The strips run radially outward to measure the muon position (z), while the anode wires run azimuthally and provide the radial measurement (R). The precise muon coordinate along the wires (ϕ) can be reconstructed by interpolating the charges read out on the strips. The CSCs provide good position resolution (50–140 μm, depending on chamber type) and time resolution (3 ns per chamber). They can operate at high particle rates and in strong and non-uniform magnetic fields. Fig. 4.19 illustrates the operation of the cathode strip chambers and shows some of the trapezoidal CSC chambers during installation in the CMS detector.

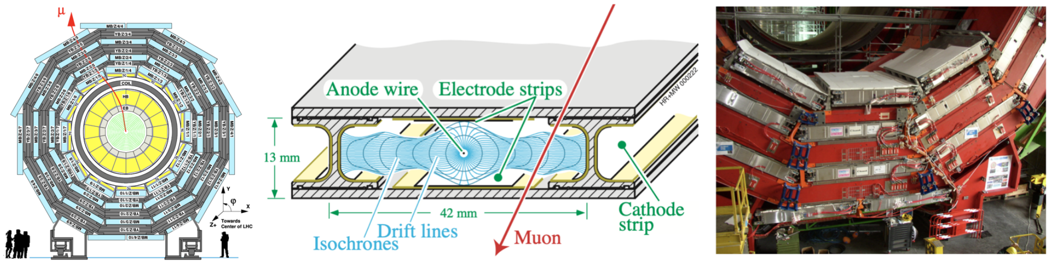

Figure 4.18: The CMS barrel muon detector (DTs). Left: Layout of the CMS barrel muon DT chambers in one of the 5 wheels. The chambers in each wheel are identical with the exception of wheels –1 and +1 where the presence of cryogenic chimneys for the magnet shortens the chambers in 2 sectors. Note that in sectors 4 (top) and 10 (bottom) the MB4 chambers are cut in half to simplify the mechanical assembly and the global chamber layout. Middle: Sketch of a cell showing drift lines and isochrones. The plates at the top and bottom of the cell are at ground potential. The voltages applied to the electrodes are +3600V for wires, +1800V for strips, and 1200V for cathodes. Right: DT chambers (aluminum) sandwiched between steel plates of the yoke (red), during installation. [15, 43]

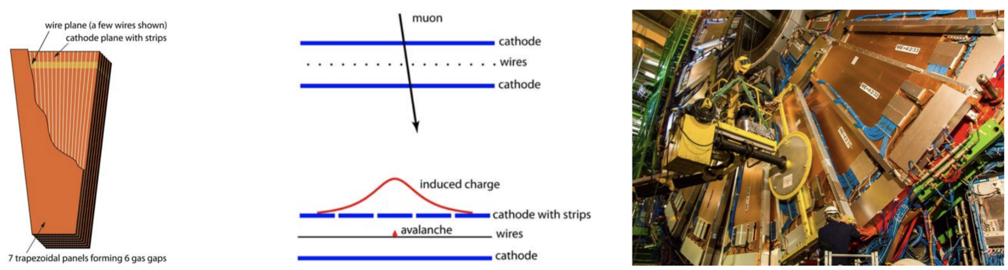

Figure 4.19: The CMS endcap muon detector (CSCs). Left: Layout of a CSC made of 7 trapezoidal panels. The panels form 6 gas gaps withplanes of sensitive anode wires. The cut-out in the top panel reveals anode wires and cathode strips. Only a few wires are shown to indicate their azimuthal direction. Strips of constant ϕ run lengthwise (radially). The 144 largest CSCs at ME2/2 and ME3/2 are 3.4 m long along the strip direction and up to 1.5 m wide along the wire direction. Middle: A schematic view of a single gap illustrating the principle of CSC operation. By interpolating charges induced on cathode strips by avalanche positive ions near a wire, one can obtain a precise localisation of an avalanche along the wire direction. Right: Outer CSC chambers ME4/2 during installation. [15, 43].

The CMS muon system also has 610 resistive plate chambers (RPCs) that form a redundant trigger system and make fast decisions on whether to keep the acquired muon data or not. As such, the CMS muon system is naturally robust and has the ability to filter out background noise. Each CMS RPC basic double-gap module consists of two gaps, referred to as upper and lower gaps, that operate in avalanche mode at high electric field. The RPCs provide accurate timing and fast triggering, with an excellent intrinsic timing resolution of around 1.5 ns for a double-gap chamber. This allows the RPC to tag the time of an ionizing event in a much shorter time than the 25 ns between two consecutive LHC bunch crossings (BX). An RPC trigger can provide the BX assignment to track candidates and estimate the transverse momenta with high efficiency in a high-rate environment at LHC. Fig. 4.20 illustrates the schematic layout and displays a photo of the endcap RPCs.

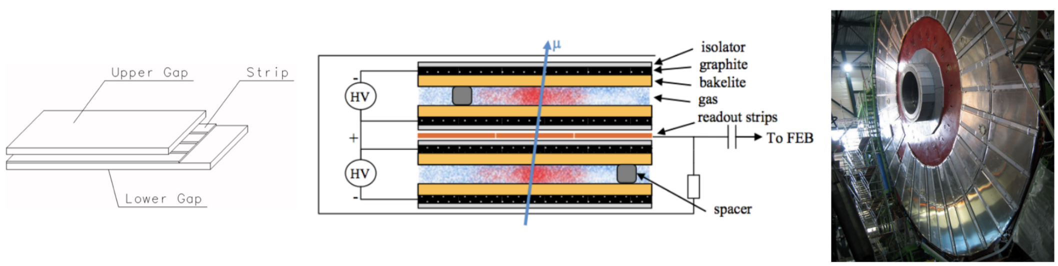

Figure 4.20: The CMS RPCs. Left: Layout of a double-gap RPC. Middle: Working principle of the double gap RPCs in CMS. Right: Outer CSC chambers ME4/2 during installation. [15, 43].

4.6 The CMS trigger and data acquisition system (TriDAS)

The CMS Trigger and Data Acquisition System (TriDAS) is specifically designed to collect and analyze detector data at the LHC crossing frequency of 40 MHz and to select events for archiving and later offline analysis, with a maximum rate of 10^2 Hz [44, 45]. The TriDAS is comprised of four main components: the detector electronics, the Level-1 trigger processors (calorimeter, muon, and global), the readout network, and the online event filter system (which executes the software for the High-Level Triggers, HLT). The schematic architecture of the CMS Data Acquisition (DAQ) system is shown in Fig. 4.21.

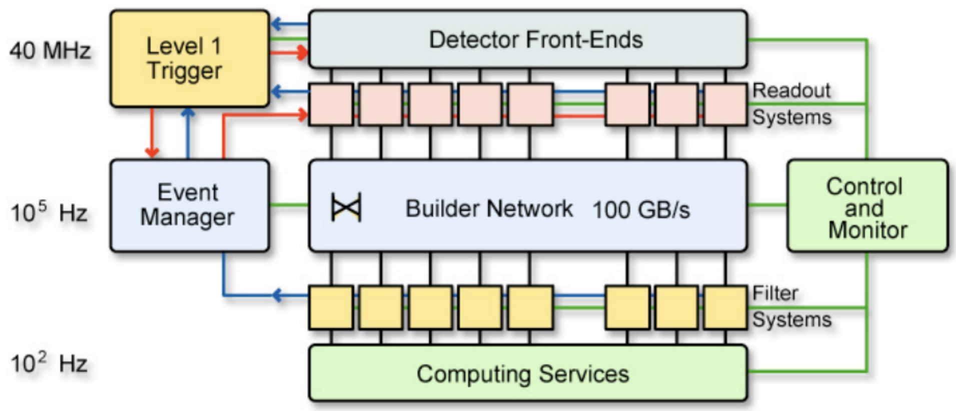

Figure 4.21: General architecture of the CMS DAQ System [28].

The CMS Level-1 (L1) trigger system processes fast trigger information from the calorimeters and muon chambers and selects events with interesting signatures [46–49]. The allowed latency for the L1 trigger, from a specific bunch crossing to the distribution of the trigger decision to the detector front-end electronics, is 3.2 s. The architecture of the CMS Level-1 trigger system is shown in Fig. 4.22, which includes local, regional, and global components. The first layer is the local triggers, also known as Trigger Primitive Generators (TPG), which are based on energy deposits in the calorimeter trigger towers and track segments or hit patterns in the muon chambers. The regional triggers, the second layer, combine their information and use pattern logic to determine ranked and sorted trigger objects such as electron or muon candidates in limited spatial regions. The muon trigger system includes three muon track finders (MTF) which reconstruct muons in the barrel (BMTF), overlap (OMTF), and endcap (EMTF) regions of the detector, and the global muon trigger (μGMT) makes the final muon selection. The global trigger (μGT) at the third layer collects muons and calorimeter objects and executes all algorithms in the menu in parallel for the final trigger decision. The BMTF, μGMT, μGT, and Layer-2 calorimeter triggers use the same type of processor card. The OMTF and EMTF electronic boards similarly share a common design, whereas Layer-1 calorimeter triggers, TwinMux, and CPPF each use a different design. All processor cards, however, use a Xilinx Virtex-7 Field Programmable Gate Array (FPGA) [50].

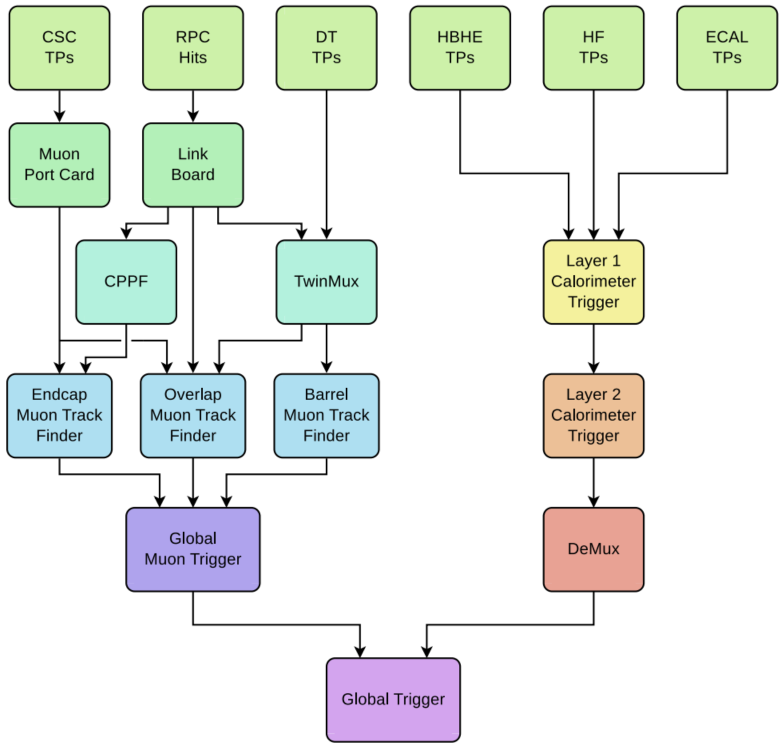

Figure 4.22: Diagram of the CMS Level-1 trigger system during Run 2 [51]. Labels in the diagram correspond to trigger primitives (TPs), cathode strip chambers (CSC), drift tubes (DT), resistive plate chambers (RPC), concentration preprocessing and fan-out (CPPF), hadron calorimeter barrel (HB) and endcap (HE), hadron calorimeter forward (HF), electromagnetic calorimeter (ECAL), demultiplexing card (DeMux).

The CMS High-Level Trigger (HLT) is an online event reconstruction system that runs on a commercial computing farm consisting of around 26,000 processor cores [15, 28]. The HLT menu has a modular structure, as shown in Fig. 4.23, with around 400 paths at 2018 data taking. Each HLT path comprises a sequence of reconstruction and filtering modules that perform object selection, such as electrons, photons, muons, jets, missing transverse momentum, and b-tagged jets, or combinations of them. The modules may also perform sophisticated analysis-relevant calculations because the HLT has access to the complete readout data.

The reconstruction or filtering modules within a HLT path are arranged in increasing complexity. Low complexity blocks run first to proceed with filters. If a filter fails, the rest of the path is skipped to keep the central processing unit (CPU) time under control. Regional object reconstruction and simplified tracking are applied to reduce the CPU time consumption [52]. The processing time distribution of the HLT menu and the typical average timing per event of the HLT jobs run on the HLT farm as a function of the instantaneous luminosity, in 2016 data taking, is shown in Fig. 4.24.

The HLT employs simplified tracking reconstruction [53], which reduces the number of iterations and applies regional tracking in some of the iterations compared to offline tracking [54, 55]. The Particle-Flow (PF) reconstruction algorithm [55] is widely used in HLT and CMS analyses. It provides a global event description using the full detector information to identify final-state particles individually and cluster them into more complex objects, such as jets, missing transverse momentum, and particle isolation. PF at HLT improves energy resolution used in trigger objects and makes the online reconstruction much closer to offline reconstruction. It also enables more efficient methods for pileup mitigation.

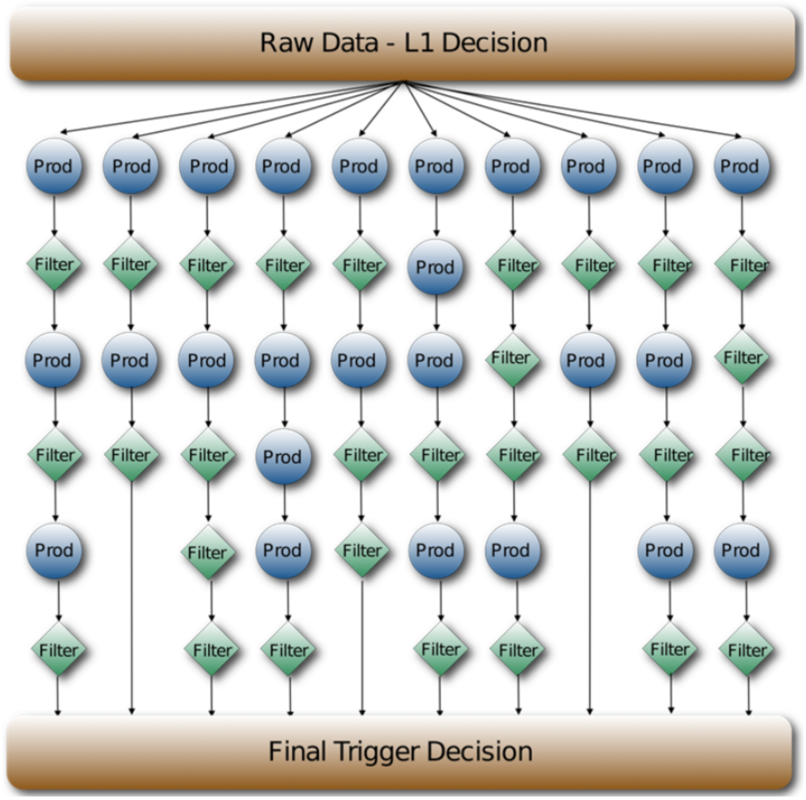

Figure 4.23: Schematic representation of a HLT menu in CMS and of the HLT paths in it [56]. The final trigger decision is the logical OR of the decisions of the single paths.

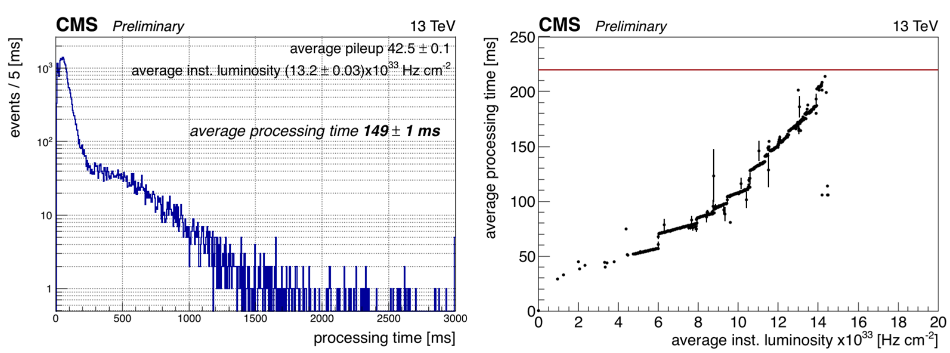

Figure 4.24: The timing distribution of the HLT menu. Left: Processing time distribution of the HLT menu used in the 2016 data taking operations. Right: Processing time distribution of the HLT menu as function of instantaneous luminosity. The red line represents the HLT farm limit in 2016 [57].

4.7 The Worldwide LHC Computing Grid (WLCG)

The Worldwide LHC Computing Grid (WLCG) consists of four levels, or “Tiers” (0, 1, 2, and 3), as shown in Fig. 4.25 [58]. Tier-0 is located at the CERN data center and is responsible for storing all the raw data produced by the experiments. It also performs the initial data processing and distribution of the processed data to Tier-1 centers. Tier-1 centers store both raw and processed data and provide computing resources for the reprocessing of data and the storage of corresponding output. Tier-2 centers are typically located at universities and research institutes and have the capability to store a significant amount of data and perform specific analysis tasks. Tier-3 centers are local clusters or even individual personal computers that have access to the Grid for distributed data analysis.

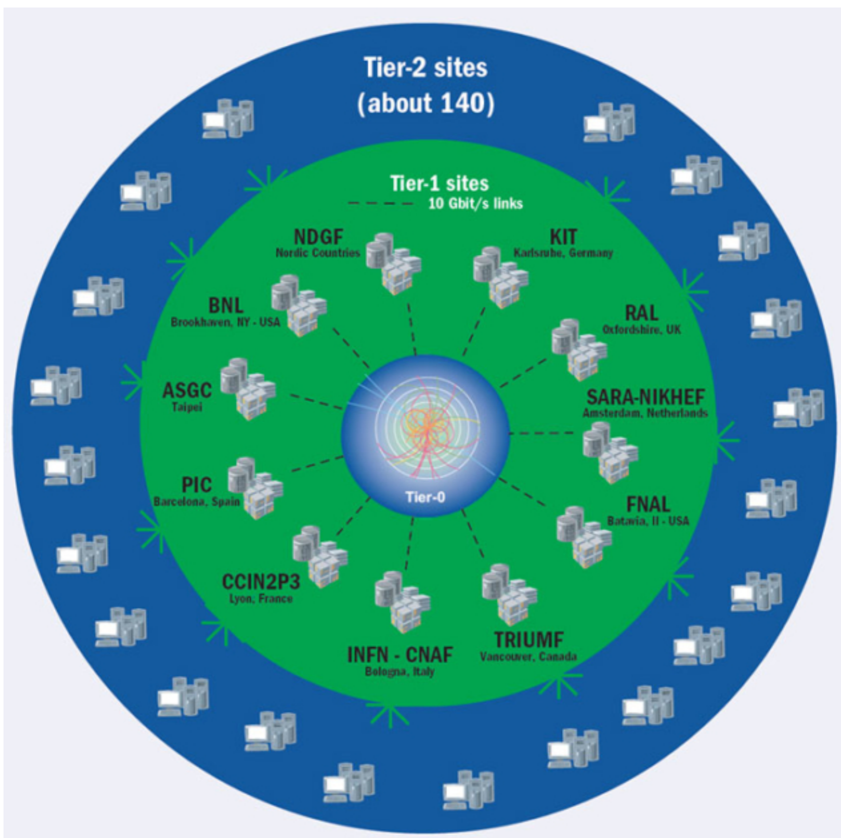

Figure 4.25: Diagram showing the tier system of WLCG, with CERN’s Tier-0 site sending data to the 11 Tier-1 sites and their corresponding Tier-2 sites. More Tier-1 and Tier-2 sites are foreseen [59].

The CMS computing model is outlined in Ref. [60]. The CMS DAQ system writes DAQ-RAW events, each of size 1.5 MB, to the HLT farm input buffer. The HLT farm processes the RAW events at a rate of approximately 150 Hz and writes out RAW events of size 1.5 MB. These RAW events are then categorized into around 50 primary datasets according to their trigger history with a predicted overlap of less than 10%. The primary datasets are organized into about 10 online streams for efficient transfer to the offline farm and subsequent reconstruction. The data transfer from HLT to the Tier-0 farm is required to happen in real-time at a rate of 225 MB/s [61].

The Tier-0 farm performs the first event reconstruction and writes RECO events of size 0.25 MB. RAW and RECO versions of each primary dataset are archived on the Tier-0 Mass Storage System (MSS) and transferred to at least one Tier-1 center. Therefore, RAW and RECO data are available either in the Tier-0 archive or at a minimum of one Tier-1 center.

The Tier-1 centers produce Analysis Object Data (AOD), which are derived from RECO events and contain a copy of all high-level physics objects along with a summary of other RECO information to support analysis operations.

Furthermore, CMS intends to produce a large number of Monte Carlo (MC) events. The MC events, each of size 2 MB, are generated and reconstructed in a distributed manner primarily at Tier-2 sites. The archiving and distribution of MC data is a collective responsibility of the Tier-1 sites. The simulated data are stored in at least one Tier-1 center.

Part III

Search for supersymmetry at the LHC

Chapter 5

SEARCH FOR SUPERSYMMETRY USING HIGGS BOSON TO DIPHOTON DECAYS AT $\sqrt{s}$ = 13 TEV

5.1 Introduction

The discovery of the Higgs boson (H) opened a new window to explore physics beyond the standard model (SM) of particle physics. Many scenarios of physics beyond the SM postulate the existence of cascade decays of heavy states involving Higgs bosons [62, 63]. In the minimal supersymmetric standard model (MSSM) [64], a Higgs boson may appear in processes involving the bottom squark ($\tilde{b}$), the supersymmetric partner of the bottom quark. Bottom squarks are produced via strong interactions and then may decay to a Higgs boson, quarks, and the lightest supersymmetric particle (LSP). Similarly, charginos or neutralinos produced through the electroweak interaction may decay to a Higgs boson and the LSP. Of particular interest are gauge-mediated supersymmetry breaking (GMSB) scenarios, where the lightest neutralino may decay to a Higgs boson and the gravitino LSP ($\tilde{G}$) [65, 66]. Similar searches for supersymmetric particles decaying to Higgs bosons have been performed by the ATLAS and CMS Collaborations using proton-proton (pp) collisions at the CERN LHC at center-of-mass energies of 8 [67, 68] and 13 TeV [69–72].

This chapter presents a search for events of supersymmetry (SUSY) with one or more Higgs bosons decaying to two photons and significant missing transverse momentum. The search is based on proton-proton (pp) collision data collected by the CMS experiment at the LHC at a center-of-mass energy of 13 TeV in 2016 and 2017, with an integrated luminosity of 77.5 fb^{-1}. The events are categorized based on kinematic variables that distinguish the SUSY signal from standard model (SM) backgrounds. The diphoton mass resulting from the $H \rightarrow \gamma\gamma$ decay is used to extract the signal from the background, assuming a branching ratio of 0.227% for $H \rightarrow \gamma\gamma$ from the SM. The dominant backgrounds consist of SM production of diphoton and photon+jets, which are modeled by functional fits to the diphoton mass distribution. The SM Higgs boson background is a minor contributor to the background in most of the phase space used in the search and is estimated using simulation samples.

This analysis is one of two described in Ref. [73], where one focuses on the electroweak production (EWP analysis) of charginos and neutralinos and the other focuses on the strong production (SP analysis) of bottom squarks. This chapter describes the EWP analysis, which extends our sensitivity beyond the previously published result [69] by introducing additional event categories containing one or two charged-lepton candidates, enhancing the sensitivity to SUSY signatures involving W and Z bosons. The search results are interpreted in various simplified models of bottom squark pair production and chargino-neutralino production, as shown in Fig. 5.1.

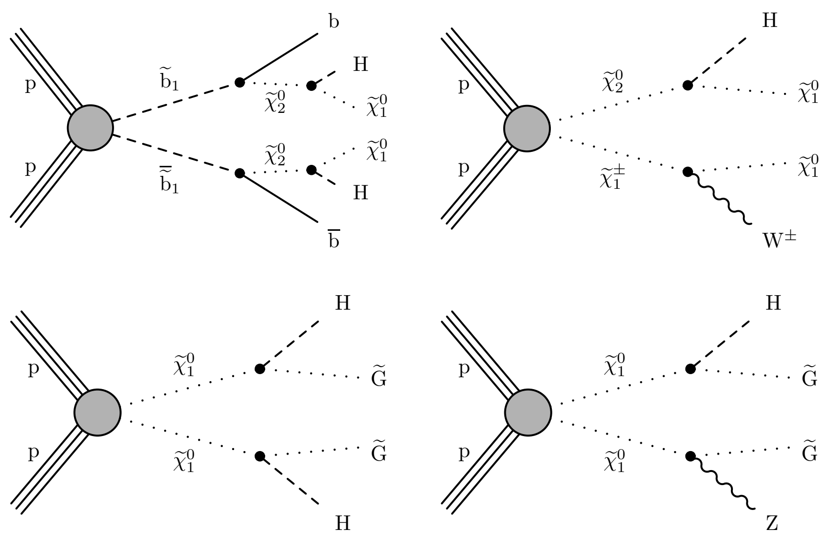

Figure 5.1: Diagrams displaying the simplified models that are being considered. Upper left: bottom squark pair production; upper right: wino-like chargino-neutralino production; lower: the two relevant decay modes for higgsino-like neutralino pair production in the GMSB scenario.

The rest of the chapter is organized as follows. Sec. 5.2 provides a summary of the datasets used in the analysis. The event reconstruction and selection are described in Sec. 5.3. Sec. 5.4 elaborates the analysis strategy, including razor variables, event categorization, and signal extraction. The background components and estimation methods are detailed in Sec. 5.5. The systematic uncertainties are discussed in Sec. 5.6. We report and interpret the results in Sec. 5.7. Finally, a summary of the EWP analysis is given in Sec. 5.8.

5.2 Event samples

5.2.1 Data samples

The `DoubleEG` primary dataset is utilized in this analysis, and the relevant details are summarized in Table 5.1. The data from the `03Feb2017` campaign are used for the 2016 dataset, while the `31Mar2018` campaign is used for the 2017 dataset.

Table 5.1: List of data samples for the 2016 and 2017 data taking.

Sample	Integrated Luminosity
/DoubleEG/Run2016B-03Feb2017-ver2-v2/MINIAOD	$35.9\ \mathrm{fb}^{-1}$
/DoubleEG/Run2016C-03Feb2017-v1/MINIAOD	
/DoubleEG/Run2016D-03Feb2017-v1/MINIAOD	
/DoubleEG/Run2016E-03Feb2017-v1/MINIAOD	
/DoubleEG/Run2016F-03Feb2017-v1/MINIAOD	
/DoubleEG/Run2016G-03Feb2017-v1/MINIAOD	
/DoubleEG/Run2016H-03Feb2017-ver2-v1/MINIAOD	
/DoubleEG/Run2016H-03Feb2017-ver3-v1/MINIAOD	
/DoubleEG/Run2016B-31Mar2018-v1/MINIAOD	$41.5\ \mathrm{fb}^{-1}$
/DoubleEG/Run2016C-31Mar2018-v1/MINIAOD	
/DoubleEG/Run2016D-31Mar2018-v1/MINIAOD	
/DoubleEG/Run2016E-31Mar2018-v1/MINIAOD	
/DoubleEG/Run2016F-31Mar2018-v1/MINIAOD	

5.2.2 Background simulation

The simulation of Monte Carlo (MC) event samples for SM Higgs boson production through gluon fusion, vector boson fusion, associated production with a W or a Z boson, $b\bar{b}$H, and $t\bar{t}$H is done using the MadGraph5_amc@nlov2.2.2 [74] event generator. The Higgs boson mass is fixed to 125 GeV, which is consistent with the best measured value of the Higgs boson mass with current experimental uncertainties [75, 76]. The Higgs boson production cross sections are taken from Ref. [77] and are computed to next-to-next-to-leading order plus next-to-next-to-leading logarithm in the quantum chromodynamics (QCD) coupling constant and to NLO in the electroweak coupling constant. For the gluon fusion production mode, the sample is generated with up to two extra partons from initial-state radiation (ISR) at NLO accuracy and uses the FxFx matching scheme described in Ref. [78]. The SUSY signal MC samples are generated using MadGraph5_amc@nlo at leading order accuracy with up to two extra partons in the matrix element calculations, with the MLM matching scheme described in Ref. [79]. For samples simulating the 2016 data set, pythia v8.212 [80] is used to model the fragmentation and parton showering with the CUETP8M1 tune [81], while for samples simulating the 2017 data set, pythia v8.226 is used with the CP5 [82] tune. The NNPDF3.0 [83] and NNPDF3.1 [84] parton distribution function (PDF) sets are used for the 2016 and 2017 simulation samples, respectively. The production cross section for squark pair production is computed at NLO plus next-to-leading logarithmic (NLL) accuracy in QCD [85–90] under the assumption that all SUSY particles other than those in the relevant diagram are too heavy to participate in the interaction. The cross sections for higgsino pair production are computed at NLO+NLL precision in the limit of mass-degenerate higgsinos $\widetilde{\chi}^0_2$, $\widetilde{\chi}^{\mp}_1$, and $\widetilde{\chi}^0_1$, with all the other sparticles assumed to be heavy and decoupled [91–93]. Following the convention of real mixing matrices and signed neutralino or chargino masses [94], we set the mass of $\widetilde{\chi}^0_1$ ($\widetilde{\chi}^0_2$) to positive (negative) values. The product of the third and fourth elements of the corresponding rows of the neutralino mixing matrix N is +0.5 (−0.5). The elements U_{12} and V_{12} of the chargino mixing matrices are set to 1.

The SM Higgs boson background samples are simulated using a GEANT4-based model [95] of the CMS detector. The simulation includes the response of the CMS detector to the particles produced in the collisions, and takes into account various effects such as energy loss, multiple scattering, and showering. To cover the large SUSY signal parameter space in reasonable computation time, the signal model samples are simulated with the CMS fast simulation package [96, 97]. This package uses parameterizations of the detector response to simulate the propagation of particles through the detector, and has been validated to produce accurate predictions of object identification efficiencies and momentum resolution. All simulated events include the effects of additional pp interactions in the same or adjacent beam bunch crossings (pileup), which are simulated using the PYTHIA event generator. The simulated events are processed with the same chain of reconstruction programs used for collision data, which includes particle flow reconstruction and identification algorithms to reconstruct and identify particles in the event.

The background samples employed in this study are presented in Table 5.2 and Table 5.3 for the years 2016 and 2017, respectively.

5.2.3 Signal simulation

To improve the MADGRAPH modeling of initial state radiation (ISR) in the SUSY signal MC samples generated by MADGRAPH, we apply shape corrections that are derived from studies of $t\bar{t}$ and Z+jets events. These corrections take into account the multiplicity of ISR jets for bottom squark pair production and the transverse momentum ($p_{\mathrm{T}}^{\mathrm{ISR}}$) of the chargino-neutralino system for chargino-neutralino production [98]. The correction factors range from 0.92 to 0.51 for the ISR jet multiplicity between one and six, and from 1.18 to 0.78 for $p_{\mathrm{T}}^{\mathrm{ISR}}$ between 125 and 600 GeV. These corrections have a small effect on the signal yields for all the considered simplified models, at the level of approximately 1%. For the bottom squark pair production signal model, we propagate the full effect of the correction as a systematic uncertainty. For the chargino-neutralino production, one half of the effect of the correction is propagated as a systematic uncertainty. The signal samples used in the analysis are listed in Table 5.4.

Table 5.2: Samples for the 2016 run period.

Sample	Cross section [pb]	BR
GluGluHToGG_M125_13TeV_amcatnloFXFX_pythia8/*	48.5800	0.00227
VBFHToGG_M125_13TeV_amcatnlo_pythia8/*	3.7820	0.00227
VHToGG_M125_13TeV_amcatnloFXFX_madspin_pythia8/*	2.2569	0.00227
ttHJetToGG_M125_13TeV_amcatnloFXFX_madspin_pythia8_v2/*	0.5071	0.00227
bbHToGG_M-125_4FS_yb2_13TeV_amcatnlo/*	0.532892	0.00227
bbHToGG_M-125_4FS_ybyt_13TeV_amcatnlo/*	0.0448916	0.00227
DiPhotonJetsBox_MGG-80toInf_13TeV-Sherpa/*	84.4	
GJet_Pt-20to40_DoubleEMEnriched_MGG-80toInf_TuneCUETP8M1_13TeV_Pythia8/**	220.0	
GJet_Pt-40toInf_DoubleEMEnriched_MGG-80toInf_TuneCUETP8M1_13TeV_Pythia8/*	850.8	
QCD_Pt-30to40_DoubleEMEnriched_MGG-80toInf_TuneCUETP8M1_13TeV_Pythia8/*	22110.0	
QCD_Pt-40toInf_DoubleEMEnriched_MGG-80toInf_TuneCUETP8M1_13TeV_Pythia8/*	113400.0	

(*) = RunIISummer16MiniAODv2-PUMoriond17_80X_mcRun2_asymptotic_2016_TrancheIV_v6(_ext1/2)-v1/MINIAODSIM.

(**) = RunIISummer16MiniAODv2-PUMoriond17_backup_80X_mcRun2_asymptotic_2016_TrancheIV_v6-v1/MINIAODSIM.

Table 5.3: Samples for the 2017 run period.

Sample	Cross section [pb]	BR
GluGluHToGG_M125_13TeV_amcatnloFXFX_pythia8/*	48.5800	0.00227
VBFHToGG_M125_13TeV_amcatnlo_pythia8/*	3.7820	0.00227
VHToGG_M125_13TeV_amcatnloFXFX_madspin_pythia8/*	2.2569	0.00227
ttHJetToGG_M125_13TeV_amcatnloFXFX_madspin_pythia8/*	0.5071	0.00227
bbHToGG_M-125_4FS_yb2_13TeV_amcatnlo/*	0.532892	0.00227
bbHToGG_M-125_4FS_ybyt does not exist (yet?)	0.0448916	0.00227
DiPhotonJetsBox_MGG-80toInf_13TeV-Sherpa/*	84.4	
GJet_Pt-20to40_DoubleEMEnriched_MGG-80toInf_TuneCP5_13TeV_Pythia8/*	220.0	
GJet_Pt-40toInf_DoubleEMEnriched_MGG-80toInf_TuneCP5_13TeV_Pythia8/**	850.8	
QCD_Pt-40toInf_DoubleEMEnriched_MGG-80toInf_TuneCP5_13TeV_Pythia8/*	22110.0	
QCD_Pt-30to40_DoubleEMEnriched_MGG-80toInf_TuneCP5_13TeV_Pythia8/*	113400.0	

(*) = RunIIFall17MiniAODv2-PU2017_12Apr2018_94X_mc2017_realistic_v14-v1/MINIAODSIM.

(**) = RunIIFall17MiniAODv2-PU2017_12Apr2018_94X_mc2017_realistic_v14-v2/MINIAODSIM.

Table 5.4: Signal samples.

Sample	Cross section [pb]	BR
SMS-T2bH_mSbottom-*_mLSP-*_TuneCUETP8M1_13TeV-madgraphMLM-pythia8/*	$2 * 0.00227 - 0.00227^2$	
SMS-TChiHH_HToGG_TuneCUETP8M1_13TeV-madgraphMLM-pythia8/**	$2 * 0.00227 - 0.00227^2$	
SMS-TChiHZ_HToGG_TuneCUETP8M1_13TeV-madgraphMLM-pythia8/**	0.00227	
SMS-TChiWH_HToGG_TuneCUETP8M1_13TeV-madgraphMLM-pythia8/**	0.00227	

(*) = RunIISummer16MiniAODv2-PUMoriond17_80X_mcRun2_asymptotic_2016_TrancheIV_v6-v1/MINIAODSIM (**) = RunIISpring16MiniAODv2-PUSpring16Fast_80X_mcRun2_asymptotic_2016_miniAODv2_v0-v2/MINIAODSIM

5.3 Event reconstruction and selection

5.3.1 Triggers

The analysis selects events from data passing diphoton triggers designed for Standard Model Higgs measurements. The trigger paths used are summarized in Table 5.5. The efficiency of the triggers is measured to be above 98% and has a plateau above 40 GeV. The triggers require events to have at least two photons, with the leading photon required to have transverse energy $E_T > 30$ GeV and the subleading photon required to have $E_T > 18$ (22) GeV for the 2016 (2017) data-taking period.

Table 5.5: Trigger paths used in the analysis.

Year	Trigger paths	
2016	`HLT_Diphoton30_18_R9Id_OR_IsoCaloId_AND_HE_R9Id_Mass95`	OR
	`HLT_Diphoton30_18_R9Id_OR_IsoCaloId_AND_HE_R9Id_Mass90`	
2017	`HLT_Diphoton30_22_R9Id_OR_IsoCaloId_AND_HE_R9Id_Mass95`	OR
	`HLT_Diphoton30_22_R9Id_OR_IsoCaloId_AND_HE_R9Id_Mass90`	

5.3.2 Vertices

A reconstructed vertex is considered good if it satisfies the following conditions:

i) It is not fake.
ii) The degree of freedom N_{dof} is greater than 4.
iii) $|z| < 24$ cm.
iv) $\rho < 2$ cm.

If more than one good vertex exists in an event, the vertices are sorted in ascending order by the sum of the associated track momentum squares $\sum p_T^2$. The first vertex with the largest $\sum p_T^2$ is chosen. The anti-k_T algorithm [99] is used to cluster the tracks. Tracks associated with other vertices are neglected when building jets or isolation variables, which is known as charged hadron subtraction (CHS), and the four-momenta of neutral candidates originate from the chosen vertex.

5.3.3 Muons

The RECO muon candidates are required to have $p_{\mathrm{T}} > 20$ GeV and $|\eta| < 2.4$. We select muons passing the Loose working point defined by the Physics Object Group (POG) [100]. The following cuts are applied:

i) isPFMuon.
ii) isGlobalMuon `OR` isTrackerMuon.

The Particle Flow (PF) algorithm reconstructs final-state particles in each collision [101]. For muon reconstruction, there are three final collection types: (i) `standalone muon`, where hits from each DT or CSC detector are clustered into track segments to form a standalone-muon track; (ii) `global muon`, where each standalone track is matched to an inner track if parameters are compatible, forming a global-muon track and associated with a global muon; and (iii) `tracker muon`, where inner tracks are extrapolated to the muon system and matched to at least one muon segment in a local (x, y) coordinate system defined in a plane transverse to the beam axis.

In the PF muon identification algorithm, muon identification is performed using selections based on global and tracker muon properties, as well as energy deposits in ECAL, HCAL, and HO associated with the muon track to improve identification performance. Only muons with $p_{\mathrm{T}} > 20$ GeV and $|\eta| < 2.4$ that pass the Physics Object Group (POG) Loose working point [100] with the cuts: (i) isPFMuon and (ii) isGlobalMuon `OR` isTrackerMuon are selected.

Additionally, we impose a selection on the impact parameter (IP) [102], which represents the distance between the track and the collision point at the point of closest approach:

i) $|d_0| < 0.2$ cm with respect to the primary vertex.
ii) $|d_z| < 0.5$ cm with respect to the primary vertex.

We also require the muons to be isolated by imposing a cut on the relative mini Particle Flow (PF) isolation: $\mathrm{miniIso}/p_T < 0.2$. The mini-isolation variable is defined by Eq. 5.1, and its definition involves shrinking the isolation cone as the p_T of the muon increases, which improves the efficiency of muon identification in events with many jets.

$$R = \begin{cases} 0.2, & p_T \leq 50 \text{ GeV} \\ \frac{10\text{GeV}}{p_T}, & 50 \text{ GeV} \leq p_T \leq 200 \text{ GeV} \\ 0.05, & p_T \geq 200 \text{ GeV} \end{cases} \tag{5.1}$$

The mini-isolation variable is corrected for the photon and neutral hadron components using an effective area that is computed for a cone size of 0.3. The effective areas are presented as a function of η in Table 5.6. To scale the effective area to the geometric area of the cone corresponding to each muon, we use the following formula: $EA = EA_{0.3\text{ cone}} \cdot (\Delta R/0.3)^2$.

Table 5.6: Effective areas used for the pileup correction for the muon mini-isolation variable.

Bin	Charged Effective Area	Photons + Neutral Hadrons Effective Area
$\lvert\eta\rvert < 0.8$	0.0106	0.0735
$0.8 \leq \lvert\eta\rvert < 1.3$	0.0096	0.0619
$1.3 \leq \lvert\eta\rvert < 2.0$	0.0079	0.0465
$2.0 \leq \lvert\eta\rvert < 2.2$	0.0058	0.0433
$2.2 \leq \lvert\eta\rvert$	0.0053	0.0577

5.3.4 Electrons

RECO electron candidates must satisfy $p_T > 20$ GeV and $|\eta| < 2.4$. We select electrons that pass the Loose working point of the EGAMMA POG-defined cut-based ID. The selection criteria are summarized in Table 5.7 and Table 5.8, where electrons with $|\eta_{\mathrm{SC}}| > 1.479$ are considered to be in the endcap.

We also require electrons to be isolated, with a cut on relative PF mini-isolation of $miniIso/p_{\mathrm{T}} < 0.1$. The mini-isolation variable is defined in the same way as for muons, described above in Eq. 5.1. Effective areas for electrons are computed using a fixed cone of size 0.3 and are summarized in Table 5.9 and Table 5.10. The effective areas are then scaled according to the geometric area of the cone corresponding to each particular electron ($EA = EA_{0.3\text{ cone}} \cdot (\Delta R/0.3)^2$).

Electron candidates within a ΔR cone of 0.4 to any selected muon are vetoed, as they may be affected by the muon's energy deposition, known as the footprint of the muon.

Table 5.7: Summary of the cuts used for the cut-based electron selection for the 2016 dataset.

Variable	Loose Selection (Barrel)	Loose Selection (Endcap)
$\sigma_{i\eta i\eta}$	< 0.011	< 0.0314
$\Delta\eta$	< 0.00477	< 0.00868
$\Delta\phi$	< 0.222	< 0.213
H/E	< 0.298	< 0.101
$1/E - 1/P$	< 0.241	< 0.14
$\lvert d_0 \rvert$	< 0.05	< 0.1
$\lvert d_z \rvert$	< 0.1	< 0.2
Missing Hits	≤ 1	≤ 1
ConversionVeto	Yes	Yes

Table 5.8: Summary of the cuts used for the cut-based electron selection for the 2017 dataset.

Variable	Loose Selection (Barrel)	Loose Selection (Endcap)
$\sigma_{i\eta i\eta}$	< 0.0112	< 0.0425
$\Delta\eta$	< 0.00377	< 0.00674
$\Delta\phi$	< 0.0884	< 0.169
H/E	$< 0.05 + 1.16/E + 0.0324 * \rho/E$	$< 0.0441 + 2.54/E + 0.183 * \rho/E$
$1/E - 1/P$	< 0.193	< 0.111
$\lvert d_0 \rvert$	< 0.05	< 0.1
$\lvert d_z \rvert$	< 0.1	< 0.2
Missing Hits	≤ 1	≤ 1
ConversionVeto	Yes	Yes

Table 5.9: Effective areas used for the pileup correction for the electron mini-isolation variable for the 2016 dataset.

Bin	Effective Area
$\lvert\eta\rvert < 1.0$	0.1703
$1.0 \leq \lvert\eta\rvert < 1.479$	0.1715
$1.479 \leq \lvert\eta\rvert < 2.0$	0.1212
$2.0 \leq \lvert\eta\rvert < 2.2$	0.1230
$2.2 \leq \lvert\eta\rvert < 2.3$	0.1635
$2.3 \leq \lvert\eta\rvert < 2.4$	0.1937
$2.4 \leq \lvert\eta\rvert < 2.5$	0.2393

Table 5.10: Effective areas used for the pileup correction for the electron mini-isolation variable for the 2017 dataset.

Bin	Effective Area
$\|\eta\| < 1.0$	0.1440
$1.0 \leq \|\eta\| < 1.479$	0.1562
$1.479 \leq \|\eta\| < 2.0$	0.1032
$2.0 \leq \|\eta\| < 2.2$	0.0859
$2.2 \leq \|\eta\| < 2.3$	0.1116
$2.3 \leq \|\eta\| < 2.4$	0.1321
$2.4 \leq \|\eta\| < 2.5$	0.1654

5.3.5 Photons

Photons are selected in the barrel region only ($|\eta| < 1.44$) according to the EGAMMA POG defined Loose ID based on electromagnetic shower shape, hadronic to electromagnetic energy ratio, and isolation around the photon candidate, which is specified in Table 5.11 with a 90% efficiency. Additionally they are required to pass the conversion safe electron veto.

Variable(s)	2016	2017
H/E	0.0597	0.04596
$sigma_{ietaieta}$	0.01031	0.0106
Rho corrected PF charged hadron isolation	1.295	1.694
Rho corrected PF neutral hadron isolation	$10.910 + 0.0148 * p_T$ $+0.000017 * p_T^2$	$24.032 + 0.01512 * p_T$ $+2.259e - 05 * p_T^2$
Rho corrected PF photon isolation photon isolation	$3.630 + 0.0047 * p_T$	$2.876 + 0.004017 * p_T$

Table 5.11: List of cut values for the loose photon ID for 2016 and 2017 for the barrel only.

The particle flow isolation is corrected to account for the effect of pileup by subtracting the average energy deposited into the isolation cone, which is estimated through the ρ observable. The ρ observable is multiplied by an effective area, which is designed to give isolation distributions that are flat as a function of pileup in Monte Carlo simulations. The effective area values for photons are given in Table 5.12 and Table 5.13 for the 2016 and 2017 datasets, respectively.

$\lvert\eta\rvert$ bin	Charged Hadron Isolation	Neutral Hadron Isolation	Photon Isolation
$\lvert\eta\rvert < 1.0$	0.0360	0.0597	0.1210
$1.0 < \lvert\eta\rvert < 1.479$	0.0377	0.0807	0.1107
$1.479 < \lvert\eta\rvert < 2.0$	0.0306	0.0629	0.0699
$2.0 < \lvert\eta\rvert < 2.2$	0.0283	0.0197	0.1056
$2.2 < \lvert\eta\rvert < 2.3$	0.0254	0.0184	0.1457
$2.3 < \lvert\eta\rvert < 2.4$	0.0217	0.0284	0.1719
$2.4 < \lvert\eta\rvert$	0.0167	0.0591	0.1998

Table 5.12: Summary of the effective areas used for the pileup correction for photon isolation for the 2016 dataset.

$\lvert\eta\rvert$ bin	Charged Hadron Isolation	Neutral Hadron Isolation	Photon Isolation
$\lvert\eta\rvert < 1.0$	0.0112	0.0668	0.1113
$1.0 < \lvert\eta\rvert < 1.479$	0.0108	0.1054	0.0953
$1.479 < \lvert\eta\rvert < 2.0$	0.0106	0.0786	0.0619
$2.0 < \lvert\eta\rvert < 2.2$	0.01002	0.0233	0.0837
$2.2 < \lvert\eta\rvert < 2.3$	0.0098	0.0078	0.1070
$2.3 < \lvert\eta\rvert < 2.4$	0.0089	0.0028	0.1212
$2.4 < \lvert\eta\rvert$	0.0087	0.0137	0.1466

Table 5.13: Summary of the effective areas used for the pileup correction for photon isolation for the 2017 dataset.

The energy of photons is measured and corrected for clustering and local geometric effects using an energy regression trained on Monte Carlo (MC) simulation, which is calibrated using a combination of $\pi^0 \to \gamma\gamma$, $\eta \to \gamma\gamma$, and $Z \to ee$ candidates [103]. The energy regression is also trained to estimate the uncertainty of the energy measurement, which is used in this analysis to categorize events into high- and low-resolution categories. The regression correction and uncertainty estimate used in this analysis are the standard versions produced by the MiniAOD data tier.

To avoid double counting, photons within a cone of $\Delta R = 1.0$ around selected electrons and $\Delta R = 0.5$ around selected muons are discarded. A larger veto cone is used for electrons to suppress photon conversions.

5.3.6 Jets and b-tagging

The PF candidates are clustered into jets using the anti-k_{T} algorithm [104, 105] within a cone of 0.4. Jets are required to satisfy $p_T > 30$GeV and $|\eta| < 2.4$, and must pass the PF jet loose ID and tight ID for the 2016 and 2017 eras, respectively [106]. B-tagged jets are identified using the combined secondary vertex (CSVv2) tagger algorithm [107] with a loose working point, requiring $p_{\mathrm{T}} > 20$ GeV. The resulting b-tagging efficiency is about 80%, while the mistag rate for light-quark and gluon jets is approximately 10%.

Jets that overlap with the selected electrons, muons, and photons in a cone of size ΔR = 0.4 are vetoed.

5.3.7 Missing transverse momentum

The missing transverse momentum $\vec{p}_{\mathrm{T}}^{\mathrm{miss}}$is defined as the negative vector sum of the transverse momenta of all particle flow (PF) candidates, and its magnitude is defined as $p_{\mathrm{T}}^{\mathrm{miss}}$(MET). Dedicated filters are applied to reject events with possible beam halo contamination or anomalous noise in the calorimeter systems, which can result in large $p_{\mathrm{T}}^{\mathrm{miss}}$values. These filters are designed to remove events with large fake $p_{\mathrm{T}}^{\mathrm{miss}}$and are based on various event-level and object-level criteria, such as the ratio of energy deposited in the calorimeter towers along the beamline to the total transverse energy in the event, the distribution of the azimuthal angles between the $\vec{p}_{\mathrm{T}}^{\mathrm{miss}}$and the jets or the muons, and the compatibility of the $\vec{p}_{\mathrm{T}}^{\mathrm{miss}}$with the nominal bunch crossing time. The filters used in this analysis follow those recommended by the CMS Collaboration [108].

5.4 Analysis strategy

The EWP analysis is focused on the electroweak production of charginos and neutralinos. Events are categorized based on the p_{T} of the diphoton Higgs boson candidate and the presence of additional leptonic candidates. For each category, search region bins are defined based on kinematic variables that distinguish SUSY signal events from SM background events. Finally, an unbinned extended maximum likelihood fit is performed on the diphoton mass distribution for all search bins simultaneously.

The primary source of background in this analysis is from the SM production of diphotons or photon+jets, which is referred to as the non-resonant background. The non-resonant background exhibits a regular exponential-like falling shape as validated in the MC simulation samples, and is modeled using a fit to a family of functions, independently in each search region bin, based on the validation of MC simulation samples. The SM Higgs boson background, on the other hand, exhibits a resonant shape in the diphoton mass spectrum, which is constrained to the MC simulation predictions within uncertainties. The SUSY signal model under test also exhibits a resonant shape. A detailed description of the background fit model and the systematic uncertainties is presented in Sec. 5.5 and Sec. 5.6, respectively.

In this analysis, we build upon the strategy used in a previous publication [69]. The events are categorized based on the p_{T} of the diphoton Higgs boson candidate, the presence of an additional Higgs boson candidate, the estimated diphoton mass resolution, and the values of the razor kinematic variables [109, 110]. To improve the analysis, we add event categories with one or two identified leptons and optimize the binning in the kinematic variables using the enlarged dataset (77 fb^{-1} vs. 36 fb^{-1}). The bin boundaries are chosen to maximize the expected signal significance, which is estimated using the simulation predictions of the signal and background yields. These enhancements improve the sensitivity of the analysis to the electroweak production of charginos and neutralinos. A more detailed description of the analysis strategy can be found in the following sections.

5.4.1 Razor variables

The Higgs boson candidate, as well as any additional identified leptons or jets, are combined into two hemispheres using the razor megajet algorithm [110]. This algorithm minimizes the sum of the squared-invariant-mass values of the two megajets, and the resulting hemispheres are illustrated in Fig. 5.2. In order to ensure the formation of two hemispheres, at least one identified lepton or jet in addition to the Higgs boson candidate is required.

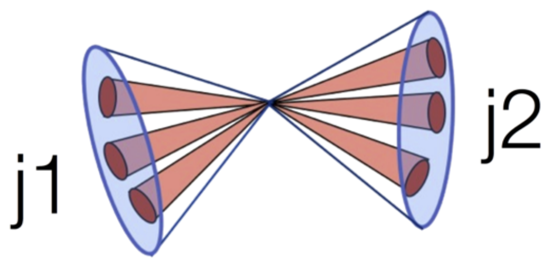

Figure 5.2: Megajets diagram.

The razor variables M_R and R^2 are calculated using the razor megajet algorithm [110] and are defined as follows:

$$M_R \equiv \sqrt{(\vec{p}^{\,j_1} + \vec{p}^{\,j_2})^2 - (p_z^{\,j_1} + p_z^{\,j_2})^2}, \tag{5.2}$$

$$R^2 \equiv \left(\frac{M_T^R}{M_R}\right)^2, \tag{5.3}$$

where $\vec{p}$ is the momentum of a megajet, p_z is its longitudinal component, and j_1 and j_2 are used to label the two megajets. The variable M_T^R is defined as:

$$M_T^R \equiv \sqrt{\frac{p_T^{miss}(p_T^{\,j_1} + p_T^{\,j_2}) - \vec{p}_T^{\,miss} \cdot (\vec{p}_T^{\,j_1} + \vec{p}_T^{\,j_2})}{2}}. \tag{5.4}$$

The razor variables provide discrimination between SUSY signal models and SM background processes, with SUSY signals typically having large values of M_{R} and R^2, while the SM diphoton and photon+jets backgrounds exhibit a falling spectrum in each variable. The use of these variables has been shown to be effective in the previous publication [110] and has been applied to this analysis to enhance the signal sensitivity.

5.4.2 Event categorization

The selected events are classified into different categories based on their characteristics, as shown in Fig. 5.3, with the following details:

i) Events are first categorized based on the number of electrons or muons. Events with two same-flavor opposite-sign leptons are placed in the "Two-Lepton" category if the dilepton mass satisfies the constraint $|m_Z - m_{\ell\ell}| \leq 20\,\mathrm{GeV}$.

ii) Among the remaining events, those with at least one muon (electron) are placed in the "Muon" ("Electron") category, with the Muon category taking precedence. Events in the Electron and Muon categories are further subdivided into the "High-p_{T}" and "Low-p_{T}" subcategories depending on whether the p_{T} of the Higgs boson candidate is larger or smaller than 110 GeV.

iii) For events with no leptons, we search for pairs of b-tagged jets with masses between 95 and 140 GeV, and place them into the "Hb$\bar{b}$" category. If no such jet pairs are found, then we search for pairs of b-tagged jets with masses between 60 and 95 GeV, and place them into the "Zb$\bar{b}$" category. Events in the Hb$\bar{b}$ and Zb$\bar{b}$ categories are further divided into High-p_{T} and Low-p_{T} subcategories using the same criteria stated above.

iv) Among the remaining events, those with the p_{T} of the Higgs boson candidate larger than 110 GeV are placed in the "High-p_{T}" category.

v) Finally, the remaining events are categorized as "High-Res" or "Low-Res" based on the diphoton mass resolution estimate σ_m/m. If σ_m/m is smaller or larger than 0.85%, the events are placed in the High-Res or Low-Res categories, respectively. Here, σ_m is defined as

$$\sigma_m = \frac{1}{2}\sqrt{(\sigma_{E\gamma1}/E_{\gamma1})^2 + (\sigma_{E\gamma2}/E_{\gamma2})^2}, \tag{5.5}$$

where $E_{\gamma1,2}$ is the energy of each photon and $\sigma_{E\gamma1,2}$ is the estimated energy resolution for each photon. The threshold of 0.85% was chosen to be identical to past results [69] and was previously optimized for signal-to-background discrimination.

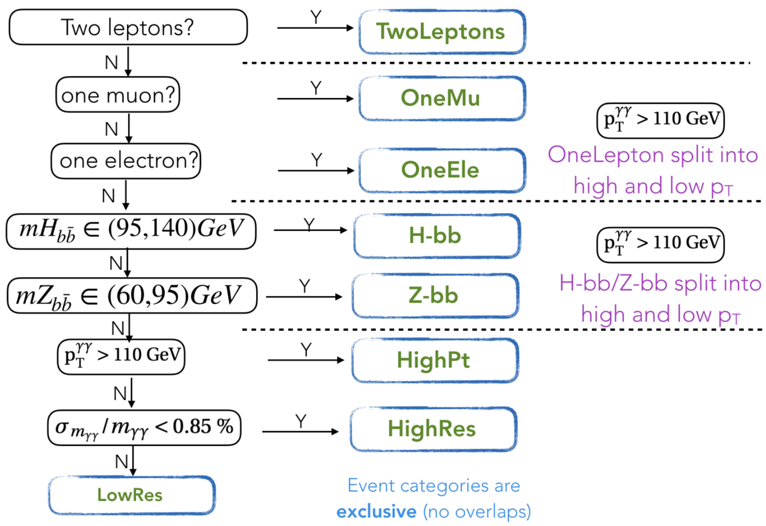

Figure 5.3: Categorization diagram.

The leptonic categories are used to select SUSY events that contain decays to W or Z bosons, while the H$b\bar{b}$ (Z$b\bar{b}$) categories are used to select events containing an additional Higgs (Z) boson that decays to a pair of b-jets. The High-p_T category is used to select SUSY events producing high-p_T Higgs bosons. The separation into the High-Res and Low-Res categories further improves the discrimination between any signal containing an $H \to \gamma\gamma$ candidate and non-resonant background in the remaining event sample. To distinguish SUSY signal events from the SM background, each event category is further divided into bins in the M_R and R^2 variables, provided that there are a sufficient number of data events in the diphoton mass sideband to estimate the background. These bins define the exclusive search regions. For all categories except the Two-Lepton category, we require $M_R > 150$ GeV to suppress the SM backgrounds. Table 5.14 summarizes the 35 search region bins for the EWP analysis.

Table 5.14: A summary of the search region bins used in the EWP analysis. Events are separated into categories based on the number of leptons, the presence of $H \to b\bar{b}$ candidates, the p_{T} of the $H \to \gamma\gamma$ candidate, and the estimated diphoton mass resolution. The High-Res and Low-Res categories are defined by the estimated diphoton resolution mass σ_m/m being smaller or larger than 0.85%, respectively. For the Two-Lepton category, "No req." means that no requirements are placed on the given observables.

Bin number	Category	$p_{\mathrm{T}}^{\gamma\gamma}$ (GeV)	M_{R} (GeV)	R^2
EWP 0	Two-Lepton	No req.	No req.	No req.
EWP 1	Muon High-p_{T}	≥110	≥150	≥0.0
EWP 2	Muon Low-p_{T}	0–110	≥150	≥0.0
EWP 3	Electron High-p_{T}	≥110	≥150	≥0.0
EWP 4	Electron Low-p_{T}	0–110	≥150	0.000–0.055
EWP 5	Electron Low-p_{T}	0–110	≥150	0.055–0.125
EWP 6	Electron Low-p_{T}	0–110	≥150	≥0.125
EWP 7	Hb$\bar{b}$ High-p_{T}	≥110	≥150	0.000–0.080
EWP 8	Hb$\bar{b}$ High-p_{T}	≥110	≥150	≥0.080
EWP 9	Hb$\bar{b}$ Low-p_{T}	0–110	≥150	0.000–0.080
EWP 10	Hb$\bar{b}$ Low-p_{T}	0–110	≥150	≥0.080
EWP 11	Zb$\bar{b}$ High-p_{T}	≥110	≥150	0.000–0.035
EWP 12	Zb$\bar{b}$ High-p_{T}	≥110	≥150	0.035–0.090
EWP 13	Zb$\bar{b}$ High-p_{T}	≥110	≥150	≥0.090
EWP 14	Zb$\bar{b}$ Low-p_{T}	0–110	≥150	0.000–0.035
EWP 15	Zb$\bar{b}$ Low-p_{T}	0–110	≥150	0.035–0.090
EWP 16	Zb$\bar{b}$ Low-p_{T}	0–110	≥150	≥0.090
EWP 17	High-p_{T}	≥110	≥150	≥0.260
EWP 18	High-p_{T}	≥110	150–250	0.170–0.260
EWP 19	High-p_{T}	≥110	≥250	0.170–0.260
EWP 20	High-p_{T}	≥110	≥150	0.000–0.110
EWP 21	High-p_{T}	≥110	150–350	0.110–0.170
EWP 22	High-p_{T}	≥110	≥350	0.110–0.170
EWP 23	High-Res	0–110	≥150	≥0.325
EWP 24	High-Res	0–110	≥150	0.285–0.325
EWP 25	High-Res	0–110	≥150	0.225–0.285
EWP 26	High-Res	0–110	≥150	0.000–0.185
EWP 27	High-Res	0–110	150–200	0.185–0.225
EWP 28	High-Res	0–110	≥200	0.185–0.225
EWP 29	Low-Res	0–110	≥150	≥0.325
EWP 30	Low-Res	0–110	≥150	0.285–0.325
EWP 31	Low-Res	0–110	≥150	0.225–0.285
EWP 32	Low-Res	0–110	≥150	0.000–0.185
EWP 33	Low-Res	0–110	150–200	0.185–0.225
EWP 34	Low-Res	0–110	≥200	0.185–0.225

5.4.3 Signal extraction

The analysis performs a combined simultaneous fit using all the search regions to test specific SUSY simplified model hypotheses. The diphoton mass distribution is independently fitted in each search region, while the expected yields for the SM Higgs background and SUSY signal model are constrained to their predicted values among the different search regions.

For SUSY signals with larger squark or neutralino masses, search region bins with large values of $p_{\mathrm{T}}^{\gamma\gamma}$ and large values of the kinematic variables M_{R} provide the best sensitivity, as the backgrounds are heavily suppressed. On the other hand, event categories with one lepton, two leptons, a $Z \to b\bar{b}$ candidate, or a $H \to b\bar{b}$ candidate yield increasing sensitivity for more compressed regions as the neutralino mass approaches the Higgs boson mass.

5.5 Background estimation

There are two types of backgrounds that can be identified in this analysis: a non-resonant background stemming from the SM production of diphotons or a photon and a jet, and a resonant background from SM Higgs boson production. The non-resonant background prediction is estimated by fitting a functional form to the diphoton mass distribution observed in data for each search region bin. The SM Higgs background is estimated using Monte Carlo (MC) simulation.

5.5.1 Non-resonant background

To model the non-resonant background, we consider a set of possible function forms, such as sums of exponential functions, Bernstein polynomials, Laurent series, and power-law functions. The most appropriate functional form to describe the background spectrum is determined using the Akaike information criterion (AIC) [111]. We follow the same procedure as the previous version of this search [69]. To assess the potential for bias, we perform bias tests by generating random events using one functional form and fitting the resulting pseudo-data set to another functional form. We choose the functional form with the best AIC measure that passes the bias test to describe the non-resonant background. Table 5.15 summarizes the selected functional form for each signal region bin.

Table 5.15: List of functional forms used to model the non-resonant background for different signal region bins, as determined by the AIC and bias tests.

Bin	Category	MR Low	MR High	R^2 Low	R^2 High	Function	AIC weight	Max bias / (σ_{stat})
0	Two-Lepton	0	∞	0	∞	singleExp	0.426	24.2 %
1	Muon High-p_T	150	∞	0	∞	singleExp	0.434	17.3 %
2	Muon Low-p_T	150	∞	0	∞	singleExp	0.317	7.5 %
3	Electron High-p_T	150	∞	0	∞	singleExp	0.376	17.9 %
4	Electron Low-p_T	150	∞	0.125	∞	singleExp	0.438	21.6 %
5	Electron Low-p_T	150	∞	0	0.055	poly2	0.504	25.4 %
6	Electron Low-p_T	150	∞	0.055	0.125	singleExp	0.314	20.6 %
7	$Hb\bar{b}$ High-p_T	150	∞	0.080	∞	singleExp	0.416	6.9 %
8	$Hb\bar{b}$ High-p_T	150	∞	0	0.080	singleExp	0.292	12.3 %
9	$Hb\bar{b}$ Low-p_T	150	∞	0.080	∞	poly2	0.124	31.2 %
10	$Hb\bar{b}$ Low-p_T	150	∞	0	0.080	singlePow	0.648	1.8 %
11	$Zb\bar{b}$ High-p_T	150	∞	0.090	∞	poly3	0.120	18.4 %
12	$Zb\bar{b}$ High-p_T	150	∞	0	0.035	singleExp	0.424	12.3 %
13	$Zb\bar{b}$ High-p_T	150	∞	0.035	0.090	singleExp	0.305	8.6 %
14	$Zb\bar{b}$ Low-p_T	150	∞	0.090	∞	singlePow	0.611	2.6 %
15	$Zb\bar{b}$ Low-p_T	150	∞	0	0.035	singlePow	0.441	4.9 %
16	$Zb\bar{b}$ Low-p_T	150	∞	0.035	0.090	singlePow	0.621	2.5 %
17	High-p_T	150	∞	0.260	∞	singlePow	0.415	28.6 %
18	High-p_T	150	250	0.170	0.260	singleExp	0.388	15.2 %
19	High-p_T	250	∞	0.170	0.260	singleExp	0.352	20.7 %
20	High-p_T	150	∞	0	0.110	singlePow	0.243	25.5 %
21	High-p_T	150	350	0.110	0.170	singleExp	0.300	7.2 %
22	High-p_T	350	∞	0.110	0.170	singleExp	0.422	24.4 %
23	High-Res	150	∞	0.325	∞	singleExp	0.419	19.8 %
24	High-Res	150	∞	0.225	0.285	poly2	0.138	23.6 %
25	High-Res	150	∞	0.285	0.325	singleExp	0.448	23.1 %
26	High-Res	150	∞	0	0.185	singleExp	0.651	2.3 %
27	High-Res	150	200	0.185	0.225	singleExp	0.307	8.3 %
28	High-Res	200	∞	0.185	0.225	singleExp	0.429	18.8 %
29	Low-Res	150	∞	0.325	∞	singleExp	0.400	11.9 %
30	Low-Res	150	∞	0.225	0.285	singleExp	0.423	7.1 %
31	Low-Res	150	∞	0.285	0.325	singlePow	0.275	25.4 %
32	Low-Res	150	∞	0	0.185	singlePow	0.818	1.0 %
33	Low-Res	150	200	0.185	0.225	doubleExp	0.241	24.0 %
34	Low-Res	200	∞	0.185	0.225	singleExp	0.441	23.6 %

5.5.2 Resonant background

The background shape of the SM Higgs boson and SUSY signals is modeled by a double Crystal Ball function [112, 113]. The diphoton mass distribution from the MC simulation is fitted separately in each search region bin to obtain the parameters of each double Crystal Ball function. During the signal extraction fit procedure, the parameters of each double Crystal Ball function are held constant. The normalization for the SM Higgs background is constrained to the best estimate from the Monte Carlo simulation prediction to within systematic uncertainties. Nuisance parameters, modeled as log-normal distributions, that take into account the systematic uncertainties on the SM Higgs background normalization due to missing higher order corrections, PDF's, trigger and selection efficiencies, jet energy scale uncertainties, and b-tagging efficiencies are incorporated into the model for the SM Higgs background as well as the signal.

5.5.3 Signal extraction

The signal is extracted by performing an unbinned maximum likelihood fit in each exclusive search region bin. The likelihood function used for the fit is as follows:

$$\begin{aligned}\mathcal{L}(\mathrm{data}|\mu\mathrm{S}+\mathrm{B}) = \frac{1}{N}\prod_{i=1}^{N}&\left\{\left(\mu S\prod_{\alpha=1}^{N_\alpha}\kappa_\alpha^{\theta_\alpha} f_s(x_i-\theta_\mu) + B_1\prod_{\beta=1}^{N_\beta}\kappa_\beta^{\theta_\beta} f_{b_1}(x_i-\theta_\mu) + B_2 f_{b_2}(x_i;\theta_\gamma)\right)\right\}\\ &\times Exp\left(-\left(\mu S\prod_{\alpha=1}^{N_\alpha}\kappa_\alpha^{\theta_\alpha} + B_1\prod_{\beta=1}^{N_\beta}\kappa_\beta^{\theta_\beta} + B_2\right)\right)\\ &\times G(\theta_\mu;0,\kappa_\mu)\prod_{\alpha=1}^{N_\alpha}G(\theta_\alpha)\prod_{\beta=1}^{N_\beta}G(\theta_\beta),\end{aligned} \tag{5.6}$$

where x_i is the diphoton invariant mass for event i, N is the total number of events in the corresponding search region bin, S is the total expected signal events, B_1 is the exptected SM higgs background, and B_2 is the exptected non-resonant background; κ_α and κ_β are constant parameters that represent the size of the systematic uncertainties for the signal and the SM higgs yields (cross-section, pdf, factorization scale uncertainties among others) respectively; while θ_α, θ_β, and θ_γ represent the floating nuisance parameters for the signal, SM higgs, and non-resonant background respectively. Finally, θ_μ is the nuisance parameter for the scale uncertainty for the signal and SM higgs line shape and κ_μ the size of the scale uncertainty.

5.6 Systematic uncertainties

In this analysis, the dominant systematic uncertainties result from the normalization and the fitted functional form of the shape for the non-resonant background. They are propagated by profiling the associated unconstrained functional form parameters. The subdominant systematic uncertainties result from the SM Higgs boson background and SUSY signal, which are propagated through independent log-normal nuisance parameters that consider both theoretical and instrumental effects. These systematic uncertainties affect the event yield predictions of the SM Higgs boson background and SUSY signal in different search region bins and are propagated as shape uncertainties. The independent systematic effects considered include missing higher-order QCD corrections, PDFs (probability density functions), trigger and object selection efficiencies, jet energy scale uncertainties, b-tagging efficiency, lepton identification efficiencies, fast simulation $p_{\mathrm{T}}^{\mathrm{miss}}$modeling, and the uncertainty in the integrated luminosity. The typical size of these effects on the signal and background yields is summarized in Table 5.16. The systematic uncertainties due to missing higher-order corrections are estimated using the procedure outlined in Ref. [114], where the factorization (μ_{F}) and renormalization (μ_{R}) scales vary independently by factors of 0.5 and 2.0. The PDF systematic uncertainties are propagated for the SM Higgs background as a shape uncertainty using the LHC4PDF procedure [115].

We observed mismodeling in the estimated mass resolution due to imperfect simulation of the effects of pileup and transparency loss from radiation damage in the ECAL crystals, which can cause events to migrate between the High-Res and Low-Res event categories for the analysis. A systematic uncertainty of 10-24% is measured using a $Z \rightarrow e^{+}e^{-}$ control sample, and is propagated to the prediction of the SM Higgs boson background and SUSY signal yields in the High-Res and Low-Res event categories. The photon energy scale systematic uncertainty is implemented as a Gaussian-distributed nuisance parameter that shifts the Higgs boson mass peak position, constrained in the fit to lie within approximately 1% of the nominal Higgs boson mass observed in simulation. Additionally, the systematic uncertainty for the modeling of ISR for the signal process is also taken into account.

Table 5.16: Summary of systematic uncertainties on the SM Higgs boson background and signal yield predictions, and the size of their effect on the signal yield.

Uncertainty source	Uncertainty size (%)
PDFs and QCD scale variations	10–30 (SM Higgs boson) 5–10 (EWK SUSY signal) 15–30 (Strong SUSY signal)
Signal ISR modeling	5–25
σ_m/m categorization	10–24
Fast simulation $p_{\mathrm{T}}^{\mathrm{miss}}$modeling	3–16
Luminosity	2.3–2.5
Trigger and selection efficiency	3
Lepton efficiency	4
Jet energy scale	1–5
Photon energy scale	1
b-tagging efficiency	4
$H \to \gamma\gamma$ branching fraction	2

5.7 Results

As stated before, the fit results for the search region bins including the data yields, fitted background, and signal yields are summarized in Table 5.17. Example fit results are shown in Fig. 5.4 to illustrate the background-only and signal plus background fits. There is no statistically significant deviation observed from the SM background expectation.

Table 5.17: The observed data, fitted nonresonant background yields, and SM Higgs boson background yields within the mass window between 122 and 129 GeV are shown for each search region bin of the EWP analysis. The uncertainties quoted are the fit uncertainties, which include the impact of all systematic uncertainties.

Search region bin	Category	Observed data	Fitted nonresonant bkg	SM Higgs boson bkg
EWP 0	Two-Lepton	2	1.5 ± 0.4	1.1 ± 0.6
EWP 1	Muon High-p_T	11	6.2 ± 0.9	3.7 ± 0.8
EWP 2	Muon Low-p_T	28	15.8 ± 1.4	3.0 ± 0.8
EWP 3	Electron High-p_T	17	11.9 ± 1.3	3.4 ± 1.1
EWP 4	Electron Low-p_T	8	5.2 ± 0.8	0.6 ± 0.2
EWP 5	Electron Low-p_T	18	31.5 ± 1.9	0.9 ± 0.4
EWP 6	Electron Low-p_T	9	13.7 ± 1.3	0.7 ± 0.3
EWP 7	$Hb\bar{b}$ High-p_T	9	7.0 ± 0.9	1.2 ± 0.4
EWP 8	$Hb\bar{b}$ High-p_T	19	17.8 ± 1.5	3.8 ± 0.7
EWP 9	$Hb\bar{b}$ Low-p_T	34	25.8 ± 1.8	0.8 ± 0.1
EWP 10	$Hb\bar{b}$ Low-p_T	60	51.0 ± 2.4	1.9 ± 0.3
EWP 11	$Zb\bar{b}$ High-p_T	3	7.2 ± 1.1	0.5 ± 0.1
EWP 12	$Zb\bar{b}$ High-p_T	17	14.0 ± 1.3	2.8 ± 1.1
EWP 13	$Zb\bar{b}$ High-p_T	10	9.4 ± 1.1	1.3 ± 0.3
EWP 14	$Zb\bar{b}$ Low-p_T	27	35.2 ± 2.0	0.8 ± 0.2
EWP 15	$Zb\bar{b}$ Low-p_T	84	75.1 ± 2.9	2.5 ± 1.3
EWP 16	$Zb\bar{b}$ Low-p_T	45	46.3 ± 2.3	1.2 ± 0.4
EWP 17	High-p_T	11	14.4 ± 1.3	1.8 ± 0.2
EWP 18	High-p_T	31	21.8 ± 1.6	2.1 ± 0.4
EWP 19	High-p_T	11	13.5 ± 1.3	1.2 ± 0.3
EWP 20	High-p_T	1834	1648 ± 14	248 ± 38
EWP 21	High-p_T	91	100.2 ± 3.7	8.9 ± 1.5
EWP 22	High-p_T	12	14.4 ± 1.4	1.2 ± 0.2
EWP 23	High-Res	30	20.6 ± 1.6	0.6 ± 0.2
EWP 24	High-Res	46	49.1 ± 4.0	1.5 ± 0.5
EWP 25	High-Res	9	17.0 ± 1.4	0.4 ± 0.1
EWP 26	High-Res	5186	5057 ± 25	219 ± 42
EWP 27	High-Res	53	63.0 ± 2.6	2.4 ± 1.0
EWP 28	High-Res	19	17.7 ± 1.5	0.5 ± 0.1
EWP 29	Low-Res	26	33.8 ± 2.1	0.3 ± 0.1
EWP 30	Low-Res	61	65.8 ± 3.0	0.9 ± 0.2
EWP 31	Low-Res	24	18.3 ± 1.5	0.2 ± 0.1
EWP 32	Low-Res	5548	5328 ± 22	141 ± 27
EWP 33	Low-Res	78	79.1 ± 2.9	1.4 ± 0.4
EWP 34	Low-Res	25	23.7 ± 1.8	0.4 ± 0.1

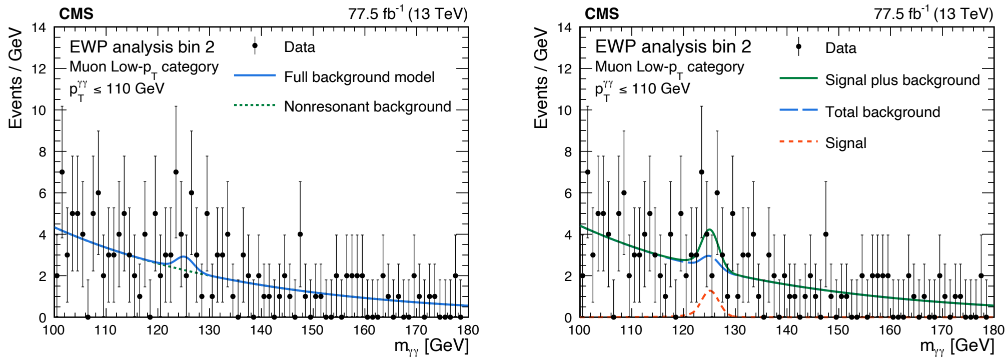

Figure 5.4: The diphoton mass distribution for two example search bin is shown with the background-only fit (Left) and the signal-plus-background fit (Right) to illustrate the signal extraction procedure. The search region bins shown corresponds to the Muon Low-p_{T} category, bin 2, of the EWP analysis.

The results of this analysis are presented as limits on the product of the production cross section and branching fraction for simplified models of bottom squark pair production and chargino-neutralino production, as shown in Fig. 5.1.

For bottom squark pair production, we consider the scenario ($\tilde{b} \rightarrow b\tilde{\chi}_2^0, \tilde{\chi}_2^0 \rightarrow H\tilde{\chi}_1^0$) where the bottom squark decays to a bottom quark and the next-to-lightest neutralino ($\tilde{\chi}_2^0$), which subsequently decays to a Higgs boson and the lightest neutralino ($\tilde{\chi}_1^0$). We assume a mass splitting of 130 GeV between the $\tilde{\chi}_2^0$ and $\tilde{\chi}_1^0$, which is slightly above the threshold for producing an on-shell Higgs boson.

For chargino-neutralino production, we consider two scenarios. In the first scenario, the chargino and the $\tilde{\chi}_2^0$ are mass-degenerate ($m_{\tilde{\chi}_2^0} \approx m_{\tilde{\chi}_1^{\mp}}$) and produced together, where the chargino decays to a W boson and the LSP ($\tilde{\chi}_1^{\mp} \rightarrow W^{\pm}\tilde{\chi}_1^0$), and the $\tilde{\chi}_2^0$ decays to a Higgs boson and the LSP ($\tilde{\chi}_2^0 \rightarrow H\tilde{\chi}_1^0$). The production cross sections are computed at NLO+NLL accuracy in QCD in the limit of mass-degenerate wino $\tilde{\chi}_2^0$ and $\tilde{\chi}_1^{\mp}$, light bino $\tilde{\chi}_1^0$, and with all the other sparticles assumed to be heavy and decoupled [91–93].

In the second scenario, a GMSB simplified model is considered, where higgsino-like charginos and neutralinos are nearly mass-degenerate ($m_{\tilde{\chi}_2^0} \approx m_{\tilde{\chi}_1^{\mp}} \approx m_{\tilde{\chi}_1^0}$) and are produced in pairs through various combinations ($\tilde{\chi}_1^0\tilde{\chi}_2^0$, $\tilde{\chi}_1^0\tilde{\chi}_1^{\mp}$, $\tilde{\chi}_2^0\tilde{\chi}_1^{\mp}$, and $\tilde{\chi}_1^{\mp}1\mp$.). Both the $\tilde{\chi}_2^0$ and $\tilde{\chi}_1^{\mp}$ will decay to $\tilde{\chi}_1^0$ and other low-p_{T} (soft) particles because of the mass degeneracy, leading to a signature with a $\tilde{\chi}_1^0$ pair. Each $\tilde{\chi}_1^0$ will subsequently decay to a Higgs boson and the $\tilde{G}$ LSP, or to a Z boson and the LSP ($\tilde{\chi}_1^0 \rightarrow H\tilde{G}$ or $\tilde{\chi}_1^0 \rightarrow Z\tilde{G}$). The case where the branching fraction of the $\tilde{\chi}_1^0 \rightarrow H\tilde{G}$ decay is 100%, and the case where the branching fraction of the $\tilde{\chi}_1^0 \rightarrow H\tilde{G}$ and $\tilde{\chi}_1^0 \rightarrow Z\tilde{G}$

decays are each 50% are both considered in this scenario, as shown in the $\widetilde{\chi}_1^0$-pair production simplified model in Fig. 5.1. The limits on the product of the production cross section and branching fraction are determined for each of these scenarios.

Table 5.18 displays the expected event yields for a representative selection of the simplified SUSY models considered in various search region bins of the analysis. The labels used in the table, such as HH, ZH, WH (200,1), $\tilde{b}$(450,1), and $\tilde{b}$(450,300) correspond to specific signal models for chargino-neutralino and bottom squark pair production, respectively. For instance, the HH and ZH labels denote the higgsino-like chargino and neutralino production scenarios where the branching fractions of the $\widetilde{\chi}_1^0$ decays are $\widetilde{\chi}_1^0 \rightarrow H\tilde{G}$ and $\widetilde{\chi}_1^0 \rightarrow Z\tilde{G}$ for 100% : 0% and 50% : 50% cases, respectively, and the mass of the chargino and next-to-lightest neutralino is 175 GeV. Similarly, WH (200,1) refers to the wino-like chargino and neutralino production scenario, where the chargino and next-to-lightest neutralino masses are 200 GeV and the LSP mass is 1 GeV. The labels $\tilde{b}$(450,1) and $\tilde{b}$(450,300) correspond to the bottom squark pair production scenarios with the bottom squark mass of 450 GeV and the LSP mass of 1 GeV and 300 GeV, respectively.

Table 5.18: The expected signal yields for the SUSY simplified model signals considered are shown for each search region bin of the EWP analysis. The category that each search region bin belongs to is also indicated in the table. The search region bins definitions are summarized in Table 5.14. The labels HH and ZH refer to the signal models for higgsino-like chargino and neutralino production where the branching fractions of the decays $\widetilde{\chi}_1^0 \to H\tilde{G}$ and $\widetilde{\chi}_1^0 \to Z\tilde{G}$ are 100% and 0%, and 50% and 50%, respectively. For the above two scenarios, the mass of the chargino and next-to-lightest neutralino is 175 GeV. The label WH (200,1) refers to the signal model for wino-like chargino and neutralino production, where the mass of the chargino and next-to-lightest neutralino is 200 GeV and the LSP mass is 1 GeV. The labels $\tilde{b}$(450,1) and $\tilde{b}$(450,300) refer to the signal models for bottom squark pair production where the bottom squark mass is 450 GeV and the LSP mass is 1 and 300 GeV, respectively.

Search region bin	Category	HH	ZH	WH (200,1)	$\tilde{b}$ (450,1)	$\tilde{b}$ (450,300)
EWP 0	Two-Lepton	0.2 ± 0.01	1.6 ± 0.1	0.0 ± 0.000	0.2 ± 0.1	0.1 ± 0.03
EWP 1	Muon High-p_T	4.5 ± 0.2	1.5 ± 0.1	3.3 ± 0.2	4.4 ± 1.8	0.9 ± 0.4
EWP 2	Muon Low-p_T	1.6 ± 0.04	0.6 ± 0.02	1.7 ± 0.05	0.6 ± 0.2	1.8 ± 0.7
EWP 3	Electron High-p_T	4.0 ± 0.2	1.5 ± 0.1	2.7 ± 0.1	3.2 ± 1.3	0.8 ± 0.3
EWP 4	Electron Low-p_T	0.5 ± 0.01	0.2 ± 0.01	0.9 ± 0.04	0.1 ± 0.03	0.7 ± 0.3
EWP 5	Electron Low-p_T	0.3 ± 0.01	0.1 ± 0.01	0.2 ± 0.02	0.2 ± 0.1	0.2 ± 0.1
EWP 6	Electron Low-p_T	0.3 ± 0.01	0.2 ± 0.004	0.3 ± 0.02	0.1 ± 0.04	0.4 ± 0.2
EWP 7	$Hb\bar{b}$ High-p_T	11.9 ± 0.5	3.4 ± 0.2	0.2 ± 0.01	4.3 ± 4.3	4.7 ± 1.9
EWP 8	$Hb\bar{b}$ High-p_T	9.1 ± 0.6	2.5 ± 0.2	0.1 ± 0.005	30.1 ± 12.1	2.2 ± 0.8
EWP 9	$Hb\bar{b}$ Low-p_T	1.9 ± 0.2	0.6 ± 0.05	0.1 ± 0.003	0.8 ± 1.0	6.5 ± 2.8
EWP 10	$Hb\bar{b}$ Low-p_T	1.2 ± 0.1	0.4 ± 0.04	0.03 ± 0.002	3.7 ± 1.5	2.4 ± 1.0
EWP 11	$Zb\bar{b}$ High-p_T	3.2 ± 0.3	1.7 ± 0.2	0.3 ± 0.02	0.6 ± 0.6	1.9 ± 0.8
EWP 12	$Zb\bar{b}$ High-p_T	1.3 ± 0.2	0.6 ± 0.1	0.1 ± 0.01	4.8 ± 2.2	0.4 ± 0.2
EWP 13	$Zb\bar{b}$ High-p_T	2.5 ± 0.1	1.1 ± 0.1	0.1 ± 0.02	2.3 ± 2.2	1.0 ± 0.4
EWP 14	$Zb\bar{b}$ Low-p_T	1.7 ± 0.2	0.8 ± 0.1	0.2 ± 0.01	0.1 ± 0.1	3.7 ± 1.5
EWP 15	$Zb\bar{b}$ Low-p_T	0.6 ± 0.2	0.2 ± 0.04	0.02 ± 0.002	0.6 ± 0.3	0.8 ± 0.4
EWP 16	$Zb\bar{b}$ Low-p_T	1.0 ± 0.05	0.4 ± 0.02	0.04 ± 0.01	0.3 ± 0.3	1.5 ± 0.6
EWP 17	High-p_T	5.3 ± 1.6	5.5 ± 0.6	7.2 ± 0.5	0.3 ± 0.2	1.4 ± 0.7
EWP 18	High-p_T	1.8 ± 0.1	0.8 ± 0.05	0.5 ± 0.03	0.01 ± 0.1	0.3 ± 0.1
EWP 19	High-p_T	6.0 ± 1.4	4.0 ± 0.7	3.6 ± 0.2	0.6 ± 0.4	1.4 ± 0.6
EWP 20	High-p_T	42.1 ± 3.9	19.6 ± 1.8	9.1 ± 0.8	40.1 ± 15.8	6.1 ± 2.4
EWP 21	High-p_T	4.9 ± 0.2	2.3 ± 0.1	1.4 ± 0.1	0.03 ± 0.04	0.9 ± 0.4
EWP 22	High-p_T	7.3 ± 1.2	4.2 ± 0.6	3.0 ± 0.2	1.5 ± 1.4	1.3 ± 0.5
EWP 23	High-Res	1.1 ± 1.2	1.0 ± 0.4	3.0 ± 0.6	0.03 ± 0.02	2.2 ± 1.2
EWP 24	High-Res	1.5 ± 0.5	0.9 ± 0.2	1.1 ± 0.1	0.03 ± 0.01	1.4 ± 0.6
EWP 25	High-Res	0.6 ± 0.3	0.4 ± 0.1	0.6 ± 0.1	0.01 ± 0.2	0.6 ± 0.3
EWP 26	High-Res	13.7 ± 2.1	6.5 ± 1.0	4.4 ± 0.7	4.1 ± 1.7	10.4 ± 4.4
EWP 27	High-Res	0.5 ± 0.1	0.3 ± 0.04	0.2 ± 0.03	0.0 ± 0.000	0.4 ± 0.2
EWP 28	High-Res	0.8 ± 0.2	0.5 ± 0.1	0.6 ± 0.1	0.1 ± 0.2	0.9 ± 0.4
EWP 29	Low-Res	0.7 ± 0.7	0.7 ± 0.3	1.9 ± 0.5	0.02 ± 0.01	1.5 ± 0.8
EWP 30	Low-Res	1.0 ± 0.3	0.5 ± 0.1	0.7 ± 0.2	0.02 ± 0.01	1.0 ± 0.5
EWP 31	Low-Res	0.5 ± 0.4	0.3 ± 0.2	0.4 ± 0.1	0.01 ± 0.003	0.5 ± 0.3
EWP 32	Low-Res	8.4 ± 2.2	4.1 ± 1.0	3.0 ± 0.8	2.7 ± 1.3	7.1 ± 3.6
EWP 33	Low-Res	0.4 ± 0.1	0.2 ± 0.05	0.2 ± 0.04	0.002 ± 0.001	0.2 ± 0.1
EWP 34	Low-Res	0.6 ± 0.2	0.3 ± 0.1	0.4 ± 0.1	0.01 ± 0.01	0.6 ± 0.3

The profile likelihood ratio test statistic and asymptotic formula [116] are used to evaluate the observed and expected 95% confidence level (CL) limits on the signal production cross sections, following the CL_s criterion [117–119]. The limits are presented in Fig. 5.5 as a function of the bottom squark mass and the LSP mass. We exclude bottom squarks with masses below approximately 510 GeV for an LSP mass of 1 GeV, which is only slightly lower (by 20 GeV) than the SP analysis, which is optimized for strong production with binning in the number of jets and b-tagged jets.

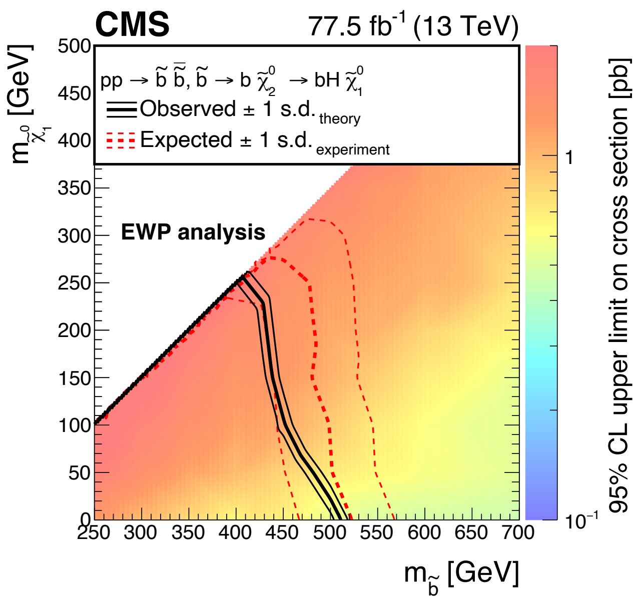

Figure 5.5: The observed 95% CL upper limits on the bottom squark pair production cross section for the EWP analysis. The bold and light solid black contours represent the observed exclusion region and the ±1 standard deviation (s.d.) band, including both experimental and theoretical uncertainties. The analogous red dotted contours represent the expected exclusion region and its ±1 s.d. band.

The EWP analysis shows slightly better expected sensitivity compared to the SP analysis for the simplified models of chargino-neutralino production, due to the inclusion of bins with smaller values of M_{R} and larger values of R^2. Events in such bins typically have lower values of $p_{\mathrm{T}}^{\mathrm{miss}}$ and are not in the regions of high signal sensitivity for the SP analysis, while the R^2 variable is able to suppress backgrounds more effectively in these regions of phase space. Fig. 5.6 shows the limits for wino-like chargino-neutralino production simplified models, as a function of the chargino mass and the LSP mass. We exclude chargino masses below approximately 235 GeV for an LSP mass of 1 GeV. Fig. 5.7 shows limits for higgsino-like chargino-neutralino production simplified models, as a function of the chargino mass for the case where the branching fraction of the $\widetilde{\chi}_1^0 \to H\tilde{G}$ decay is 100%, and for the case where the branching fractions of the $\widetilde{\chi}_1^0 \to H\tilde{G}$ and $\widetilde{\chi}_1^0 \to Z\tilde{G}$ decays are both 50%. We exclude charginos below approximately 290 and 230 GeV in the former and latter cases, respectively.

The search region bins with large diphoton transverse momentum $p_{\mathrm{T}}^{\gamma\gamma}$ in the Hb$\bar{b}$ category (EWP bin 7 and 8) provide the best overall sensitivity for the search. For signal models where the squark or neutralino masses exceed the Higgs boson mass by 100 GeV or more, the search region bins with large $p_{\mathrm{T}}^{\gamma\gamma}$ and large values of the kinematic variables M_{R} in the High-p_{T} category in the EWP analysis also contribute significantly to the search sensitivity. In more compressed regions of the signal model parameter space, where the neutralino mass approaches the Higgs boson mass, the search region bins with large $p_{\mathrm{T}}^{\gamma\gamma}$ in the leptonic categories contribute significantly to the search sensitivity. The search region bins with small values of $p_{\mathrm{T}}^{\gamma\gamma}$ and small values of the kinematic variables M_{R} and R^2 usually have low sensitivity to the simplified models considered due to higher levels of background but are included to maintain inclusivity for this search.

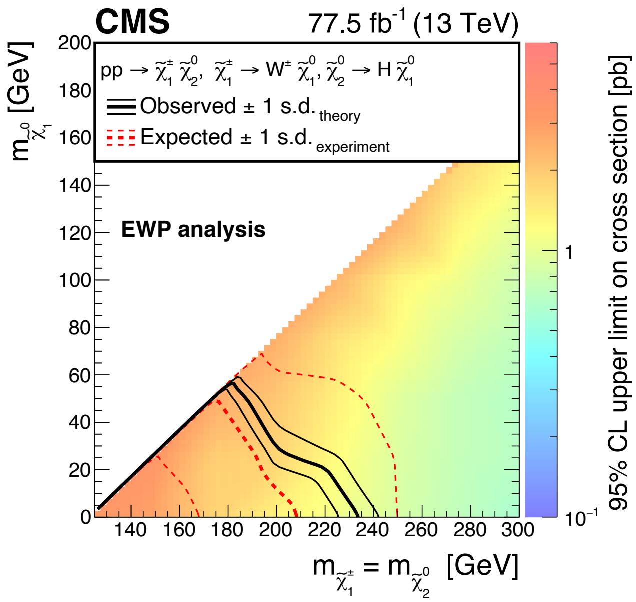

Figure 5.6: The observed 95% CL upper limits on the wino-like chargino-neutralino production cross section are shown for the EWP analysis. The bold and light black contours represent the observed exclusion region and the ±1 standard deviation (s.d.) band, including both experimental and theoretical uncertainties. The analogous red dotted contours represent the expected exclusion region and its ±1 s.d. band.

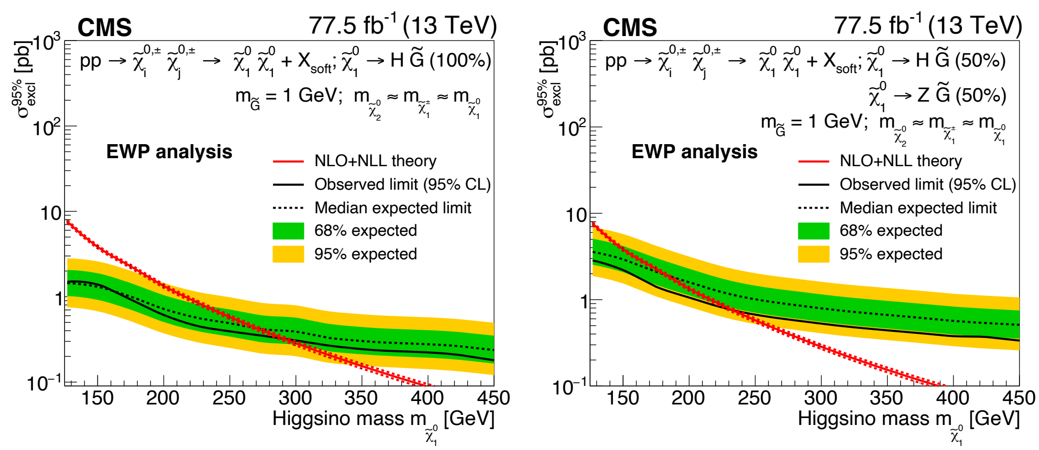

Figure 5.7: The observed 95% CL upper limits on the production cross section for higgsino-like chargino-neutralino production are shown for the EWP analysis. We present limits in the scenario where the branching fraction of $\widetilde{\chi}_1^0 \to H\tilde{G}$ decay is 100% (left plot), and where the $\widetilde{\chi}_1^0 \to H\tilde{G}$ and $\widetilde{\chi}_1^0 \to Z\tilde{G}$ decays are each 50% (right plot). The dotted and solid black curves represent the expected and observed exclusion region, and the green dark and yellow light bands represent the ±1 and ±2 standard deviation regions, respectively. The red solid and dotted lines show the theoretical production cross section and its uncertainty band.

5.8 Summary

This chapter describes a search for supersymmetry (SUSY) in the final state with a Higgs boson (H) decaying to a pair of photons, using 77.5 fb^{-1} of integrated luminosity collected by the CMS detector at the LHC in 2016 and 2017. Photon pairs in the central region of the detector are used to reconstruct Higgs boson candidates, while charged leptons and b-jets are used to tag the decay products of an additional boson. Kinematic quantities, such as the razor variables M_{R} and R^2, are used to suppress standard model backgrounds. Data-driven fits determine the shape and normalization of the non-resonant background, while the resonant background from standard model Higgs boson production is estimated from simulation. We optimized the search for electroweak SUSY production in the EWP analysis to improve sensitivity over previously published results [69, 70]. The results are interpreted in terms of exclusion limits on the production cross section of simplified models of bottom squark pair production and chargino-neutralino production. Thanks to improvements in the event categorization and the larger dataset, we extend the mass limits over the previous best CMS results by about 100 GeV for bottom squark pair production and about 50 GeV for chargino-neutralino production. We exclude bottom squark pair production for bottom squark masses below 510 GeV for a lightest neutralino mass of 1 GeV, wino-like chargino-neutralino production for chargino and neutralino ($\widetilde{\chi}_1^0$) masses of up to 235 GeV and a gravitino ($\tilde{G}$) mass of 1 GeV, and higgsino-like chargino-neutralino production for chargino and neutralino ($\widetilde{\chi}_1^0$) masses of up to 290 and 230 GeV, respectively, in cases where the branching fraction of the lightest neutralino $\widetilde{\chi}_1^0 \rightarrow H\tilde{G}$ decay is 100%, and where the branching fractions of the $\widetilde{\chi}_1^0 \rightarrow H\tilde{G}$ and $\widetilde{\chi}_1^0 \rightarrow Z\tilde{G}$ decays are both 50%.

Chapter 6

THE COMBINATION OF ELECTROWEAK SUPERSYMMETRY SEARCHES AT THE CMS

The results of the 2016 diphoton analysis [69] are included in the paper [120], which presents a statistical combination of multiple searches for the electroweak production of charginos and neutralinos using 35.9 fb^{-1} of proton-proton collision data at a center-of-mass energy of 13 TeV recorded with the CMS detector at the LHC in 2016. The interpretation is based on simplified models of chargino-neutralino or neutralino pair production. The combined analysis leads to improved limits on the mass of charginos and neutralinos compared to the individual analyses, with an extension of the observed exclusion limit of up to 200 GeV. The paper also presents a targeted analysis focusing on a challenging scenario where the mass difference between the two least massive neutralinos is approximately equal to the mass of the Z boson, and obtains improved exclusion limits on the masses of the neutralinos, extending the observed limit achieved in the previous CMS result by around 60 GeV in both masses. The combination also fills some intermediate gaps in the mass coverage of the individual analyses.

The 2016 diphoton analysis [69], referred to as the "H($\gamma\gamma$)" search, provides additional insights into the electroweak production of the Higgs boson, which complements the other searches and helps to improve the overall sensitivity of the analysis.

The combination paper [120] presents exclusion limits for the models of $\widetilde{\chi}_1^{\mp}\widetilde{\chi}_2^0$ production at a 95% confidence level in the plane of $m_{\widetilde{\chi}_1^{\mp}}$ and $m_{\widetilde{\chi}_1^0}$. Fig. 6.1 (left) displays the observed and expected limit contours for each of the individual analyses considered in the combination, while Fig. 6.1 (right) shows the results from the combination for all three topologies considered. For a massless LSP $\widetilde{\chi}_1^0$, the combined result gives an observed (expected) limit in $m_{\widetilde{\chi}_1^0}$ of approximately 650 (570) GeV for the WZ topology, 480 (455) GeV for the WH topology, and 535 (440) GeV for the mixed topology. Moreover, the combination excludes intermediate mass $m_{\widetilde{\chi}_1^0}$ values that were not excluded by individual analyses, including values between 180 and 240 GeV for a massless LSP in the WH topology.

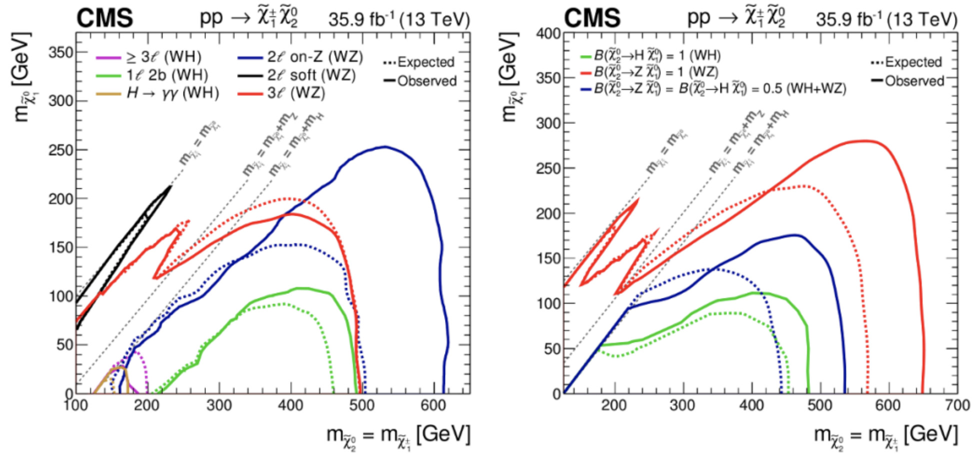

Figure 6.1: Exclusion contours at 95% CL in the plane of $m_{\widetilde{\chi}_1^{\mp}}$ and $m_{\widetilde{\chi}_1^0}$ for the models of $\widetilde{\chi}_1^{\mp}\widetilde{\chi}_2^0$ production (left) for the individual analyses and (right) for the combination of analyses. The decay modes assumed for each contour are given in the legends.

The exclusion limits for the models of $\widetilde{\chi}_1^0\widetilde{\chi}_1^0$ production are presented in the $m_{\widetilde{\chi}_1^0}$ and $\mathcal{B}(\widetilde{\chi}_1^0 \to H\tilde{G})$ plane, assuming the remaining branching fraction is $\widetilde{\chi}_1^0 \to Z\tilde{G}$. Fig. 6.2 displays the observed limits from each analysis separately compared to the combined result. For the combined analysis, the observed limit ranges between about 650 and 750 GeV, allowing exclusion of masses below 650 GeV independent of this branching fraction. Fig. 6.3 shows the analysis with the best expected exclusion limit for each point in the same plane. At higher $m_{\widetilde{\chi}_1^0}$ values, the searches for at least one hadronically decaying boson provide the best sensitivity, with the 4b search being dominant when $\mathcal{B}(\widetilde{\chi}_1^0 \to H\tilde{G})$ is large and the on-Z dilepton search when it is smaller. For $m_{\widetilde{\chi}_1^0}$ values below approximately 200 GeV, the H($\gamma\gamma$) analysis is most sensitive when $\mathcal{B}(\widetilde{\chi}_1^0 \to H\tilde{G})$ is larger. On the other hand, the search for events with three or more leptons is dominant when $\mathcal{B}(\widetilde{\chi}_1^0 \to H\tilde{G})$ is smaller.

In Figure 6.4, the exclusion limits are presented as a function of $m_{\widetilde{\chi}_1^0}$ for three different scenarios of $\mathcal{B}(\widetilde{\chi}_1^0 \to H\tilde{G})$: 0% for the ZZ topology, 100% for the HH topology, and 50% for a combination of events from the ZZ, HH, and ZH topologies.

Various searches have been conducted for the electroweak production of charginos and neutralinos in supersymmetry (SUSY) in different final states. These searches used proton-proton collision data at $\sqrt{s}$ = 13 TeV, obtained from the LHC with the CMS detector, corresponding to an integrated luminosity of 35.9 fb^{-1}. None of the searches revealed any significant deviation from the expected results of the standard model.

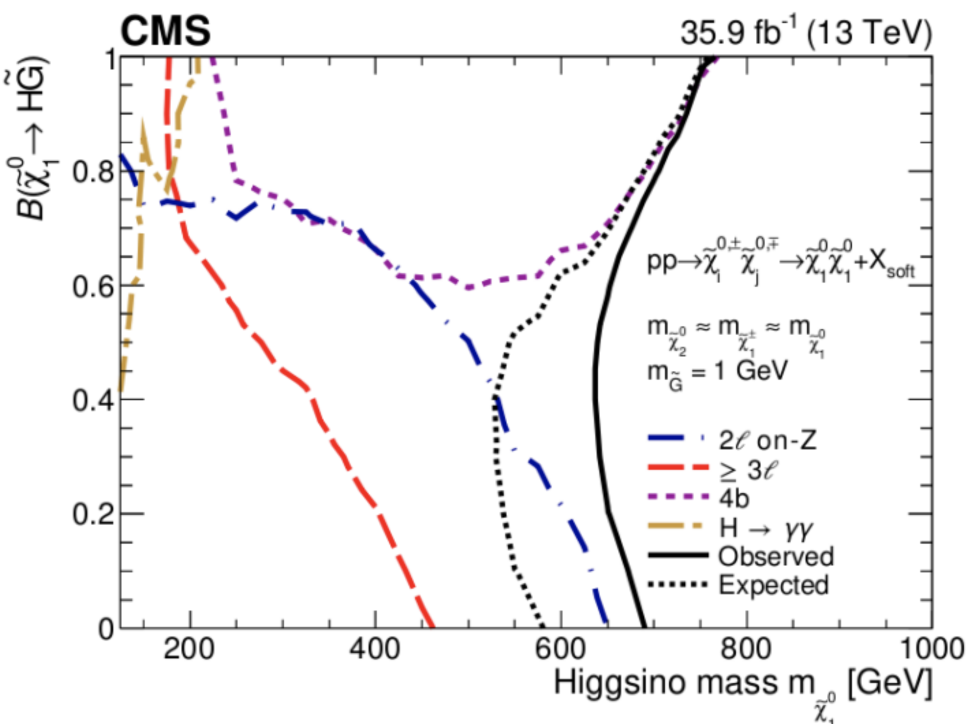

Figure 6.2: Observed exclusion contours at the 95% CL in the plane of $m_{\tilde{\chi}_1^0}$ and $\mathcal{B}(\tilde{\chi}_1^0 \to H\tilde{G})$ for the models of $\tilde{\chi}_1^0\tilde{\chi}_1^0$ production for each individual analysis compared with the combination. For the 4b contour, the region above is excluded, while for all others, the region to the left is excluded. The 4b search drives the exclusion at large values of $\mathcal{B}(\tilde{\chi}_1^0 \to H\tilde{G})$ while the on-Z dilepton and multilepton searches are competing at lower values of $\mathcal{B}(\tilde{\chi}_1^0 \to H\tilde{G})$.

The combination study integrates various searches that explore the electroweak production of charginos and neutralinos anticipated in supersymmetry. The results are interpreted in simplified models of either chargino-neutralino production or neutralino pair production under a gauge-mediated SUSY breaking (GMSB) scenario. It improves the observed exclusion limit in the masses of $\tilde{\chi}_1^\pm$ and $\tilde{\chi}_2^0$ in the chargino-neutralino model by up to 40 GeV compared to individual analyses. For the WZ, WH, and mixed topologies, the observed (expected) limits in the mass of $\tilde{\chi}_1^\pm$ are about 650 (570) GeV, 480 (455) GeV, and 535 (440) GeV, respectively, with the combination excluding intermediate mass values that were not excluded by individual analyses, such as $\tilde{\chi}_1^\pm$ masses between 180 and 240 GeV in the WH topology.

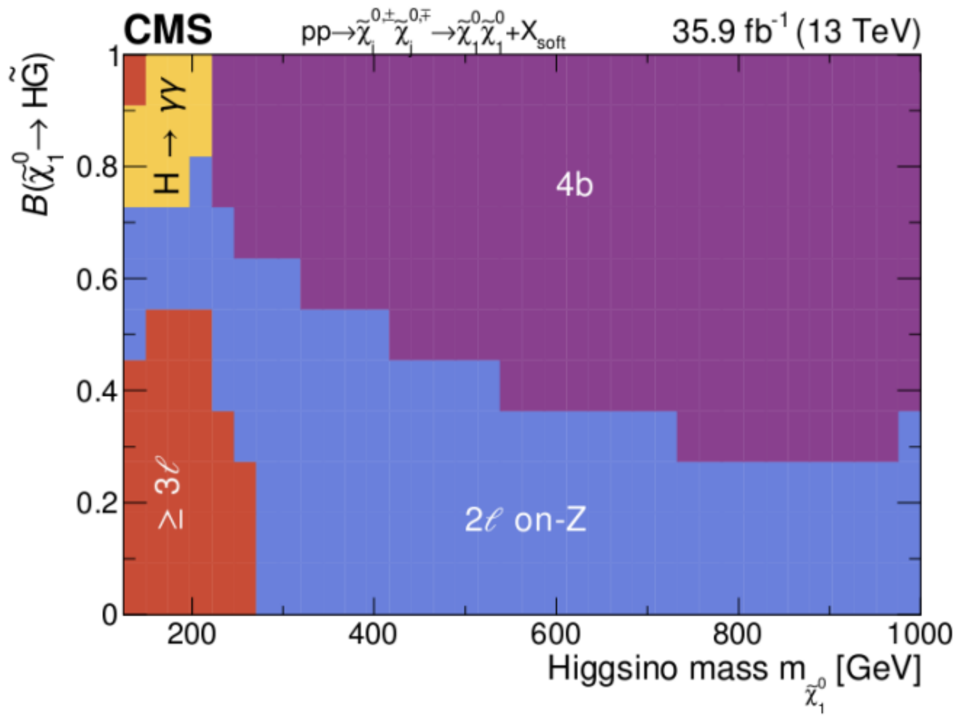

Figure 6.3: The analysis with the best expected exclusion limit at each point in the plane of $m_{\tilde{\chi}_1^0}$ and $\mathcal{B}(\tilde{\chi}_1^0 \rightarrow H\tilde{G})$ for the models of $\tilde{\chi}_1^0\tilde{\chi}_1^0$ production.

The GMSB neutralino pair model is subject to an observed (expected) limit in the mass of $\tilde{\chi}_1^0$ of 650-750 (550-750) GeV, with the combination improving the observed limit by up to 200 GeV in the mass of $\tilde{\chi}_1^0$, depending on the branching fractions for the SUSY particle decays. These results are the most rigorous constraints to date for all models examined.

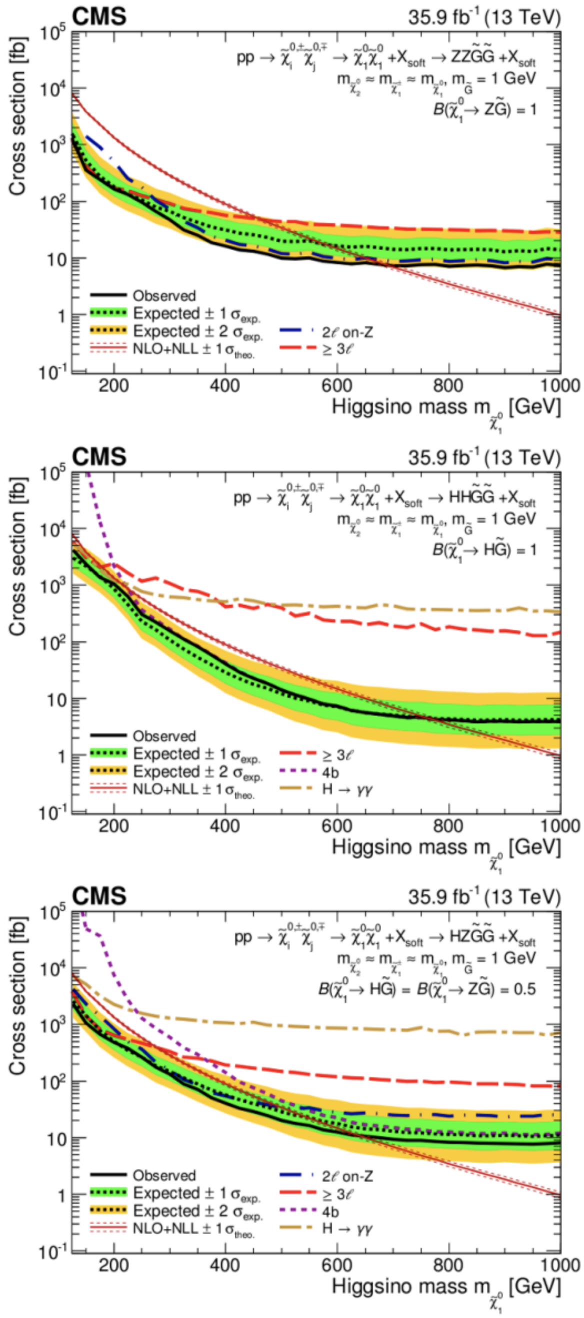

Figure 6.4: The 95% CL upper limits on the production cross sections as a function of $m_{\tilde{\chi}_1^0}$ for the model of $\tilde{\chi}_1^0\tilde{\chi}_1^0$ production with three choices of $\mathcal{B}(\tilde{\chi}_1^0 \to H\tilde{G})$: (upper) 0%, yielding the ZZ topology, (middle) 100%, yielding the HH topology, and (lower) 50%, yielding the ZH mixed topology. The solid black line represents the observed exclusion. The dashed black line represents the expected exclusion, while the green and yellow bands indicate the ± and 2σ uncertainties in the expected limit. The red line shows the theoretical cross section with its uncertainty. The other lines in each plot show the observed exclusion for individual analyses.

Part IV

Search for long-lived particles at the LHC

Chapter 7

SEARCH FOR LONG-LIVED PARTICLES USING OUT-OF-TIME TRACKLESS JETS AT $\sqrt{s}$ = 13 TEV

7.1 Introduction

Many extensions of the standard model (SM) predict the existence of neutral, weakly-coupled particles that have long proper lifetimes. These extensions include supersymmetry (SUSY), which encompasses gauge-mediated SUSY breaking (GMSB) [121–123], split SUSY [124–129], and SUSY with weak R-parity violation [130–133]. Other extensions include scenarios with hidden valleys [134–136], baryogenesis triggered by weakly interacting massive particles (WIMP) [137–139], inelastic dark matter [140], and twin Higgs mechanisms [141–143].

These extensions of the standard model (SM) predict that there are particles that interact weakly and have long lifetimes. SUSY, for example, has various formulations, including GMSB and split SUSY, which describe the relationship between different types of particles. Another SUSY extension allows for the violation of R-parity, a quantity that determines the conservation of SUSY particles. Other extensions, such as those with hidden valleys or twin Higgs mechanisms, propose alternative ways of addressing issues within the standard model. Additionally, scenarios involving WIMP baryogenesis or inelastic dark matter describe possible mechanisms for the creation and interaction of dark matter particles.

This chapter outlines a search for LLPs at the LHC using data from proton-proton (pp) collisions collected by the CMS detector from 2016 to 2018 at a center-of-mass energy of $\sqrt{s}$ = 13 TeV, corresponding to an integrated luminosity of 138 fb^{-1}. The focus of this analysis is on LLPs that decay in the outer regions of the CMS tracker or within the calorimeters, leading to a signature with trackless and delayed (TD) jets.

The term "trackless" refers to the low track multiplicity for jets produced by LLP decays that occur in the calorimeters or in the last few layers of the silicon tracker, in contrast to prompt jets that originate directly from the primary collision point. The term "delayed" describes the significant time delays of these signal jets compared to those produced by SM backgrounds. The decay products of the LLP (X) arrive at the ECAL inner-surface with a time delay given by Eq. 7.5, where ℓ_X and ℓ_i are the path lengths of the LLP decay product and the i-th SM particle, respectively, and β is the velocity of the particle relative to the speed of light.

As shown in Fig. 7.1, the time delay arises because LLP decays occur at macroscopic distances from the primary collision point, resulting in decay products that take a longer path to reach the calorimeters, or from high-mass LLPs that travel measurably slower than the speed of light. To distinguish between jets from LLP decays and those from SM backgrounds, a deep neural network (DNN) discriminator is used, which utilizes information from the tracks and ECAL hits associated with the jets.

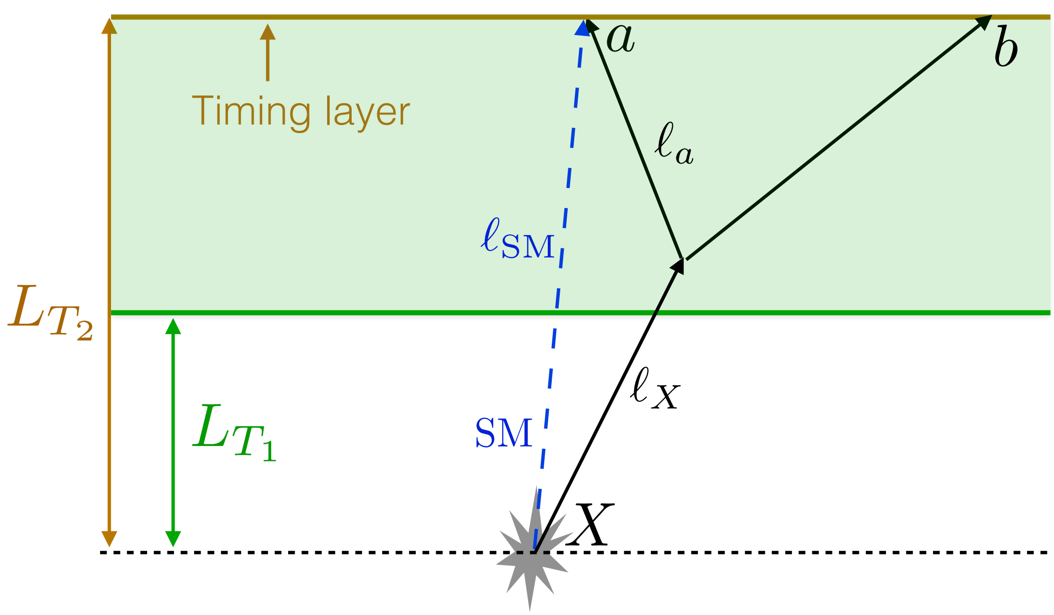

Figure 7.1: An event topology with an LLP X decaying into two light SM particles a and b. A timing layer, at a transverse distance L_{T_2} away from the beam axis (horizontal gray dotted line), is placed at the end of the detector volume (shaded region). The trajectory of a reference SM background particle is also shown (blue dashed line). The gray polygon indicates the primary vertex. [144]

Previous searches by the ATLAS and CMS collaborations have explored the discovery potential of LLPs using jets with displaced tracks or vertices [145–148]. These searches have shown excellent sensitivity to LLPs with proper decay lengths ($c\tau$) either above 1m or below ≈0.2m. However, this search focuses on the intermediate $c\tau$ range of 0.3–1.0m and builds upon a previous CMS analysis using delayed jets [149]. A dedicated TD jet tagger is used in this work to improve the sensitivity to LLPs with masses as small as 127 GeV by taking advantage of the time delay and trackless features of the jet signature.

The search results are interpreted using a simplified model of GMSB chargino-neutralino production [65, 66], which is the same electroweak production model as in Chap. 5. The simplified model describes Higgsino-like charginos ($\widetilde{\chi}_1^{\mp}$) and neutralinos ($\widetilde{\chi}_1^0$, $\widetilde{\chi}_2^0$) that are almost mass-degenerate ($m_{\widetilde{\chi}_2^0} \approx m_{\widetilde{\chi}_1^{\mp}} \approx m_{\widetilde{\chi}_1^0}$) and are produced in pairs via four different combinations: $\widetilde{\chi}_1^0\widetilde{\chi}_2^0$, $\widetilde{\chi}_1^0\widetilde{\chi}_1^{\mp}$, $\widetilde{\chi}_2^0\widetilde{\chi}_1^{\mp}$, and $\widetilde{\chi}_1^{\mp}\widetilde{\chi}_1^{\mp}$. Since the masses are nearly equal, both $\widetilde{\chi}_2^0$ and $\widetilde{\chi}_1^{\mp}$ decay to $\widetilde{\chi}_1^0$ and other low transverse momentum (p_T) particles, effectively producing pairs of $\widetilde{\chi}_1^0$. Subsequently, each $\widetilde{\chi}_1^0$ decays to a Higgs or Z boson and a gravitino ($\tilde{G}$), which is the lightest supersymmetric particle (LSP), thereby conserving R-parity. Signal events typically exhibit large missing transverse momentum resulting from the momentum of the gravitinos, which do not interact with the detector. The Feynman diagrams illustrating the effective neutralino pair production in the simplified model are presented in Fig. 7.2.

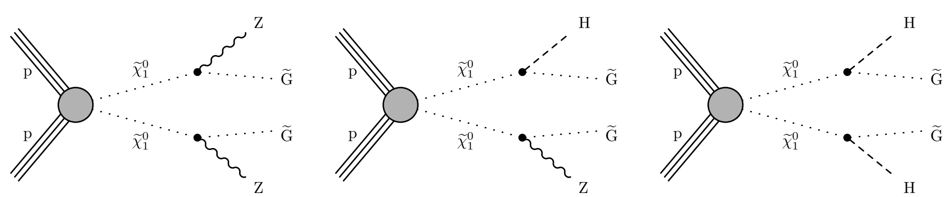

Figure 7.2: Feynman diagrams of the effective neutralino pair production in the GMSB simplified model in which the two neutralinos decay into two gravitinos and two Z bosons (left), a Z and a Higgs boson (H) (center), or two Higgs bosons (right).

The structure of the chapter is outlined in the following sections. Sec. 7.2 provides a summary of the datasets used in the analysis. The event reconstruction and selection are described in Sec. 7.3 and Sec. 7.4, respectively. The DNN-based TD jet discriminator is discussed in Sec. 7.5. The background components and estimation methods are detailed in Sec. 7.6. The systematic uncertainties are discussed in Sec. 7.7. We report and interpret the results in Sec. 7.8. Sec. 7.9 gives a summary of the search.

7.2 Event samples

7.2.1 Data samples

This analysis is based on data obtained from proton-proton (pp) collisions at the Large Hadron Collider (LHC) operating at a center-of-mass energy of 13 TeV. The data was collected by the Compact Muon Solenoid (CMS) experiment, corresponding to an integrated luminosity of 138 fb^{-1}. For this analysis, we used the Analysis Object Data (AOD) data-tier, which provides access to lower-level tracking information necessary for reconstructing potentially displaced tracks.

In practice, we used the “HighMET” skim datasets for our analysis. These datasets store the RAW-RECO data-tier and include all the AOD data-tier information that we need. The HighMET skim datasets were selected based on an offline missing transverse energy (MET) cut of 200 GeV. The list of HighMET skim datasets used in this analysis is presented in Table 7.1.

Table 7.1: AOD MET datasets used in this analysis.

/MET/Run2016B-HighMET-07Aug17_ver1-v1/RAW-RECO
/MET/Run2016B-HighMET-07Aug17_ver2-v1/RAW-RECO
/MET/Run2016C-HighMET-07Aug17-v1/RAW-RECO
/MET/Run2016D-HighMET-07Aug17-v1/RAW-RECO
/MET/Run2016E-HighMET-07Aug17-v1/RAW-RECO
/MET/Run2016F-HighMET-07Aug17-v1/RAW-RECO
/MET/Run2016G-HighMET-07Aug17-v1/RAW-RECO
/MET/Run2016H-HighMET-07Aug17-v1/RAW-RECO
/MET/Run2017B-HighMET-17Nov2017-v1/RAW-RECO
/MET/Run2017C-HighMET-17Nov2017-v1/RAW-RECO
/MET/Run2017D-HighMET-17Nov2017-v1/RAW-RECO
/MET/Run2017E-HighMET-17Nov2017-v1/RAW-RECO
/MET/Run2017F-HighMET-17Nov2017-v1/RAW-RECO
/MET/Run2018A-HighMET-17Sep2018-v1/RAW-RECO
/MET/Run2018B-HighMET-17Sep2018-v1/RAW-RECO
/MET/Run2018C-HighMET-17Sep2018-v1/RAW-RECO
/MET/Run2018D-HighMET-PromptReco-v1/RAW-RECO
/MET/Run2018D-HighMET-PromptReco-v2/RAW-RECO

7.2.2 Signal simulation

This analysis uses the Gauge Mediated Supersymmetry Breaking (GMSB) neutralino model as a benchmark model in the search for long-lived particles (LLPs). The supersymmetric particle χ_1^0 can have macroscopic lifetimes depending on the SUSY breaking scale and can decay to the Z boson and the lightest supersymmetric particle (LSP) ($\widetilde{\chi}_1^0 \to Z\tilde{G}$) or the Higgs boson and the LSP ($\widetilde{\chi}_1^0 \to H\tilde{G}$). The Higgs boson decays to $b\bar{b}$ ($H \to b\bar{b}$), and the Z boson decays inclusively to quarks ($Z \to q\bar{q}$). The χ_1^0 particle is referred to as "the LLP" since it is the only long-lived particle in the signal model considered. The simulated signal sample is provided in Table 7.2 and contains a mixture of various $\widetilde{\chi}_1^0$ masses. The branching ratio for the $\widetilde{\chi}_1^0$ decays is set to 50% for both the Z boson and the LSP and the Higgs boson and the LSP (BR($\widetilde{\chi}_1^0 \to Z\tilde{G}$) = BR($\widetilde{\chi}_1^0 \to H\tilde{G}$) = 50%). Signal sample events can be reweighted to simulate any values of the $\widetilde{\chi}_1^0$ decay branching ratios. The signal MC sample includes lifetimes for the $\widetilde{\chi}_1^0$ of 0.5m and 3.0m, and the samples can be reweighted to achieve any desired $\widetilde{\chi}_1^0$ lifetime. A detailed description of the lifetime reweighting procedure is provided in Sec. 7.2.

The SUSY signal samples were generated using the leading-order (LO) perturbative QCD MadGraph5_amc@nlo 2.4.2 generator[74] with up to two additional partons in the final state at the ME level, and the MLM jet matching scheme [150]. The cross sections for effective $\widetilde{\chi}_1^0\widetilde{\chi}_1^0$ production, assuming mass-degenerate Higgsino-like $\widetilde{\chi}_1^{\mp}$, $\widetilde{\chi}_2^0$, and $\widetilde{\chi}_1^0$, were computed to next-to-leading-order (NLO) accuracy including next-to-leading-logarithmic (NLL) corrections [85–90, 92, 93]. The calculation assumed that all SUSY particles except $\widetilde{\chi}_1^{\mp}$, $\widetilde{\chi}_2^0$, $\widetilde{\chi}_1^0$, and $\tilde{G}$ are too heavy to participate in the interaction. In accordance with previous CMS searches [151, 152], we followed the convention of using real mixing matrices and signed masses for the neutralinos and charginos.

For the simulated samples corresponding to the data-taking periods in 2016 and 2017–2018, the NNPDF v3.0 and v3.1 NLO and NNLO (next-to-next-to-leading-order) parton distribution functions (PDFs) are used, respectively, as reported in [83, 84]. Moreover, the CUETP8M1 tune [153] and the CP5 tune [154] are respectively used for the simulated samples corresponding to the 2016 and 2017–2018 data-taking periods. To simulate the shower and hadronization of partons, along with the underlying event description, the simulated events at the matrix-element level are interfaced with pythia 8.226 or a later version.

For all samples, the detector response is simulated using a detailed description of the CMS detector based on Geant4 [155]. Object and event reconstruction are performed with the same algorithms as are used for the data. Minimum bias events are superimposed on each simulated hard scattering event to reproduce the effect of extra pp interactions within the same or neighboring bunch crossings as the recorded event (pileup). Events are weighted such that the distribution of the number of interactions per bunch crossing agrees with that observed during each data-taking period.

Table 7.2: Signal MC samples used in the analysis. The wildcards given in the names represent the different Pythia8 tunes and the MC campaign names, which differ among the years 2016 to 2018. The range of neutralino masses range from 127 to 1800 GeV.

/SMS-TChiHZ_ZToQQ_HToBB_LongLivedN2N3_mC2-127to1800_Tune*_13TeV-madgraphMLM-pythia8/*/AODSIM

7.2.2.1 LLP lifetime reweighting

Only a discrete number of LLP lifetimes (0.5m and 3m) are simulated. Therefore, samples with intermediate lifetimes can be generated by reweighting the available signal samples.

The decay position of the two LLPs in each event is independent, and each LLP decays with an exponential probability. Thus, the distribution of events is simply the product of the two LLP decay probabilities:

$$p(t_1, t_2|\tau) = \frac{1}{\tau^2} \exp^{-t_1/\tau} \exp^{-t_2/\tau} . \tag{7.1}$$

The lifetime of the first and second LLPs in their own rest frame, denoted by t_1 and t_2 respectively, are calculated using the formula $t_i = L_{\text{LLP, lab frame}}/(\gamma_i \beta_i)$, where L_{LLP} represents the travel distance of the LLP in the lab frame, and γ_i and β_i are the Lorentz factor and velocity of the i-th LLP, respectively.

To obtain a sample with a new mean lifetime τ_{new} from a sample with an old lifetime τ_{old}, we simply assign a weight that is the ratio of equation 7.1 with parameter τ_{new} and τ_{old} to the original sample:

$$w = \left(\frac{\tau_{old}}{\tau_{new}}\right)^2 \exp\left[(t_1 + t_2) \times \left(\frac{1}{\tau_{old}} - \frac{1}{\tau_{new}}\right)\right] . \tag{7.2}$$

Practically, we reweight each intermediate lifetime using the centrally-produced signal sample with the smallest lifetime that is larger than the intermediate lifetime. For example, a proper lifetime of 1m is reweighted using the signal sample produced with a proper lifetime of 0.5m. We make this choice to minimize the statistical uncertainty of the reweighted sample.

7.2.3 Background simulation

Simulated samples of $t\bar{t}$ events, W+jets and Z+jets (collectively called V+jets events), and QCD multijet events are generated with the Monte Carlo generator MadGraph5_amc@nlo 2.2.2[74] at leading-order (LO). For the generation of V+jets events, up to three additional partons are considered in the matrix element (ME) calculations, while up to four additional partons are included for $t\bar{t}$ events. The MLM jet matching scheme [150] is utilized. The background samples are normalized using the most precise cross section calculations available, typically at next-to-leading-order (NLO) or next-to-next-to-leading-order (NNLO) accuracy [74, 156–159].

Background Monte Carlo samples are used to validate event-level variables such as MET and the leading jet p_T, quantify systematic uncertainties, and optimize the signal-to-background ratio. The final background estimation is performed using a data-driven method.

Table 7.3: MC samples used in the analysis.

/QCD_HT50to100_Tune*_13TeV-madgraphMLM-pythia8/*/AODSIM
/QCD_HT100to200_Tune*_13TeV-madgraphMLM-pythia8/*/AODSIM
/QCD_HT200to300_Tune*_13TeV-madgraphMLM-pythia8/*/AODSIM
/QCD_HT300to500_Tune*_13TeV-madgraphMLM-pythia8/*/AODSIM
/QCD_HT500to700_Tune*_13TeV-madgraphMLM-pythia8/*/AODSIM
/QCD_HT700to1000_Tune*_13TeV-madgraphMLM-pythia8/*/AODSIM
/QCD_HT1000to1500_Tune*_13TeV-madgraphMLM-pythia8/*/AODSIM
/QCD_HT1500to2000_Tune*_13TeV-madgraphMLM-pythia8/*/AODSIM
/QCD_HT2000toInf_Tune*_13TeV-madgraphMLM-pythia8/*/AODSIM
/WJetsToLNu_HT-70To100_Tune*_13TeV-madgraphMLM-pythia8/*/AODSIM
/WJetsToLNu_HT-100To200_Tune*_13TeV-madgraphMLM-pythia8/*/AODSIM
/WJetsToLNu_HT-200To400_Tune*_13TeV-madgraphMLM-pythia8/*/AODSIM
/WJetsToLNu_HT-400To600_Tune*_13TeV-madgraphMLM-pythia8/*/AODSIM
/WJetsToLNu_HT-600To800_Tune*_13TeV-madgraphMLM-pythia8/*/AODSIM
/WJetsToLNu_HT-800To1200_Tune*_13TeV-madgraphMLM-pythia8/*/AODSIM
/WJetsToLNu_HT-1200To2500_Tune*_13TeV-madgraphMLM-pythia8/*/AODSIM
/WJetsToLNu_HT-2500ToInf_Tune*_13TeV-madgraphMLM-pythia8/*/AODSIM
/ZJetsToNuNu_HT-100To200_Tune*_13TeV-madgraph/*/AODSIM
/ZJetsToNuNu_HT-200To400_Tune*_13TeV-madgraph/*/AODSIM
/ZJetsToNuNu_HT-400To600_Tune*_13TeV-madgraph/*/AODSIM
/ZJetsToNuNu_HT-600To800_Tune*_13TeV-madgraph/*/AODSIM
/ZJetsToNuNu_HT-800To1200_Tune*_13TeV-madgraph/*/AODSIM
/ZJetsToNuNu_HT-1200To2500_Tune*_13TeV-madgraph/*/AODSIM
/ZJetsToNuNu_HT-2500ToInf_Tune*_13TeV-madgraph/*/AODSIM
/TTJets_Tune*_13TeV-madgraphMLM-pythia8/*/AODSIM
/WW_Tune*_13TeV-pythia8/*/AODSIM
/WZ_Tune*_13TeV-pythia8/*/AODSIM
/ZZ_Tune*_13TeV-pythia8/*/AODSIM

7.3 Event reconstruction

7.3.1 Triggers

The targeted signal model generates large MET primarily due to the momentum of the escaping LSP and the long-lived $\tilde{\chi}_1^0$ decaying outside of the calorimeter acceptance. Thus, the search relies on the MET trigger to collect the data events. The trigger paths utilized in different years are summarized in Table 7.4.

Table 7.4: Trigger paths used in the analysis.

Year	Trigger paths
2016	HLT_PFMETNoMu120_PFMHTNoMu120_IDTight
2017	HLT_PFMETNoMu120_PFMHTNoMu120_IDTight OR HLT_PFMETNoMu140_PFMHTNoMu140_IDTight OR HLT_PFMETNoMu120_PFMHTNoMu120_IDTight_PFHT60
2018	HLT_PFMETNoMu120_PFMHTNoMu120_IDTight OR HLT_PFMETNoMu140_PFMHTNoMu140_IDTight OR HLT_PFMETNoMu120_PFMHTNoMu120_IDTight_PFHT60

The trigger and offline MET cut (MET > 200 GeV) efficiency, which is calculated with respect to the geometric acceptance, ranges from a few percent to 93 percent, depending on the LLP mass.

To measure the trigger efficiency, a control region is used, consisting of events from the SingleMuon dataset and WJetsToLNu MC samples. To be included in this control region, events must pass the HLT IsoMu27 trigger and have exactly one reconstructed muon. The muon must have p_T between 30 and 100 GeV, pass the tight identification and isolation requirements [160], and not be mismeasured.

The trigger efficiency is measured as a function of $\mathrm{MET_{NoMu}}$, which is the missing transverse momentum calculated ignoring the muon in the event (as described in Eq.7.3). The efficiency measurement is performed separately for each year and is shown in Fig.7.3.

$$\mathrm{MET_{NoMu}} = \left\| \vec{E}_T^{miss} + \sum_i \vec{p}_T^{\,iMu} \right\| \tag{7.3}$$

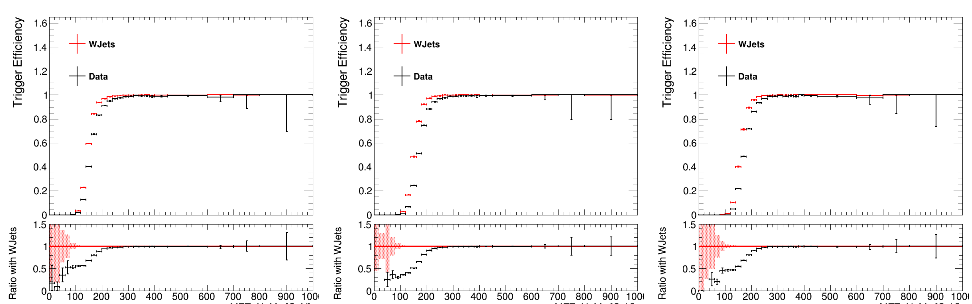

Figure 7.3: The trigger efficiency as a function of MET NoMu, for data and MC in 2016 (Left), 2017 (Middle), and 2018 (Right) condition.

The trigger efficiency Data/MC ratio (displayed in the bottom panel of Fig.7.3) is used to correct the mis-modelling of the trigger efficiency in the signal simulated samples. The scale factors obtained from this correction are shown in Fig.7.4. Overall, the application of the scale factor correction decreases the signal yield by 5% across all signal models.

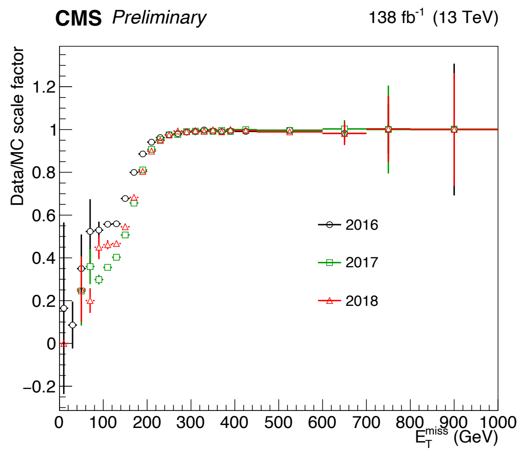

Figure 7.4: The trigger scale factors MET NoMu, for 2016, 2017, and 2018 (Right) condition.

7.3.2 Muons

The analysis uses the standard muon objects and follows the muon identification requirements defined by the Muon POG [161] to reconstruct muon candidates. To suppress backgrounds from W+jets and top quark, events containing isolated muons with $p_T > 10$ GeV that pass the Muon POG loose ID criteria are vetoed from the signal region selection. The veto muons are required to have PF-based combined relative isolation (as given in Eq. 7.3) less than 0.25.

The cuts can be summarized as:

i) $p_T^{\text{Muon}} > 10$ GeV.
ii) Pass Muon POG loose ID criteria [161].
iii) $\text{Iso}_{\text{relative}}^{\text{Muon}} < 0.25$.
iv) Vetoed in signal region (nMuons = 0).

The definition of the PF-based combined relative isolation is defined as follows:

$$\mathrm{Iso}^{\mathrm{Muon}}_{\mathrm{relative}} = \left(\mathrm{Iso}^{\mathrm{Muon}}_{\mathrm{Charged\ Hadron}} + \max\left(\mathrm{Iso}^{\mathrm{Muon}}_{\mathrm{Neutal\ Hadron}} + \mathrm{Iso}^{\mathrm{Muon}}_{\mathrm{Photon}} - 0.5 \times \mathrm{Iso}^{\mathrm{Muon}}_{\mathrm{Pileup}}, 0\right)\right) / p_T^{\mathrm{Muon}},$$

$$\mathrm{Iso}^{\mathrm{Muon}}_{\mathrm{Charged\ Hadron}} = \sum p_T^{\mathrm{iCharged\ Hadron}}(\Delta R(\mathrm{iCharged\ Hadron, Muon}) < 0.4, \mathrm{iCharged\ Hadron}) \in \mathrm{Primary\ Vertex}),$$

$$\mathrm{Iso}^{\mathrm{Muon}}_{\mathrm{Neutal\ Hadron}} = \sum p_T^{\mathrm{iNeutal\ Hadron}}(\Delta R(\mathrm{iNeutal\ Hadron, Muon}) < 0.4),$$

$$\mathrm{Iso}^{\mathrm{Muon}}_{\mathrm{Photon}} = \sum p_T^{\mathrm{iPhoton}}(\Delta R(\mathrm{iPhoton, Muon}) < 0.4),$$

$$\mathrm{Iso}^{\mathrm{Muon}}_{\mathrm{Pileup}} = \sum p_T^{\mathrm{iCharged\ Hadron}}(\Delta R(\mathrm{iCharged\ Hadron, Muon}) < 0.4, \mathrm{iCharged\ Hadron}) \in \mathrm{Pileup}).$$

(7.4)

7.3.3 Electrons

Standard electron reconstruction and identification requirements, as defined by the EGamma POG [162], are employed to reconstruct electron candidates. Events that contain isolated electrons with $p_T > 10$ GeV and that pass the EGamma POG veto electron ID criteria are vetoed for the signal region selection in order to suppress backgrounds from W+jets and top quarks.

The cuts can be summarized as:

i) $p_T^{\mathrm{Electron}} > 10$ GeV.
ii) Pass EGamma POG veto electron ID criteria [162].
iii) Vetoed in signal region (nElectrons = 0).

7.3.4 Photons

Standard photon reconstruction and identification requirements are used to reconstruct photon candidates. Events with isolated photons with $p_T > 15$ GeV and passing the EGamma POG [162] loose photon ID criteria are vetoed in order to suppress γ+jets background.

The cuts can be summarized as:

i) $p_T^{\text{Photon}} > 15$ GeV.
ii) Pass EGamma POG loose photon ID criteria [162].
iii) Vetoed in signal region (nPhotons = 0).

7.4.5 Taus

Tau candidates are reconstructed using standard reconstruction and identification requirements. For the signal region selection, events containing isolated taus with $p_T > 18$ GeV and passing the loose tau ID criteria defined by the Tau POG [163] are vetoed in order to reduce the contribution from W+jets and top quark backgrounds.

The cuts can be summarized as:

i) $p_T^{\text{Tau}} > 18$ GeV.
ii) Pass Tau POG loose tau ID criteria [163].
iii) Vetoed in signal region (nTaus = 0).

7.3.6 Jets

Jets in this analysis are reconstructed from PF (particle flow) candidates using the infrared and collinear safe anti-k_{T} algorithm [99, 105] with a distance parameter of 0.4. The PF algorithm is used to reconstruct individual particles in the event [55]. The momentum of each jet is determined as the vector sum of all particle momenta in the jet. In this analysis, only jets with $p_T > 30$ GeV are considered.

The signal jets in this analysis are expected to originate from LLP decays late in the tracking volume or within the calorimeters. As the standard tracking algorithm is inefficient for charged particles produced more than a few tens of centimeters away from the primary interaction point, such signal jets are expected to have relatively few reconstructed tracks. Additionally, many signal jets have a delayed signature in their time of arrival, either due to a massive LLP traveling at a speed significantly slower than the speed of light or due to a detectable large decay angle resulting in a measurably longer path length. To reconstruct an arrival time for such signal-like jets, timing measurements in the ECAL hits are used. In this analysis, only jets in the barrel with $\eta < 1.48$ are used for tagging signal-like jets due to significantly better calibrated time measurements in the ECAL barrel. A neutral network tagger is used to identify trackless and delayed jets consistent with a signal LLP decay, which includes associated track features as well as the ECAL rechit and timing properties. Further details of the "trackless and delayed jet" tagger can be found in Section 7.5.

Additional cuts are applied to jet energy fractions to remove jets that may be dominated by anomalous contributions from various sub-detector components or reconstruction failures. Specifically, we require that the jet muon energy fraction is less than 0.6, the jet electron energy fraction is less than 0.6, and the jet photon energy fraction is less than 0.8. Any jets that do not meet these requirements are discarded. Additionally, jets are rejected if any muon, electron, photon, or tau passing the veto selection criteria described above is within a distance parameter of 0.4 from the jet.

The cuts can be summarized as:

i) $p_T^{\text{Tau}} > 30$ GeV.
ii) Jet muon energy fraction < 0.6.
iii) Jet electron energy fraction < 0.6.
iv) Jet photon energy fraction < 0.8.
v) Vetoed muon, electron, photon or tau within $\Delta R < 0.4$.

7.3.6.1 Jet timing

The delayed arrival time of jets from signal events compared to prompt particles produced at the primary vertex (PV) by 1–10 ns (depending on the LLP mass) is a consequence of their longer lifetime (Fig.7.1). To discriminate between signal and background, the delay in the jet arrival time with respect to a prompt particle traveling at nearly the speed of light can be measured (Eq. 7.5). The arrival time of the jet at the ECAL, t_{ECAL}, is determined by calculating an energy-weighted sum of the arrival times of the signal pulse in each ECAL crystal associated with the jet (within a $\Delta R = 0.4$ cone of the jet axis).

$$t_{\text{ECAL}} = \frac{\sum_{i=1}^{N_{\text{crystal}}} t_{\text{ECAL}}^i E_{\text{ECAL}}^i}{\sum_{i=1}^{N_{\text{crystal}}} E_{\text{ECAL}}^i}, \tag{7.5}$$

where t_{ECAL}^i and E_{ECAL}^i are the timestamp and reconstructed energy of the signal pulse in crystal i [164], respectively, and N_{crystal} is the number of crystals associated with the jet.

The algorithm and performance of ECAL time reconstruction are detailed in Ref. [165]. Accounting for clock jitter, collision beam spot size, and time-dependent calibration effects, the effective jet time resolution is approximately 400-600 ps for jets with p_T ranging from 30-150 GeV.

7.3.6.2 Jet time smearing

A correction is applied to the mean jet time and time resolution in simulation samples using a pure sample of b-tagged jets from dilepton $t\bar{t}$ events, due to variations in clock distribution between different regions of the ECAL and different data-taking runs that may degrade the mean time response and time resolution for jets [166]. The high purity of the b-tagged jets from the dilepton $t\bar{t}$ sample ensures that no contamination from pileup jets affects the jet time measurement, which have different timing properties. The correction is done using a Gaussian smearing procedure [167]. Specifically, the jet time in the $t\bar{t}$ simulation sample is added by a random number drawn from a Gaussian distribution with mean μ and width σ. The values of μ and σ that minimize the chi-square (χ^2) test statistic [168] between the data and the simulation-based prediction are determined.

We perform a crystal ball fit in MC ($CB^{t\bar{t}}_{MC}$) and data (MuonEG datatsets, $CB^{t\bar{t}}_{data}$) on the jet time distribution requiring exactly one loose muon and one loose electron, passing cut of MET> 200 GeV to improve data/MC agreement ($t\bar{t}$ MC samples have a gen MET cut at 150-180 depending on the era). The Gaussian smearing procedure is as the following:

$$t^{\mathrm{MC}}_{\mathrm{ECAL\,smeared}} = t^{\mathrm{MC}}_{\mathrm{ECAL}} + \mathrm{random}.CB^{t\bar{t}}_{smear}, \tag{7.6}$$

where $CB^{t\bar{t}}_{smear}$ is obtained from $CB^{t\bar{t}}_{data}$, and we modify the mean and σ of the gaussian core as follows:

$$\mathrm{mean}_{CB^{t\bar{t}}_{smear}} = \mathrm{mean}_{CB^{t\bar{t}}_{data}} - \mathrm{mean}_{CB^{t\bar{t}}_{MC}}; \tag{7.7}$$

$$\sigma_{CB^{t\bar{t}}_{smear}} = \sqrt{\left|\sigma^2_{CB^{t\bar{t}}_{data}} - \sigma^2_{CB^{t\bar{t}}_{MC}}\right|}. \tag{7.8}$$

A similar time smearing procedure to signal in SR is applied, by using the function described in Eq. 7.6. Any uncertainty related to this procedure will be taken into account as systematic uncertainties.

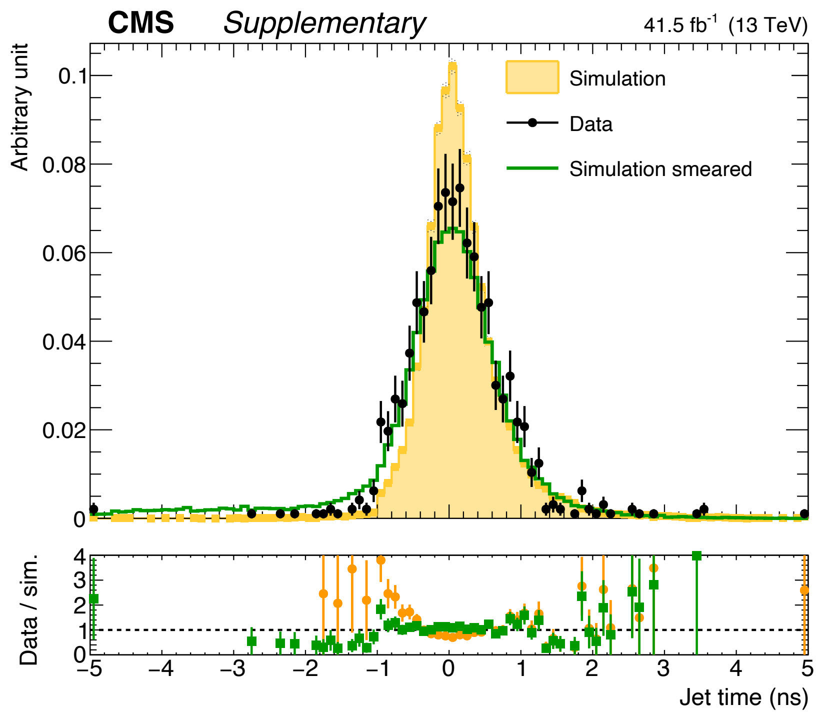

Figure 7.5: Jet time distribution in a sample of b-tagged jets from dilepton $t\bar{t}$ events in 2017 data-taking period (black round markers) and simulation (filled histogram). A Gaussian smearing procedure is applied to the jet time in the $t\bar{t}$ sample (green line) to correct for effects that are difficult to simulate (timing drift caused by crystal transparency loss due to detector aging, electronics jitter).

7.3.7 Missing transverse momentum

The missing transverse momentum (also known as missing transverse energy) is the magnitude of the negative vector sum of all particle flow candidates in the event. In this analysis, Type-I Corrected PFMET [169] is used, which utilizes the AK4PF jet collections and incorporates the jet energy corrections (JEC) into the calculation of $p_{\mathrm{T}}^{\mathrm{miss}}$.

7.4 Event selection

The events in this analysis are collected by the CMS experiment through a high-level $p_{\mathrm{T}}^{\mathrm{miss}}$ trigger that requires $p_{\mathrm{T}}^{\mathrm{miss}}$ to be greater than 120 GeV [170] when reconstructed online. To ensure a trigger selection efficiency above 99%, a pre-selection of $p_{\mathrm{T}}^{\mathrm{miss}} > 200$ GeV is applied when reconstructed offline. Due to the mis-measurement of large p_{T} jets, the ϕ coordinates of the $\vec{p}_{\mathrm{T}}^{\mathrm{miss}}$ and the nearby mis-measured jet often align in background events. To distinguish between signal and background events, we define the $\Delta\phi_{\mathrm{min}}$ variable as the minimum $\Delta\phi$ between the $\vec{p}_{\mathrm{T}}^{\mathrm{miss}}$ and any jet with $p_{\mathrm{T}} > 30$ GeV ($\Delta\phi_{\mathrm{min}} = \underset{\min \Delta R}{\Delta\phi}\ (\vec{p}_{\mathrm{T}}^{\mathrm{miss}}, \text{jet})$). The $\Delta\phi_{\mathrm{min}}$ distribution has a large component near zero for the QCD multi-jet background, whereas for signal events, the distribution is more uniform since the $p_{\mathrm{T}}^{\mathrm{miss}}$ results from the escaping $\tilde{G}$ and not any mis-measured jets. To reduce the QCD multi-jet background by one order of magnitude, we apply a selection cut of $\Delta\phi_{\mathrm{min}} > 0.5$.

The primary method utilized in this analysis to differentiate between the signal and background events is the TD jet tagger, which is elaborated in Section 7.5. We consider jets with $p_{\mathrm{T}} > 30$ GeV and $\eta < 1.0$ and count the number of jets that pass the TD jet tagger selection defined in Section 7.5. To ensure that no isolated electrons, muons, or photons are misidentified as jets, we apply a veto selection based on jet energy fraction. Additionally, we apply a veto selection based on the distance between jets and any identified and isolated muon, electron, or photon ($\Delta R = \sqrt{(\Delta\phi)^2 + (\Delta\eta)^2} < 0.4$), to further reduce the background.

In order to suppress background from W+jets and $t\bar{t}$, events are rejected if they contain an identified and isolated muon, electron, or hadronically decaying tau candidate. The TD jet tagger is used to determine the number of TD-tagged jets (N_{TDJ}) in each event, which is used to define the different data samples used in the analysis. The signal region (SR) consists of events with $N_{\mathrm{TDJ}} \geq 2$, while a background-enriched control region (CR) that contains events with exactly one TD-tagged jet is used to estimate the background in the SR. Events with zero TD-tagged jets, which are primarily from background processes, are used to validate the background estimation method, as described in Sec. 7.6. Because each additional TD-tagged jet provides a large background suppression factor exceeding 10^3, the impact of signal contamination in the zero and one TD-tagged jet region on the analysis sensitivity was found to be less than 1%.

Non-collision backgrounds originating from cosmic ray muons or beam halo particles are usually trackless because their trajectories do not intersect the luminous region called the beam spot, which the track reconstruction algorithm assumes to be the origin of particle trajectories [171]. These non-collision backgrounds can enter the SR only if the particles are oriented in specific ways, as we require at least two TD-tagged jets. Due to the specific trajectory configurations required, such backgrounds are rare. To suppress them to negligible levels, we use particular features of such events to veto them as described in the following sections.

7.4.1 Cosmic ray muon veto

Events that contain a cosmic ray muon can enter the SR if the muon passes through the calorimeter volume without leaving a track in the tracker, resulting in multiple apparent jets that are delayed in time. To identify these events, we search for track segments in the DT muon detector planes that align with the calorimeter hits. We use a density-based clustering algorithm [172] with a minimum distance parameter of 1.4 m, requiring segments from at least three different sets of DT muon detector planes in each cluster. If two or more DT segment clusters are found, we define a line using the geometric centroid positions of the two clusters closest to the calorimeter hits in the z coordinate. If the distance of closest approach from the centroid of the ECAL hits to the line is less than 0.5 m, the event is identified as a cosmic ray muon event and rejected from the SR and CRs. This cosmic ray muon veto has a signal efficiency larger than 99.9%.

A high MET region enriched in cosmic muons is selected to study the potential background of cosmic muon events in this analysis. The dedicated standalone muon reconstruction algorithm, `CosmicMuonOneLeg`, is used with all detectors enabled, which connects the upper and lower legs of a cosmic muon and considers it as a single candidate, providing the best achievable resolution [173]. The SR preselections are applied in the study of cosmic muon background, and events falling in the SR with $N_{\mathrm{TDJ}} \leq 1$ are blinded.

Fig. 7.6 and Fig. 7.7 show event displays of a cosmic event mimicking a trackless jet. In these figures, blue dots represent DT segments, yellow dots represent CSC segments, red dots represent ECAL reconstruction hits, and green empty dots represent ECAL reconstruction hits belonging to a tagged jet. By connecting the DT segments as a single line, we can geometrically identify the cosmic trajectory, which is clearly tangent to the ECAL reconstruction hits.

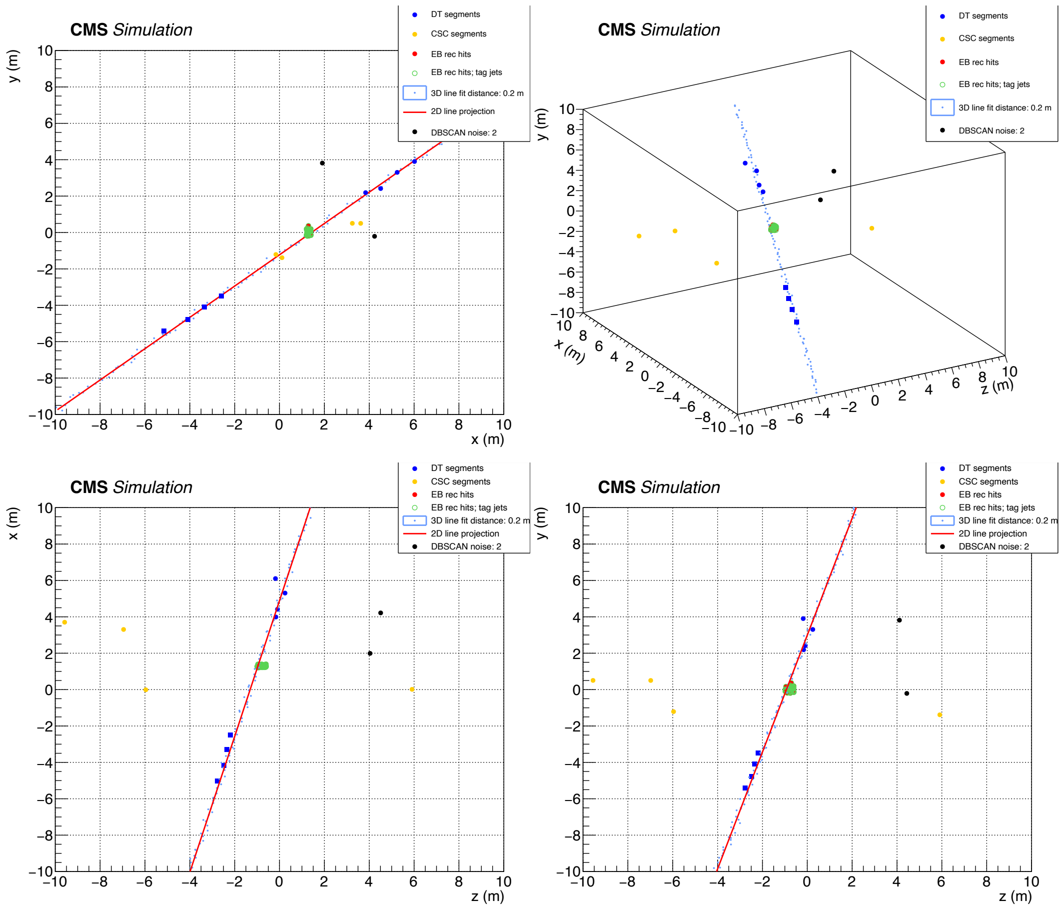

Figure 7.6: Display of a cosmic event in 2017 data taking era: 3D and 2D projections.

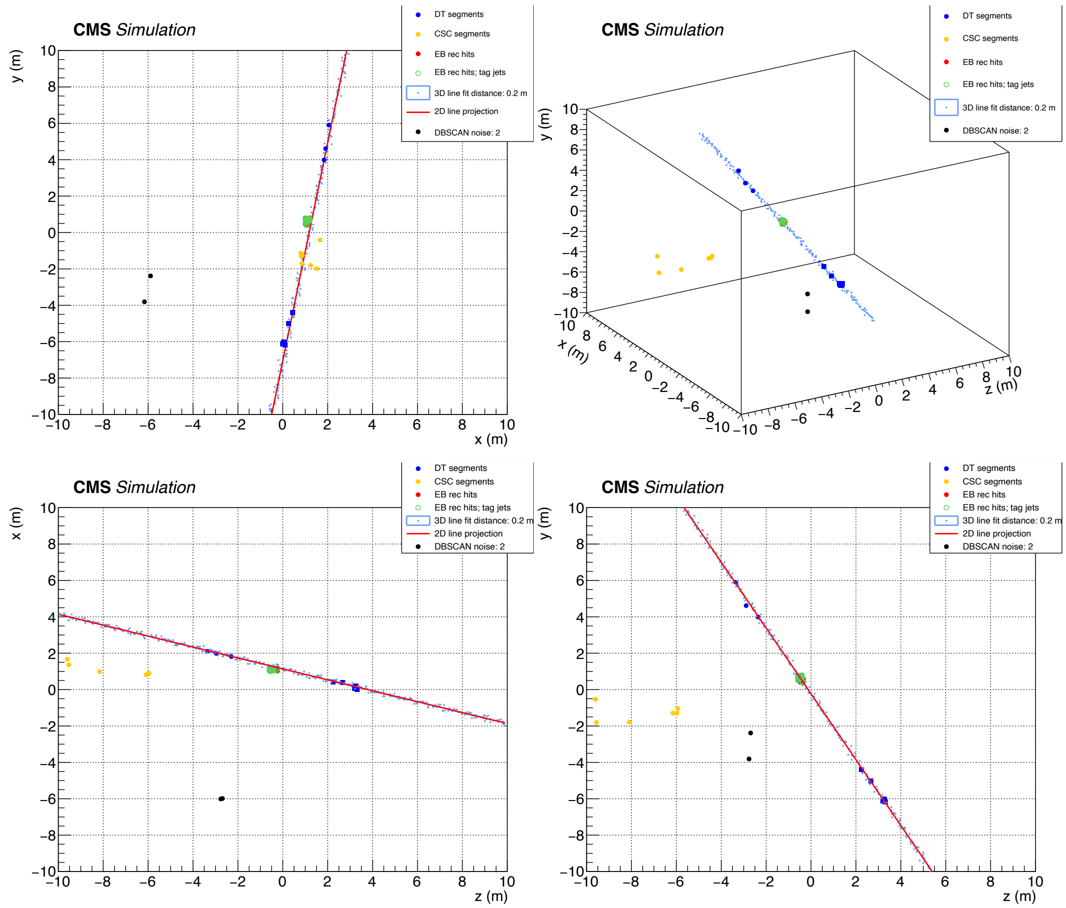

Figure 7.7: Display of a cosmic event in 2017 data taking era: 3D and 2D projections.

We developed an algorithm to identify cosmic muons and reject them as background events without compromising the signal event yields. The algorithm involves the following steps:

1. Events are required to have at least one `CosmicMuonOneLeg` object ($n_{\texttt{CosmicMuonOneLeg}} \geq 1$).

2. The upper and lower legs of the cosmic muon are reconstructed independently by clustering DT segments with the DBSCAN algorithm [172]. Each cluster must contain at least three DT segments, and different clusters should be at least 1.4 m apart ($n_{\text{DT segments}\in\text{cluster}} \geq 3, \text{dist}_{\text{clusters}} \geq 1.4\ m$). DT segments that are not clustered are discarded and considered noise. This allows us to resolve the upper and lower legs of the cosmic trajectory, located on the positive and negative sides of the y-axis.

3. Events are selected when they contain at least two DT segment clusters ($n_{\text{clusters}} \geq 2$). If there are more than two DT segment clusters in the event, we select the two clusters that are closest to the tagged jets in the z direction. The two clusters are required to have opposite signs of their x, y, or z coordinates of the cluster center of mass to ensure that they belong to opposite semi-spheres.

4. We perform a linear fit in three dimensions (x, y, and z) with all the DT segments belonging to the two opposite clusters. If the 3D distance between the linear fit and the center of mass of the ECAL rec hits belonging to the tagged jet is less than 0.5 m, the event is rejected, as the tagged jet is faked by a cosmic muon ($\text{dist}^{3D}_{(\text{linear fit of DT segments,center of mass of rec hits}\in\text{tagged jet})} < 0.5$ m).

The results of the cosmic veto reconstruction are illustrated in Fig. 7.6 and Fig. 7.7. The 3D linear fit is shown by light blue dots, and its 2D projections in each plane are represented by red lines. Black dots in the figures represent the DT segments identified as noise by the DBSCAN algorithm.

Fig. 7.8 displays a signal event where a displaced jet generates a shower in the muon system. The pattern of DT segments appears to be highly irregular, and the distance between the DT segments and the ECAL rec hits is larger than in the case of cosmic muon events.

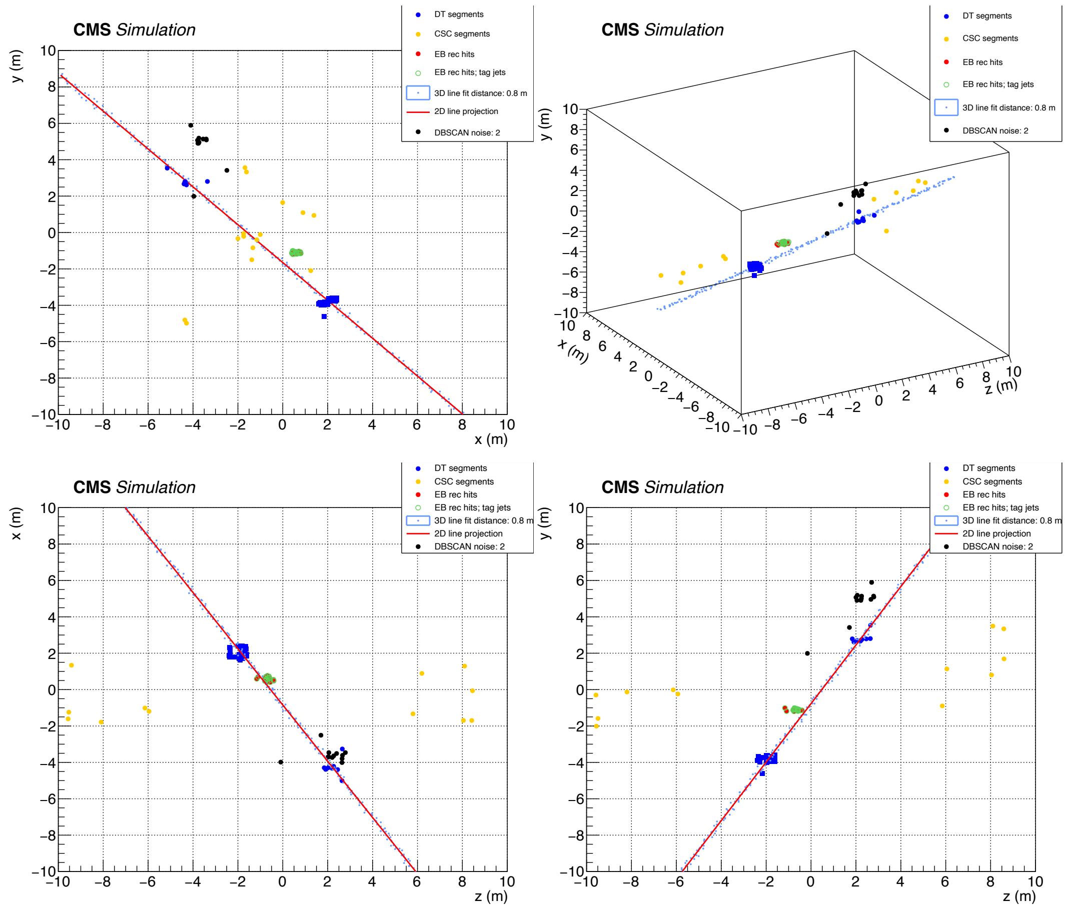

Figure 7.8: Display of a signal event: 3D and 2D projections.

Fig. 7.9 shows the distance between the 3D line fit and the center of mass of the ECAL rec hits belonging to tagged jets. SR pre-selections are applied, and black dots show bin 1 data ($N_{\mathrm{TDJ}} = 1$) with all the data eras added together to enhance statistics. We can observe a clear abundance of data when the distance is smaller than 0.5 m. We apply a cut of $\mathrm{distance}(\mathrm{DT\ fit}, \mathrm{ECAL}) > 0.5$ m to suppress cosmic background. This cut has a negligible impact on the signal, which remains below 1

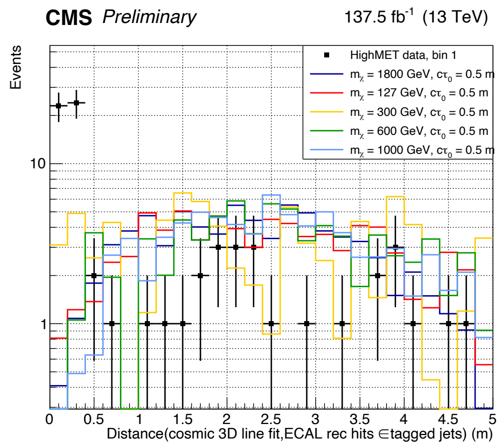

Figure 7.9: Distance between the 3D line fit performed with DT segments matching criteria described in text, and the center-of-mass of the ECAL rec hits belonging to tagged jets. Data are taken from HighMET dataset. We apply all the pre-selections and we select events in bin 1. We do not apply specific requirements on the number of tagged jets for signal. All data eras have been added together to increase statistics.

7.4.2 Beam halo veto

When beam protons collide with an upstream collimator, they can produce beam halo particles that pass through the calorimeter parallel to the beam axis. These particles may create energy deposits in the calorimeter, leading to delayed signals that are mistakenly reconstructed as multiple jets with almost identical ϕ coordinates [174]. Such jets also tend to have very few ECAL hits. To address this issue, we employ a veto on events in which both TD-tagged jets have $|\Delta\phi| < 0.05$ and at least one jet has 10 or fewer ECAL hits. This veto, which has a signal efficiency ranging from 98 to 100%, depending on the signal mass and $c\tau$, helps to suppress this background. Additionally, events containing reconstructed tracks parallel to the beam axis using CSC segments are rejected by the CSC beam halo filter [174].

Beam halo particles can produce fake signal-like tagged jets when they skim the surface of the ECAL and evade the beam halo filter due to their large radius. These fake signal jets tend to have large t_{ECAL} values as they pass through the detector along the z direction.

The beam halo filter has been disabled in both the `HighMET` (Fig.7.10, left) and `SingleMuon` (Fig.7.10, right) datasets. As shown in the left plot of Fig.7.10, the distribution of MET φ values is enhanced at $\varphi \sim 0$ and $\varphi \sim \pi$, leading to a 4% increase in event yield for the `HighMET` dataset. In contrast, the effect of disabling the beam halo filter is negligible in the `SingleMuon` dataset (right plot of Fig.7.10).

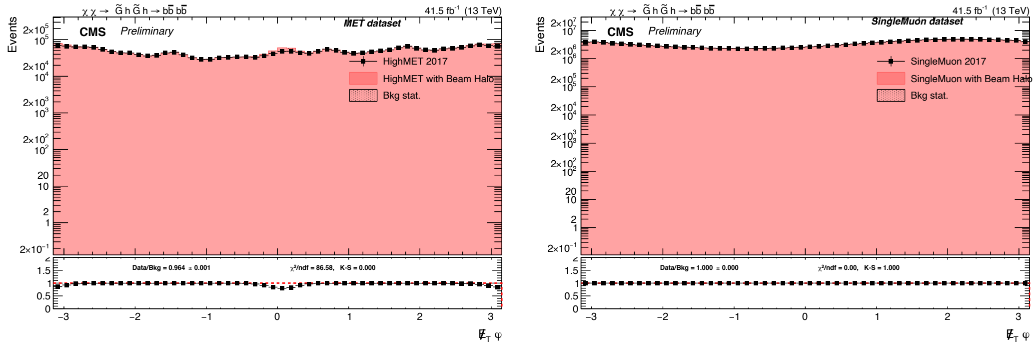

Figure 7.10: Distributions of MET φ in 2017 data, `HighMET` dataset (left) and `SingleMuon` dataset (right). The black dots represent data with beam halo filter switched on. Red histograms include events that failed the beam halo filter. A 4% effect can be observed in `HighMET` dataset (left), whilst the effect is negligible in `SingleMuon` dataset (right)

.

Jets produced by beam halo muons have different characteristics compared to signal jets. They tend to be softer, point mainly in the directions of $\varphi \sim 0$ and $\varphi \sim \pi$ [175], have relatively few matched ECAL rec hits, and their ECAL time distribution exhibits a large spread (large root mean square). Furthermore, the beam halo sample has more jets with high DNN scores compared to non-beam halo data.

To distinguish these fake jets from signal jets, we measure the relative distance in φ between two jets with a high DNN score. Beam halo jets are expected to be close in φ since they are mostly pointing in the $\varphi \sim (0, \pi)$ direction, while signal jets should be homogeneously distributed around the φ range. Fig. 7.11 shows the minimum $\Delta\varphi$ distance between two jets plotted against the jet's DNN score. In the beam halo dataset (left), a strong correlation is observed, whereas the distribution is uniform in both the signal (center) and non-beam halo data (right).

To reject most of the beam halo data, we apply a cut of min$\Delta\varphi$ smaller than 0.05. To minimize the impact on signal efficiency, we reject events where tagged jets have a small number of ECAL rec hits ($n_{\text{ECAL rec hits}} \leq 10$) and are closer than min$\Delta\varphi < 0.05$. The impact on the signal ranges from negligible to 2%.

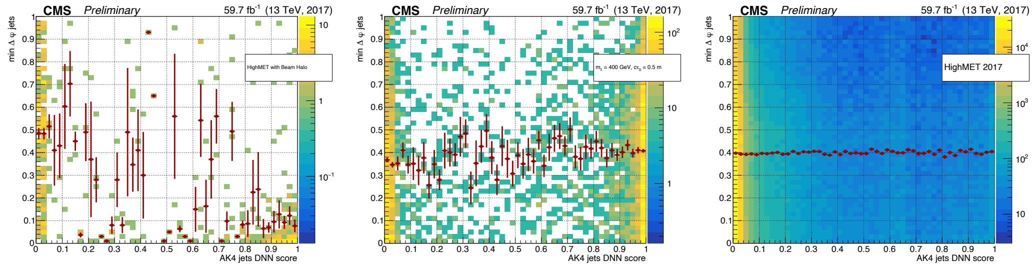

Figure 7.11: The min$\Delta\varphi$ variable versus jets DNN score in beam halo enriched data (left), signal (center), and non beam halo data (right).

7.5 DNN tagger

Jets produced by LLPs that decay in the outer region of the CMS tracking volume or inside the calorimeters exhibit characteristics that are not typically seen in SM backgrounds, such as being trackless and delayed in time. To discriminate between TD and SM jets based on these features, we trained a DNN. A comparison between nominal and signal-like jets is shown in Fig. 7.12. The DNN was implemented using a simple fully connected architecture and trained using Keras [176] with TensorFlow [177] as the deep learning framework.

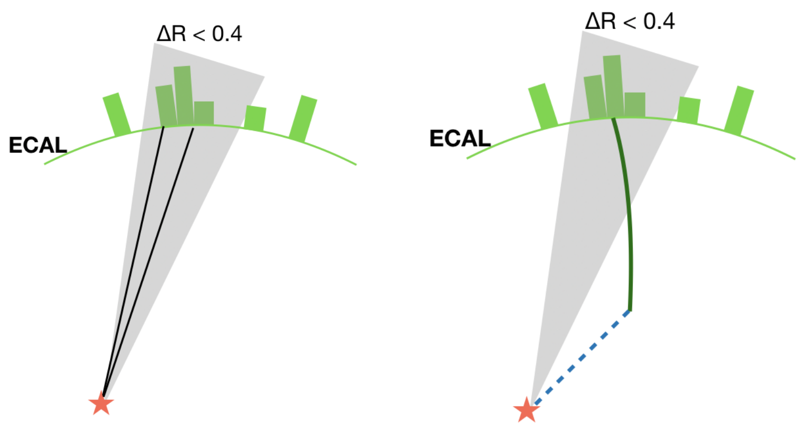

Figure 7.12: A cartoon of nominal (left) and signal-like (right) jets are shown. The red star represents the primary vertex (PV); the green arc represents the ECAL surface; the green bars represent ECAL hits; the gray cone represents the jet cone of $\Delta R < 0.4$. In the left plot, the black lines connecting the PV and the ECAL surface are charged particles whose tracks are reconstructed with very high efficiency. In the right plot, the blue dashed line represents neutral LLP which is undetected, and the green track represents particles that result from the decay products of the LLP traveling towards the ECAL. Such particles have very low efficiency to be reconstructed by the nominal tracking algorithm due to the large displacement.

7.5.1 Input features

The TD jet tagger relies on 22 input features derived from the jet's tracks, PF candidates, and calorimeter hits.

1. *Number of charged constituents*: It is defined as the number of charged PF constituents in a jet. Jets originating from the decay of LLPs typically have a lower charged multiplicity compared to SM background jets, because charged particles produced far away from the primary collision point have a suppressed track reconstruction efficiency.

2. *Number of selected tracks*: It is a quantity used as an input to b-tagging algorithms, which are used to identify jets containing heavy-flavored hadrons. Trackless jets, which are often produced by decays of long-lived particles, typically have a smaller number of selected tracks due to the suppression of track reconstruction efficiency for particles produced far from the primary collision point.

3. α_{max}: This variable, described in detail in [178], represents the ratio between the maximum transverse momentum (p_T) of tracks associated with the primary vertex (PV) inside the jet cone and the sum of the p_T of all tracks inside the jet cone, including those not associated with the PV.

$$\alpha_{\max} = \frac{\max_{\mathrm{trk}\in\mathrm{jet}\cap\mathrm{PV}} p_{\mathrm{T}}^{\mathrm{trk}}}{\sum_{\mathrm{trk}\in\mathrm{jet}} p_{\mathrm{T}}^{\mathrm{trk}}}, \tag{7.9}$$

   where trk $\in$ jet $\cap$ PV denotes the track that belongs to the jet and is associated with the PV, trk $\in$ jet denotes the track that belongs to the jet, $p_{\mathrm{T}}^{\mathrm{trk}}$ is the track p_{T}.

   Trackless jets typically have fewer tracks associated with the PV, resulting in a distribution of $\alpha_{\max}$ that peaks towards zero in signal events.

4. β_{max}: The quantity $\beta_{\max}$ is defined as the ratio between the maximum p_T of tracks associated with the primary vertex (PV) inside the jet cone, and the total jet p_T.

$$\beta_{\max} = \frac{\max_{\text{trk}\in\text{jet}\cap\text{PV}} p_{\text{T}}^{\text{trk}}}{p_{\text{T}}^{\text{jet}}}, \tag{7.10}$$

   where trk $\in$ jet $\cap$ PV denotes the track that belongs to the jet and is associated with the PV, and $p_{\text{T}}^{\text{jet}}$ is the jet p_{T}.

   In signal events, where the jets originate from decays of LLPs, trackless jets tend to have a smaller fraction of momentum carried by tracks associated with the PV, leading to a peak of the $\beta_{\max}$ distribution towards lower values.

5. γ_{max}: The $\gamma_{\max}$ variable is defined as the ratio between the maximum transverse momentum of tracks associated with a primary vertex and the energy of the jet, which is the sum of the energies of all particles in the jet.

$$\gamma_{\max} = \frac{\max_{\text{trk}\in\text{jet}\cap\text{PV}} p_{\text{T}}^{\text{trk}}}{E^{\text{jet}}}, \tag{7.11}$$

   where trk $\in$ jet $\cap$ PV denotes the track that belongs to the jet and is associated with the PV, and E^{jet} is the jet energy. Trackless jets tend to have a smaller amount of momentum held by tracks associated with a primary vertex, resulting in a lower value of $\gamma_{\max}$.

6. γ_{max}^{EM}: It is defined as the maximum p_T of tracks associated with a primary vertex in the jet cone divided by the electromagnetic energy of the jet, which is the sum of the energies of photons and electrons in the jet.

$$\gamma_{\max}^{\text{EM}} = \frac{\max_{\text{trk}\in\text{jet}\cap\text{PV}} p_{\text{T}}^{\text{trk}}}{E_{\text{EM}}^{\text{jet}}}, \tag{7.12}$$

   where trk $\in$ jet $\cap$ PV denotes the track that belongs to the jet and is associated with the PV, and $E_{\text{EM}}^{\text{jet}}$ is the jet electromagnetic energy. The amount of momentum held by tracks associated with a primary vertex is smaller in trackless jets.

7. $\gamma_{max}^{Hadronic}$: The variable is defined as the ratio of the maximum p_T of tracks in the jet cone associated with a primary vertex to the energy of hadrons in the jet.

$$\gamma_{\text{max}}^{\text{Hadronic}} = \frac{\max_{\text{trk}\in\text{jet}\cap\text{PV}} p_{\text{T}}^{\text{trk}}}{E_{\text{Hadronic}}^{\text{jet}}}, \tag{7.13}$$

where trk $\in$ jet $\cap$ PV denotes the track that belongs to the jet and is associated with the PV, and $E_{\text{Hadronic}}^{\text{jet}}$ is the jet hadronic energy. It quantifies the fraction of hadronic energy in the jet carried by tracks associated with the primary vertex. Trackless jets tend to have a smaller $\gamma_{\text{max}}^{\text{Hadronic}}$ value, indicating that they have a reduced amount of hadronic energy carried by tracks associated with the primary vertex.

8. γ_{max}^{ET}: It is also known as *track momentum fraction*. It is defined as the ratio between the maximum p_T of tracks in the jet cone associated to a primary vertex and the jet's transverse energy.

$$\gamma_{\text{max}}^{\text{ET}} = \frac{\max_{\text{trk}\in\text{jet}\cap\text{PV}} p_{\text{T}}^{\text{trk}}}{E_{\text{ET}}^{\text{jet}}}, \tag{7.14}$$

where trk $\in$ jet $\cap$ PV denotes the track that belongs to the jet and is associated with the PV, and $E_{\text{ET}}^{\text{jet}}$ is the jet transverse energy. This variable provides information about the fraction of jet momentum carried by tracks. Trackless jets have a smaller track momentum fraction, indicating that they have a lower amount of momentum held by tracks associated to a primary vertex.

9. *p_T of tracks in jet cone*: This variable is defined as the sum of the transverse momenta of all the tracks in the jet cone, i.e., $\sum_{\text{trk}\in\text{jet}} p_T$. This variable is smaller for trackless jets compared to prompt jets with more associated tracks.

10. *min ΔR(jet, all tracks)*: The minimum ΔR between the jet axis and all tracks within the jet cone is used as an input variable. In signal events, trackless jets tend to have fewer tracks inside the jet cone, resulting in a higher minimum ΔR value compared to background events.

11. *p_T of tracks associated to a PV in jet cone*: This variable is defined as the sum of the transverse momenta of all tracks in the jet cone that are associated with a primary vertex, i.e., $\sum_{\text{trk}\in\text{jet}\cap\text{PV}} p_{\text{T}}^{\text{trk}}$. In trackless jets, the tracks associated with primary vertices tend to have a softer p_{T} spectrum compared to those in standard model jets.

12. *min* ΔR(*jet, PV tracks*): This variable represents the minimum distance in ΔR between the jet and tracks associated with the primary vertex (PV). Since PVs are often far from trackless jets, the distribution of this variable tends to peak at larger values in signal events.

13. *Number of ECAL barrel rec hits*: It is the number of ECAL reconstructed hits in the jet cone. Trackless jets tend to have a larger number of ECAL reconstructed hits.

14. *Energy fraction of ECAL barrel rec hits*: The variable is defined as the ratio of the sum of the energy of all the valid ECAL rec hits in the jet cone to the jet energy, in order to make this variable independent from jet momentum. It is given by

$$\mathrm{Frac}_{\text{ECAL rec hits Energy}} = \frac{\sum\limits_{\text{rec hit}\in\text{jet}} E_{\text{rec hit}}}{E_{\text{jet}}}. \tag{7.15}$$

Trackless jets have a larger fraction of their energy held by ECAL deposits, hence the $\mathrm{Frac}_{\text{ECAL rec hits Energy}}$ distribution peaks at higher values in signal.

15. *Time of ECAL barrel rec hits*: The jet time is calculated as described in Sec. 7.3. Trackless jets show on average a larger delay.

16. *Major axis of ECAL barrel rec hits shower*: This variable is described by Eq. 7.21 in Sec. 7.5.

17. *Minor axis of ECAL barrel rec hits shower*: This variable is described by Eq. 7.21 in Sec. 7.5.

18. *Fragmentation function of ECAL barrel rec hits shower*: variable described by Eq. 7.22 in Sec. 7.5. It is a function that describes how the ECAL hits contribute to the jet energy considering their multiplicity [179].

19. *Charged hadron energy fraction*: variable described in Sec. 7.4.

$$\mathrm{Frac}_{\text{Charged Hadron Energy}} = \frac{\sum\limits_{\text{charged hadron}\in\text{jet}} E_{\text{charged hadron}}}{E_{\text{jet}}^{\text{raw}}}. \tag{7.16}$$

Trackless jets have a smaller amount of energy held by charged hadrons not because of a different jet composition, but rather due to the reduced tracking efficiency for charged particles produced at large displacement, which causes the PF algorithm to misidentify particle types.

20. *Neutral hadron energy fraction*: It is the ratio between the energy sum of the neutral hadron constituents of the jet, divided by the raw jet energy.

$$\mathrm{Frac}_{\text{Neutral Hadron Energy}} = \frac{\displaystyle\sum_{\text{neutral hadron}\in\text{jet}} E_{\text{neutral hadron}}}{E_{\text{jet}}^{\text{raw}}}. \tag{7.17}$$

Trackless jets have a larger amount of energy held by neutral hadrons.

21. *Electron energy fraction*: It is the ratio between the energy sum of the electrons clustered in the jet, divided by the raw jet energy.

$$\mathrm{Frac}_{\text{Electron Energy}} = \frac{\displaystyle\sum_{\text{electron}\in\text{jet}} E_{\text{electron}}}{E_{\text{jet}}^{\text{raw}}}. \tag{7.18}$$

Trackless jets have a smaller amount of energy held by electrons.

22. *Photon energy fraction*: It is the ratio between the energy sum of the photons clustered in the jet, divided by the raw jet energy.

$$\mathrm{Frac}_{\text{Photon Energy}} = \frac{\displaystyle\sum_{\text{photon}\in\text{jet}} E_{\text{photon}}}{E_{\text{jet}}^{\text{raw}}}. \tag{7.19}$$

Trackless jets have a larger amount of energy held by photons.

The tracking-related observables we use include the number (2) and p_{T} sum (9) of tracks in the jet, the p_{T} sum of tracks matched to the PV (11) in the jet, the minimum ΔR between the jet axis and any track (10), the minimum ΔR between the jet axis and any track associated with the PV (12), and three variables sensitive to pileup: α_{max} (3), β_{max} (4), and γ_{max} $(5-8)$. The number of PF candidate constituents of the jet (1) and the charged hadron (19), neutral hadron (20), electron (21), and photon (22) energy fractions are also used as input to the TD jet tagger. Finally, several variables calculated using ECAL hits associated with the jet are used: the number of ECAL hits in the jet (13), the ratio of the energy sum of all ECAL hits in the jet to the jet energy (14), the jet time (15) calculated as in Eq. 7.5, the semi-major (16) and semi-minor (17) axes of the ECAL hits in the jet [180], and the fragmentation function (18) calculated using the ECAL hits [179]. The most discriminating input variables are the tracking-related ones, which can identify a jet as trackless, and the jet time, which can identify a jet as delayed. Signal-like jets tend to have low values of α_{max}, β_{max}, and γ_{max}, large values of ΔR between the jet axis and tracks, low values of the charged energy fraction, low values of the semi-major and semi-minor axes, and low values of the fragmentation function.

7.5.1.1 Jet shower shapes and fragmentation function

Jets are cone-shaped, and their projection onto the (φ, η) plane forms an ellipse. The widths of the jet axes can be used to distinguish signal from background. This approach has been previously used to differentiate quark-initiated jets from gluon-initiated jets [179] using PF jet constituents. In our analysis, we use ECAL rec hits associated with the jet to capture signal signatures. We construct a symmetric second-moment matrix as follows:

$$\begin{aligned} M_{11} &= \sum_i E_{T,i}^2 \Delta\eta_i^2 \\ M_{22} &= \sum_i E_{T,i}^2 \Delta\varphi_i^2 \\ M_{12} = M_{21} &= \sum_i E_{T,i}^2 \Delta\varphi_i \Delta\eta_i . \end{aligned} \tag{7.20}$$

The second-moment matrix is constructed using the transverse energy E_T of each ECAL rec hit and its distance from the jet axis in the (φ, η) plane, denoted by $\Delta\eta$ and $\Delta\varphi$, respectively. The major axis of the ellipse (σ_1) and the minor axis (σ_2) can be expressed in terms of the eigenvalues of M, denoted by λ_1 and λ_2:

$$\begin{aligned}\sigma_1 &= \sqrt{\frac{\lambda_1}{\sum_i E_{T,i}^2}} \\ \sigma_2 &= \sqrt{\frac{\lambda_2}{\sum_i E_{T,i}^2}}.\end{aligned} \tag{7.21}$$

An additional variable that can be used for discrimination is the fragmentation function [179], which is defined for ECAL rec hits as follows:

$$p_T D = \frac{\sqrt{\sum E_{T,i}^2}}{\sum E_{T,i}}. \tag{7.22}$$

The fragmentation variable [179] provides discrimination between signal and background. The value of the fragmentation $p_T D$ is near 1 when a jet is made of a single rec hit carrying all the transverse energy, and near 0 when a jet has an infinite number of rec hits. Signal jets tend to have smaller widths of the shower shape axes, and the fragmentation function exhibits a slightly softer distribution in signal.

7.5.2 Training datasets

The DNN is trained and evaluated using simulation samples. The signal sample consists of GMSB events with a $\widetilde{\chi}_1^0$ mass of 400 GeV and $c\tau$ of 1 m. These events are used exclusively for training and evaluation of the DNN and are not used for predicting the signal yields in the final statistical analysis. Signal jets are identified as displaced jets that originate from LLP decays occurring between the last layers of the tracker and the outer surface of the HCAL, with decay radii between 0.30 and 1.84 m. Jets with $\eta < 1.48$ are included in the training sample. The background sample is a mixture of QCD multijet, W+jets, Z$\nu\bar{\nu}$+jets, and $t\bar{t}$ events. The signal and background samples contain 0.3 and 2.2 million events, respectively, after applying the event selection criteria. The full set of simulation samples is divided into three sets: training, validation, and testing, which account for 40%, 10%, and 50% of the total samples, respectively. The training set is used to optimize the DNN model parameters, the validation set is used to evaluate the model's performance during training, and the testing set is used to measure the final performance of the trained model. This division helps to avoid overfitting and ensures that the DNN can generalize to new data. The simulation predictions are validated by comparing the simulation and observed data distributions for several key input variables (the charged hadron energy fraction, neutral hadron energy fraction, and number of track constituents) to the TD jet tagger (Figs. 7.13). These comparisons show that the simulation provides an accurate description of the observed data.

7.5.3 DNN architecture

The DNN architecture was developed using the Keras [176] and TensorFlow [177] machine learning software frameworks. It has four fully connected hidden layers, with 64, 32, 16, and 8 nodes, respectively, and an output layer with two nodes representing the two classes: signal and SM background. The hidden layers use rectified linear unit (ReLU) [181, 182] activation functions, while the output layer uses a softmax activation function [183, 184]. To prevent overfitting, a 10% dropout rate [185] is applied to all layers. The network is trained using a batch size of 512, categorical cross-entropy loss function, and the Adam optimizer [186] with an initial learning rate of 10^{-3}. The training process is stopped if after 100 successive epochs, the validation loss does not decrease to mitigate overfitting. The training is performed for up to 1,000 epochs over the full training set, and the model with the smallest validation loss is used.

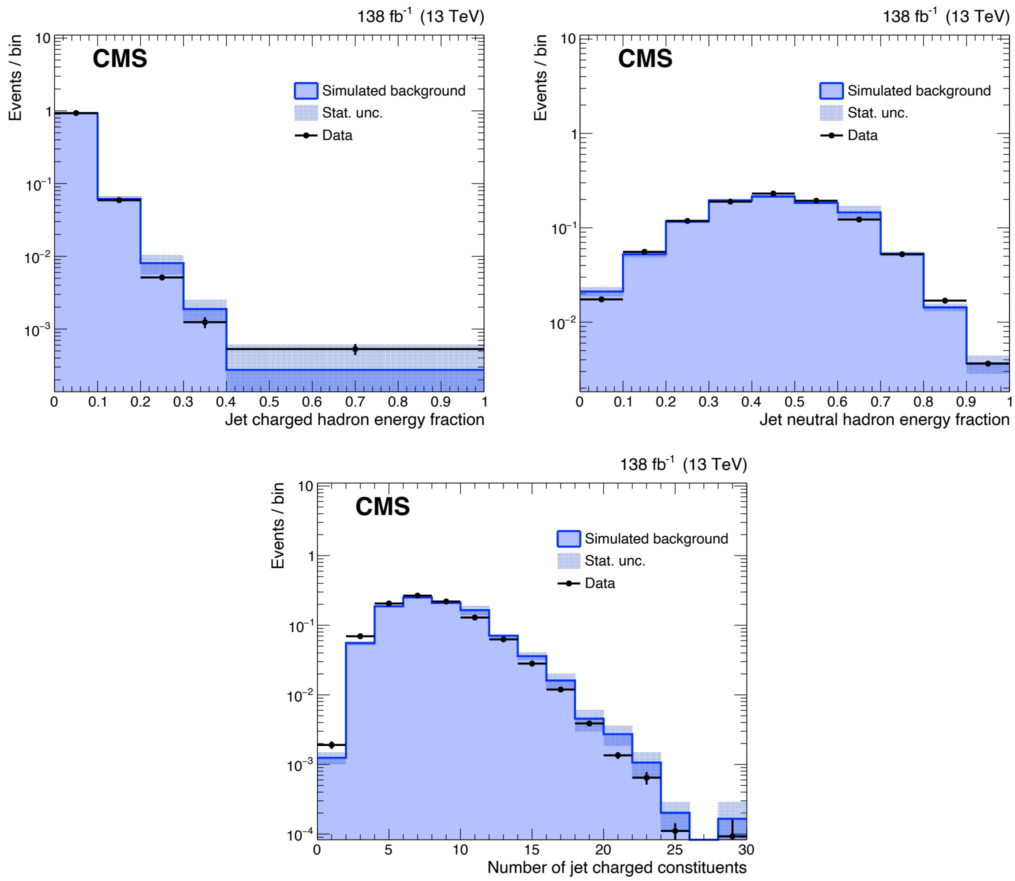

Figure 7.13: The distributions of the jet charged hadron energy fraction (top left), jet neutral hadron energy fraction(top right), and number of track constituents in the jet (bottom),variables used as input to the TD jet tagger score, for simulation (shaded histogram) and data (black markers) when using electrons from W→ $e\nu_e$ events as proxy objects for signal jets. The histograms and data points have been normalized to unit area. Similar levels of agreement are observed for photon proxy objects from the Z→ $l^+l^-\gamma$ sample.

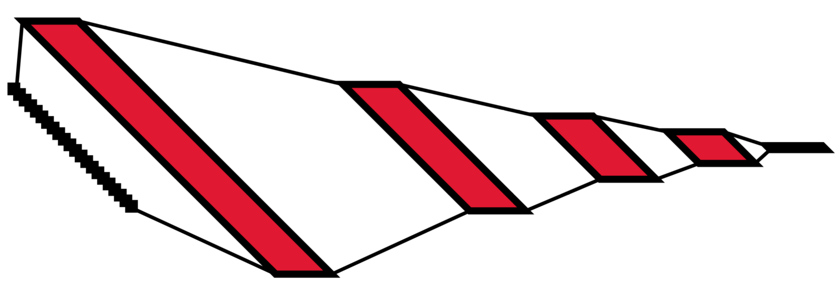

Figure 7.14: Schematic display of the neural network architecture used to identify trackless jets.

7.5.4 DNN performance

Fig. 7.15 shows the distributions of the most impactful input variables for the TD jet tagger, out of the 22 training variables described in Sec. 7.5. These variables are the charged hadron energy fraction (19), neutral hadron energy fraction (20), number of track constituents in the jet (1), ΔR between the jet axis and the closest track associated with any reconstructed primary vertex (12), and jet time (15). The distributions are shown separately for the signal (red) and background (blue) events. Non-collision backgrounds are not included.

The TD jet tagger score distribution for the testing set is displayed in Fig. 7.16 (left), indicating excellent discrimination between signal and background. The identification probability versus misidentification probability is shown in Fig. 7.16 (right). The TD jet tagger score cut is chosen to be 0.996, providing the highest signal sensitivity, and jets with a score above this threshold are tagged as signal. The efficiency of the TD jet tagger for identifying signal jets is presented in Fig. 7.17 as a function of the transverse decay length in the lab frame, with a background efficiency of approximately 4×10^{-4} per candidate jet on average.

7.5.1 Signal efficiency modeling

An important aspect of the TD jet tagger is the use of input features that are sensitive to the trackless nature of signal jets, which have not yet been fully validated in simulation. To address this, photons or electrons are used as proxy objects to represent the LLP decays occurring in the outer tracking or calorimeter volume. These particles, with their own tracks removed from consideration, are the best approximations to trackless jets that can be effectively isolated in collision events. By using them, the accuracy of the simulation for the TD jet tagger signal efficiency can be measured and validated.

Specifically, we take photons in Z→ $l^+l^-\gamma$ events as proxies for signal jets from LLP decays with p_{T} below 70 GeV, and electrons in W→ $e\nu_e$ events as proxies for signal jets from LLP decays with p_{T} above 70 GeV.

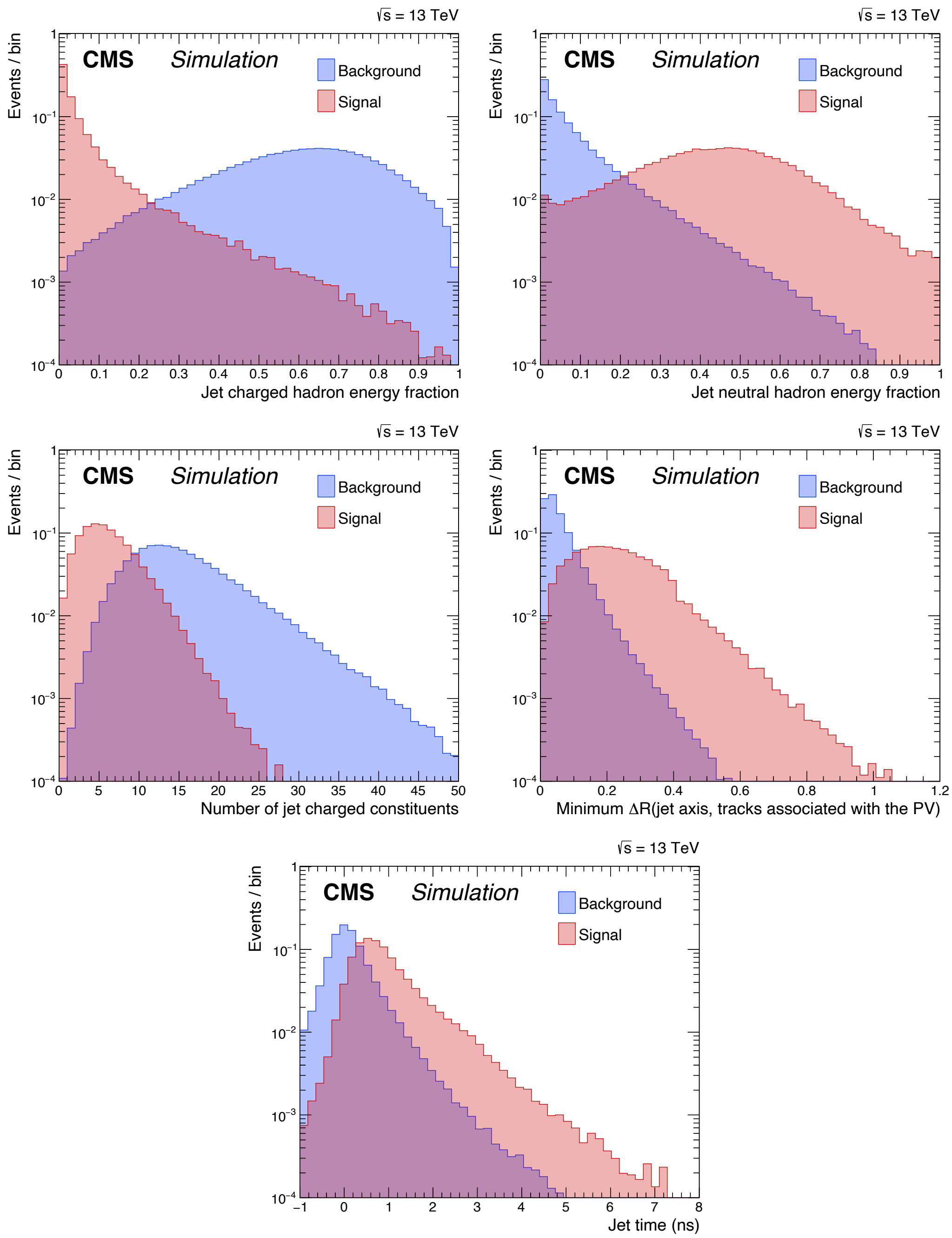

Figure 7.15: The distributions of the most impactful input variables to the TD jet tagger for signal (red) and background (blue). They include the charged and neutral hadron energy fraction, the number of track constituents in the jet, the ΔR between the jet axis and the closest track associated to any reconstructed primary vertex, and the jet time.

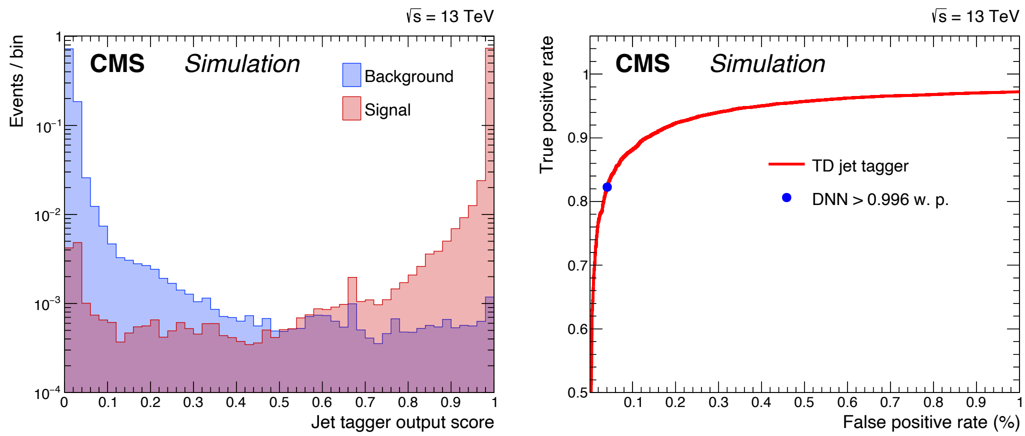

Figure 7.16: The performance of the TD jet tagger. Left: TD jet tagger score distributions for signal, in red, and background, in blue. Right: Identification probability for the signal versus the misidentification probability for the background with the tagger working point used in the analysis shown as a blue marker.

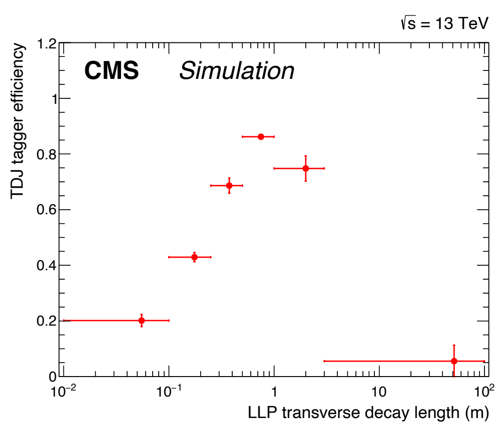

Figure 7.17: The efficiency of the TD jet tagger working point used in the analysis is shown as a function of the lab frame transverse decay length for simulated signals with $\widetilde{\chi}_1^0$ mass of 400 GeV. The uncertainties shown account for lifetime dependence and statistical uncertainty.

7.5.1.1 Photon proxy in Z→ $l^+l^-\gamma$ events

To represent signal jets from LLP decays with $p_{\mathrm{T}} < 70\,\mathrm{GeV}$, we use photons as proxy objects. We select Z→ $l^+l^-\gamma$ events, in which one of the leptons (ℓ = muon or electron) radiates a photon. To ensure that the sample is not contaminated by jets misidentified as photons, we require the mass of the $l^+l^-\gamma$ system to be between 70–110 GeV. In contrast to typical photon veto requirements used in other analyses, we invert the photon veto on jets and require that at least one jet overlaps with the radiated photon. This way, the photon object represents a proxy object for signal jets from LLP decays. However, since the photon in the Z→ $l^+l^-\gamma$ sample has a relatively soft momentum spectrum, this control region is only applicable to LLP candidate jets with $p_{\mathrm{T}} < 70\,\mathrm{GeV}$.

We observe that variables related to tracks from photons closely resemble those of signal jets, as expected since photon jets are trackless. To account for this, we shift a few DNN input variables using Eqs. 7.7- 7.8 to match the distributions of photon jets to those of signal jets. These variables include the number of ECAL barrel rec hits (13), energy fraction of ECAL barrel rec hits (14), fragmentation function of ECAL barrel rec hits shower (18), neutral hadron energy fraction (20), and photon energy fraction (22).

For the jet time variable (15), we introduce an artificial delay of 1–2 ns to the mean of both data and MC background distributions, which simulates the delayed arrival of jets from signal. We also apply the same smearing procedure described in Sec. 7.3 to the MC background.

7.5.1.2 Electron proxy in W→ $e\nu_e$ events

To assess the efficiency of the TD jet tagger for LLP candidate jets with $p_{\mathrm{T}} > 70\,\mathrm{GeV}$, we use electrons from W→ $e\nu_e$ events as proxy objects. These electrons are selected from events that satisfy standard isolation and identification criteria [187], along with a requirement of $p_{\mathrm{T}}^{\mathrm{miss}} > 70\,\mathrm{GeV}$. We also require this exact one electron ($p_{\mathrm{T}} > 70\,\mathrm{GeV}$) overlap with the one jet ($p_{\mathrm{T}} > 70\,\mathrm{GeV}$) in the event. Furthermore, we remove jet cuts based on the photon and electron energy fractions (mentioned in Sec. 7.3), to avoid suppressing jets induced by electrons and increase statistics.

To account for differences between the proxy objects and signal jets, we smear the distributions of the TD jet tagger input variables for both electrons and photons in both data and simulation. For the electrons, we remove the track produced by the electron candidate and treat it as a photon. The input variables include the number of ECAL barrel rec hits, the energy fraction of ECAL barrel rec hits, the fragmentation function of ECAL barrel rec hits shower, the neutral hadron energy fraction, and the photon energy fraction. The details of the smearing procedure are as follows:

i) We set jet electron energy fraction (21) to be 0 ($\mathrm{Frac}_{\text{Electron Energy}} = 0$).
ii) We set jet photon energy fraction (22) to be the sum of the photon and electron energy fraction ($\mathrm{Frac}_{\text{Photon Energy}} = \mathrm{Frac}_{\text{Photon Energy}} + \mathrm{Frac}_{\text{Electron Energy}}$) and the smearing procedure similar to Subsec. 7.5 is applied to make data and MC background match signal.
iii) We also subtract the electron p_T from the variable consists of the sum of all the tracks included in the jet cone including $\alpha_{\max}$ (3) and ${}_{track\in jet}p_T$ (9).
iv) The smearing procedure is also applied to the variables of the neutral hadron energy fraction (20), multiplicity of the ECAL rec hits (13), energy fraction of the ECAL rec hits (14), fragmentation function (18).

7.5.1.3 DNN data/MC corrections

After correcting and validating the simulation's jet time response, as discussed in Sec. 7.3, we proceeded to validate the simulation's prediction of the TD tagger discriminator after accounting for the impact of the jet time measurement.

To achieve this, we replicated the time of arrival distribution for signal jets by introducing an artificial delay of 1–2ns in the corresponding distribution for prompt proxy objects. This artificial delay was sufficient to cover the majority of the expected TD tagger scores for signal jets. The choice of proxy objects, i.e., photons or electrons, was based on the jet p_{T}.

Since the electron proxy (W$\rightarrow e\nu_e$) probes the modeling of jets with $p_T > 70$ GeV, while the photon proxy (Z$\rightarrow l^+l^-\gamma$) probes mostly low-p_T jets, we applied the former to signal jets with $p_T > 70$ GeV (electron proxy, $p_{\mathrm{T}} > 70$ GeV), and the latter otherwise (photon proxy, $p_{\mathrm{T}} < 70$ GeV).

We calculate the TD jet tagger scores for these proxy objects and compare them to the threshold of 0.996 used to tag signal jets. The measured efficiencies are then compared to the efficiencies predicted by the simulation (shown in Fig. 7.18), and data-to-simulation correction factors are obtained. The uncertainties are propagated from the difference in the correction factors obtained using delay times of 1 and 2 ns.

The correction factors are found to be independent of jet p_{T} and η, and fall within the range 0.9–1.1. These factors are used to correct the simulation, and a systematic uncertainty is assigned based on the difference in correction factors obtained using the different delay times.

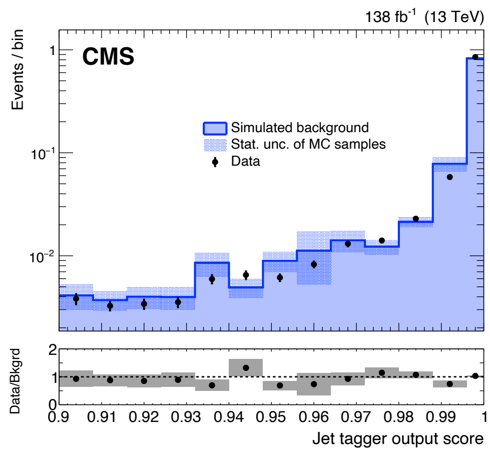

Figure 7.18: The TD jet tagger score distributions for simulation (shaded histogram) and data (black markers) when using electrons from W$\rightarrow e\nu_e$ events as proxy objects for signal jets. The histograms and data points have been normalized to unit area. The last bin contains jets with tagger scores greater than 0.996, the threshold used to tag signal jets. Similar levels of agreement are observed for photon proxy objects from the Z$\rightarrow l^+l^-\gamma$ sample.

7.6 Background estimation

The primary background processes in the two-tag signal region (SR) are QCD multijet, W+jets, Z$\rightarrow$ $\nu\bar{\nu}$+jets, and $t\bar{t}$ production, where prompt jets are misidentified as signal jets by the TD jet tagger. This misidentification occurs very rarely, as shown in Fig. 7.20, with a rate of less than 0.1%, and is primarily due to outliers in the jet composition and time measurement. The prompt jets that pass the TD jet tagger may result from tracking inefficiencies or instances where the fragmentation and hadronization mostly involve photons or neutral hadrons, resulting in approximately trackless jets. Misidentified jets may also have larger measured times, causing them to appear delayed. As the misidentification probability per jet ϵ_{bkg} primarily results from instrumental and resolution effects, it does not depend strongly on the process or presence of other objects in the event. To estimate the background contribution to the two-tag SR, we employ a matrix method [188, 189].

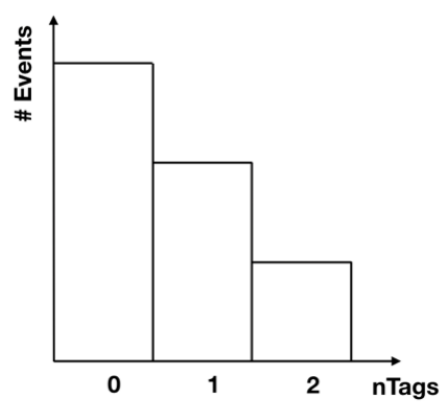

Figure 7.19: Number of tag(s) histogram. Two-tag SR (signal region) is bin 2, which contains events with more or equal to two tagged jets.

7.6.1 Background estimation strategy

We use jets with p_{T} > 30 GeV as the basic objects for the matrix method and measure the misidentification probability ϵ_{bkg} as a function of jet η in signal-depleted measurement regions (MRs). We observe that ϵ_{bkg} is independent of jet p_{T} and thus only parameterize it as a function of jet η.

To predict the number of background events in the two-tag SR, two methods are used. In the first method, each untagged jet i with $p_{\mathrm{T}} > 30\mathrm{GeV}$ in events passing the preselection with exactly one TD-tagged jet is assigned a probability $\epsilon_{\mathrm{bkg}}(\eta_{\mathrm{jet}\ i})$ to be misidentified as a TD jet. The total background prediction $N_{\geq 2\text{-tag bkg}}$ is obtained by summing over all untagged jets in the event, as given by the following equation:

$$N_{\geq 2\text{-tag bkg}} = \sum_{k=1}^{N_{1\text{-tag}}} \left(\sum_{i=1}^{N^k_{\mathrm{untagged}}} \epsilon_{\mathrm{bkg}}(\eta_{\mathrm{jet}\ i}) \right). \tag{7.23}$$

Here, $N_{1\text{-tag}}$ is the number of one-tag events in data, and N^k_{untagged} is the number of untagged jets in event k. This method ignores contributions of order $\epsilon^2_{\mathrm{bkg}}$ and is accurate when ϵ_{bkg} is small, which is the case here as ϵ_{bkg} is below 10^{-3}.

In the second method, events with zero TD-tagged jets are selected, and each pair of untagged jets (jets i and j) is considered as a potential source of misidentified jets. Each untagged jet pair is assigned a weight $\epsilon_{\mathrm{bkg}}(\eta_{\mathrm{jet}\ i})\epsilon_{\mathrm{bkg}}(\eta_{\mathrm{jet}\ j})$, and the alternative background prediction is given by

$$N'_{\geq 2\text{-tag bkg}} = \sum_{k=1}^{N_{0\text{-tag}}} \left(\sum_{i=1}^{N^k_{\mathrm{untagged}}} \sum_{j>i}^{N^k_{\mathrm{untagged}}} \epsilon_{\mathrm{bkg}}(\eta_{\mathrm{jet}\ i})\epsilon_{\mathrm{bkg}}(\eta_{\mathrm{jet}\ j}) \right), \tag{7.24}$$

where $N_{0\text{-tag}}$ is the number of zero-tag events in data. The two background predictions agree if ϵ_{bkg} is jet- and process-independent. Thus, the prediction $N_{\geq 2\text{-tag bkg}}$ obtained using the first method is considered the nominal background prediction, and the difference between the two predictions is used to estimate the systematic uncertainty of the method resulting from any additional process dependence. This systematic uncertainty is found to be 13%.

7.6.2 Measurement regions

7.6.2.1 Nominal measurement regions

The nominal MR is defined by selecting events with one electron or muon satisfying standard isolation and identification criteria [187, 190], with $p_{\mathrm{T}} > 35$ or 30 GeV, respectively. We require $p_{\mathrm{T}}^{\mathrm{miss}} > 40$ GeV to suppress QCD multijet background and the transverse mass to be smaller than 100 GeV to suppress a potential beyond the SM signal. Figure 7.20 shows the ϵ_{bkg} measurement, which is derived per jet, for two data-taking periods. We observe a higher misidentification probability for the first 19.9 fb^{-1} of data collected in 2016 due to sub-optimal settings on the tracker readout chip in the presence of large pileup. For the last 16.4 fb^{-1} of data collected in 2016, the readout chip parameters were re-optimized, leading to improved tracking efficiency and less misidentification.

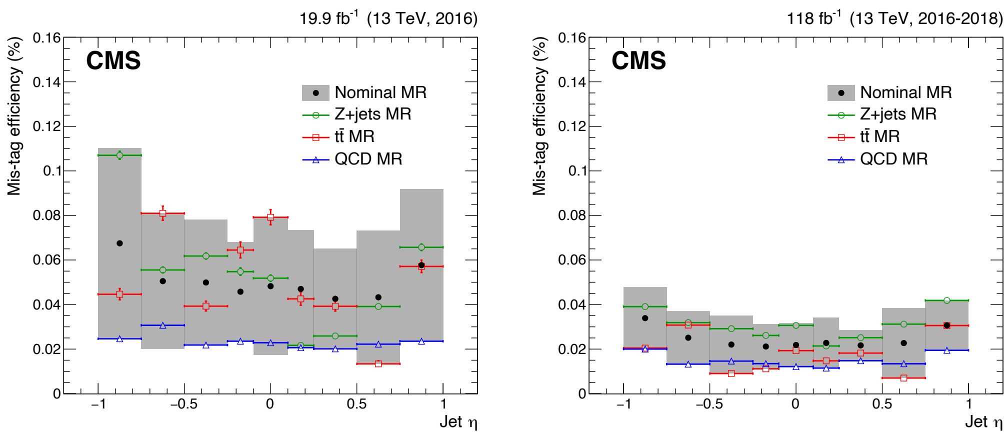

Figure 7.20: The TD jet tagger misidentification probability measured using the nominal W+jets MR (black round markers) is shown along with the systematic uncertainty (gray band), quantifying the degree of process dependence measured from alternative MRs. The measurements in the alternative MRs are displayed as well (Z+jets MR as green round markers, $t\bar{t}$ MR as red squared markers, QCD MR as blue triangular markers) along with their respective statistical uncertainty. On the left, this probability is shown for the first 19.9 fb^{-1} of data collected in 2016, while on the right it is shown for the last 16.4 fb^{-1} of data collected in 2016 combined with data collected in 2017–2018.

Table 7.5: Definitions of the measurement regions used to quantify the process dependence of the TD jet misidentification probability.

Measurement region	Selection
Nominal	1 electron (muon) with $p_{\mathrm{T}} > 35$ (30) GeV, $p_{\mathrm{T}}^{\mathrm{miss}} > 40$ GeV, < 100 GeV
Z+jets	2 electrons (2 muons) with $p_{\mathrm{T}} > 35$ (30) GeV, $60 < m\ (m) < 120$ GeV, $p_{\mathrm{T}}^{\mathrm{miss}} < 30$ GeV
$t\bar{t}$	1 electron and 1 muon with $p_{\mathrm{T}} > 35$ and 30 GeV, $p_{\mathrm{T}}^{\mathrm{miss}} > 30$ GeV
QCD multijet	1 jet with $p_{\mathrm{T}} > 140$ GeV online, $p_{\mathrm{T}}^{\mathrm{miss}} < 25$ GeV offline

7.6.2.2 Alternative measurement regions

An investigation of the process dependence of the misidentification probability is performed by measuring misidentification probabilities from three alternative measurement regions (MRs). The first MR, called the Z+jets MR, is intended to represent the $Z(\nu\bar{\nu})$+jets background and is obtained by selecting events with two electrons or two muons with $p_{\mathrm{T}} > 35$ or 30 GeV, respectively, and with a dilepton mass between 60 and 120 GeV. The $p_{\mathrm{T}}^{\mathrm{miss}}$ is required to be less than 30 GeV to suppress other background processes. The second MR, called the $t\bar{t}$ MR, is obtained by selecting events with one electron and one muon, with the same p_{T} requirements as the Z+jets MR, and $p_{\mathrm{T}}^{\mathrm{miss}} > 30$ GeV. The third MR is intended to represent the QCD multijet background and is obtained by requiring the presence of a jet with $p_{\mathrm{T}} > 140$ GeV online, and $p_{\mathrm{T}}^{\mathrm{miss}} < 25$ GeV offline to avoid signal contamination. Table 7.5 provides a summary of the different MRs. The range of misidentification probabilities measured in the nominal and three alternative MRs is used to derive an envelope that covers the systematic uncertainty quantifying the degree of process dependence. This systematic uncertainty is found to be 45% relative to the collision background and 30% relative to the total background prediction and is shown in Fig. 7.20.

To evaluate the impact of process dependence, the misidentification probabilities from three alternative measurement regions (MRs) are measured. The Z($\nu\bar{\nu}$)+jets background is estimated using the Z+jets MR, which requires events with two electrons or two muons, each with $p_{\mathrm{T}} > 35$ or 30 GeV, respectively, and a dilepton mass between 60 and 120 GeV. The $p_{\mathrm{T}}^{\mathrm{miss}}$ is required to be less than 30 GeV to reduce contributions from other background processes. The $t\bar{t}$ MR is used to represent the top-quark background and is obtained by selecting events with one electron and one muon with the same p_{T} requirements as in the Z+jets MR and $p_{\mathrm{T}}^{\mathrm{miss}} > 30$ GeV. For the QCD multijet background, events with a jet with $p_{\mathrm{T}} > 140$ GeV online and $p_{\mathrm{T}}^{\mathrm{miss}} < 25$ GeV offline are chosen as the QCD multijet MR to avoid contamination from signal events. A summary of the different MRs is provided in Table 7.5. The envelope covering the range of misidentification probabilities measured in the nominal and three alternative MRs is used to derive a systematic uncertainty. This systematic uncertainty quantifies the degree of process dependence and is shown in Fig. 7.20. It is found to be 45% relative to the collision background and 30% relative to the total background prediction.

7.6.3 Validation tests

To validate the accuracy of our background prediction method, we define a validation region (VR) using events that satisfy the nominal MR selection with two misidentified TD jets. Using the ϵ_{bkg} values measured in the MR and the matrix method, we predict 1.1 ± 0.7 background events in the VR, while observing 1 event in data. We perform another validation test by relaxing the jet η requirement to $\eta < 1.48$ to reduce the statistical uncertainty. For this alternative test, we estimate 5.1 ± 3.1 events in the VR and observe 4 events in data. Both tests show excellent agreement between the predicted and observed yields, thus validating our background estimation method. In addition, we validate the η dependence of ϵ_{bkg} by comparing the η distribution of TD-tagged jets in the one tag bin of the signal region data with the predicted background, as shown in Fig. 7.21.

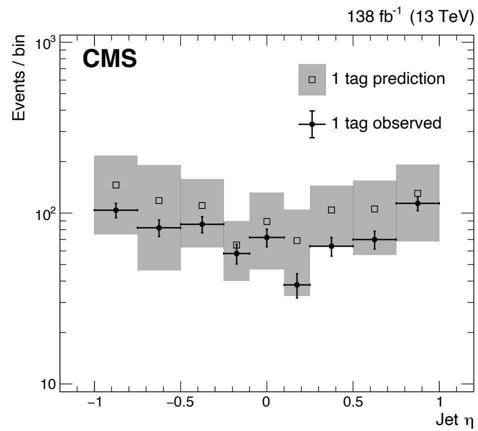

Figure 7.21: The η distribution of TD-tagged jets in a background-enriched control region that comprises events with exactly one TD-tagged jet. Observed data (black round markers) and the corresponding prediction based on control samples in data (empty squared markers), measured using the nominal W+jets MR, are compared. The prediction uncertainty (gray band) includes the systematic uncertainty quantifying the degree of process dependence measured from alternative MRs. The predictions for the shape and the normalization of the η distribution are consistent with the data.

7.6.4 Predictions

7.6.4.1 Collision background

Using this method and the matrix method described above (Sec. 7.6), a collision background yield of 0.15 ± 0.08 is predicted for the two-tag SR.

7.6.4.2 Non-collision background

To estimate contributions from non-collision sources, such as cosmic ray muons and beam halo particles, we perform measurements in dedicated MRs with high purity for each source. The cosmic ray muon MR consists of events with cosmic ray triggers, which are enabled when the LHC is not colliding proton beams. These events contain a muon that traverses the entire detector and a jet. The beam halo MR is composed of events selected by an alternative beam halo filter that identifies beam halo particles using matching segments in the CSC endcap muon detector.

To estimate the cosmic ray muon and beam halo contributions, we first measure the efficiencies of the corresponding vetoes in the respective MRs. To prevent bias from the instrumental misidentified collision background, we subtract this contribution using the matrix method in the beam halo MR. We then invert the cosmic ray muon and beam halo vetoes described in Sec. 7.4 to obtain two separate CRs.

Next, we multiply the event yields in the CRs by transfer factors accounting for the measured efficiencies of the cosmic ray muon and beam halo vetoes. The resulting predictions for the cosmic ray muon and beam halo backgrounds are 0.03 ± 0.02 and 0.05 ± 0.05 events, respectively. These predictions are consistent with zero events in each case. Although the dominant background contribution comes from instrumental misidentification, these small contributions from non-collision sources are also considered in the analysis.

7.6.4.3 Final results

Source	Prediction	Observed
Mis-tag	0.15 ± 0.08	0
Cosmic	0.03 ± 0.02	-
Non collision	0.05 ± 0.05	-
Tot.	0.23 ± 0.10	-

Table 7.6: Final background prediction in the two-tag SR.

7.7 Systematic uncertainties

To estimate the uncertainties in the background and signal yields, several systematic uncertainties are considered. The dominant uncertainty in the background estimation is related to the misidentified TD jet background, which includes contributions from the CR sample size, ϵ_{bkg} process dependence, and the validity of the matrix method, amounting for 4%, 30%, and 13%, respectively, relative to the total background prediction. The non-collision background uncertainties correspond to about 23% relative to the total background prediction.

For the signal yield prediction, the largest uncertainty arises from the TD jet tagger efficiency, which includes a component from the jet time correction uncertainty as well as a component estimated using the methods discussed in Section 7.5, and amounts to up to 29% relative to the signal yield, depending on the signal model parameters. Other sources of uncertainty include the integrated luminosities for the 2016, 2017, and 2018 data-taking years, which have 1.2–2.5% individual uncertainties [191–193], while the overall uncertainty for the 2016–2018 period is 1.6%.

Uncertainties related to jet energy scale and resolution [194, 195], PDFs, missing higher order QCD corrections, pileup modeling, simulation sample size, and lepton and photon veto efficiency are also considered and their impacts are summarized in Table 7.7.

Table 7.7: Summary of combined statistical and systematic uncertainties, the size of their effect, and whether it applies to the signal or background yield predictions. Ranges for signal systematic uncertainties reflect their impact on different signal parameter space points.

Uncertainty source	Process	Uncertainty [%]
Background CR sample size	Background	4
TD jet tagger misidentification process dependence	Background	30
Background estimation method	Background	13
Noncollision background	Background	23
TD jet tagger efficiency	Signal	8–29
Jet energy scale	Signal	0.1–11
Jet energy resolution	Signal	0.2–10
PDFs	Signal	$\leq$1
Missing higher-order QCD corrections	Signal	$\leq$1
Pileup	Signal	0.3–6.3
Integrated luminosity	Signal 5–8	
Lepton and photon veto efficiency	Signal	$\ll$1

7.8 Results

The number of TD jets (N_{TDJ}) is shown in Fig. 7.22, with separate bins for $N_{\text{TDJ}} = 0$, $N_{\text{TDJ}} = 1$, and $N_{\text{TDJ}} \geq 2$. For the $N_{\text{TDJ}} = 0$ bin, the observed data and expected background agree well. In the most sensitive SR bin, corresponding to $N_{\text{TDJ}} \geq 2$, we observe 0 events with an expected background of 0.23 ± 0.10 events, indicating good agreement between the data and the background prediction.

In this analysis, we consider a simplified model of GMSB chargino-neutralino production [65, 66], where the long-lived neutralinos are produced in pairs and subsequently decay to either $H\tilde{G}$ or $Z\tilde{G}$, as discussed in Sec. 7.1. We vary the branching fraction $\mathcal{B}(\tilde{\chi}_1^0 \to H\tilde{G})$ from 0 to 1, assuming $\mathcal{B}(\tilde{\chi}_1^0 \to H\tilde{G}) + \mathcal{B}(\tilde{\chi}_1^0 \to Z\tilde{G}) = 1.0$, and use a test statistic based on the profile likelihood ratio [119] to extract the signal.

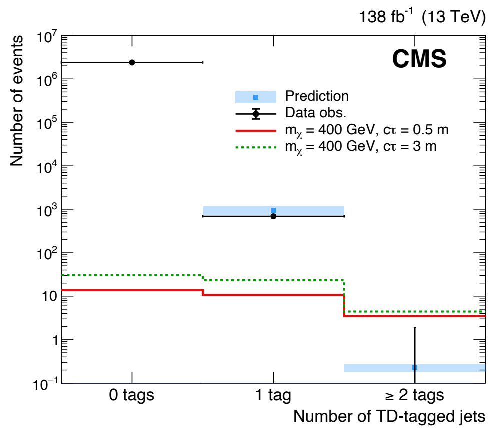

Figure 7.22: Distribution of the number of TD tagged jets for the $m_{\widetilde{\chi}_1^0=400\,\mathrm{GeV}}$ signal samples with $c\tau_{\widetilde{\chi}_1^0=0.5m}$ (red line) and $c\tau_{\widetilde{\chi}_1^0=3m}$ (dotted green line), estimated background (blue markers), and data (black markers). The blue shaded region indicates the systematic uncertainty of the background prediction. No background prediction is shown for the bin with zero TD tagged jets as it is the main control region used to predict the background for the remaining two bins.

We derive upper limits at 95% confidence level (CL) on the product of the neutralino pair production cross section ($\sigma_{\widetilde{\chi}_1^0\widetilde{\chi}_1^0}$) and the relevant branching fraction using the modified frequentist $\mathrm{CL_s}$ criterion [117, 118] and an asymptotic formula [116]. Systematic uncertainties are incorporated into the analysis via nuisance parameters with log-normal probability density functions and are treated according to the frequentist paradigm.

The upper limits on $\sigma_{\widetilde{\chi}_1^0\widetilde{\chi}_1^0}$ as functions of the $\widetilde{\chi}_1^0$ mass ($m_{\widetilde{\chi}_1^0}$) and proper decay length ($c\tau_{\widetilde{\chi}_1^0}$), assuming $\mathcal{B}(\widetilde{\chi}_1^0 \to H\tilde{G}) = 0.5$, are shown in Figures 7.23 and 7.24, respectively. Figure 7.25 shows the observed upper limits as a function of both $m_{\widetilde{\chi}_1^0}$ and $c\tau_{\widetilde{\chi}_1^0}$. The upper limits are relatively independent of the branching fraction $\mathcal{B}(\widetilde{\chi}_1^0 \to H\tilde{G})$, varying by less than 10% over the full range.

We exclude cross sections of 160, 2.6, and 0.8 fb for $m_{\widetilde{\chi}_1^0}$ of 200, 400, and 600 GeV, respectively, at $c\tau_{\widetilde{\chi}_1^0} = 0.5$ m. Compared to previous searches for promptly decaying $\widetilde{\chi}_1^0$ in the same simplified model [196], the sensitivity of the current search expressed in terms of the cross section limit is about 20 (10) times better at $m_{\widetilde{\chi}_1^0} =$ 400 (600) GeV. We exclude $\widetilde{\chi}_1^0$ masses up to approximately 1180 (990) GeV when $c\tau_{\widetilde{\chi}_1^0}$ is 0.5 (3.0) m at a 95% CL. For $m_{\widetilde{\chi}_1^0} = 400$ (1000) GeV, we exclude in the range from 0.04 to 20 (0.1 to 3) m. Tabulated results are provided in the HEPData record for this analysis [197].

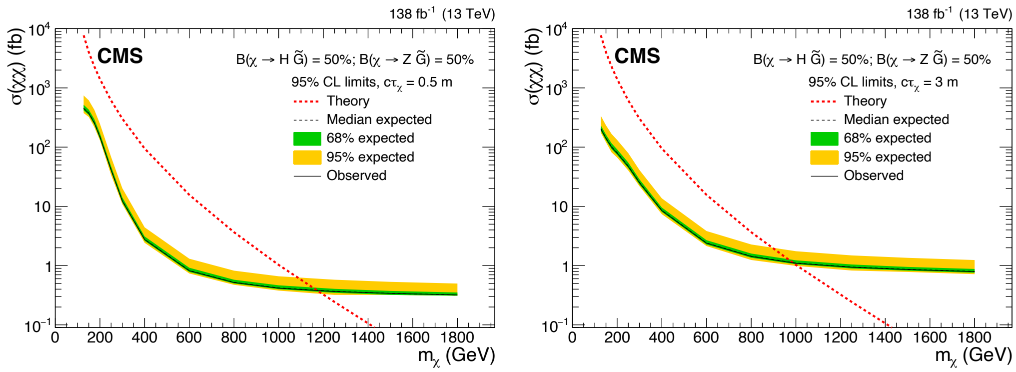

Figure 7.23: 95% CLexpected upper limits on $\sigma_{\tilde{\chi}_1^0\tilde{\chi}_1^0}$ as a function of $m_{\tilde{\chi}_1^0}$in a scenario with $\mathcal{B}(\tilde{\chi}_1^0 \to H\tilde{G}) = 0.5$ and $c\tau = 0.5m$ (left) or 3m (right).

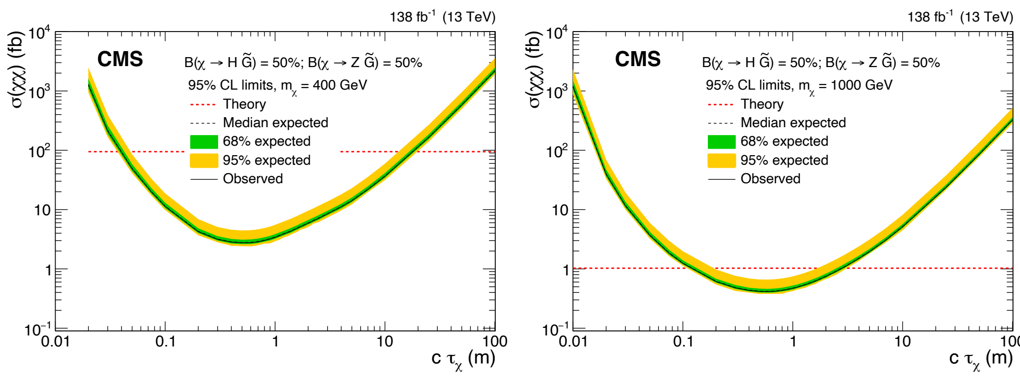

Figure 7.24: 95% CLexpected upper limits on $\sigma_{\tilde{\chi}_1^0\tilde{\chi}_1^0}$ as a function of $c\tau_{\tilde{\chi}_1^0}$ in a scenario with $\mathcal{B}(\tilde{\chi}_1^0 \to H\tilde{G}) = 0.5$ and $m_{\tilde{\chi}_1^0=400\,\mathrm{GeV}}$ (left) or 1000 GeV(right).

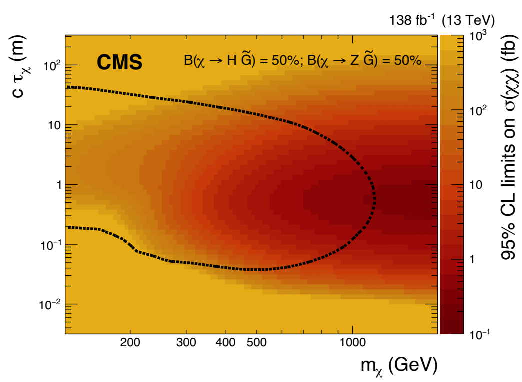

Figure 7.25: 95% CLobserved upper limits on $\sigma_{\tilde{\chi}_1^0\tilde{\chi}_1^0}$ as a function of $m_{\tilde{\chi}_1^0}$ and $c\tau_{\tilde{\chi}_1^0}$ in a scenario with $\mathcal{B}(\tilde{\chi}_1^0 \to H\tilde{G}) = 0.5$.

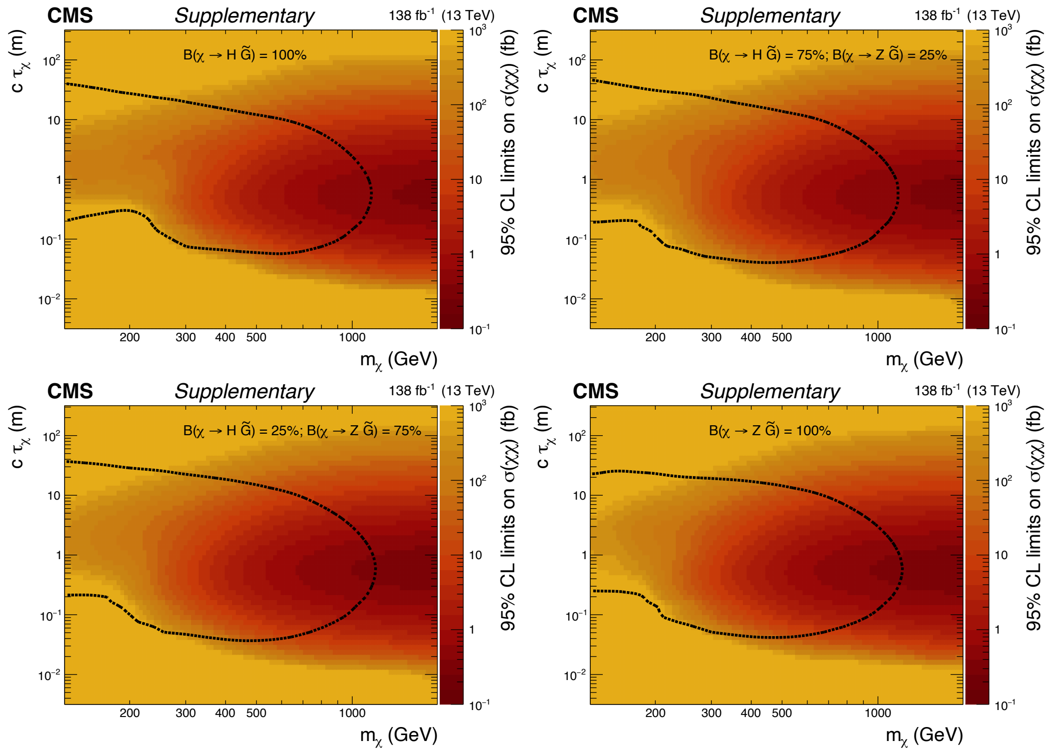

Figure 7.26: The observed 95% CL upper limit on $\sigma_{\tilde{\chi}_1^0\tilde{\chi}_1^0}$ as a function of $m_{\tilde{\chi}_1^0}$ and $c\tau_{\tilde{\chi}_1^0}$ in scenarios with $\mathcal{B}(\tilde{\chi}_1^0 \to H\tilde{G}) = 1$ (top left); $\mathcal{B}(\tilde{\chi}_1^0 \to H\tilde{G}) = 0.75, \mathcal{B}(\tilde{\chi}_1^0 \to Z\tilde{G}) = 0.25$ (top right); $\mathcal{B}(\tilde{\chi}_1^0 \to H\tilde{G}) = 0.25, \mathcal{B}(\tilde{\chi}_1^0 \to Z\tilde{G}) = 0.75$ (bottom left), and $\mathcal{B}(\tilde{\chi}_1^0 \to Z\tilde{G}) = 1$ (bottom right). The area enclosed by the dotted black line corresponds to the observed excluded region.

7.9 Summary

In this chapter, we conducted a search for long-lived particles using proton-proton collision data at a center-of-mass energy of $\sqrt{s} = 13$ TeV, corresponding to an integrated luminosity of 138fb^{-1}. The search utilized a novel and highly discriminating deep neural network tagger for trackless and delayed (TD) jets, along with missing transverse momentum, to identify the signal. We required at least two TD-tagged jets to suppress the standard model background processes by more than three orders of magnitude while maintaining a signal efficiency above 80%. To estimate the background, we employed a method based on control samples in data, which utilized the tagger's measured misidentification probability to extrapolate from event samples with one or fewer tagged jets to the signal region comprising events with two or more tagged jets.

We interpreted the results in the context of a simplified model of electroweak production of chargino-neutralino pairs, where the long-lived neutralinos are effectively pair produced and decay to either $\mathrm{H}\tilde{G}$ or $\mathrm{Z}\tilde{G}$. For a neutralino proper decay length of $c\tau_{\widetilde{\chi}_1^0}$ = 0.5 m, we excluded cross sections of 160, 2.6, and 0.8 fb for $\widetilde{\chi}_1^0$ masses ($m_{\widetilde{\chi}_1^0}$) of 200, 400, and 600 GeV, respectively, at 95% confidence level. Compared to previous searches for promptly decaying $\widetilde{\chi}_1^0$ in the same simplified model, the sensitivity of the current search expressed in terms of cross section limit is about 20 (10) times better at $m_{\widetilde{\chi}_1^0}$ = 400 (600) GeV. We also excluded $\widetilde{\chi}_1^0$ masses up to 1.18 TeV at 95% confidence level for the case of a long-lived $\widetilde{\chi}_1^0$ with $c\tau_{\widetilde{\chi}_1^0}$ = 0.5 m. This result represents the best to date in the mass range from the kinematic limit imposed by the Higgs boson mass up to 1.8 TeV. The HEPData record for this analysis provides more details and tabulated results [197].

Part V

Conclusion

Chapter 8

CONCLUSION

This thesis covered several important concepts in particle physics, including the Standard Model and its Lagrangian. Additionally, it discussed the Higgs mechanism, which provides a mechanism for fundamental particles to acquire mass. Through a brief review of these fundamental principles, we established the foundation for the research presented in this thesis.

We discussed the motivation for exploring new physics beyond the Standard Model, specifically through a supersymmetric extension of the model. Notably, the mass-degenerate guage mediated supersymmetry breaking (GMSB) signal model holds significant promise for searches of long-lived particles, a topic of great importance in modern particle physics research.

We provided a comprehensive overview of the Large Hadron Collider (LHC) and the Compact Muon Solenoid (CMS). The LHC is a powerful particle accelerator that delivers high-energy proton-proton collisions at a center-of-mass energy of 13 TeV, providing an excellent environment to study the fundamental particles and interactions predicted by the Standard Model, as well as search for new physics beyond it. The CMS detector, on the other hand, is a state-of-the-art detector specifically designed to study the products of proton-proton collisions at the LHC. With its exceptional tracking and energy measurement capabilities, the CMS detector played a crucial role in the searches for new particles at the LHC described in this thesis.

We conducted a search for supersymmetry (SUSY) in the decay channel of a Higgs boson (H) into a pair of photons. Our analysis used 77.5 fb^{-1} of integrated luminosity collected by the CMS detector at the LHC during 2016 and 2017. Higgs boson candidates were reconstructed from photon pairs in the central region of the detector, while charged leptons and b-jets were used to tag the decay products of an additional boson. We used kinematic variables such as M_{R} and R^2 (razor variables) to suppress standard model backgrounds. Data-driven fits determine the shape and normalization of the non-resonant background, while the resonant background from standard model Higgs boson production is estimated from simulation. We interpreted the results in terms of exclusion limits on the production cross section of simplified models of bottom squark pair production and chargino-neutralino production. We improved the mass limits over previous CMS results [69, 70] by about 100 GeV for bottom squark pair production and about 50 GeV for chargino-neutralino production due to improvements in event categorization and the larger dataset. We excluded bottom squark pair production for bottom squark masses below 510 GeV for a lightest neutralino mass of 1 GeV, wino-like chargino-neutralino production for chargino and neutralino ($\widetilde{\chi}_1^0$) masses of up to 235 GeV and a gravitino ($\tilde{G}$) mass of 1 GeV, and higgsino-like chargino-neutralino production for chargino and neutralino ($\widetilde{\chi}_1^0$) masses of up to 290 and 230 GeV, respectively, in cases where the branching fraction of the lightest neutralino $\widetilde{\chi}_1^0 \to H\tilde{G}$ decay is 100%, and where the branching fractions of the $\widetilde{\chi}_1^0 \to H\tilde{G}$ and $\widetilde{\chi}_1^0 \to Z\tilde{G}$ decays are both 50%.

We also presented a search for long-lived particles using proton-proton collision data at a center-of-mass energy of $\sqrt{s} = 13$ TeV and an integrated luminosity of 138fb^{-1}. Our search utilized a deep neural network tagger for trackless and delayed (TD) jets, combined with missing transverse momentum, to identify the signal. We required at least two TD-tagged jets to achieve a signal efficiency above 80% and suppress the standard model background by more than three orders of magnitude. To estimate the background, we employed a data-driven method based on control samples, which used the tagger's measured misidentification probability to extrapolate from event samples with one or fewer tagged jets to the signal region with two or more tagged jets. We interpreted the results in the context of a simplified model of electroweak production of chargino-neutralino pairs, where the long-lived neutralinos are pair produced and decay to either H$\tilde{G}$ or Z$\tilde{G}$. For a neutralino proper decay length of $c\tau_{\widetilde{\chi}_1^0} = 0.5$ m, we excluded cross sections of 160, 2.6, and 0.8 fb for $\widetilde{\chi}_1^0$ masses ($m_{\widetilde{\chi}_1^0}$) of 200, 400, and 600 GeV, respectively, at a 95% confidence level. Our search achieved a sensitivity about 20 (10) times better than previous searches for promptly decaying $\widetilde{\chi}_1^0$ in the same simplified model, at $m_{\widetilde{\chi}_1^0} = 400$ (600) GeV. We also excluded $\widetilde{\chi}_1^0$ masses up to 1.18 TeV at 95% confidence level for the case of a long-lived $\widetilde{\chi}_1^0$ with $c\tau_{\widetilde{\chi}_1^0} = 0.5$ m. This result represents the best to date in the mass range from the kinematic limit imposed by the Higgs boson mass up to 1.8 TeV.

Part VI

Appendix

Chapter 9

THE MIP (MINIMUM IONIZING PARTICLES) TIMING DETECTOR (MTD)

The MIP Timing Detector (MTD) is a new detector currently under development for use in the High-Luminosity LHC (HL-LHC or Phase II) era within the CMS experiment. The MTD is designed to provide precision timing measurements for minimum ionizing particles (MIP) at a luminosity of up to 200 pile-up interactions per collision (PU). In the HL-LHC, the instantaneous luminosity is expected to reach $5 \times 10^{34} cm^{-2} s^{-1}$ (140 PU), with a maximum luminosity of $7.5 \times 10^{34} cm^{-2} s^{-1}$ (200 PU). The MTD is expected to achieve a time resolution of 30-40 ps at the beginning of HL-LHC operation, before radiation damage affects its performance.

Combining timing information with tracking data will give the CMS experiment excellent association of tracks to vertices, even when the vertices are very close together in space. The Phase II ECAL will provide time measurement of electromagnetic showers with 30-50 ps resolution, allowing photons to be associated with the correct charged particle vertices. Therefore, the performance of the Particle Flow algorithm is expected to be comparable at 200 PU during HL-LHC, thanks to the timing information provided by the MTD and Phase II ECAL.

9.1 Physics impact

MTD is crucial to the HL-LHC scientific program for both SM and BSM sides (summarized in Tab. 9.1). In particular, MTD is able to reconstruct the time of displaced vertices (DV), which will provide enhanced capability to search for LLPs by measuring β_{LLP}, where β is the relativistic velocity parameter, and, in certain cases, permitting the reconstruction of the LLP's mass. Also, the track-time reconstruction enables new capabilities for searches for neutral LLPs, postulated in many extensions of the SM like GMSB SUSY models and many others [198], even for cases in which the decays are partially invisible. If the decay products of LLPs are all captured by the detector, it can reconstruct the displaced decay vertex. Along with the 4D space-time information, it provides the kinematic constraints that are needed to get a direct measurement of the LLP mass.

Table 9.1: Expected scientific impact of the MIP Timing Detector [199, 200]

.

Signal	Physics measurement	MTD impact
H$\rightarrow \gamma\gamma$ and H$\rightarrow$ 4 leptons	+ 15-25% (statistical) precision on the cross section $\rightarrow$ Improve coupling measurements	Isolation and Vertex identification
VBF$\rightarrow$H$\rightarrow \tau\tau$	+ 30% (statistical) precision on the cross section $\rightarrow$ Improve coupling measurements	Isolation and VBF tagging, $p_{\mathrm{T}}^{\mathrm{miss}}$
HH	+ 20% gain in signal yield $\rightarrow$ Consolidate searches	Isolation b-tagging
EWK SUSY	+40% background reduction 150 GeV incerase in mass search	MET b-tagging
LLP	Peaking mass reconstruction Unique discovery potential	β_{LLP} from timing of displaced vertices

On the left of Fig. 9.1, it shows an exotic model in which a Higgs boson mediates the production of two long-lived, scalar bosons (X) that subsequently decay into quarks. The masses of the Higgs boson and X particles are fixed at 125 GeV and 50 GeV, respectively. The LLPs (X) are generated at the primary vertex (PV) and travel some distance before decaying into pairs of jets. On the right of Fig. 9.1, the jet time delay is calculated based on Eq. 7.5, which describes the time difference between the jet production and the LLP decay. This delayed feature can be exploited to discriminate signal from background, as described in Chap. 7.

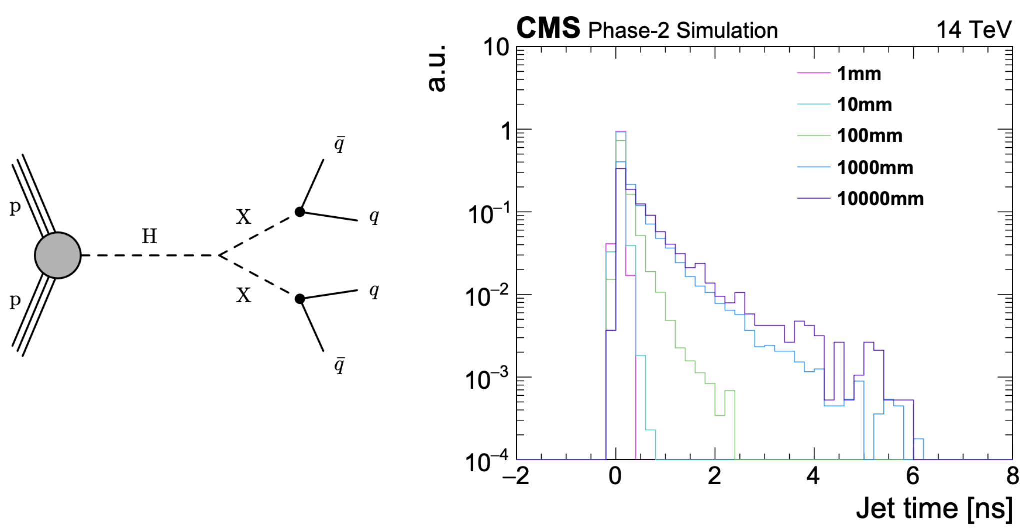

Figure 9.1: Long-lived particle search at the Phase-2 LHC. Left: Diagram for the production of displaced jets in a model mediated by a Higgs boson decaying into two long-lived scalar bosons. Right: Time difference between the measured jet time at the MTD and the expectation from the propagation of a particle from the PV at the speed of light. [199].

9.2 The MTD design

The MTD is divided into two sections: the Barrel Timing Layer (BTL), which covers $|\eta| < 1.5$, and the Endcap Timing Layer (ETL), which covers $1.6 < |\eta| < 3.0$. Fig. 9.2 shows a schematic view of the MTD, with the BTL located at the interface between the tracker and the ECAL, and the ETL situated in front of the endcap calorimeter[199]. For the remainder of this chapter, the focus is on the BTL, for which Caltech plays an essential role in research and development (RD).

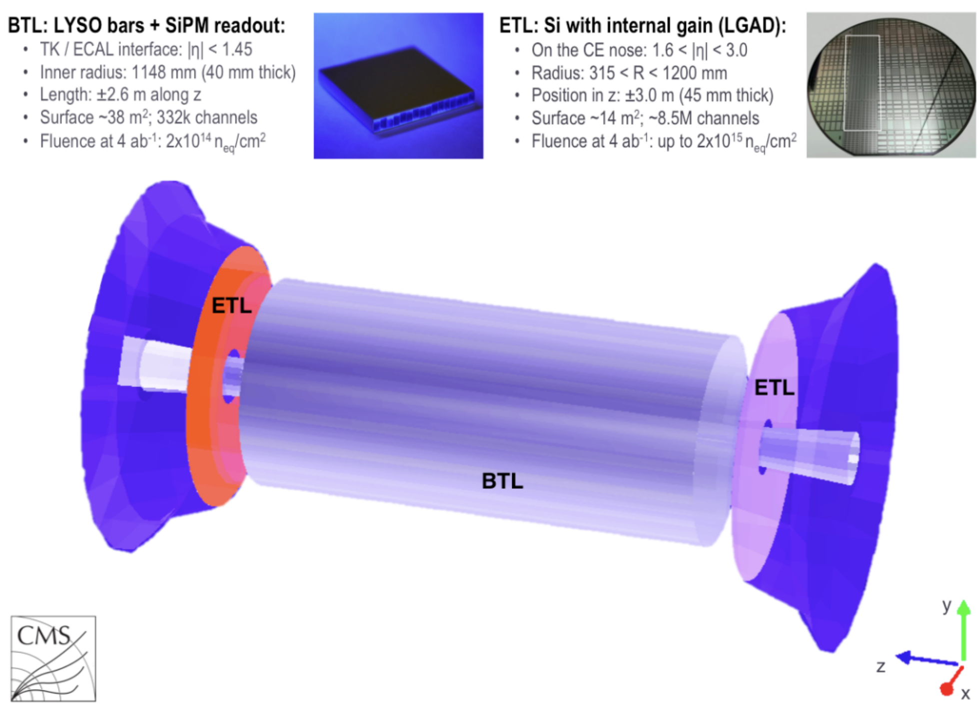

Figure 9.2: A schematic view of the GEANT geometry of the timing layers implemented in CMSSW [201] for simulation studies comprising a barrel layer (grey cylinder), at the interface between the tracker and the ECAL, and two silicon endcap (orange and light violet discs) timing layers in front of the endcap calorimeter [199].

9.3 The Barrel Timing Layer (BTL)

The BTL is a thin, cylindrical detector housed inside the Tracker Support Tube (TST), as shown in Fig. 9.3. The BTL will be built with LYSO:Ce (Lutetium Yttrium Orthosilicate doped with Cerium ($(Lu_{1-x}Y_x)_2SiO_5$:Ce)) scintillating crystals and Silicon photomultipliers (SiPMs), which meet the operational requirements of the HL-LHC. Both the crystals and the SiPMs are proven to be radiation-tolerant up to a neutron equivalent fluence of at least $2 \times 10^{14} cm^{-2}$ and a total integrated dose of 25 kGy (kilogray, 1 Gy = 1 J/kg = 1 m^2/s^2), when cooled to approximately −30°C.

Fig. 9.3 provides an orientation to the BTL and its components. The left side of the figure illustrates how the 16 crystal bars are grouped to form a module, how 24 modules constitute a Readout Unit (RU), and how six RUs are integrated into a tray. On the right side, the position of the trays on the periphery of TST is depicted.

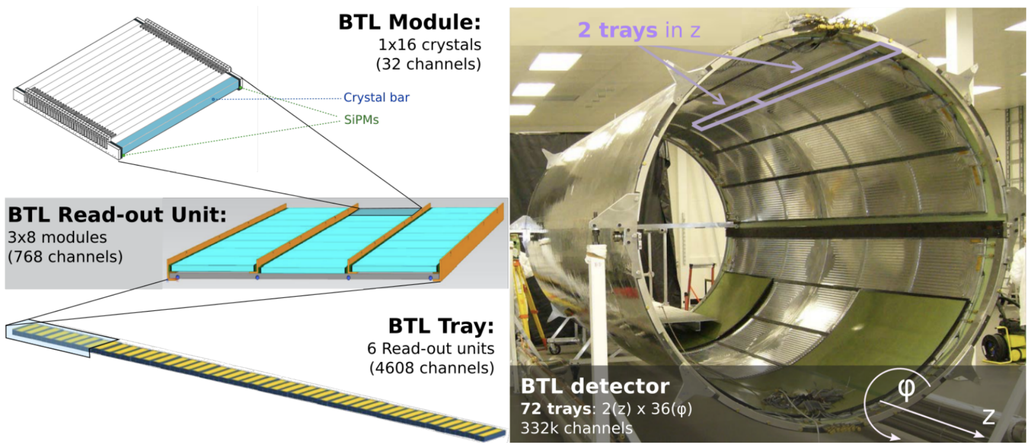

Figure 9.3: Overview of the BTL showing (left) the hierarchical arrangement of the various components, bars, modules, and Readout Units, and (right) trays (purple rectangles near the top), inside the Tracker Support Tube (TST) [199].

The BTL module consists of a LYSO:Ce crystal bar, with a length of approximately 5.7 cm and oriented along the ϕ direction in CMS. Its width is 3.0 mm along the z direction, and its radial thickness varies in three different $|\eta|$ intervals: 3.7 mm for $|\eta| < 0.7$; 3.0 mm for $0.7 \leq |\eta| \leq 1.1$; and 2.4 mm for $|\eta| > 1.1$. This design allows for an approximately constant slant depth that particles coming from the IP will cross.

Each end of the crystal bar is coupled to a SiPM, which has dimensions of 3 mm along the z direction and a variable thickness chosen to approximately match the bar's dimensions. At each end of the bar, there is a readout channel that measures the time of arrival of a MIP. By combining the measurements of the two time of arrivals, the effect of the time delay of the light traveling along the crystal is eliminated.

The detector is divided longitudinally into $+z$ and $-z$ ends, each end having a length of 2.6 m and consisting of 36 azimuthal segments. Each azimuthal segment corresponds to one tray, as shown in Fig. 9.3, covering a span of 10°. Each tray contains 6 RUs and 4,608 SiPMs, resulting in a total of 72 trays and 331,776 SiPMs. The modularity and channel count of the BTL are summarized in Table 9.2.

Table 9.2: Summary of the BTL modularity and channel count. The number of items in each module, readout unit and tray are shown [199].

	Module	RU	Tray	Total
Channels (SiPMs)	32	768	4608	331776
Crystals	16	384	2304	165888
ASCIs	1	24	144	10368
Modules	-	24	144	10368
Readout Units (RUs)	-	-	6	432
Trays	-	-	-	72

SiPMs operate above the breakdown voltage (V_{BD}) with a gain of the order of 10^5. To reduce dark current, which increases by roughly a factor of two for each increment of $7-10°$C, the SiPMs will be operated at a low temperature of about $-30°$C. The dark current, a noise source, produced by the over-voltage (OV) also increases as the radiation dose accumulates. The OV controls the photon detection efficiency (PDE). There is a trade-off between noise rate and signal size, and, therefore, the time resolution. During the detector lifetime, the operation voltage of SiPMs will have to be smoothly decreased to limit the noise level while maintaining good time resolution.

The dedicated ASIC (Application-Specific Integrated Circuit) chip for the BTL is TOFHIR (Time-of-flight, High Rate). Each TOFHIR delivers precision timing information for 32 SiPMs, based on the discrimination of the leading edges (LE) of their pulses, followed by measurement with a time-to-digital converter (TDC). The input to the discriminator must have a very fast rise time, dV/dt, to achieve high precision, which requires a lot of amplification and consequently a lot of power. As the radiation dose accumulates to around 0.7×10^{14} neq/cm^2, which corresponds to an integrated luminosity of about 1000 fb^{-1}, dark/leakage current becomes the dominant part of the power consumption and must be compensated for by the circuitry in the ASIC. The fluctuations in the dark current cause a jitter that degrades the time resolution, especially at high integrated doses, towards the end of the HL-LHC operation, when it will be the dominant contribution to the time resolution.

9.4 Test beam results

This section presents the results from the April 2019 test beam at Fermilab, which used a 120 GeV proton beam to measure the time resolution of un-irradiated sensors on a prototype of the BTL module based on the MTD design. Fig. 9.4 shows the beam line setup, where the trigger is based on a 10 cm^2 scintillation counter located a few meters upstream of the experimental setup. A silicon tracker telescope [202] is positioned upstream of the crystals and SiPMs under test. The crystals and SiPMs are placed inside a dark box that can rotate the sensors with respect to the beam direction. A Photek 240 Micro Channel Plate-PMT (MCP-PMT), with a time resolution of about 12 ps, is used to measure a reference time and is positioned just behind the crystals and SiPMs along the beam line.

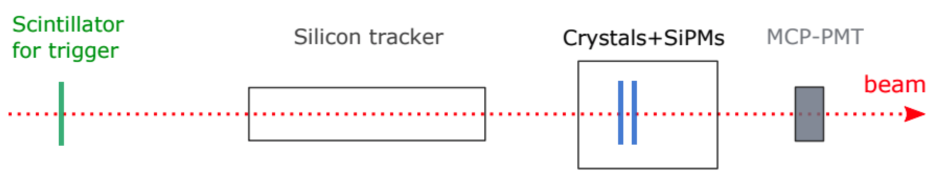

Figure 9.4: Schematic view of the beam line [199]. From left to right, the scintillator is used for the trigger, the silicon tracker defines the MIP impinging position in the xy plane, the MCP-PMT is used to define the reference time. The two crystal+SiPMs test setups, one for the 1-bar and the other for the 3-bar array, are positioned along the beamline.

Fig. 9.5 shows a visual of a bar in xy plane where the probability to pass the minimum amplitude (0.8 MPV, 2.08 MeV) and time range selection criteria ([35,50] ns) is close to 1. The x-axis along the crystal longest axis, the y-axis along the crystal shorter axis, and the z-axis runs along the beam direction.

The time resolution of the bar is measured from a Gaussian fit to the distribution of Δt_{bar} after subtracting in quadrature the time resolution of the MCP-PMT:

$$\sigma_{t_{average}} = \sqrt{\sigma^2_{\Delta t_{bar}} - \sigma^2_{t_{MCP}}}. \tag{9.1}$$

The Δt_{bar} is the difference between the $t_{average}$ and t_{MCP}, where $t_{average}$ is the time of a MIP incident on a crystal bar, which is the average between the times of arrival measured at the two ends, t_{left} and t_{right}, and t_{MCP} is the time measured by the MCP-PMT.

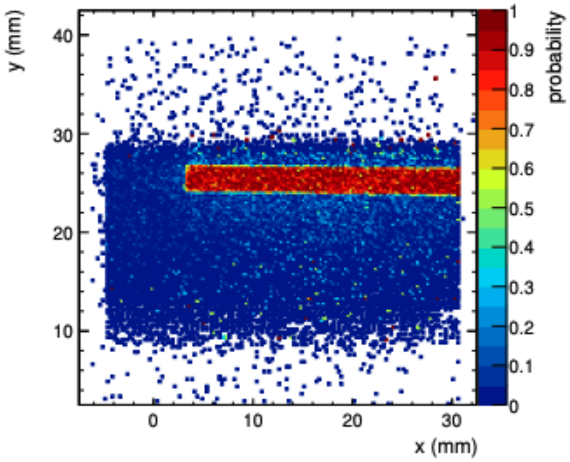

Figure 9.5: Probability to have a SiPM signal with an amplitude compatible with an energy deposit from a MIP crossing a 3 mm thick crystal bar, as a function of the x and y track coordinates: the xy region where the probability is close to 1 allows one to determine the precise location of the bar [199].

$$\Delta t_{bar} = t_{average} - t_{MCP} = \frac{1}{2}(t_{left} + t_{right}) - t_{MCP}. \tag{9.2}$$

An alternative way to estimate the time resolution is to measure half of the width of the difference $t_{diff} = t_{left} - t_{right}$ between the times of arrival measured at the two bar ends:

$$\frac{1}{2}\sigma_{t_{diff}} = \frac{1}{2}\sqrt{\sigma^2_{t_{left}} + \sigma^2_{t_{right}}} = \sigma_{t_{average}} \tag{9.3}$$

Fig. 9.6 shows the time resolution for various impact point positions of the tracks along the x direction for t_{left}, t_{right}, $t_{average}$ and $t_{diff}/2$ at about 6 V OV. The performance is relatively flat along the bar. A local bar resolution ($t_{average}$, t_{diff}) of about 30 ps and 25 ps is achieved for a $3 \times 3 \times 57$ mm^3 LYSO:Ce bar coupled to HPK SiPMs and for a $3 \times 4 \times 57$ mm^3 LYSO:Ce bar coupled to FBK SiPMs, respectively. The FBK SiPMs setup achieves better performance due to the larger energy deposited in the thicker crystal and the larger light collection efficiency. The $t_{average}$ combines the measurements of the two SiPMs and improves the time resolution by about $\sqrt{2}$ with respect to the individual SiPM (t_{left}, t_{right}), since the dominant stochastic fluctuations from photostatistics are uncorrelated between the two ends. The time resolution estimated using $t_{diff}/2$ in the configuration with HPK SiPMs is slightly better than the time resolution estimated using $t_{average}$ because the contribution of the correlated electronics noise is canceled in t_{diff}.

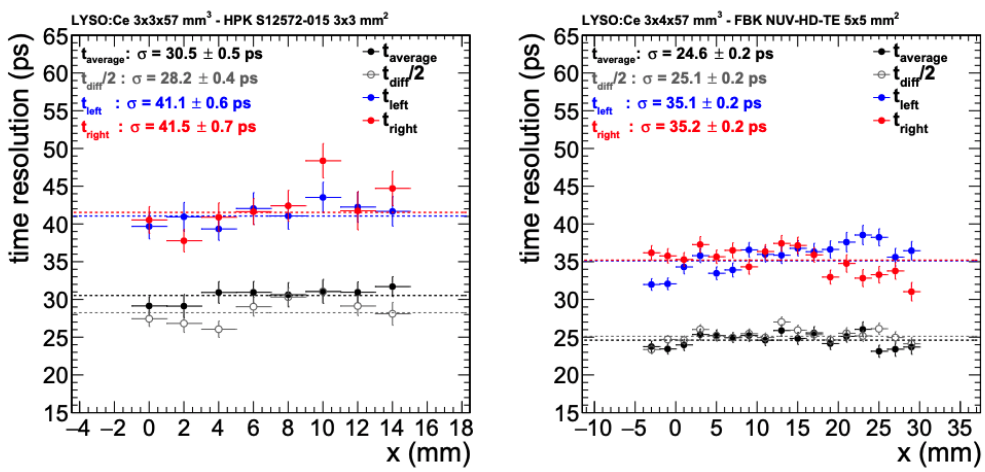

Figure 9.6: Time resolution of the left and right SiPMs, their average, and half of the time difference [199] as a function of the MIP impact point for a $3 \times 3 \times 57$ mm^3 LYSO:Ce bar coupled to HPK SiPMs (left) and for a $3 \times 4 \times 57$ mm^3 LYSO:Ce bar coupled to FBK SiPMs (right). For t_{left}, t_{right}, $t_{average}$, the estimated contribution from the resolution of the MCP-PMT (12 ps) was subtracted in quadrature.

Chapter 10

THE TIMING LEVEL-1 TRIGGER AT THE HL-LHC

At the HL-LHC, the CMS detector requires a trigger and data acquisition system with exceptional performance to collect 400 to 450 fb^{-1} of integrated luminosity per year. The Phase II upgrade will maintain a two-level strategy for the trigger system but increase the L1 maximum rate from 100 to 750 kHz. The total latency will also be increased from 4 to 12.5 μs, allowing for the first time the inclusion of the tracker and high-granularity calorimeter information. Furthermore, the longer latency will enable higher-level object reconstruction and identification, as well as the evaluation of complex global event quantities and correlation variables to optimize physics selectivity.

The goal of the Phase II upgrade of the L1 trigger system is not only to maintain the performance of existing signal selection but also to significantly enhance or enable physics selectivity, or in other words, enable the discovery of new physics. The functional diagram of the architecture and data flow of the Phase II trigger system is presented in Fig. 10.1, which includes the calorimeter trigger, muon trigger, track trigger, particle flow trigger (also known as the correlator trigger, or CT), and global trigger.

The particle flow trigger path is a new and central feature of the Phase II L1 trigger system design. The correlator trigger (CT) is composed of two layers, namely, the particle flow layer-1 and particle flow layer-2. The particle flow layer-1 generates particle-flow candidates by matching calorimeter clusters and tracks. The particle flow layer-2 constructs and sorts the final trigger objects while also applying additional identification and isolation criteria.

At the HL-LHC, it is extremely challenging to trigger signals with fully hadronic final states featuring soft jets. As an extension of searches for long-lived particles (LLPs), the Phase II L1 trigger system implements new paths designated for soft displaced and delayed jets to explore a completely new phase space for signals featuring exotic Higgs decays while keeping the rate at an acceptable level. The remainder of this section focuses on time-displaced calorimeter-based jets, targeting jet displacement between 50 cm and 150 cm. The signal model used is the exotic Higgs decay ($H \to ss, s \to \bar{b}b$, where s is the LLP).

The availability of precision timing information at the Phase II L1 trigger can significantly enhance our capability to tag LLP decays. Ref. [204] suggests that the delayed timing signature is among the best for triggering and background rejection for LLP lifetimes between 10 cm and 100 cm. In particular, for LLP lifetimes between 50 cm and 150 cm, when decays occur in the vicinity of the calorimeters away from the primary interaction vertex, timing information provides a unique signature to discriminate between signal and background. Both the barrel ECAL and HCAL subsystems will provide timing information to the L1 trigger, while the endcap HGCAL will not have this capability due to bandwidth constraints.

We investigate the potential of using the barrel ECAL timing information to trigger on LLP decays between 10 cm and 100 cm. The signal model considered is the most challenging one to trigger on, where the SM Higgs boson decays to two LLPs with a mass of 50 GeV, and each LLP decays to a pair of b-quarks. The jets produced in this model are relatively low in transverse momentum and peak around 20 to 30 GeV. Timestamps are reconstructed for calorimeter-based jets by averaging the measured timestamp of each ECAL trigger primitive (TP) comprising the jet, weighted by its measured energy.

Figure 10.2 shows how the single calorimeter-based jet trigger rate varies with signal efficiency for four different time delay requirements. Tighter timing requirements allow higher signal efficiencies to be achieved for a given background rate, because the requirements on jet p_T are less stringent. When a time delay of over 1 ns is required, the rate of a trigger with 20% signal efficiency is 25 kHz, while the rate of a trigger with 14% signal efficiency is 10 kHz.

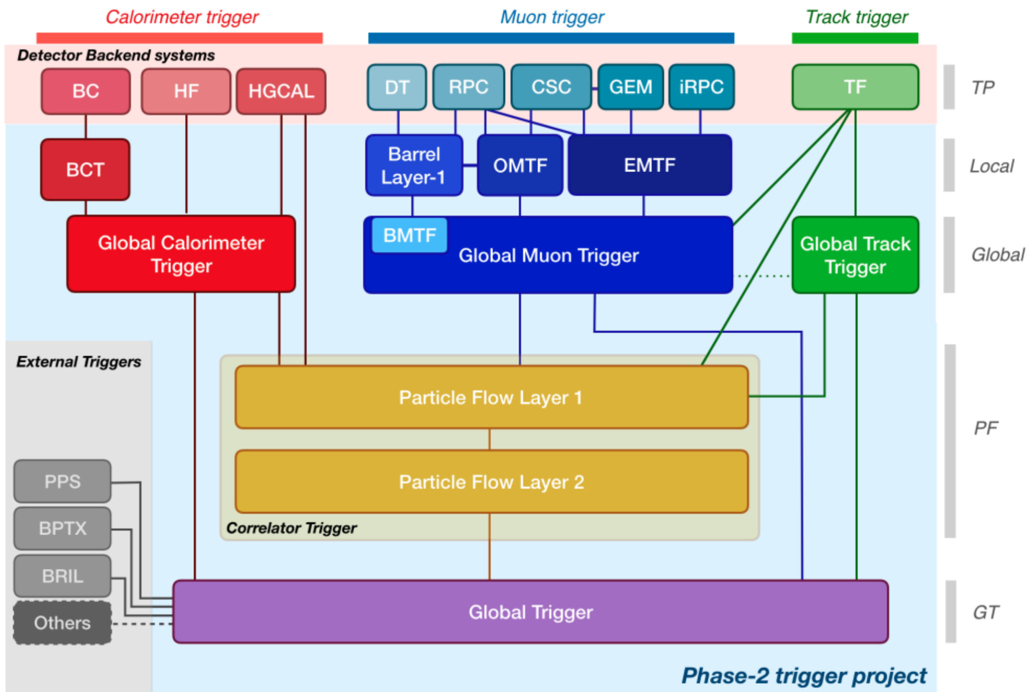

Figure 10.1: Functional diagram of the CMS L1 Phase-2 upgraded trigger design [203]. The Phase-2 L1 trigger receives inputs from the calorimeters, the muon spectrometers and the track finder. The calorimeter trigger inputs include inputs from the barrel calorimeter (BC), the high-granularity calorimeter (HGCAL) and the hadron forward calorimeter (HF). It is composed of a barrel calorimeter trigger (BCT) and a global calorimeter trigger (GCT). The muon trigger receives input from various detectors, including drift tubes (DT), resistive plate chambers (RPC), cathode strip chambers (CSC), and gas electron multipliers (GEM). It is composed of a barrel layer-1 processor and muon track finders processing data from three separate pseudorapidity regions and referred to as BMTF, OMTF and EMTF for barrel, overlap and endcap, respectively. The muon track finders transmit their muon candidates to the global muon trigger (GMT), where combination with tracking information is possible. The track finder (TF) provides tracks to various parts of the design including the global track trigger (GTT). The correlator trigger (CT) in the center (yellow area) is composed of two layers dedicated to particle-flow reconstruction. All objects are sent to the global trigger (GT) issuing the final L1 trigger decision. External triggers feeding into the GT are also shown including potential upscope (mentioned as “others”) such as inputs from the MTD. The dashed lines represent links that could be potentially exploited. The components under development within the Phase-2 L1 trigger project are grouped in the same area (blue area). The various levels of processing are indicated on the right: trigger primitives (TP), local and global trigger reconstruction, particle-flow trigger reconstruction (PF) and global decision.

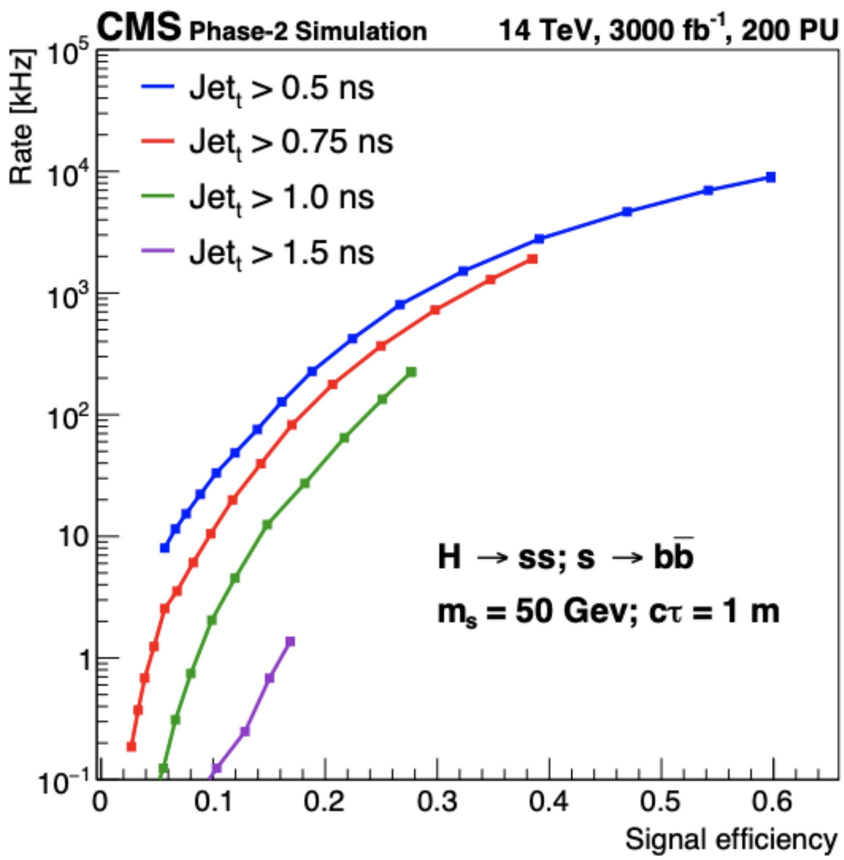

Figure 10.2: The rate of the proposed single time-displaced calorimeter-based jet seed is plotted against the signal efficiency for different requirements on the jet timestamp and p_{T}. A single calorimeter-based jet is required and the different curves represent different jet-time requirements. The points along the curve represent different requirements on the jet p_{T}, varying between 20–100 GeV. The signal model considered is SM Higgs boson production decaying to two scalar long-lived particles of mass 50 GeV, each decaying to a pair of b-quarks. The proper lifetime of the scalar is 1 m [203].

BIBLIOGRAPHY

[1] Symmetry Magazine. *The Standard Model of Particle Physics*. URL: https://www.symmetrymagazine.org/standard-model/.

[2] Julia Woithe, Gerfried J Wiener, and Frederik F Van der Veken. "Let's have a coffee with the Standard Model of particle physics!" In: *Phys. Educ.* 52.3 (2017), p. 034001. DOI: 10.1088/1361-6552/aa5b25. URL: https://cds.cern.ch/record/2848100.

[3] "Review of Particle Physics, 2012-2013. Review of Particle Properties". In: *Phys. Rev. D* 86.1 (2012). The 2012 edition of Review of Particle Physics is published for the Particle Data Group as article 010001 in volume 86 of Physical Review D. This edition should be cited as: J. Beringer et al. (Particle Data Group), Phys. Rev. D 86, 010001 (2012)., p. 010001. DOI: 10.1103/PhysRevD.86.010001. URL: https://cds.cern.ch/record/1481544.

[4] Lyndon Evans and Philip Bryant. "LHC Machine". In: *Journal of Instrumentation* 3.08 (Aug. 2008), S08001–S08001. DOI: 10.1088/1748-0221/3/08/s08001. URL: https://doi.org/10.1088/1748-0221/3/08/s08001.

[5] Esma Mobs. "The CERN accelerator complex. Complexe des accélérateurs du CERN". In: (July 2016). General Photo. URL: https://cds.cern.ch/record/2197559.

[6] J. P. Blewett. "200-GeV Intersecting Storage Accelerators". In: *eConf* C710920 (1971). Ed. by Myrtle Hildred Blewett and Nils Vogt-Nilsen, p. 501.

[7] Oliver Sim Brüning et al. *LHC Design Report*. CERN Yellow Reports: Monographs. Geneva: CERN, 2004. DOI: 10.5170/CERN-2004-003-V-1. URL: http://cds.cern.ch/record/782076.

[8] CMS Collaboration. *CMS Luminosity - Public Results*. URL: https://twiki.cern.ch/twiki/bin/view/CMSPublic/LumiPublicResults (visited on 08/09/2020).

[9] CMS Collaboration. "Measurement of the inelastic proton-proton cross section at $\sqrt{s} = 13$ TeV." In: *Journal of High Energy Physics* 07 (2018), p. 161. DOI: 10.1007/JHEP07(2018)161. arXiv: 1802.02613 [hep-ex].

[10] TOTEM Collaboration. "First measurement of elastic, inelastic and total cross-section at $\sqrt{s} = 13$ TeV by TOTEM and overview of cross-section data at LHC energies." In: *The European Physical Journal C* 79.103 (Feb. 2019). ISSN: 1434-6052. DOI: 10.1140/epjc/s10052-019-6567-0. arXiv: 1712.06153 [hep-ex]. URL: https://doi.org/10.1140/epjc/s10052-019-6567-0.

[11] T. Sakuma. "Cutaway diagrams of CMS detector." In: (May 2019). URL: http://cds.cern.ch/record/2665537.

[12] S. R. Davis. "Interactive slice of the CMS detector." In: (Aug. 2016). URL: https://cds.cern.ch/record/2205172.

[13] J. C. Lottin et al. "Conceptual design of the CMS 4 Tesla solenoid." In: *Advances in Cryogenic Engineering: Part A*. Ed. by Peter Kittel. Boston, MA: Springer US, 1996, pp. 819–826. ISBN: 978-1-4613-0373-2. DOI: 10.1007/978-1-4613-0373-2_106. URL: https://doi.org/10.1007/978-1-4613-0373-2_106.

[14] F. Kircher et al. "Final design of the CMS solenoid cold mass." In: *16th International Conference on Magnet Technology (MT-16)*. Oct. 1999.

[15] S. Chatrchyan et al. "The CMS Experiment at the CERN LHC". In: *JINST* 3 (2008), S08004. DOI: 10.1088/1748-0221/3/08/S08004.

[16] Alain Hervé. "The CMS detector magnet". In: *IEEE transactions on applied superconductivity* 10.1 (2000), pp. 389–394.

[17] CMS Collaboration. "Precise Mapping of the Magnetic Field in the CMS Barrel Yoke using Cosmic Rays." In: *Journal of Instrumentation* 5.03 (Mar. 2010), T03021–T03021. ISSN: 1748-0221. DOI: 10.1088/1748-0221/5/03/t03021. arXiv: 0910.5530 [physics.ins-det]. URL: http://dx.doi.org/10.1088/1748-0221/5/03/T03021.

[18] V. Karimäki et al. *The CMS tracker system project: technical design report.* Technical Design Report CMS. Geneva: CERN, 1997. URL: https://cds.cern.ch/record/368412.

[19] S. Spannagel. *Status of the CMS Phase I Pixel detector upgrade*. Tech. rep. CMS-CR-2015-272. CMS-CR-2015-272. Geneva: CERN, Oct. 2015. DOI: 10.1016/j.nima.2016.03.028. URL: https://cds.cern.ch/record/2102893.

[20] *Sketches of the CMS Tracker Detector*. URL: https://twiki.cern.ch/twiki/bin/view/CMSPublic/DPGResultsTRK (visited on 08/26/2020).

[21] *Tracker Material Budget plots*. URL: https://twiki.cern.ch/twiki/bin/view/CMSPublic/TrackerMaterialBudgetplots (visited on 08/26/2020).

[22] A Dominguez et al. *CMS Technical Design Report for the Pixel Detector Upgrade*. Tech. rep. Additional contacts: Jeffrey Spalding, Fermilab, Jeffrey.Spalding@cern.ch Didier Contardo, Universite Claude Bernard-Lyon I, didier.claude.contardo@cern.ch. Sept. 2012. URL: https://cds.cern.ch/record/1481838.

[23] CMS Collaboration. "Particle-flow reconstruction and global event description with the CMS detector." In: *Journal of Instrumentation* 12.10 (Oct. 2017), P10003–P10003. ISSN: 1748-0221. DOI: 10.1088/1748-0221/12/10/p10003. arXiv: 1706.04965 [physics.ins-det]. URL: http://dx.doi.org/10.1088/1748-0221/12/10/P10003.

[24] *The CMS electromagnetic calorimeter project: Technical Design Report*. Technical design report. CMS. Geneva: CERN, 1997. URL: https://cds.cern.ch/record/349375.

[25] S Baccaro et al. *Radiation damage effect on avalanche photodiodes*. Tech. rep. Geneva: CERN, Apr. 1998. DOI: 10.1016/S0168-9002(98)01493-4. URL: https://cds.cern.ch/record/395153.

[26] Z Antunovic et al. "Radiation hard avalanche photodiodes for the CMS detector". In: *Nucl. Instrum. Methods Phys. Res., A* 537 (2005), pp. 379–382. DOI: 10.1016/j.nima.2004.08.047. URL: https://cds.cern.ch/record/903007.

[27] K.W. Bell et al. "Vacuum phototriodes for the CMS electromagnetic calorimeter endcap". In: *IEEE Transactions on Nuclear Science* 51.5 (2004), pp. 2284–2287. DOI: 10.1109/TNS.2004.836053.

[28] CMS Collaboration. *CMS physics: Technical design report Volume 1: Detector performance and software*. CMS Technical Design Report CERN-LHCC-2006-001. 2006. URL: http://cds.cern.ch/record/922757.

[29] Adolf Bornheim. "The CMS ECAL Laser Monitoring System". In: *AIP Conference Proceedings* 867.1 (Oct. 2006). ISSN: 0094-243X. DOI: 10.1063/1.2396979. URL: https://www.osti.gov/biblio/20891892.

[30] Serguei Chatrchyan et al. "Energy Calibration and Resolution of the CMS Electromagnetic Calorimeter in pp Collisions at $\sqrt{s} = 7$ TeV". In: *JINST* 8 (2013), P09009. DOI: 10.1088/1748-0221/8/09/P09009. arXiv: 1306.2016 [hep-ex].

[31] "CMS ECAL Response to Laser Light". In: (Mar. 2019). URL: https://cds.cern.ch/record/2668200.

[32] "ECAL 2016 refined calibration and Run2 summary plots". In: (Apr. 2020). URL: https://cds.cern.ch/record/2717925.

[33] Daniele Re. "Timing performance of the CMS ECAL and prospects for the future". In: *Journal of Physics: Conference Series* 587 (Feb. 2015). DOI: 10.1088/1742-6596/587/1/012003.

[34] "Performance of electron and photon reconstruction in Run 2 with the CMS experiment". In: (July 2020). URL: https://cds.cern.ch/record/2725004.

[35] *Technical proposal*. LHC technical proposal. Cover title : CMS, the Compact Muon Solenoid : technical proposal. Geneva: CERN, 1994. URL: http://cds.cern.ch/record/290969.

[36] *The CMS hadron calorimeter project: Technical Design Report*. Technical design report. CMS. Geneva: CERN, 1997. URL: https://cds.cern.ch/record/357153.

[37] *The CMS Barrel Calorimeter Response to Particle Beams from 2 to 350 GeV/c*. Tech. rep. Geneva: CERN, June 2008. URL: https://cds.cern.ch/record/1166316.

[38] Andrea Perrotta. "CMS event reconstruction status in Run 2". In: *EPJ Web Conf.* 214 (2019), 02015. 8 p. DOI: 10.1051/epjconf/201921402015. URL: https://cds.cern.ch/record/2728524.

[39] N Strobbe. "The upgrade of the CMS hadron calorimeter with silicon photomultipliers. The upgrade of the CMS hadron calorimeter with silicon 5 photomultipliers". In: *JINST* 12 (2017), C01080. 8 p. DOI: 10.1088/1748-0221/12/01/C01080. URL: http://cds.cern.ch/record/2291316.

[40] Federico Guio. "First results from the CMS SiPM-based hadronic endcap calorimeter". In: *Journal of Physics: Conference Series* 1162 (Jan. 2019), p. 012009. DOI: 10.1088/1742-6596/1162/1/012009.

[41] A. M. Sirunyan et al. "Performance of the CMS muon detector and muon reconstruction with proton-proton collisions at $\sqrt{s} = 13$ TeV". In: *JINST* 13.06 (2018), P06015. DOI: 10.1088/1748-0221/13/06/P06015. arXiv: 1804.04528 [physics.ins-det].

[42] J. G. Layter. *The CMS muon project: Technical Design Report*. Technical design report. CMS. Geneva: CERN, 1997. URL: https://cds.cern.ch/record/343814.

[43] *The Phase-2 Upgrade of the CMS Muon Detectors*. Tech. rep. This is the final version, approved by the LHCC. Geneva: CERN, Sept. 2017. URL: https://cds.cern.ch/record/2283189.

[44] *CMS TriDAS project: Technical Design Report, Volume 1: The Trigger Systems*. Technical design report. CMS. URL: https://cds.cern.ch/record/706847.

[45] Sergio Cittolin, Attila Rácz, and Paris Sphicas. *CMS The TriDAS Project: Technical Design Report, Volume 2: Data Acquisition and High-Level Trigger. CMS trigger and data-acquisition project*. Technical design report. CMS. Geneva: CERN, 2002. URL: http://cds.cern.ch/record/578006.

[46] A Tapper and Darin Acosta. *CMS Technical Design Report for the Level-1 Trigger Upgrade*. Tech. rep. Additional contacts: Jeffrey Spalding, Fermilab, Jeffrey.Spalding@cern.ch Didier Contardo, Universite Claude Bernard-Lyon I, didier.claude.contardo@cern.ch. June 2013. URL: https://cds.cern.ch/record/1556311.

[47] Alexandre Zabi et al. *The CMS Level-1 Calorimeter Trigger for LHC Run II*. Tech. rep. Geneva: CERN, Nov. 2016. DOI: 10.1088/1748-0221/12/01/C01065. URL: https://cds.cern.ch/record/2233176.

[48] B. Kreis et al. “Run 2 Upgrades to the CMS Level-1 Calorimeter Trigger”. In: *JINST* 11.01 (2016), p. C01051. DOI: 10.1088/1748-0221/11/01/C01051. arXiv: 1511.05855 [physics.ins-det].

[49] N Amapane. *The CMS Muon Trigger System*. Tech. rep. Geneva: CERN, Nov. 2003. URL: https://cds.cern.ch/record/785537.

[50] *Xilinx Virtex-7 FPGA*. URL: https://www.xilinx.com/products/silicon-devices/fpga/virtex-7.html.

[51] Albert M Sirunyan et al. “Performance of the CMS Level-1 trigger in proton-proton collisions at $\sqrt{s} = 13$ TeV”. In: *JINST* 15.10 (2020), P10017. DOI: 10.1088/1748-0221/15/10/P10017. arXiv: 2006.10165 [hep-ex].

[52] Mia Tosi. “The CMS trigger in Run 2”. In: *PoS* EPS-HEP2017 (2017), p. 523. DOI: 10.22323/1.314.0523.

[53] Mia Tosi. “Tracking at High Level Trigger in CMS”. In: *Nucl. Part. Phys. Proc.* 273-275 (2016). Ed. by M Aguilar-Benıtez et al., pp. 2494–2496. DOI: 10.1016/j.nuclphysbps.2015.09.436.

[54] Serguei Chatrchyan et al. “Description and performance of track and primary-vertex reconstruction with the CMS tracker”. In: *JINST* 9.10 (2014), P10009. DOI: 10.1088/1748-0221/9/10/P10009. arXiv: 1405.6569 [physics.ins-det].

[55] A. M. Sirunyan et al. “Particle-flow reconstruction and global event description with the CMS detector”. In: *JINST* 12.10 (2017), P10003. DOI: 10.1088/1748-0221/12/10/P10003. arXiv: 1706.04965 [physics.ins-det].

[56] Andrea Perrotta. *Performance of the CMS High Level Trigger*. Tech. rep. Geneva: CERN, May 2015. DOI: 10.1088/1742-6596/664/8/082044. URL: https://cds.cern.ch/record/2061511.

[57] CMS Collaboration. *Plots approved for CHEP2016, San Francisco*. URL: https://twiki.cern.ch/twiki/bin/view/CMSPublic/HLTplotsCHEP2016.

[58] “The Grid: A system of tiers”. In: (Aug. 2012). URL: https://cds.cern.ch/record/1997396.

[59] “The LHC’s worldwide computer”. In: (Mar. 2013). URL: https://cerncourier.com/a/the-lhcs-worldwide-computer/.

[60] G L Bayatyan et al. *CMS computing: Technical Design Report*. Technical design report. CMS. Submitted on 31 May 2005. Geneva: CERN, 2005. URL: https://cds.cern.ch/record/838359.

[61] K. Bos et al. *LHC computing Grid: Technical Design Report. Version 1.06 (20 Jun 2005)*. Technical design report. LCG. Geneva: CERN, 2005. URL: https://cds.cern.ch/record/840543.

[62] Maurizio Monaco et al. "Phenomenology of minimal unified tree level gauge mediation at the LHC". In: *JHEP* 07 (2013), p. 078. DOI: 10.1007/JHEP07(2013)078. arXiv: 1302.1305 [hep-ph].

[63] J. Duarte et al. "Squark-mediated Higgs+jets production at the LHC". 2017. arXiv: 1703.06544 [hep-ph].

[64] Savas Dimopoulos and Howard Georgi. "Softly Broken Supersymmetry and SU(5)". In: *Nucl. Phys. B* 193 (1981), p. 150. DOI: 10.1016/0550-3213(81)90522-8.

[65] Savas Dimopoulos et al. "Experimental signatures of low-energy gauge mediated supersymmetry breaking". In: *Phys. Rev. Lett.* 76 (1996), p. 3494. DOI: 10.1103/PhysRevLett.76.3494. arXiv: hep-ph/9601367 [hep-ph].

[66] Konstantin T. Matchev and Scott D. Thomas. "Higgs and Z boson signatures of supersymmetry". In: *Phys. Rev. D* 62 (2000), p. 077702. DOI: 10.1103/PhysRevD.62.077702. arXiv: hep-ph/9908482 [hep-ph].

[67] Georges Aad et al. "Search for direct pair production of a chargino and a neutralino decaying to the 125 GeV Higgs boson in $\sqrt{s} = 8$ TeV pp collisions with the ATLAS detector". In: *Eur. Phys. J. C* 75 (2015), p. 208. DOI: 10.1140/epjc/s10052-015-3408-7. arXiv: 1501.07110 [hep-ex].

[68] Vardan Khachatryan et al. "Searches for electroweak neutralino and chargino production in channels with Higgs, Z, and W bosons in pp collisions at 8 TeV". In: *Phys. Rev. D* 90 (2014), p. 092007. DOI: 10.1103/PhysRevD.90.092007. arXiv: 1409.3168 [hep-ex].

[69] Albert M Sirunyan et al. "Search for supersymmetry with Higgs boson to diphoton decays using the razor variables at $\sqrt{s} = 13$ TeV". In: *Phys. Lett. B* 779 (2018), p. 166. DOI: 10.1016/j.physletb.2017.12.069. arXiv: 1709.00384 [hep-ex].

[70] Morad Aaboud et al. "Search for chargino and neutralino production in final states with a Higgs boson and missing transverse momentum at $\sqrt{s} = 13$ TeV with the ATLAS detector". In: *Phys. Rev.* D100.1 (2019), p. 012006. DOI: 10.1103/PhysRevD.100.012006. arXiv: 1812.09432 [hep-ex].

[71] Morad Aaboud et al. "Search for bottom-squark pair production with the ATLAS detector in final states containing Higgs bosons, b-jets and missing transverse momentum". Submitted to: JHEP. 2019. arXiv: 1908.03122 [hep-ex].

[72] M. Aaboud et al. "Search for pair production of higgsinos in final states with at least three b-tagged jets in $\sqrt{s}$ = 13 TeV pp collisions using the ATLAS detector". In: *Phys. Rev. D* 98.9 (2018), p. 092002. DOI: 10.1103/PhysRevD.98.092002. arXiv: 1806.04030 [hep-ex].

[73] CMS Collaboration. "Search for supersymmetry using Higgs boson to diphoton decays at \sqrt{s} = 13 TeV". In: *Journal of High Energy Physics* 2019.11 (Nov. 2019). DOI: 10.1007/jhep11(2019)109. URL: https://doi.org/10.1007%2Fjhep11%282019%29109.

[74] J. Alwall et al. "The automated computation of tree-level and next-to-leading order differential cross sections, and their matching to parton shower simulations". In: *JHEP* 07 (2014), p. 079. DOI: 10.1007/JHEP07(2014)079. arXiv: 1405.0301 [hep-ph].

[75] ATLAS and CMS Collaborations. "Combined Measurement of the Higgs Boson Mass in pp Collisions at $\sqrt{s}$ = 7 and 8 TeV with the ATLAS and CMS Experiments". In: *Phys. Rev. Lett.* 114 (2015), p. 191803. DOI: 10.1103/PhysRevLett.114.191803. arXiv: 1503.07589 [hep-ex].

[76] Albert M Sirunyan et al. "Measurements of properties of the Higgs boson decaying into the four-lepton final state in pp collisions at $\sqrt{s}$ = 13 TeV". In: *JHEP* 11 (2017), p. 047. DOI: 10.1007/JHEP11(2017)047. arXiv: 1706.09936 [hep-ex].

[77] D. de Florian et al. *Handbook of LHC Higgs cross sections: 4. Deciphering the nature of the Higgs sector*. CERN Report CERN-2017-002-M. 2016. DOI: 10.23731/CYRM-2017-002. arXiv: 1610.07922 [hep-ph].

[78] Rikkert Frederix and Stefano Frixione. "Merging meets matching in MC@NLO". In: *JHEP* 12 (2012), p. 061. DOI: 10.1007/JHEP12(2012)061. arXiv: 1209.6215 [hep-ph].

[79] J. Alwall et al. "Comparative study of various algorithms for the merging of parton showers and matrix elements in hadronic collisions". In: *Eur. Phys. J. C* 53 (2008), p. 473. DOI: 10.1140/epjc/s10052-007-0490-5. arXiv: 0706.2569 [hep-ph].

[80] Torbjörn Sjöstrand et al. "An Introduction to PYTHIA 8.2". In: *Comput. Phys. Commun.* 191 (2015), p. 159. DOI: 10.1016/j.cpc.2015.01.024. arXiv: 1410.3012 [hep-ph].

[81] P. Skands, S. Carrazza, and J. Rojo. "Tuning PYTHIA 8.1: the Monash 2013 tune". In: *Eur. Phys. J. C* 74 (2014), p. 3024. DOI: 10.1140/epjc/s10052-014-3024-y.

[82] Albert M Sirunyan et al. "Extraction and validation of a new set of CMS PYTHIA8 tunes from underlying-event measurements". Submitted to EPJC. 2019. arXiv: 1903.12179 [hep-ex].

[83] Richard D. Ball et al. "Parton distributions for the LHC Run II". In: *JHEP* 04 (2015), p. 040. DOI: 10.1007/JHEP04(2015)040. arXiv: 1410.8849 [hep-ph].

[84] Richard D. Ball et al. "Parton distributions from high-precision collider data". In: *Eur. Phys. J. C* 77 (2017), p. 663. DOI: 10.1140/epjc/s10052-017-5199-5. arXiv: 1706.00428 [hep-ph].

[85] W. Beenakker et al. "Squark and gluino production at hadron colliders". In: *Nucl. Phys. B* 492 (1997), p. 51. DOI: 10.1016/S0550-3213(97)80027-2. arXiv: hep-ph/9610490 [hep-ph].

[86] A. Kulesza and L. Motyka. "Threshold resummation for squark-antisquark and gluino-pair production at the LHC". In: *Phys. Rev. Lett.* 102 (2009), p. 111802. DOI: 10.1103/PhysRevLett.102.111802. arXiv: 0807.2405 [hep-ph].

[87] A. Kulesza and L. Motyka. "Soft gluon resummation for the production of gluino-gluino and squark-antisquark pairs at the LHC". In: *Phys. Rev. D* 80 (2009), p. 095004. DOI: 10.1103/PhysRevD.80.095004. arXiv: 0905.4749 [hep-ph].

[88] W. Beenakker et al. "Soft-gluon resummation for squark and gluino hadroproduction". In: *JHEP* 12 (2009), p. 041. DOI: 10.1088/1126-6708/2009/12/041. arXiv: 0909.4418 [hep-ph].

[89] W. Beenakker et al. "Squark and gluino hadroproduction". In: *Int. J. Mod. Phys. A* 26 (2011), p. 2637. DOI: 10.1142/S0217751X11053560. arXiv: 1105.1110 [hep-ph].

[90] C. Borschensky et al. "Squark and gluino production cross sections in pp collisions at $\sqrt{s}$ = 13, 14, 33 and 100 TeV". In: *Eur. Phys. J. C* 74 (2014), p. 3174. DOI: 10.1140/epjc/s10052-014-3174-y. arXiv: 1407.5066 [hep-ph].

[91] W. Beenakker et al. "Production of Charginos, Neutralinos, and Sleptons at Hadron Colliders". In: *Phys. Rev. Lett.* 83 (1999). [Erratum: 10.1103/PhysRevLett.100.029901], p. 3780. DOI: 10.1103/PhysRevLett.83.3780. arXiv: hep-ph/9906298 [hep-ph].

[92] Benjamin Fuks et al. "Gaugino production in proton-proton collisions at a center-of-mass energy of 8 TeV". In: *JHEP* 10 (2012), p. 081. DOI: 10.1007/JHEP10(2012)081. arXiv: 1207.2159 [hep-ph].

[93] Benjamin Fuks et al. "Precision predictions for electroweak superpartner production at hadron colliders with RESUMMINO". In: *Eur. Phys. J. C* 73 (2013), p. 2480. DOI: 10.1140/epjc/s10052-013-2480-0. arXiv: 1304.0790 [hep-ph].

[94] Peter Z. Skands et al. "SUSY Les Houches accord: interfacing SUSY spectrum calculators, decay packages, and event generators". In: *JHEP* 07 (2004), p. 036. DOI: 10.1088/1126-6708/2004/07/036. Arxiv: Hep-Ph/0311123 (hep-Ph).

[95] S. Agostinelli et al. "GEANT4—a simulation toolkit". In: *Nucl. Instrum. Meth. A* 506 (2003), p. 250. DOI: 10.1016/S0168-9002(03)01368-8.

[96] S. Abdullin et al. "The fast simulation of the CMS detector at LHC". In: *J. Phys. Conf. Ser.* 331 (2011), p. 032049. DOI: 10.1088/1742-6596/331/3/032049.

[97] Andrea Giammanco. "The fast simulation of the CMS experiment". In: *J. Phys. Conf. Ser.* 513 (2014), p. 022012. DOI: 10.1088/1742-6596/513/2/022012.

[98] Serguei Chatrchyan et al. "Search for top-squark pair production in the single-lepton final state in pp collisions at $\sqrt{s} = 8$ TeV". In: *Eur. Phys. J. C* 73.12 (2013), p. 2677. DOI: 10.1140/epjc/s10052-013-2677-2. arXiv: 1308.1586 [hep-ex].

[99] Matteo Cacciari, Gavin P. Salam, and Gregory Soyez. "The anti-k_t jet clustering algorithm". In: *JHEP* 04 (2008), p. 063. DOI: 10.1088/1126-6708/2008/04/063. arXiv: 0802.1189 [hep-ph].

[100] *https://twiki.cern.ch/twiki/bin/view/CMSPublic/SWGuideMuonId*. URL: https://twiki.cern.ch/twiki/bin/view/CMSPublic/SWGuideMuonId.

[101] CMS Collaboration. "Particle-flow reconstruction and global event description with the CMS detector. Particle-flow reconstruction and global event description with the CMS detector". In: *JINST* 12 (June 2017). Replaced with the published version. Added the journal reference and DOI. All the figures and tables can be found at http://cms-results.web.cern.ch/cms-results/public-results/publications/PRF-14-001 (CMS Public Pages), P10003. 82 p. DOI: 10.1088/1748-0221/12/10/P10003. arXiv: 1706.04965. URL: https://cds.cern.ch/record/2270046.

[102] C Magliocca. "Measurement of the track impact parameters resolution with the ATLAS experiment at LHC using 2016-2018 data". In: *Nuovo Cimento C* 44 (2021), 55. 4 p. DOI: 10.1393/ncc/i2021-21055-0. URL: https://cds.cern.ch/record/2791559.

[103] Vardan Khachatryan et al. "Performance of photon reconstruction and identification with the CMS detector in proton-proton collisions at $\sqrt{s} = 8$ TeV". In: *JINST* 10.08 (2015), P08010. DOI: 10.1088/1748-0221/10/08/P08010. arXiv: 1502.02702 [physics.ins-det].

[104] Matteo Cacciari, Gavin P. Salam, and Gregory Soyez. "The anti-k_{T} jet clustering algorithm". In: *JHEP* 04 (2008), p. 063. DOI: 10.1088/1126-6708/2008/04/063. arXiv: 0802.1189 [hep-ph].

[105] Matteo Cacciari, Gavin P. Salam, and Gregory Soyez. "FastJet user manual". In: *Eur. Phys. J. C* 72 (2012), p. 1896. DOI: 10.1140/epjc/s10052-012-1896-2. arXiv: 1111.6097 [hep-ph].

[106] *https://twiki.cern.ch/twiki/bin/view/CMS/JetID*. URL: https://twiki.cern.ch/twiki/bin/view/CMS/JetID.

[107] Serguei Chatrchyan et al. "Identification of b-quark jets with the CMS experiment". In: *JINST* 8 (2013), P04013. DOI: 10.1088/1748-0221/8/04/P04013. arXiv: 1211.4462 [hep-ex].

[108] Serguei Chatrchyan et al. "Missing transverse energy performance of the CMS detector". In: *JINST* 6 (2011), P09001. DOI: 10.1088/1748-0221/6/09/P09001. arXiv: 1106.5048 [physics.ins-det].

[109] Christopher Rogan. "Kinematical variables towards new dynamics at the LHC". 2010. arXiv: 1006.2727 [hep-ph].

[110] Vardan Khachatryan et al. "Inclusive search for supersymmetry using razor variables in pp collisions at $\sqrt{s}$ = 13 TeV". In: *Phys. Rev. D* 95 (2017), p. 012003. DOI: 10.1103/PhysRevD.95.012003. arXiv: 1609.07658 [hep-ex].

[111] H. Akaike. "A new look at the statistical model identification". In: *IEEE Transactions on Automatic Control* 19-6 (1974), p. 716. DOI: 10.1109/TAC.1974.1100705.

[112] M. J. Oreglia. "A study of the reactions $\psi' \to \gamma\gamma\psi$". SLAC Report SLAC-R-236, see Appendix D. PhD thesis. Stanford University, 1980. URL: http://www.slac.stanford.edu/pubs/slacreports/slac-r-236.html.

[113] J. Gaiser. "Charmonium Spectroscopy From Radiative Decays of the J/ψ and ψ'". PhD thesis. SLAC, 1982. URL: http://www-public.slac.stanford.edu/sciDoc/docMeta.aspx?slacPubNumber=slac-r-255.html.

[114] Alexis Kalogeropoulos and Johan Alwall. "The SysCalc code: A tool to derive theoretical systematic uncertainties". 2018. arXiv: 1801.08401 [hep-ph].

[115] Jon Butterworth et al. "PDF4LHC recommendations for LHC Run II". In: *J. Phys. G* 43 (2016), p. 023001. DOI: 10.1088/0954-3899/43/2/023001. arXiv: 1510.03865 [hep-ph].

[116] Glen Cowan et al. "Asymptotic formulae for likelihood-based tests of new physics". In: *Eur. Phys. J. C* 71 (2011). [Erratum: 10.1140/epjc/s10052-013-2501-z], p. 1554. DOI: 10.1140/epjc/s10052-011-1554-0. arXiv: 1007.1727 [physics.data-an].

[117] Thomas Junk. "Confidence level computation for combining searches with small statistics". In: *Nucl. Instrum. Meth. A* 434 (1999), p. 435. DOI: 10.1016/S0168-9002(99)00498-2. arXiv: hep-ex/9902006 [hep-ex].

[118] Alexander L. Read. “Presentation of search results: The CL_s technique”. In: *J. Phys. G* 28 (2002), p. 2693. DOI: 10.1088/0954-3899/28/10/313.

[119] ATLAS and CMS Collaborations. *Procedure for the LHC Higgs boson search combination in summer 2011*. Tech. rep. ATL-PHYS-PUB-2011-011, CMS-NOTE-2011-005. 2011. URL: http://cds.cern.ch/record/1379837.

[120] CMS Collaboration. “Combined search for electroweak production of charginos and neutralinos in proton-proton collisions at \sqrt{s}=13 TeV”. In: *Journal of High Energy Physics* 2018.3 (Mar. 2018). DOI: 10.1007/jhep03(2018)160. URL: https://doi.org/10.1007%5C%2Fjhep03%5C%282018%5C%29160.

[121] G. F. Giudice and R. Rattazzi. “Theories with gauge mediated supersymmetry breaking”. In: *Phys. Rept.* 322 (1999), p. 419. DOI: 10.1016/S0370-1573(99)00042-3. arXiv: hep-ph/9801271 [hep-ph].

[122] Patrick Meade, Nathan Seiberg, and David Shih. “General gauge mediation”. In: *Prog. Theor. Phys. Suppl.* 177 (2009), p. 143. DOI: 10.1143/PTPS.177.143. arXiv: 0801.3278 [hep-ph].

[123] Matthew Buican et al. “Exploring general gauge mediation”. In: *JHEP* 03 (2009), p. 016. DOI: 10.1088/1126-6708/2009/03/016. arXiv: 0812.3668 [hep-ph].

[124] G. F. Giudice and A. Romanino. “Split supersymmetry”. In: *Nucl. Phys. B* 699 (2004). [Erratum: 10.1016/j.nuclphysb.2004.11.048], p. 65. DOI: 10.1016/j.nuclphysb.2004.08.001. arXiv: hep-ph/0406088 [hep-ph].

[125] JoAnne L. Hewett et al. “Signatures of long-lived gluinos in split supersymmetry”. In: *JHEP* 09 (2004), p. 070. DOI: 10.1088/1126-6708/2004/09/070. arXiv: hep-ph/0408248 [hep-ph].

[126] N. Arkani-Hamed et al. “Aspects of split supersymmetry”. In: *Nucl. Phys. B* 709 (2005), p. 3. DOI: 10.1016/j.nuclphysb.2004.12.026. arXiv: hep-ph/0409232 [hep-ph].

[127] P. Gambino, G. F. Giudice, and P. Slavich. “Gluino decays in split supersymmetry”. In: *Nucl. Phys. B* 726 (2005), p. 35. DOI: 10.1016/j.nuclphysb.2005.08.011. arXiv: hep-ph/0506214 [hep-ph].

[128] Asimina Arvanitaki et al. “Mini-Split”. In: *JHEP* 02 (2013), p. 126. DOI: 10.1007/JHEP02(2013)126. arXiv: 1210.0555 [hep-ph].

[129] Nima Arkani-Hamed et al. “Simply unnatural supersymmetry”. 2012. arXiv: 1212.6971 [hep-ph].

[130] Pierre Fayet. “Supergauge invariant extension of the Higgs mechanism and a model for the electron and its neutrino”. In: *Nucl. Phys. B* 90 (1975), p. 104. DOI: 10.1016/0550-3213(75)90636-7.

[131] Glennys R. Farrar and Pierre Fayet. "Phenomenology of the production, decay, and detection of new hadronic states associated with supersymmetry". In: *Phys. Lett. B* 76 (1978), p. 575. DOI: 10.1016/0370-2693(78)90858-4.

[132] Steven Weinberg. "Supersymmetry at ordinary energies. Masses and conservation laws". In: *Phys. Rev. D* 26 (1982), p. 287. DOI: 10.1103/PhysRevD.26.287.

[133] R. Barbier et al. "*R*-parity violating supersymmetry". In: *Phys. Rept.* 420 (2005), p. 1. DOI: 10.1016/j.physrep.2005.08.006. arXiv: hep-ph/0406039 [hep-ph].

[134] Matthew J. Strassler and Kathryn M. Zurek. "Echoes of a hidden valley at hadron colliders". In: *Phys. Lett. B* 651 (2007), p. 374. DOI: 10.1016/j.physletb.2007.06.055. arXiv: hep-ph/0604261 [hep-ph].

[135] Matthew J. Strassler and Kathryn M. Zurek. "Discovering the Higgs through highly-displaced vertices". In: *Phys. Lett. B* 661 (2008), p. 263. DOI: 10.1016/j.physletb.2008.02.008. arXiv: hep-ph/0605193 [hep-ph].

[136] Tao Han et al. "Phenomenology of hidden valleys at hadron colliders". In: *JHEP* 07 (2008), p. 008. DOI: 10.1088/1126-6708/2008/07/008. arXiv: 0712.2041 [hep-ph].

[137] Yanou Cui, Lisa Randall, and Brian Shuve. "A WIMPy baryogenesis miracle". In: *JHEP* 04 (2012), p. 075. DOI: 10.1007/JHEP04(2012)075. arXiv: 1112.2704 [hep-ph].

[138] Yanou Cui and Raman Sundrum. "Baryogenesis for weakly interacting massive particles". In: *Phys. Rev. D* 87 (2013), p. 116013. DOI: 10.1103/PhysRevD.87.116013. arXiv: 1212.2973 [hep-ph].

[139] Yanou Cui and Brian Shuve. "Probing baryogenesis with displaced vertices at the LHC". In: *JHEP* 02 (2015), p. 049. DOI: 10.1007/JHEP02(2015)049. arXiv: 1409.6729 [hep-ph].

[140] David Smith and Neal Weiner. "Inelastic dark matter". In: *Phys. Rev. D* 64 (2001), p. 043502. DOI: 10.1103/PhysRevD.64.043502. arXiv: hep-ph/0101138.

[141] Z. Chacko, Hock-Seng Goh, and Roni Harnik. "Natural electroweak breaking from a mirror symmetry". In: *Phys. Rev. Lett.* 96 (2006), p. 231802. DOI: 10.1103/PhysRevLett.96.231802. arXiv: hep-ph/0506256 [hep-ph].

[142] David Curtin and Christopher B. Verhaaren. "Discovering uncolored naturalness in exotic Higgs decays". In: *JHEP* 12 (2015), p. 072. DOI: 10.1007/JHEP12(2015)072. arXiv: 1506.06141 [hep-ph].

[143] Hsin-Chia Cheng et al. "Exotic quarks in twin Higgs models". In: *JHEP* 03 (2016), p. 074. DOI: 10.1007/JHEP03(2016)074. arXiv: 1512.02647 [hep-ph].

[144] Jia Liu, Zhen Liu, and Lian-Tao Wang. "Enhancing Long-Lived Particles Searches at the LHC with Precision Timing Information". In: *Physical Review Letters* 122.13 (Apr. 2019). DOI: 10.1103/physrevlett.122.131801. URL: https://doi.org/10.1103%2Fphysrevlett.122.131801.

[145] Albert M Sirunyan et al. "Search for long-lived particles using displaced jets in proton-proton collisions at $\sqrt{s} = 13\,\text{TeV}$". In: *Phys. Rev. D* 104 (2021), p. 012015. DOI: 10.1103/PhysRevD.104.012015. arXiv: 2012.01581 [hep-ex].

[146] Morad Aaboud et al. "Search for long-lived, massive particles in events with displaced vertices and missing transverse momentum in $\sqrt{s} = 13$ TeV pp collisions with the ATLAS detector". In: *Phys. Rev. D* 97.5 (2018), p. 052012. DOI: 10.1103/PhysRevD.97.052012. arXiv: 1710.04901 [hep-ex].

[147] Georges Aad et al. "Search for events with a pair of displaced vertices from long-lived neutral particles decaying into hadronic jets in the ATLAS muon spectrometer in pp collisions at $\sqrt{s} = 13$ TeV". In: (Mar. 2022). arXiv: 2203.00587 [hep-ex].

[148] Armen Tumasyan et al. "Search for Long-Lived Particles Decaying in the CMS End Cap Muon Detectors in Proton-Proton Collisions at $\sqrt{s} = 13$ TeV". In: *Phys. Rev. Lett.* 127 (2021), p. 261804. DOI: 10.1103/PhysRevLett.127.261804. arXiv: 2107.04838 [hep-ex].

[149] Albert M Sirunyan et al. "Search for long-lived particles using nonprompt jets and missing transverse momentum with proton-proton collisions at $\sqrt{s} = 13\,\text{TeV}$". In: *Phys. Lett. B* 797 (2019), p. 134876. DOI: 10.1016/j.physletb.2019.134876. arXiv: 1906.06441 [hep-ex].

[150] Stefan Hoeche et al. "Matching Parton Showers and Matrix Elements". 2006. arXiv: hep-ph/0602031.

[151] A. M. Sirunyan et al. "Combined search for electroweak production of charginos and neutralinos in proton-proton collisions at $\sqrt{s} = 13\,\text{TeV}$". In: *JHEP* 03 (2018), p. 160. DOI: 10.1007/JHEP03(2018)160. arXiv: 1801.03957 [hep-ex].

[152] Albert M Sirunyan et al. "Search for supersymmetry with Higgs boson to diphoton decays using the razor variables at $\sqrt{s} = 13\,\text{TeV}$". In: *Phys. Lett. B* 779 (2018), p. 166. DOI: 10.1016/j.physletb.2017.12.069. arXiv: 1709.00384 [hep-ex].

[153] V. Khachatryan et al. "Event generator tunes obtained from underlying event and multiparton scattering measurements". In: *Eur. Phys. J. C* 76 (2016), p. 155. DOI: 10.1140/epjc/s10052-016-3988-x. arXiv: 1512.00815 [hep-ex].

[154] Albert M Sirunyan et al. "Extraction and validation of a new set of CMS PYTHIA8 tunes from underlying-event measurements". In: *Eur. Phys. J. C* 80 (2020), p. 4. DOI: 10.1140/epjc/s10052-019-7499-4. arXiv: 1903.12179 [hep-ex].

[155] S. Agostinelli et al. "GEANT4—a simulation toolkit". In: *Nucl. Instrum. Meth. A* 506 (2003), p. 250. DOI: 10.1016/S0168-9002(03)01368-8.

[156] Ryan Gavin et al. "FEWZ 2.0: A code for hadronic production at next-to-next-to-leading order". In: *Comput. Phys. Commun.* 182 (2011), p. 2388. DOI: 10.1016/j.cpc.2011.06.008. arXiv: 1011.3540 [hep-ph].

[157] Ryan Gavin et al. " physics at the LHC with FEWZ 2.1". In: *Comput. Phys. Commun.* 184 (2013), p. 208. DOI: 10.1016/j.cpc.2012.09.005. arXiv: 1201.5896 [hep-ph].

[158] Michal Czakon and Alexander Mitov. "TOP++: A program for the calculation of the top-pair cross-section at hadron colliders". In: *Comput. Phys. Commun.* 185 (2014), p. 2930. DOI: 10.1016/j.cpc.2014.06.021. arXiv: 1112.5675 [hep-ph].

[159] Simone Alioli et al. "NLO single-top production matched with shower in POWHEG: s- and t-channel contributions". In: *JHEP* 09 (2009). [Erratum: 10.1007/JHEP02(2010)011], p. 111. DOI: 10.1088/1126-6708/2009/09/111. arXiv: 0907.4076 [hep-ph].

[160] *Baseline muon selections for Run-II*. URL: https://twiki.cern.ch/twiki/bin/viewauth/CMS/SWGuideMuonIdRun2.

[161] *https://twiki.cern.ch/twiki/bin/viewauth/CMS/SWGuideMuonIdRun2*. URL: https://twiki.cern.ch/twiki/bin/viewauth/CMS/SWGuideMuonIdRun2.

[162] *https://twiki.cern.ch/twiki/bin/view/CMS/CutBasedElectronIdentificationRun2*. URL: https://twiki.cern.ch/twiki/bin/view/CMS/%5C%5C%20CutBasedElectronIdentificationRun2.

[163] *https://twiki.cern.ch/twiki/bin/view/CMSPublic/SWGuidePFTauID*. URL: https://twiki.cern.ch/twiki/bin/view/CMSPublic/SWGuidePFTauID2.

[164] S Chatrchyan et al. "Time Reconstruction and Performance of the CMS Electromagnetic Calorimeter". In: *JINST* 5 (2010), T03011. DOI: 10.1088/1748-0221/5/03/T03011. arXiv: 0911.4044 [physics.ins-det].

[165] CMS Collaboration. "Time reconstruction and performance of the CMS electromagnetic calorimeter". In: *Journal of Instrumentation* 5.03 (Mar. 2010), T03011–T03011. DOI: 10.1088/1748-0221/5/03/t03011. URL: https://doi.org/10.1088%2F1748-0221%2F5%2F03%2Ft03011.

[166] Daniele del Re. "Timing performance of the CMS ECAL and prospects for the future". In: *16th International Conference on Calorimetry in High Energy Physics (CALOR)*. Vol. 587. 2015, p. 012003. DOI: 10.1088/1742-6596/587/1/012003.

[167] Vardan Khachatryan et al. "Jet energy scale and resolution in the CMS experiment in collisions at 8 TeV". In: *JINST* 12 (2017), P02014. DOI: 10.1088/1748-0221/12/02/P02014. arXiv: 1607.03663 [hep-ex].

[168] G. Cowan, "Statistics", Ch. 40 in Particle Data Group, P. A. Zyla, et al. "Review of particle physics". In: *PTEP* 2020 (2020), p. 083C01. DOI: 10.1093/ptep/ptaa104. URL: https://pdg.lbl.gov/2021/reviews/rpp2021-rev-statistics.pdf.

[169] *MET Corrections and Uncertainties for Run-II*. URL: https://twiki.cern.ch/twiki/bin/viewauth/CMS/MissingETRun2Corrections.

[170] Vardan Khachatryan et al. "The CMS trigger system". In: *JINST* 12 (2017), P01020. DOI: 10.1088/1748-0221/12/01/P01020. arXiv: 1609.02366 [physics.ins-det].

[171] The CMS Collaboration. "Description and performance of track and primary-vertex reconstruction with the CMS tracker". In: *Journal of Instrumentation* 9.10 (Oct. 2014), P10009–P10009. DOI: 10.1088/1748-0221/9/10/p10009. URL: https://doi.org/10.1088%2F1748-0221%2F9%2F10%2Fp10009.

[172] Martin Ester et al. "A Density-Based Algorithm for Discovering Clusters in Large Spatial Databases with Noise". In: *Proc. of 2nd International Conference on Knowledge Discovery and*. 1996, pp. 226–231.

[173] *Cosmic and Beam-Halo Muon Reconstruction Algorithms*. URL: https://twiki.cern.ch/twiki/bin/view/CMSPublic/SWGuideCosmicMuonReco.

[174] "Performance of missing transverse momentum reconstruction in proton-proton collisions at $\sqrt{\text{is/i}}$ = 13 TeV using the CMS detector". In: *Journal of Instrumentation* 14.07 (July 2019), P07004–P07004. DOI: 10.1088/1748-0221/14/07/p07004. URL: https://doi.org/10.1088%2F1748-0221%2F14%2F07%2Fp07004.

[175] *Beam Halo Filter*. URL: https://indico.cern.ch/event/518559/contributions/2132815/attachments/1264581/1871184/beamhalostatus.pdf.

[176] François Chollet et al. *Keras*. https://keras.io. 2015.

[177] Martín Abadi et al. "TensorFlow: Large-Scale Machine Learning on Heterogeneous Systems". 2015. eprint: 1603.04467.

[178] Albert M Sirunyan et al. "Search for new long-lived particles at $\sqrt{s}$ = 13 TeV". In: *Phys. Lett. B* 780 (2018), p. 432. DOI: 10.1016/j.physletb.2018.03.019. arXiv: 1711.09120 [hep-ex].

[179] CMS Collaboration. *Performance of quark/gluon discrimination in* 8 *TeV data*. CMS Physics Analysis Summary CMS-PAS-JME-13-002. 2013. URL: https://cds.cern.ch/record/1599732.

[180] Albert M Sirunyan et al. "Search for long-lived particles using delayed photons in proton-proton collisions at $\sqrt{s} = 13\,\text{TeV}$". In: *Phys. Rev. D* 100 (2019), p. 112003. DOI: 10.1103/PhysRevD.100.112003. arXiv: 1909.06166 [hep-ex].

[181] Vinod Nair and Geoffrey E. Hinton. "Rectified Linear Units Improve Restricted Boltzmann Machines". In: *Proceedings of the 27th International Conference on International Conference on Machine Learning (ICML)*. 2010, p. 807. ISBN: 9781605589077. URL: https://icml.cc/Conferences/2010/papers/432.pdf.

[182] Xavier Glorot, Antoine Bordes, and Yoshua Bengio. "Deep Sparse Rectifier Neural Networks". In: *Proceedings of the 14th International Conference on Artificial Intelligence and Statistics (AISTATS)*. Ed. by Geoffrey Gordon, David Dunson, and Miroslav Dudík. Vol. 15. 2011, p. 315. URL: http://proceedings.mlr.press/v15/glorot11a.html.

[183] John S. Bridle. "Probabilistic Interpretation of Feedforward Classification Network Outputs, with Relationships to Statistical Pattern Recognition". In: *Proc. of the NATO Advanced Research Workshop on Neurocomputing Algorithms, Architectures and Applications*. Ed. by Françoise Fogelman Soulié and Jeanny Hérault. Vol. 68. Springer Berlin Heidelberg, 1990, p. 227. ISBN: 978-3-642-76153-9. DOI: 10.1007/978-3-642-76153-9_28.

[184] John S. Bridle. "Training Stochastic Model Recognition Algorithms as Networks can Lead to Maximum Mutual Information Estimation of Parameters". In: *Advances in Neural Information Processing Systems*. Ed. by D. Touretzky. Vol. 2. Morgan-Kaufmann, 1989, p. 211. URL: https://proceedings.neurips.cc/paper/1989/file/0336dcbab05b9d5ad24f4333c7658a0e-Paper.pdf.

[185] Nitish Srivastava et al. "Dropout: A Simple Way to Prevent Neural Networks from Overfitting". In: *J. Mach. Learn. Res.* 15 (2014), p. 1929. URL: http://jmlr.org/papers/v15/srivastava14a.html.

[186] Diederik P. Kingma and Jimmy Ba. "Adam: A Method for Stochastic Optimization". In: *3rd International Conference on Learning Representations (ICLR), Conference Track Proceedings*. Ed. by Yoshua Bengio and Yann LeCun. 2015. arXiv: 1412.6980 [cs.LG].

[187] Albert M Sirunyan et al. "Electron and photon reconstruction and identification with the CMS experiment at the CERN LHC". In: *JINST* 16 (2021), P05014. DOI: 10.1088/1748-0221/16/05/P05014. arXiv: 2012.06888 [hep-ex].

[188] Georges Aad et al. "Measurement of the top quark-pair production cross section with ATLAS in pp collisions at $\sqrt{s} = 7\,\text{TeV}$". In: *Eur. Phys. J. C* 71 (2011), p. 1577. DOI: 10.1140/epjc/s10052-011-1577-6. arXiv: 1012.1792 [hep-ex].

[189] Serguei Chatrchyan et al. "Measurement of the Production Cross Section in the Dilepton Channel in Collisions at $\sqrt{s} = 7$ TeV". In: *JHEP* 11 (2012), p. 067. DOI: 10.1007/JHEP11(2012)067. arXiv: 1208.2671 [hep-ex].

[190] Albert M Sirunyan et al. "Performance of the reconstruction and identification of high-momentum muons in proton-proton collisions at $\sqrt{s} = 13$ TeV". In: *JINST* 15 (2020), P02027. DOI: 10.1088/1748-0221/15/02/P02027. arXiv: 1912.03516 [physics.ins-det].

[191] Albert M Sirunyan et al. "Precision luminosity measurement in proton-proton collisions at $\sqrt{s} = 13$ TeV in 2015 and 2016 at CMS". In: *Eur. Phys. J. C* 81 (2021), p. 800. DOI: 10.1140/epjc/s10052-021-09538-2. arXiv: 2104.01927 [hep-ex].

[192] CMS Collaboration. *CMS luminosity measurement for the 2017 data-taking period at $\sqrt{s} = 13$ TeV*. CMS Physics Analysis Summary CMS-PAS-LUM-17-004. 2018. URL: https://cds.cern.ch/record/2621960/.

[193] CMS Collaboration. *CMS luminosity measurement for the 2018 data-taking period at $\sqrt{s} = 13$ TeV*. CMS Physics Analysis Summary CMS-PAS-LUM-18-002. 2019. URL: https://cds.cern.ch/record/2676164/.

[194] CMS Collaboration. *Jet algorithms performance in 13 TeV data*. CMS Physics Analysis Summary CMS-PAS-JME-16-003. 2017. URL: http://cds.cern.ch/record/2256875.

[195] Albert M Sirunyan et al. "Performance of missing transverse momentum reconstruction in proton-proton collisions at $\sqrt{s} = 13$ TeV using the CMS detector". In: *JINST* 14 (2019), P07004. DOI: 10.1088/1748-0221/14/07/P07004. arXiv: 1903.06078 [hep-ex].

[196] Albert M Sirunyan et al. "Search for Higgsino pair production in collisions at $\sqrt{s} = 13$ TeV in final states with large missing transverse momentum and two Higgs bosons decaying via →". In: *Phys. Rev. D* 97 (2018), p. 032007. DOI: 10.1103/PhysRevD.97.032007. arXiv: 1709.04896 [hep-ex].

[197] *HEPData record for this analysis*. 2022. DOI: 10.17182/hepdata.NNNNN.

[198] Andrea Coccaro et al. "Data-driven model-independent searches for long-lived particles at the LHC". In: *Physical Review D* 94.11 (Dec. 2016). DOI: 10.1103/physrevd.94.113003. URL: https://doi.org/10.1103%2Fphysrevd.94.113003.

[199] Collaboration CMS. *A MIP Timing Detector for the CMS Phase-2 Upgrade*. Tech. rep. Geneva: CERN, 2019. URL: https://cds.cern.ch/record/2667167.

[200] *Technical proposal for a MIP timing detector in the CMS experiment Phase 2 upgrade*. Tech. rep. Geneva: CERN, 2017. DOI: 10.17181/CERN.2RSJ.UE8W. URL: https://cds.cern.ch/record/2296612.

[201] P Elmer, B Hegner, and L Sexton-Kennedy. "Experience with the CMS Event Data Model". In: *J. Phys.: Conf. Ser.* 219 (2010), p. 032022. DOI: 10.1088/1742-6596/219/3/032022. URL: http://cds.cern.ch/record/1354519.

[202] Simon Kwan et al. "The Pixel Tracking Telescope at the Fermilab Test Beam Facility". In: *Nucl. Instrum. Meth. A* 811 (2016), pp. 162–169. DOI: 10.1016/j.nima.2015.12.003.

[203] *The Phase-2 Upgrade of the CMS Level-1 Trigger*. Tech. rep. Final version. Geneva: CERN, 2020. URL: https://cds.cern.ch/record/2714892.

[204] Jia Liu, Zhen Liu, and Lian-Tao Wang. "Enhancing Long-Lived Particles Searches at the LHC with Precision Timing Information". In: *Phys. Rev. Lett.* 122 (13 Apr. 2019), p. 131801. DOI: 10.1103/PhysRevLett.122.131801. URL: https://link.aps.org/doi/10.1103/PhysRevLett.122.131801.